THE UNIVERSITY of ADELAIDE

School of Chemical Engineering and Advanced Materials

Elemental Detection at Ambient Condition by LIBS and Microwave-assisted LIBS

Md Abdul Wakil

PhD Thesis

July 2020

Table of Contents

Table of Contents

List of Figures and Table

Abstract

Contactless and sensitive elementals detection in real-time is important in wide range of industrial applications. Precise, accurate and fast detections are needed for the pharmaceutical industries, biological and medical samples, aerosol analysis and mining industry, exploration, space and defence.

Laser induced breakdown spectroscopy (LIBS) has become popular due to its outstanding advantages, including minimum sample preparation, fast, easy to operate, almost non-destructive, in situ analysis, real-time measurement. This work reports on the detection of several elements using LIBS and Microwave-assisted LIBS (MW-LIBS) in solid, liquid and gas phase at ambient conditions. These elements are chlorine, fluorine, bromine, sulphur, silver, palladium, ruthenium and potassium.

One of the focus of this study was to identify the minimum laser energy for quantifying the elements. For solid, samples from minerals and fabricated chemicals are calibrated to yield the detection limit. Elements such as sulphur, silver and palladium were detected using their strongest atomic emission transitions. It was found by using MW-LIBS the Limit of Detection (LoD) for palladium and sulphur was improved by 8 and 1.5 folds respectively. While, for palladium and sulphur, 92-times and 2-times signal enhancement were observed respectively.

For detecting the halogens such as chlorine, fluorine, and bromine, molecular emissions band were considered instead of atomic emissions. It was found by using MW-LIBS; the LoD for Cl, F and Br was improved 4 folds.

To assess the applicability of MW-LIBS for the detection of Cl, F, Br, Pd, S and Ag, the LoD was measured as 47±7 $\mu g.g^{-1}$, 106±6 $\mu g.g^{-1}$, 0.2±0.04%, 5 $\mu g.g^{-1}$, 312 $\mu g.g^{-1}$ and 4.5 $\mu g.g^{-1}$, respectively. Without the use of microwave, the values of the LoD were 139±23 $\mu g.g^{-1}$, 406.54 $\mu g.g^{-1}$, 0.8%, 40 $\mu g.g^{-1}$, 400 $\mu g.g^{-1}$ for Cl, F, Br, Pd and S respectively.

The applicability of MW-LIBS to detect silver and ruthenium in liquid phase was evaluated. Using MW-LIBS and based on the strongest atomic transitions, it was observed that MW-LIBS can generate significantly high signal at small laser energy, The LoD of silver and ruthenium in aqua phase was measured as 385 ppb and 957 ppb respectively. Without the use of microwave, the detection these elements, at the same low laser energy, was not possible.

To find common enhancement behaviour of MW-LIBS, the tendency of signal enhancement for solid matrix at ambient conditions was determined. It was observed that the Upper Energy Level (UEL) of each transition plays key role in signal enhancement. Significant enhancement is possible for the elements with upper state energy level below 5eV. However, no signal enhancement was observed for transition with UEL higher than 7eV. This is termed as the cut-off limit of signal enhancement. A simple model was developed to predict the MW-LIBS vs LIBS signal-to-noise (SNR) improvement concerning all elements in periodic table. The model predicts that the highest SNR improvements can be achieved for potassium, which are 370 times and 100 times, with and without detector gain, respectively. Based on atomic detection, it was demonstrated that microwave radiation will not improve SNR for elements such as fluorine, chlorine, bromine and iodine.

Finally, LIBS was applied in gas-phase, to study the temporal behaviour of potassium release in biomass with Si contents. The results indicate that the potassium release rate is different for different biomass combustion in three stages of combustion such as devolatilisation, char and ash. Using LIBS it was possible to conclude that the combustion of willow wood with different Si contents significantly inhibited the K release during both char combustion and ash-cooking stage.

Preface

The work outlined in this thesis was performed in the School of Chemical Engineering and Advanced materials at The University of Adelaide from November 2016 to March 2020. This thesis by publication consists of nine chapters, proceeded by short summary of each publication. The first chapter introduces traditional offline detection techniques, Laser Induced Breakdown Spectroscopy (LIBS) technique and signal enhancement techniques including Microwave-assisted Laser Induced Breakdown Spectroscopy (MW-LIBS). The second chapter covers the background for this thesis including MW-LIBS mechanism, MW-LIBS plasma parameters measurement technique. This chapter also describes some background on detection of elements in solid, liquid and gas phase and a link between each of the publications. The next six chapters consist of six journal articles as first author, two of them are pear reviewed, written jointly with other researchers from Laser Diagnostics Lab. One article as co-author namely additional paper is added as additional paper. Chapter III, IV, VI and additional paper presents various elements limit of detection at ambient conditions using MW-LIBS technique in solid samples. Chapter V and part of Chapter VI deals with element detection in liquid samples using the same technique. Chapter VII presents the signal enhancement tendency of MW-LIBS. Chapter VIII represents the potassium release and temperature profile in biomass combustion. The conclusions and implications are described in the last chapter of the thesis.

Thesis Declaration

I certify that this work contains no material which has been accepted for the award of any other degree or diploma in my name, in any university or other tertiary institution and, to the best of my knowledge and belief, contains no material previously published or written by another person, except where due reference has been made in the text. In addition, I certify that no part of this work will, in the future, be used in a submission in my name, for any other degree or diploma in any university or other tertiary institution without the prior approval of the University of Adelaide and where applicable, any partner institution responsible for the joint-award of this degree.

I acknowledge that copyright of published works contained within this thesis resides with the copyright holder(s) of those works.

I also give permission for the digital version of my thesis to be made available on the web, via the University's digital research repository, the Library Search and also through web search engines, unless permission has been granted by the University to restrict access for a period of time.

Md Abdul Wakil, 14th July 2020

List of Publications

Paper I: M.A. Wakil, Z.T. Alwahabi, Microwave-assisted laser induced breakdown molecular spectroscopy: quantitative chlorine detection, J. Anal. At. Spectrom., 34 (2019) 1892-1899.

Paper II: M.A. Wakil, Z.T. Alwahabi, Quantitative Fluorine and Bromine detection at ambient condition via Molecular Emission (Submitted for publication in J. Anal. At. Spectrom).

Paper III: M.A. Wakil, Z.T. Alwahabi, Gated and non-gated Silver Detection using Microwave-assisted Laser Induced Breakdown Spectroscopy (Submitted for publication in J. Anal. At. Spectrom).

Paper IV: Abu Farhan Abu Kasim[‡], M. A. Wakil[‡], Kevin Grant, Milton Hearn, and Zeyad T. Alwahabi, Contactless ruthenium detection at low level in real time (Submitted for publication in Optics and Laser Technology).

Paper V: M.A. Wakil, Z.T. Alwahabi, Signal Enhancement Tendency of Microwave-assisted Laser Induced Breakdown Spectroscopy: Application to Sulphur Detection (Submitted for publication in Spectrochimica Acta Part B: Atomic Spectroscopy).

Paper VI: Haibo Zhao, M.A. Wakil, Jan Viljanen, Qiang Song, Qiang Yao, C. W. Kwong, and Zeyad T. Alwahabi, In Situ Measurement of Potassium Release during Biomass Combustion Using Laser-Induced Breakdown Spectroscopy: Effect of Silicate on Potassium Release, *Energy & Fuels 34* (2020), 3262-3271.

Paper VII (Additional): A.A. Al Shuaili, A.M. Al Hadhrami, M.A. Wakil, Z.T. Alwahabi, Improvement of palladium limit of detection by microwave-assisted laser induced breakdown spectroscopy, Spectrochimica Acta Part B: Atomic Spectroscopy, 159 (2019) 105666.

Acknowledgements

All praise is due to Allah, the Lord of the heaven and the earth, the all merciful, the very merciful Who allow me to accomplish such a target which I desired most in this worldly life. The completion of this thesis could not have achieved without the contributions and support from those people listed below.

I would like express my gratitude to my principal supervisor, Associate Professor Zeyad Alwahabi, for providing me the opportunity to do research in such interesting areas of elemental detection incorporated with microwave-assisted laser induced breakdown spectroscopy diagnostic technique. I really appreciate his unwavering guidance, confidence and support throughout my PhD candidature. Thank you Zeyad. Support from my co-supervisor, Dr. Philip Kwang is also gratefully acknowledged.

All the financial support is gratefully acknowledged. Support for this work was provided by Adelaide Scholarship International (ASI). Special Thanks to the school of Chemical Engineering and Advanced materials for their support. Also thanks to all of my lab mates, especially Waxia Zhao who support me a lot in ordering my experimental equipment, my previous lab mates Haibo Zhao in data processing. I would like to thank the colleagues in Chemical Engineering workshop, particularly Jesan who assisted me in experimental setup.

The editors and the anonymous journal reviewers are gratefully acknowledged for their insight comments on the papers listed in this thesis.

My Aussie and home country friends in Australia have always been available to give me advice. This is gratefully appreciated which is unforgettable. Thank you all.

Last, not least, I want to express my gratitude to my wife, my parents, and my brothers for their endless love and encouragement throughout the journey of completing this thesis.
Thank you.

Md Abdul Wakil

Summary of Each paper

Paper I

This paper reports the quantitative detection of chlorine, through molecular emission form CaCl, using microwave assisted Laser Induced Breakdown spectroscopy (MW-LIBS). CaCl emission is utilised at the spectral range of 617.9-621.5 nm. Using time-resolved emission spectra of CaCl at 617.9 nm, following 1.5 ms microwave pulse, an optimum gate-width and gate-delay have been established. A linear relationship between the intensity of CaCl molecular emission and chlorine concentration on cement surface has been validated. This yields a limit of chlorine detection (LoD) of 47±7 $\mu g.g^{-1}$ and ~170±59 $\mu g.g^{-1}$, based on 100 shots averaged and single shot respectively. The results represent a 10-fold improvement in the chlorine LoD on cement.

Paper II

This paper reports the limit of detection (LoD) of fluorine and bromine, based on emission from CaF and CaBr, using Microwave-assisted Laser Induced Breakdown Spectroscopy (MW-LIBS). Molecular emission bands of CaF and CaBr in the spectral range of 605 nm and 627.1 nm are utilised for quantitative fluorine and bromine detection. The optimum gating has been established for the CaF, at 603.3 nm and 605 nm, following 1.5 ms long microwave pulses. The MW-LIBS plasma temperature and electron density against laser energy have been demonstrated at constant microwave power coupling to optimise laser energy using Ca I lines. A linear relationship between CaF signal strength and fluorine concentration, and CaBr signal strength and bromine in cement has been validated. The recorded limit of fluorine and bromine detection was 106±6 μg/g and 0.2±0.04%, respectively. The results represent an improved detection limit at low laser energy and 4-fold improved detection limit for bromine.

Paper III

This paper reports the quantitative ruthenium detection in liquid phase using Microwave-assisted Laser Induced Breakdown Spectroscopy (MW-LIBS). Aqueous ruthenium, in flow jet, was detected in real-time at ambient condition. A 10mJ laser energy and 750W microwave power were directed at an open liquid jet sample of ruthenium, as a 5% (v/v) aqueous hydrochloric acid solution, with concentrations ranging from 50ppm to 2000ppm. At low concentration of ruthenium, using 10mJ of laser energy per pulse and without microwave application, no ruthenium signal could be reliably detected at high sensitivity. It was observed, for liquid flow, the coupling efficiency between the microwave and the laser-induced plasma was limited to 43%. The ruthenium's signal-to-noise ratio improvement for MW-LIBS, with respect to LIBS, was 76-fold. Based on MW-LIBS, the limit of detection (LoD) for ruthenium was determined to be 957±84ppb. This first example on real-time aqueous ruthenium detection paves the way for online monitoring of low concentration of Ru in industrial processes.

Paper IV

This paper reports on detection of silver in solid and liquid phase using microwave-assisted laser induced breakdown spectroscopy (MW-LIBS). For solid sample analysis, the limit of detection (LoD) with a gated detector has been compared with a portable spectrometer with non-gated detector. The LoD achieved by the gated and non-gated detectors are 4.5±1.0 ppm and 7±2.3 ppm, respectively. For aqueous silver, The LoD was found to be 385±51 ppb. The LoD using MW-LIBS is more effective in liquid samples analysis than solid sample analysis for atomic detection. For MW-LIBS, it was observed that relatively low laser energy is sufficient to develop calibration curve and achieve outstanding LoD.

Paper V

This study reports the signal enhancement tendency of Microwave-assisted Laser Induced Breakdown Spectroscopy (MW-LIBS). Six elements with emission lines at upper energy level (UEL) ranging from 3.65 eV to 6.86 eV were selected, namely Ag, Cu, Fe, Mg, Pb and S. The signal-to-noise (SNR) improvement, for each element, has been examined experimentally and the effects of microwave power and detector gain on signal enhancement were assessed. The plasma temperature has been evaluated, based on Ca I and Pb I lines, as function of microwave power and time delay. It is found that the SNR improvement inversely depends on the value of UEL. Using microwave radiation, significant enhancement is possible for the elements with the UEL below 5eV and the cut-off limit of signal enhancement is found to be ~7eV. Based on data, a simple model is developed to predict the SNR improvement for elements. The model predicts that the highest SNR improvements may be achieved for potassium, namely 530±15 times and 150±4 times, with and without detector gain, respectively. Based on atomic detection, it is demonstrated that microwave radiation will not improve SNR for elements such as fluorine, chlorine, bromine and iodine. It confirms that plasma temperature in MW-LIBS plasma is virtually independent of delay-time and the microwave exerts no reheating impact in plasma. The detection of sulphur at 180.73 nm, using a portable spectrometer equipped with a non-gated detector validated the model. Employing 10 mJ at 532 nm, 2-fold signal enhancement and 312 µg/g limit of detection was recorded experimentally. The model is based on 5 mJ laser energy.

Paper VI

In this study, an improved calibration method for the in-situ measurement of potassium (K), concentration in the flame field was developed using laser induced breakdown spectroscopy (LIBS). The temporal behaviours of K release and particle temperature were recorded simultaneously during biomass combustion. During combustion of raw willow wood, the majority of K was released during ash-cooking stage, followed by char combustion stage, only a small amount of K was released during the initial devolatilization stage. The results indicated during devolatilization stage K was released due to the decomposition of organic K. Char- K was subsequently converted to K_2CO_3 and most K_2CO_3 was subsequently released during final ash-cooking stage. In the case of rice straw combustion, K was mainly released during the initial devolatilization stage, most likely as KCl. The transformation of char-K and the K-Si reaction forming K-silicates mainly occurred during char combustion stage, K was found to be released slowly from K-silicates during ash-cooking stage. The combustion of willow wood with different Si contents demonstrated that Si significantly inhibited the K release during both char combustion and ash-cooking stage.

Paper VII (Additional work)

In this paper, we demonstrate microwave-assisted laser-induced breakdown spectroscopy (MW-LIBS) to detect palladium (Pd) in solid samples at ambient conditions. Microwave radiation was introduced by a near field applicator to couple the microwave radiation with the plasma. The results were a 92–fold enhancement in palladium signal with 8-fold improvement in the limit of detection at laser energy levels below 5 mJ (1250 J/cm2 laser pulse fluence). We also investigate the optimum experimental parameters of palladium detection for both laser-induced breakdown spectroscopy (LIBS) and MW-LIBS. The maximum signal to noise ratio improvement was achieved at microwave power of 750W and laser pulse fluence of 157 J/cm2 for Pd I 340.46 nm. Finally, we examine the location of the near field applicator (NFA) with respect to the sample to show that the MW-LIBS signal strength was significantly affected by the vertical position compared to the horizontal. The detection limits of palladium with LIBS and MW-LIBS were 40 ppm and 5 ppm respectively.

Chapter 1

Introduction

Due to the wide range of potential elements applicable to modern technological developments, elemental detection techniques, at ambient conditions, are important. These have significant input in environmental, chemical processing, space and defence, pharmaceutical, food industries, medical and mineral resources. In addition, it is crucial to understand the element release behaviour of different fuels during combustion because journey of the adverse chemical compounds start during combustion when they are released from the fuels. Most of the traditional methods are offline such as atomic absorption spectrometry (AAS), X-ray fluorescence (XRF) and inductively coupled plasma spectroscopy (ICP) for industrial process analysis. Optical techniques are sensitive, selective and enable spatially localized, temporal measurements without physical sampling. They can offer precise, accurate and fast detection in real-time of precious or toxic elements.

Atomic absorption spectrometry (AAS) is a technique that has interesting characteristics such as simple instrumental arrangement, high selectivity and specificity, reduced spectral interference caused by overlapping of molecular lines and bands of other elements, excellent robustness of atomizer for the elimination of the matrix of the samples [1]. However, one of the main limitations is the mono-element determination, which can compromise the analytical throughput if a high quantity of analytes needs to be determined in several sets of samples [2].

Inductively coupled plasma (ICP) spectroscopy techniques in which, atomized samples can be detected using different methods, such as atomic emission [3] or by a mass spectrometer [4]. For simultaneous multi-element determination, ICP OES and ICP MS are the most commonly used techniques due to their accurate and precise analysis, low limit of detection (LoD) and versatility regarding different types of samples. ICP OES, commercial apparatus mainly use liquids for the analysis but the application of argon gas caused an inferior LoD of trace element [5]. However, ICP is not feasible for fast dynamic measurements as the signal integration times are typically fairly long compared with optical methods and hence, mostly be suitable for emission monitoring of continuous processes [6]. On the other hand, these techniques require a dissolution step, as sample preparation can be laborious, with high reagent and time consumption (and waste generation) in addition to analyte loss and possible sample contamination. Bonta et al. demonstrated that laser ablated ICP MS is not capable of analysing H, N, O, C due to high background signal [7]. The addition of electro-thermal vaporization (ETV) ICP OES/ ICP MS can eliminate or reduce sample preparation step and can be coupled with ICP OES and ICP MS to increase its potentialities [8]. The versatility of the coupled ETV-ICP OES and ETV-ICP MS allows the analysis of small liquid, slurry, and solid samples [1].

X-ray fluorescence spectrometry (XRF) is a versatile and commonly used technique for solid sample analysis in geological and mineral survey, environmental pollution investigation, alloy analysis, cultural relic identification and industrial process analysis [9, 10]. Another important aspect of the technique is the possibility of in situ analysis, allowing, for example, direct determination in works of art to identify materials and their eventual corrosion products determination of their origin, processing and use, understanding their processes of deterioration. XRF has been used by geochemists for the past 50 years as a first-order technique to determine the whole-rock chemistry of geological samples [11]. The main advantages of XRF analysis are the limited preparation required for solid samples, non-destructive analysis, increased total speed, decreased production of hazardous waste, low running costs and portability[11, 12]. Accurate determination of composition depends on proper sample preparation, sample introduction, instrumental setup of the XRF [13], the energy level of the element, scanning time, particle size and moisture content of the sample [14]. Sapkota et al. demonstrated that the proper drying and grinding of the samples could cause better results using XRF [15].

Conventional XRF spectrometers can normally be divided into two categories: energy disperse XRF (EDXRF) and wavelength disperse XRF (WDXRF). The WDXRF has some analytical advantages over EDXRF such as better resolution, low LoD, high accuracy and ability to analyse a wide range of elements [1, 10]. However, there are some disadvantages of XRF such as poor sensitivity to light elements (low Z matrix) due to broad and large background, [16, 17], strict adherence to sets of standards and principle of sample preparation [18], comparably long measuring time [19] and inferior LoD. Moreover, there are interference factors such as uneven measurement surface, sample composition change (matrix effect) and humidity change which need to be corrected to ensure the accuracy of element analysis [9]. James Terrel [20] mentioned in his report that elements lighter than magnesium cannot be measured using XRF. It is reported that XRF cannot be used for beryllium content, which is a distinct disadvantage when measuring alloy or other materials that contains beryllium [21, 22]. In addition, XRF is much more accurate for measuring large crystalline structure rather than small ones.

However, XRF is considered to be popular method till today for variety of field as portable XRF [11, 15]. To increase the sensitivity of XRF, several techniques have been applied. Luo et al. observed that the application of filter in primary X-ray channel and collimation of secondary characteristic X-ray could effectively improve the spectral composition and improve the signal to noise ratio (SNR) [23]. E. Margu´ et al. claimed the use of a Gd anode x-ray tube and a Ge semiconductor detector overcomes the problems of reduced sensitivity and spectral interferences inherent [24]. Holmes et al. analysed filter membranes (not infinitely thick) loaded with variable masses of powdered obsidian and demonstrated that at low membrane mass loadings, XRF signal intensity is a linear function of the sample mass [25]. Hagen Stosnach et al. [19] claimed that the use of total reflection XRF (TXRF) could cause the sample preparation easy and quantification does not require extra calibration and correction of matrix effect. Klockenkamper et al. mentioned in their study that the use of TXRF could minimize or remove matrix effect [26]. Richard Arthur et al. applied TXRF for quantifying cobalt concentration in the presence of high iron concentration and estimated cobalt concentration of 50µg/L in the presence of 400-fold iron concentration [27].

However, XRF is, by its nature, preferentially used for solid samples and is not very suitable for the assessment of dissolved components in aqueous samples; some pre-concentration is often necessary. Eva margui et al. described two general methods used for liquid samples analysis such as a (1) liquid deposited in a special samples holder and (2) evaporated onto a support under a vacuum including technical difficulties [28]. For example, when using first method, bubbles released from solutions due to inadequate sample holder filling and heating of the solution can give certain problems. Moreover, liquid samples usually provide a high X-ray scatter background resulting poor SNR. Malkov et al. demonstrated TXRF method in aqua samples of seawater and came to the conclusion that TXRF is unable to detect trace heavy metals by direct dosing of a sample [29]. They also demonstrated that the sample pre-concentration could help to determine the concentration of heavy metals in seawater.

Laser induced breakdown spectroscopy (LIBS) is a promising fast detection technique that may satisfy the requirements of mining industries due to its substantial unique characteristics such as *in situ*, online and multi-element analysis with minimal or no sample preparation. However, LIBS technique has been lacking the dynamic measurement range required for versatile elemental detection. With samples containing high concentration of desired analyte element, LIBS measurement sensitivity suffers from optically thick conditions that leads to self-absorption deteriorating the attainable emission signal. In addition, LIBS falls behind its competing techniques in LoD that hinders the detection of trace elements. In this thesis, the possibility to use microwave radiation to mitigate the shortcomings of LIBS is studied in detail among the other techniques to enhance the properties of LIBS. This work reports on the detection of several elements using LIBS and Microwave-assisted LIBS (MW-LIBS) in solid, liquid and gas phase at ambient conditions.

1.1 Basic mechanism of plasma formation and fundamental of LIBS

LIBS is a type of atomic emission spectroscopy, which usually uses highly intensive laser light to form a plasma. The high laser light heats the sample, made them ionized, and collide each other to form plasma. LIBS is able to detect the element of a sample regardless its physical state of the sample rather it is solid, liquid or gas. Qualitative and quantitative analyses are carried out by monitoring emission line positions and intensities. This technique is mainly based on collecting the emission from ionic, atomic and molecular species in a plasma spark. LIBS can detect the element limited by the laser energy as well as the sensitivity and wavelength range of the spectrometer. The obvious advantage of this technique is simplicity, no sample preparation, ability to analyse sample in real time in-situ measurement quantitatively [30]. LIBS is also applicable to conductive and non-conductive samples and to the analysis of extremely hard materials that are difficult to digest or dissolve, such as ceramics and semi or super-conductors [30, 31].

To produce a spark in air or gas requires laser intensities of the order of 10^{11} Wcm^{-2}. The sparks are produced by the breakdown of gas due to the electric field associated with light wave. Breakdown results from strong ionization and absorption by gases that usually transparent to light. Breakdown thresholds are the order of 10^6 to 10^7 Wcm^{-1} [32]. When a highly intensive laser beam focuses onto a material and breakdown the threshold of a material, (~1-10MW/cm^2) causes to generate a transient high-density plasma. This diagnostics technique is termed as LIBS. When a laser pulse is focused on a surface, the breakdown happens in two steps. Firstly, the generation of free electrons that serves as an energy receptor through three-body collision with photons and neutrals. Secondly, the avalanche ionization in the focal region. Generally, the free electrons are accelerated by the electric field associated with the optical pulse during collision which thermalize the electron energy distribution with the increase of electron energy, collision produce ionization, other electrons, more energy absorption and an avalanche [33]. Due to collision, the material starts to evaporate and within the vapour and surrounding atmosphere, a plasma is generated leading to their spontaneous emission of radiation [30]. The plasma decays and emits element-specific radiation. The emission is resolved spectrally and is detected by a spectrometer.

Because the laser plasma is a pulsed source, the resulting spectrum evolves rapidly in time. The temporal history of a laser-induced plasma is illustrated schematically in figure 1.1. The majority of LIBS measurements are conducted by using the RSS (repetitive single spark) in which a series of individual laser sparks are formed on the sample at the laser repetition rate (e.g. 10 Hz).

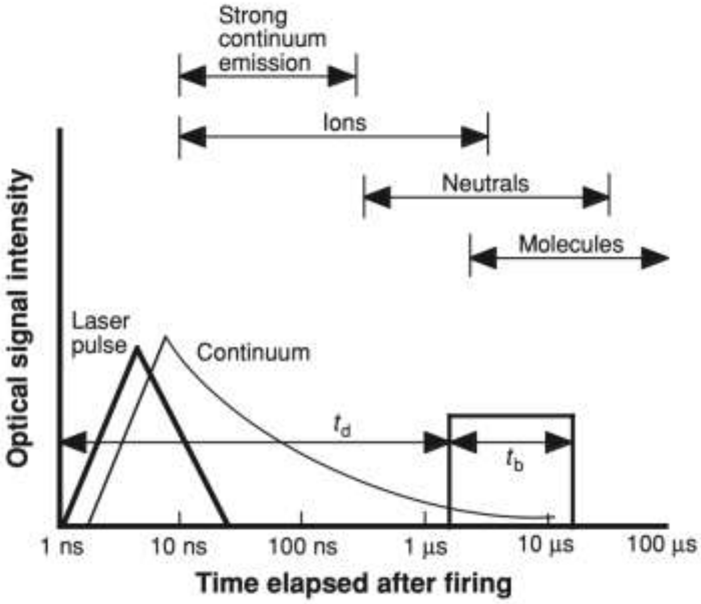

Figure 1.1. Temporal history of laser induced plasma [30]. Here t_d is the time delay and t_b is the gate pulse width

When the laser irradiance is less than the threshold, no significant attenuation is observed but with exceeding irradiance of threshold causes the absorption so strong that it is often used as critical test of whether breakdown has actually occurred [32]. For a solid target when a high laser beam strike, it produces a plasma due to rapid melting and/or vaporizing the solid sample surface.

The shorter pulse with high power do not produce much vaporization but removes only a small amount of material from the surface whereas, low power pulse creates deep, narrow holes in the target [32].

1.2 Application of LIBS in diversifying field

LIBS method was started about four decades before, prior to 1980 in a ruby crystal [30]. Today, the application of LIBS is widespread in the range from clean energy and biomedicine to space exploration because of its unique advantage than other techniques [31, 34]. LIBS is useful to detect the element in wide variety of atmosphere. For example, agricultural application to trace the toxic and nutrient element in soil [35-38], in analysing the concentration of element at sample surface [39, 40], to understand the composition of an alloy [41-43]. In addition, to analyse environmental emission [44-48], industrial waste [49-51], trace element in water [52], low concentration of the elements [53], contamination of element in food [54, 55], elemental concentration at different combustion phase [56-59], in aqueous solution [52, 60], enhancement of elemental emission [47], elemental detection in gunshot residue [61], and explosive [62, 63]. This technique is also useful for analysing the enhancement of molecular band emission [64, 65], chemical imaging [66], cultural heritage application [67], pharmaceutical materials [68] and matrix effect of a sample on element detection [69].

1.3 LIBS signal enhancement

Although LIBS is found as, a valuable tool for elemental analysis as discussed above but in comparison with other analytical techniques, it has been realized that the poor LoD is the most serious limitation of LIBS technique. The major limitations of LIBS for practical applications results from self-absorption, matrix effect, line broadening [31]. It is found to be less sensitive to the elements (nuclear fuel) which has complex structure [70], low excitation efficiency [71] and high ionization energy [72] such as halogens. In addition, the elemental analysis with low concentration as well as the heavier molecules require high resolution of detection.

To increase the sensitivity of LIBS and to improve the LoD, several techniques associated with LIBS are available in literature such as spatial confined LIBS, magnetic confined LIBS, double pulse LIBS, spark discharge LIBS, laser induced fluorescence LIBS, resonant LIBS and microwave assisted LIBS. A brief description of each enhanced technique is given as follows.

Spatial confined LIBS is a flexible cost-effective method where the plasma is confined in a small size cavity such as cylindrical or hemi-sphere in order to improve the detection sensitivity. It is worth to noting that the cavity size plays an important role in signal enhancement. Li et al. investigated the effect of wall distance and observed an enhancement of 5.2 times for Cu at a wall distance of 9 mm [73]. Guo et al. optimized the hemispheric cavity dimension with a diameter of 5 mm and obtained an enhancement of 3.9 time than LIBS [74]. Although this method is easy to operate but it is not widely used in real life due to low enhancement factor.

In **Magnetic confined LIBS** method, magnetic field is applied to confine the laser-produced plasma in LIBS. Xiao et al. investigated the TEXTOR tokamak and observed a significant enhancement in the spectral line in the presence of magnetic field in LIBS [75]. Rai et al. examined magnetic field confined LIBS for both solid and liquid phase and claimed an enhancement of 2 times for Al and 1.5 times for Mn solution [76]. Hao et al. demonstrated that the use of ring magnet could cause an improvement in LoD than in open air. They claimed the LoD improved by 4 time for V and 2 times for Mn [77].

In **Double pulse or dual pulse LIBS** (DP-LIBS), laser ablation has been coupled with an additional source such as another laser or high voltage power supply. DP-LIBS is considered an effective approach to improve the analytical performance of LIBS technique. According to the direction and sequence of laser beams, several geometrical configurations have been suggested such as collinear, cross beam, orthogonal reheating and orthogonal pre-ablation [78]. Lifeng et al. applied collinear double pulse LIBS on Mg alloy and observed 4.7 times enhancement than single pulse LIBS [79]. Hai et al. investigated DP-LIBS using combination of circular and annular nanosecond laser pulse and observed 4 time signal enhancement and 3 times improved LoD for Li and Mg [80]. Zhao et al. found 3 times improved LoD for Pb in soil using DP-LIBS [81]. Yang et al. achieved 30 times signal enhancement of femtosecond LIBS combining with nanoparticle and dual pulse for Si at 288 nm [82]. Zhang et al. investigated DP-LIBS in Cu aqua solution and reported 15 times improved LoD for Cu [83].

Spark discharge LIBS (SD-LIBS) is an analytical technique that draws from both spark spectroscopy and laser-induced breakdown spectroscopy. SD-LIBS combines conventional LIBS instrument with a high voltage and fast pulse discharge circuit. This technique is limited with conductive samples and currently predominately used for alloy analysis [84]. Akhtar et al. claimed that the LoD of trace, minor and toxic elements can be improved using SD-LIBS and they reported Cu LoD of 0.028 ppm [85]. Nassef et al. observed 6 times enhancement in signal to background ratio (S/B) of Al II at 358.56 nm using SD-LIBS [86]. Li et al. observed 2-3 times improved signal to noise ratio (S/R) for Si in soil samples [87]. Jiang et al. demonstrated 3-9 times improved LoD for Pb I, Fe I and Al I at 368.35 nm, 358.12 nm and 396.15 nm respectively using SD-LIBS than LIBS [88]. Kang et al. claimed that the self-absorption of LIBS can be avoided with SD-LIBS [89].

Laser induced fluorescence LIBS is a type of resonant enhancement method for LIBS spectral signal. In this approach, a secondary laser beam with a specially tuned wavelength is focused on the plasma generated by LIBS. Target atoms in the plasma are resonantly exited by laser beam with a specific wavelength whilst the laser beam is ineffective to other atoms. Thus, the spectral intensity of targeted atom, which improves the analytical sensitivity [90, 91]. Gao et al. observed an enhanced signal for Sb I at 287.79 nm using laser-induced fluorescence assisted LIBS (LIBS-LIF) while only LIBS failed to detect Sb I. They used very low laser energy of 3 mJ [92]. Guo et al. determined B using BO molecular emission and reported LoD for B of 0.0993% by LIBS-LIF [93]. Li et al. claimed in their study that the signal of CN was 2 time stronger with LIBS-LIF than LIBS [91]. Similarly, Zhao et al. achieved signal enhancement of 32 times for Al I at 396.15 nm [94]. Wang et al. applied LIBS-LIF in water and found an order of 4-5 times improved LoD for Cu [95]. Similarly, Li et al. reported 6 times improved LoD for U II at 409.01 nm in their study [96].

Resonant LIBS (RELIBS) is a signal enhancing technique where plasma is formed and heated by photo-resonant excitation of the host species in the plume. In RELIBS technique, the excitation wavelength is tuned to a strong absorption line of one of the major species, which causes energy transfer to the analyte through multi-step collision processes [97]. The main advantage of RELIBS over LIBS is the simultaneous multiple species determination [98]. Xiong et al. reported in their study that the signal intensity of Ti can be enhanced to 130 times at 282.34 nm with RELIBS compared with LIBS [99]. Similarly, khachatrian et al. claimed the significant enhancement for H, C and Si with RELIBS [100]. Rifai et al. achieved 50 and 60 times better LoD for Mg and Al with RELIBS than LIBS [98]. Tang et al. achieved more than 3 times improved LoD for Pb I at 405.78 nm with double pulse RELIBS than RELIBS [101].

Microwave-assisted LIBS is a technique where, the addition of microwave radiation as an excitation source in LIBS instead of using additional laser or photo-resonant or high voltage discharge circuit to form Microwave-assisted LIBS (MW-LIBS) is another prospective method for signal enhancement. MW-LIBS offers several benefits, for example long plasma life cycle, larger volume, strong emission intensity, stability over time and the ability to reduce self-absorption [102-105], which subsequently enhances the signal’s intensity. MW-LIBS is a popular method in which low laser energy is sufficient for element detection instead of high laser energy in LIBS to improve the LoD. Khumaeni et al. [103] have demonstrated that the sensitivity of MW assisted LIBS is about 8 times higher than DP-LIBS (dual pulse LIBS). A laser-assisted microwave plasma spectroscopy (LAMPS) technique was reported by Efthimion [106], with the achievement of ~ 200 times enhancement. Tampo et al. had achieved a 50-fold enhancement of Gd lines at a low-pressure of 0.6 kPa [107]. Viljanen et al. observed about 93-fold higher LoD with MW-LIBS for copper using solid samples [105]. Wall et al. reported

11.5-fold improved LoD for indium in aqua solution [108]. MW-LIBS has been demonstrated for gas samples for the detection of Na, K and Ca in flames [109]. Furthermore, Iqbal demonstrated MW-LIBS with spectrometer free detection of indium, based on imaging [110].

The objectives of this study are to apply MW-LIBS in both solid and liquid phase for elemental detection such as Chlorine, Fluorine, Bromine, Sulphur, Silver, Palladium, Ruthenium using their most strong atomic lines or molecular emission bands. As the MW-LIBS is a signal enhancing technique, so it is necessary to find the factors responsible for MW-LIBS signal enhancement. This thesis reports the MW-LIBS signal enhancement rules and a simple model for assessing the enhancement of an element. In addition, application of LIBS in gas phase to study the temporal behavior of potassium release in biomass. Detailed aims are presented in turn within each paper.

Chapter 2

Background

2.1 Microwave-assisted LIBS mechanism

The MW-LIBS mechanism relies on the coupling of microwave radiation with laser induced plasma at a critical electron density. The critical electron density is about 7×10^{10} cm^{-3} for a microwave radiation at 2.45 GHz [111]**.** Initially, the laser-induced plasma has high electron density in the order of 10^{17} -10^{19} cm^{-3} where the plasma acts as a reflector [111] but during the relaxation of plasma, the electron density at the periphery of the plasma falls to below the critical electron density. This allows microwave radiation, through the electromagnetic field, to drive the motion of free electrons and provides them with kinetic energy to excite the surrounding atoms and ions via multiple electron-atom or electron-ion collisions. As long as the microwave is coupled with plasma, the emission's lifetime increases to the microwave duration. The consequence is the higher emission due to larger integration time. Ikeda et al. have shown plasma size and plasma life in their study as shown in figure 2.1 (a, b) [102]. This extends the plasma lifetime resulting in promising improvement in sensitivity.

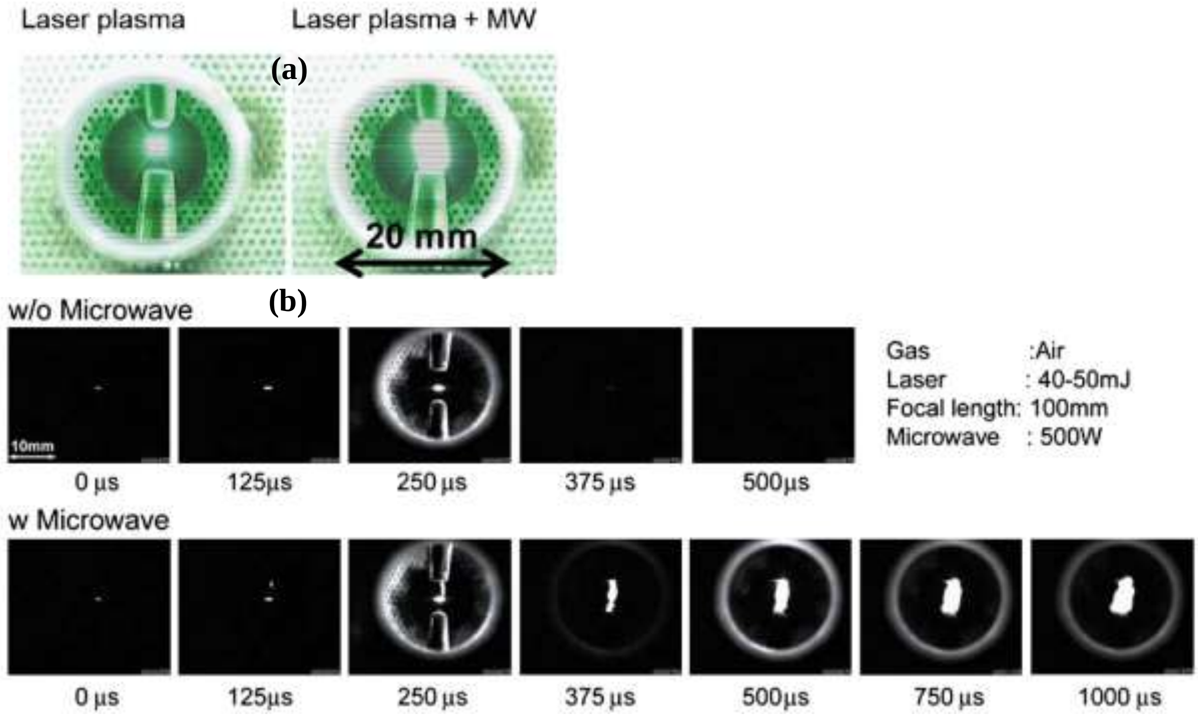

Figure 2.1. Laser and spark-induced plasma with and without microwave (MW) (a), Plasma photos were taken by a standard commercially available digital camera (GX200, Ricoh); high-speed images of laser-induced plasma with and without MWs, these were produced using a high-speed camera (frame rate 125 µs⁄frame, time range 0 to 1000 µs) [102].

However, the use of MW-assisted LIBS methods started in few year back due its underlined benefits such as long lifetime, larger volume, strong emission intensity and stability with time [102]. Several methods have been applied for the injection of microwave radiation into the plasma. For instance, enclosed microwave cavity [111], a loop shaped antenna [70], an antenna with microwave shield [102] and the use of near-field applicator (NFA) [105]. Liu et al. used microwave cavity between focusing lens and sample so that plasma can expand into the cavity and get coupled with microwave [111]. Khumaeni et al. utilized loop shape antenna with 30 mm length and 3-9 mm dia. and found good results with 3mm loop dia. microwave LIBS system.[70]. Ikeda et al. conducted their study with cone shaped antenna with a mesh chamber, which functioned as resonator and microwave leakage shield [102]. Viljanen and his group made coupling the plasma with microwave by using a sharp end (~45° angle) at the tip of a near field applicator to maximize the electric field near the tip without microwave radiation emission [105]. Chen, S. et al. [112] conducted their study on optimum design of near field applicator (NFA) in order to maximize the electric field strength at the location of plasma created and found the design with 30 mm diameter ground plane located close to the conductor gave the significant signal enhancement. They applied this technique on solid copper containing ore samples and found about 849-fold enhancement than LIBS.

Many studies have focused on different aspect using MW-assisted LIBS. For instance, Kearton et al. have found that the addition of microwave cavity in the LIBS system improves the plasma life time up to 2-10 ms [113]. Khumaeni et al. have demonstrated the plasma characteristics enhancement with MW-LIBS using loop antenna and found plasma lifetime extended up to 500 µs. In addition to that, they found improved plasma temperature and electron density to approximately 10900K and 1.5×10^{18} cm^{-3} [103]. In their study, Khumaeni et al. have shown that, the loop diameter of the antenna has impact on electromagnetic field [70]. They also claimed that the total emission intensity enhancement was 30 times higher with MW-LIBS [114]. Liu et al. used microwave cavity and found 23-fold increased sensitivity than LIBS considering copper as a detecting element. They succeeded to observe silver (23.3 mg Kg^{-1}) as a trace element using their methods [115]. Similarly, Tampo et al. observed 50-fold emission enhancement using loop antenna MW-LIBS and they conducted their research in an argon atmosphere [107]. Viljanen et al. applied near field applicator (NFA) in microwave assisted LBS system, examined a significant improvement in LoD about 93-fold higher than LIBS for solid copper sample [105]. Similarly, Hu et al. tested heavy metal (cadmium) in rice and found about 9-27fold signal enhancement with MW-LIBS than LIBS [116]. Moreover, Wall et al. used MW-assisted LIBS for aqua solution first time and succeeded with about 11.5-fold improvement in LoD for Indium in aqua solution [117]. However, Khumaeni et al. did experiment on the effect of ambient gas for calcium impurity in different atmosphere on MW-LIBS system. They found the enhanced LoD of calcium in He and Ar environment comparing air atmosphere using pelletized gadolinium oxide [118].

However, in this study, Near-Field Applicator (NFA) is used for microwave coupling because introduction of NFA for microwave coupling can manage to couple microwave radiation at ambient conditions as shown in many research [105, 108-110, 112]. NFA is a tip manufactured from rigid coaxial cable by removing the shielding and insulation layer for $1/4\lambda_{MW}$ length from the end of the cable. NFA tip is made from an alloy material of stainless steel coated with copper and silver. This NFA tip has been used for **Paper I, II and III, and Paper V** but for **Paper IV** the tip was replaced by 99.99% pure platinum because **Paper IV** deals with silver detection. The NFA tip creates high electric field near the antenna. A grounding plate is inserted to the beginning of the shielded part of the cable in order to increase the confinement of electric field [112]. The position of NFA near the LIBS plasma is shown in figure 2.2. The microwave source used in the work of this thesis was magnetron-based system (Sairem) as microwave radiation can be produced by using magnetron or solid-state source. The microwave radiation was coupled to the NFA using a waveguide-to-coaxial adapter. It is observed that the microwave coupling depends on sample physical state. Microwave coupling is found ~95% for solid samples but for liquid samples, the coupling efficiency reduced to 43% [**Paper III**].

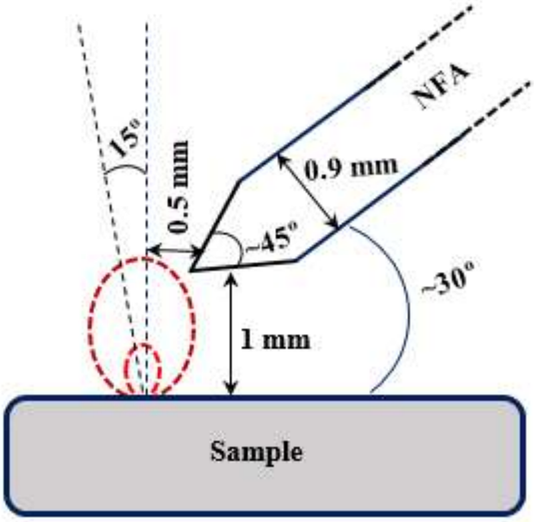

Figure 2.2. Schematic of Near-Field Applicator (NFA) positioning on solid surface. The smaller and larger dashed circles represent approximate size of a laser-induced plasma and a microwave assisted LIBS plasma [105].

Essentially, the plasma lifetime is determined by the duration of microwave injection. To avoid overheating of the waveguide-to-axial adapter and NFA tip, pulsed injection of microwave radiation to the plasma is mandatory. Hence, the microwave pulse length limits the signal integration time. Typical pulse length and integration time have been 1.5 ms and 1 ms respectively for [**Paper I, II, III, IV** and **additional Paper I**] but for **Paper V**, pulse length and integration time was 2.5 ms and 2 ms respectively. This is well beyond the typical LIBS measurement, which is usually 10 µs. Microwave pulse is launched before the laser pulse to ensure that the microwave radiation is reaching the laser induced plasma. The timing scheme of MW-LIBS measurement is shown schematically in a timing diagram of figure 2.3. Figure 2.4 (a, b, c) shows some of the experimental validation of MW-LIBS advantages

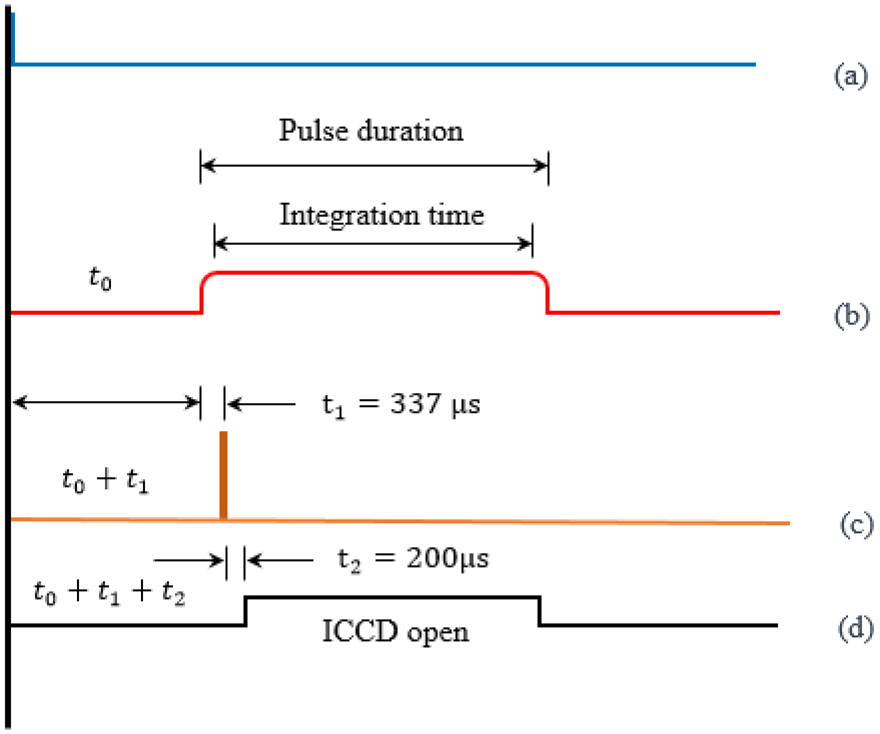

Figure 2.3. Timing diagram of t_0 (a), Microwave (b), Laser (c) and ICCD (d) for the experimental setup

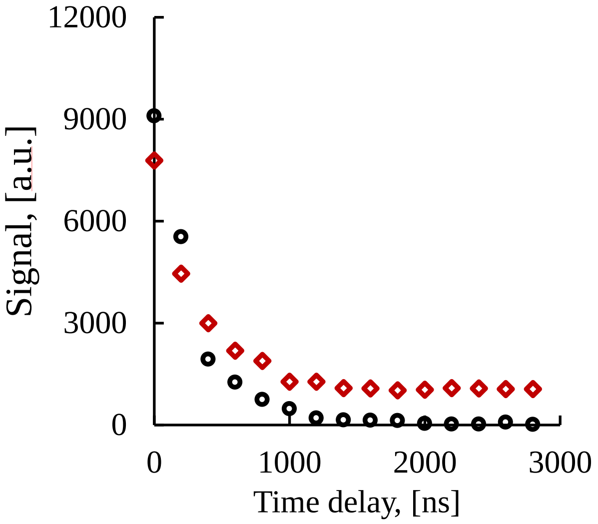

Figure 2.4 (a). Effect of microwave on LIBS signal intensity of Ca I at 445.5 nm with time. Experiment was done at 4-mJ laser energy with MW power 600 W (red) and without MW power (black)

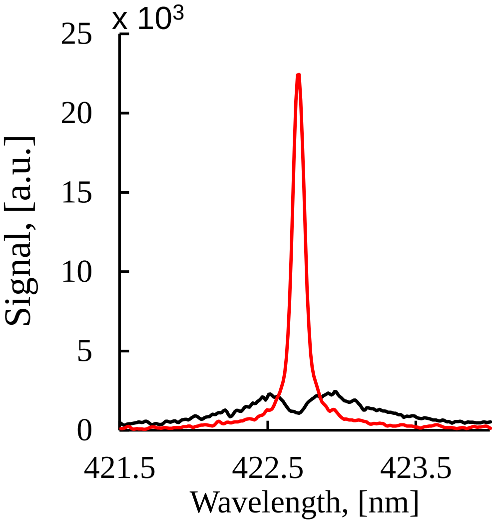

Figure 2.4 (b). Signal intensity of Ag I (338.3 nm) at 2-mJ laser energy with 600 W microwave power (red) and without microwave power (black)

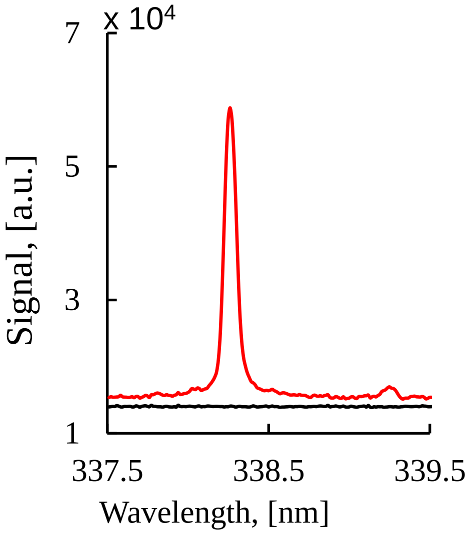

Figure 2.4 (c). Effect of MW to reduce self-absorption of high Ca content cement sample (~40 %) at Ca I 422.67 nm. The spectra recorded at 4 mJ laser energy with 600 W MW power (red) and without MW power (black)

The quantitative analytical performance of LIBS is often assessed by means of LoD. As LIBS is not an absolute method, it requires calibration that is obtained by analysing the instrumental response against tested calibration standards containing the desired analyte at know concentration. Ideally, the curve of growth, i.e. the calibration curve is linear but in optically thick conditions, the linearity is lost due to self-absorption compromising sensitivity. In this thesis, sensitivity refers to the linearity of the slope of the calibration curve. Although MW-LIBS is able to eliminate the self-absorption of LIBS for high concentration as mentioned above, but in this thesis, low concentrations are used to achieve the linearity of slope with LIBS and MW-LIBS. The slope of the calibration curve is related with LoD that is one of the common figures-of-merits for LIBS arrangement. LoD refers to the concentration when the instrument response equals to the background noise level and thus the atomic line or molecular emissions cannot be distinguished unambiguously from the obtained spectrum. In this thesis, the requirement for obtained emission signal to be distinguishable is that it exceeds 3 times the background standard deviation (S_{bi}). Hence, the LoD is defined as

$$\mathrm{LoD} = \frac{3S_{\mathrm{bi}}}{\mathrm{b}} \qquad (1)$$

Where b is the slope of the linear part of calibration curve [119, 120]. LIBS signal fluctuated between successive laser pulses. Therefore, LIBS is often acquired as an average of multiple spectra and relative standard deviation is used to describe the pulse-to-pulse repeatability of the signal formation [120, 121]. The ability of microwave radiation to prolong the lifetime of laser-induced plasma leads to extended time window for signal integration. This is the main reason for improved analytical performance of MW-LIBS in terms of LoD compared to conventional LIBS. In this thesis, equation 1 is used for LoD calculation [**Paper I, II, III, IV, V additional paper I**]. A typical example of the slope of the signals using MW-LIBS and LIBS are shown in figure 2.5.

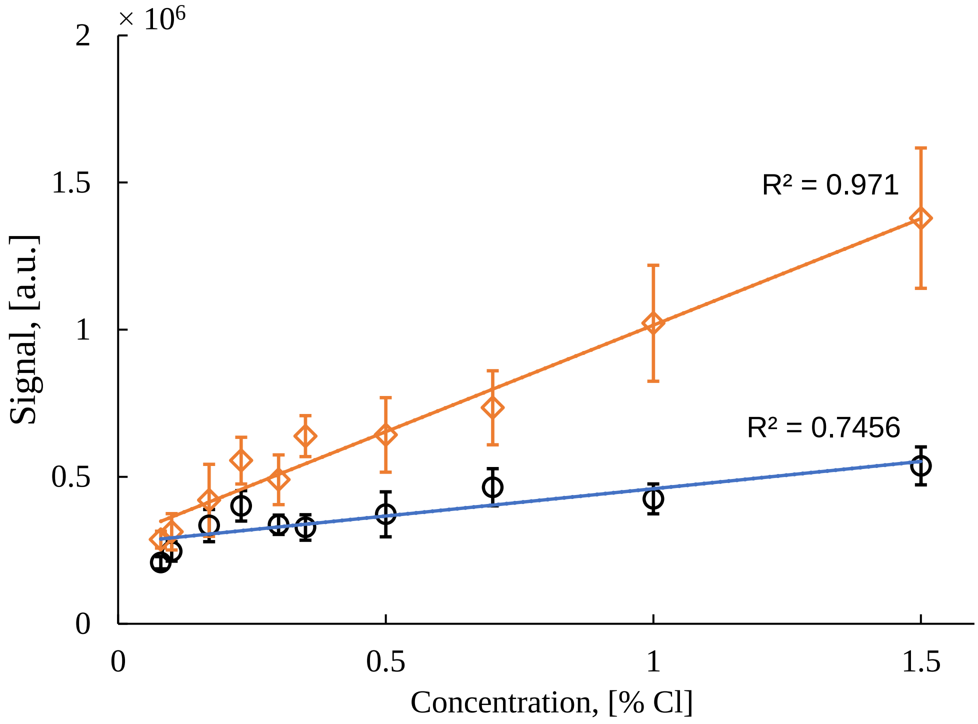

Figure 2.5. Calibration curve of [Cl] with LIBS, blue, and MW-LIBS, red, at 7.5mJ laser energy, 600 W microwave power, 500 ns gate-delay and 300 µs gate-width with accumulation of 100 shots. [**Paper I**]

2.2 Measurement of MW-LIBS Plasma parameters

2.2.1 Microwave power

The signal enhancing ability of MW-LIBS makes it advantageous in terms of analytical performance compared with conventional LIBS technique. The external energy supplied, using the microwave radiation, sustains the free electrons present within the laser-induced plasma. These reenergized free electrons act as an excitation source, via collisional processes, leading to the lifetime extension which finally leading to the signal enhancement [108, 115]. It is observed that the microwave power has an impact on signal to noise ratio (SNR) both in solid and liquid sample. In this thesis, SNR of atomic or molecular emission is demonstrated against microwave power (300 W – 900 W) for solid samples and found 600 W microwave power to be optimum [**Paper I, IV and V**]. For the solid sample, SNR increases until 600 W is reached and beyond this figure, there is no significant impact of microwave power on SNR [**Paper I, V**]. On the other hand, microwave power wields a significant impact on SNR in the case of liquid samples [**Paper IV**]. There is always an increasing order of SNR when the microwave power also increases. A microwave power below 600 W is not feasible in liquid samples due to the instability of microwave plasma. The other reason for the weaker plasma from LIBS is explained by the reflective nature of the thin water jet, which requires more microwave power for proper coupling with LIBS plasma.

2.2.2 Line Broadening

The intensity of the spectral line as well as its profile plays an important role in the spectroscopic study of line emission from the plasma. The emission line profile is important because it contains information related with the emitter and surrounding plasma environment. Various types of line broadening have been observed in the plasma emission. Natural broadening occurs due to the finite lifetime of exited states and results in a Lorentzian profile [33]. It is well known that the measured line profiles normally contain contribution from instrument resolution width also, if the spectrometers are used for wavelength analysis. The instrument width needs to be measured experimentally for a given spectrometer, which is dependent on the parameters such as slit width, the gating depression and the dynamic behavior of the photon detector [33]. In this thesis, the instrumental width has been measured experimentally using most strong Hg I line at 253.6 nm at 15 micron slit width. The experiment was repeated 10 times and the instrument width measured as an average of 10 experimental data. The actual line width has been extracted from the measured line width by using a simple equation [33].

$$\Delta\lambda_{measured} = \Delta\lambda_{line} + \Delta\lambda_{insturement} \qquad (2)$$

2.2.3 Electron density

The width of Stark-broadened spectral lines in plasma depends mainly on the electron density N_e. Both the linear and the quadratic stark effect are encountered in spectroscopy. The electron density can be determined using the following equation [122].

$$\Delta\lambda_{FWHM} \approx 2 \times 10^{-16} \omega N_e \qquad (3)$$

Where $\Delta\lambda_{FWHM}$ is the experimental full width at half maximum (FWHM) of the emission line, ω is the theoretical stark width parameter and N_e is the electron density. ω is derived from literature for electron density calculation [123, 124]. A sample FWHM of Hg I at 253.6 nm as instrumental error is shown in figure 2.6. FWHM from instrument is calculated as 0.03211 nm.

The first choice for electron density determination in LIBS plasma containing hydrogen is the H_β (with an error of 5%) [125] because of its large intensity and sufficiently large line broadening, which can be measured precisely using a spectrometer of moderate resolution. It is also found that in addition to the hydrogen lines, resonance lines of aluminium and calcium at 396.15 nm and 422.67 nm respectively can be used to estimate electron-densities considering that these lines exhibit quadratic Stark broadening [33]. In this thesis, Ca I at 422.67 nm is used for electron density calculation. For analytical plasma, the condition of local thermal equilibrium (LTE) is considered very much vital for getting any reliable quantitative information. The following criterion must be satisfied by the plasma to be in the LTE [126].

$$N_e \geq 1.6 \times 10^{12} \, \Delta E^3 T_e^{\frac{1}{2}} \qquad (4)$$

Where ΔE (eV) is the largest observed transition energy for which the condition holds, and T_e, is the excitation temperature (K)

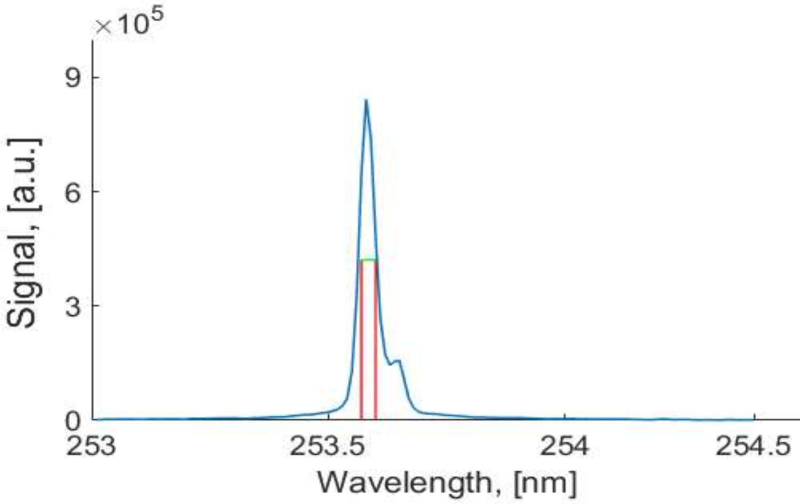

Figure 2.6. Instrumental error using Hg I at 253.6 nm. Full-width at half-maximum (FWHM) from instrument calculated as 0.03211 nm

2.2.3 Plasma temperature

In this thesis, plasma temperature measurement was done using two different elements, these being lead and calcium, which consist of many strong lines. The atomic database in NIST is presented in Table 2. Plasma temperature can be calculated using equation 5 [103, 127] as follows:

$$ln\left(\frac{I\lambda}{Ag}\right) = -\frac{E}{KT} + ln\left(\frac{hcN}{4\pi U}\right) \dots \dots (5)$$

Where I is the recorded peak intensity of the related wavelength, h is the plank’s constant, c is velocity of light, λ is the wavelength, g is the statistical weight of upper state, E is the energy of the upper state, U is the partition function, K is Boltzmann constant, and, T is the Plasma temperature. The spectral lines used for plasma temperature measurement in this work are listed in table 1.

Plotting $ln\left(\frac{I\lambda}{Ag}\right)$ against E for number yields a straight line of a slope of $-\frac{1}{KT}$ and an intercept $ln\left(\frac{hcN}{4\pi U}\right)$ as illustrated in figure 2.7. The slope is then used to evaluate plasma temperature.

Table 2.1: Spectral lines in the present work [128]

Element	**Wavelength (nm)**	**Transition strength, A_{ki}, (S^{-1})**	**Upper state energy level, E_k, (eV)**	**g**
Pb	280.2	1.61×10^{08}	5.74	7
	287.3	3.80×10^{07}	5.634	5
	363.95	3.20×10^{07}	4.375	3
	368.35	1.37×10^{08}	4.33	1
Ca	364.44	3.55×10^{07}	5.3	7
	422.67	2.18×10^{08}	2.93	3
	430.25	1.36×10^{08}	4.779	5
	445.48	4.70×10^{07}	4.681	7
	458.59	2.29×10^{07}	5.228	9

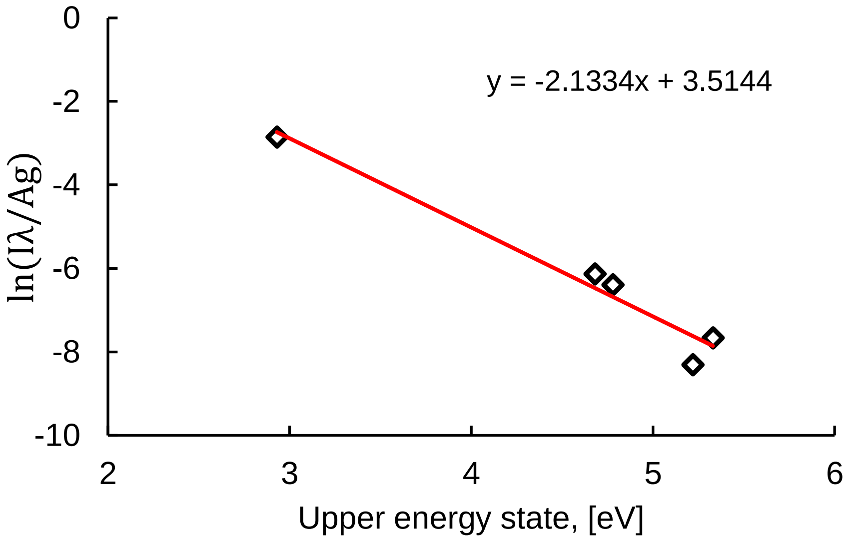

Figure 2.7. Boltzmann plot made from Ca I lines at 5mJ laser energy, 600 W microwave power, 1ns gate-delay and 1000 µs gate-width.

2.3 Microwave-assisted LIBS for Sulphur, Silver and Palladium detection in solid phase

Sulphur is one of the most important elements that affects the matrix of a material. For instance, the machinability and magnetism of steel can be improved by adding appropriate amounts of sulphur but too large an amount may decrease steel's plasticity and wear resistance ability [129]. Sulphur is considered to be a macronutrient, which is widely used to synthesise amino acids and proteins in plants and helps the human immune system to function properly [130, 131]. Conversely, sulphur adversely affects the oil refining system in that it causes catalyst poisoning and corrosion in process lines and can trigger serious environmental pollution through SO_x generation during fuel combustion [132]. Liu, H. et al. reported that sulphur content plays an important role in arsenic volatilisation and especially in coal burning [133]. LIBS has been considered to be the best technique in most studies for detecting sulphur because of its successfully direct quantitative elemental analysing ability [134]. Yonghoon et al. [131] conducted their study on edible oils and found 0.12% LoD of sulphur under helium ambient gas. Trichard et al. [132] used oil products and reported the detection range of 0.2% under a helium atmosphere. Timur et al. [135] applied the double pulse option and achieved 1500 ppm LoD for sulphur analysis of their concrete samples. Quantitative detection of sulphur has been carried out using MW-LIBS and a portable spectrometer at ambient condition [**Paper V**].

Silver is one of the world's most precious metals of the platinum family with uses across a wide range of industries, such as commercial and scientific appliances. Several analytical techniques involving digestion methods for analysing quantification of precious metals are reported in the literature. These include, for instance fire assay, wet acid treatment, direct chlorination, alkaline oxidation fusion, etc.[136] However, only a few studies have been found in the literature on silver detection with LIBS. Daniel et al. detected silver in ore samples [137] and reported a limit of detection (LoD) of 1 ppm. R W Septianti et al. [138] checked the authenticity of silver jewellery and calculated the LoD of 2.74%. I. Rehan et al. [139] used monosodium glutamate and reported a detection limit of 0.57 ppm. The quantitative detection of silver with MW-LIBS is demonstrated for mineral samples in this study [**Paper IV**].

Palladium is one of the platinum group metal and it plays a key role in several industrial applications as approximate 40% of the automobile catalyst consist of Pd [140] and it is also a cheaper alternative of platinum fuel cell [141, 142]. However, Pd has a limited natural resources and the cost of extracting and recycling is costly [143]. Another application of palladium detection is in the pharmaceutical and the food industry [144] where Pd is used in some of the pharmaceutical tools. A study done by Asimellis, G. et al. [140] investigated the palladium detection in a real automobile catalyst at a low concentration of 127 ppm where, several lines were observed for Pd detection with high intensity lines located at the wavelength of 340.46 nm and 342.12 nm. MW-LIBS has been demonstrated for palladium (Pd) detection in solid sample at ambient conditions [**Additional paper I**].

2.4 Microwave-assisted LIBS for halogenated elements (Cl, F, Br) detection

It is reported that the halogens such as chlorine, fluorine and bromine produce weak emission making them more difficult to characterise compared to the elements with prominent peaks such as alkalis, alkaline earth element and transition metals [72, 145]. Detection limits for halogens are less than satisfactory for demanding applications. Direct detection of halogens based on atomic emission is difficult because of the resonance lines of the three elements belong to the deep vacuum ultra-violate (VUV) region, which have very high excitation energy and difficult to populate. The use of buffer gas as an inert environment was an effective solution. Gonzalez et al. reported the LoD of fluorine (F) was 109 µg/g under reduced argon (Ar) and helium (He) atmosphere using the atomic line at F I 685.6 nm [146]. Pavel et al. found a 150 ppm LoD under a low pressure He environment [147]. Radziemski et al. used the vacuum ultra violet region and reported the LoD of Br was 5.6% at 163.3 nm atomic line [148]. Barbier et al. reported the LoD for Br were 3.6% and 0.9% under air and helium atmospheres, respectively. Other possible alternative to direct measurement of chlorine is to use the detection of alkali metals as a surrogate to infer the presence of salts that have chlorine (Cl), assuming that the concentration of these metals is proportional to Cl [135, 149] but in this case, homogeneous salt deposition is also essential. Another prospective alternative for chlorine detection is to use molecular emission because molecular structure has a strong influence on final emission pattern [150].

MW-LIBS offers the extension of the lifetime of the laser induced plasma. This is usually followed by a relatively longer detection gate ~500 µs. A longer plasma lifetime along with a prolonged detection gate provides some difficulties because emission from molecules and radicals become stronger, blocking large atomic spectral range. However, when the process of molecular formation and emission is carefully used, the process can benefit the detection of few elements such as chlorine, fluorine and bromine. This thesis reports on the application of MW-LIBS directed towards quantitative detection of Cl, F and Br through molecular emission namely CaCl, CaF and CaBr respectively [**Paper I and Paper II**].

2.5 Microwave-assisted LIBS for Silver and Ruthenium detection in aqua solution

Ruthenium is a hard-metallic element that is part of the platinum-group metals and is considered a rare material due to its very low mining rate [151]. In its early discovery, Ruthenium was commercially used as an alloying agent for the hardening of platinum and palladium [152]. In addition to that, as Ruthenium (Ru) is a transition element, its compounds can be utilized as catalysts. Although some studies have been made to develop more stable and more sturdy catalyst matrix to hold Ru [153, 154], losses are inevitable and can pose a significant business threat because of its high in demand but low supply. However, [**Paper III**] deals with the Ru LoD using MW-LIBS technique in liquid phase for the first time in literature. Similarly, silver has been detected in liquid phase using MW-LIBS and a LoD is reported [**Paper IV**].

2.6 Rules for microwave-assisted LIBS signal enhancement

It is already discussed about the obvious benefits of MW-LIBS in introduction section. It is interesting to consider that the signal enhancement with MW-LIBS is different as noted in the literature although the experimental conditions were not the same. Viljanen et al. observed ~100 times greater signal enhancement with MW-LIBS than LIBS at 0.8 mJ laser energy for Cu I at 324.75 nm [105]. Tampo et al. observed a ~50 times enhancement at 5 mJ for Gd II at 367.12 nm [107], while Khumaeni et al. observed two things: firstly, a 10-fold improvement for Ca I at 422.6 nm; and secondly, a 40-fold enhancement for Gd I at 470.9 nm at 5 mJ [103, 118]. Meanwhile, Liu et al. found enhancement of 33, 22, 16 and 11 for Na I at 589.6 nm, Ca I at 422.7 nm, Mg I at 285.2 nm and Al I at 396.2 nm, respectively [111]. Wall et al. obtained a signal enhancement of 60 times for In I at 451.13 nm [108]. Ahlam et al. achieved 92 times enhancement for Pd I at 340.46 nm [155]. Abu et al. observed 76 times signal to noise ration improvement in ruthenium aqua solution at 10 mJ [paper submitted]. In this study, the signal enhancement rules of MW-LIBS are reported for solid matrix in ambient conditions because no such study is available. MW-LIBS is becoming a prominent method for improved analytical performance of LIBS in terms of LoD. **Paper V** is dealing with this issue. It is observed that the Upper Energy Level (UEL) of each transition plays key role in signal enhancement.

Significant enhancement is possible for the elements with upper state energy level below 5eV. However, no signal enhancement was observed for transition with UEL higher than 7eV. This is termed as the cut-off limit of signal enhancement. It is also observed that plasma temperature is independent of time and there is no reheating impact of microwave on LIBS plasma. Microwave only increases the lifetime of emission intensity [**Paper V**].

2.7 Application of LIBS for potassium release in biomass combustion

This section deals with the application of LIBS, without microwave enhancement, for quantitative detection of element in gas phase, in real-time. Usually biomass contains abundant mineral elements, such as potassium (K), calcium (Ca), magnesium (Mg), chlorine (Cl), silicon (Si), phosphorus (P), which can induce serious technical problems, such as slagging, fouling and corrosion in thermal conversion systems [156-160]. Among those elements, K plays an important role on the ash-related problems because of its high concentration and volatility [156, 161]. Therefore, it is necessary to carry out detailed investigation to understand the K release characteristics and mechanisms during biomass thermal conversion process. In most studies, biomass was investigated using fixed-bed or drop tube reactor, and the ash residues were analyzed in order to obtain the distribution of K in gas and solid phases. It was found that a significant part of K (20%~100%) is released to the gas phase in the form of KCl, KOH or K [157, 162, 163]. On the other hand, the combustion temperature can also affect the release ratio. K exists in biomass as the form of inorganic salts and/or associated with other organics [157, 164, 165]. Furthermore, studies indicated that Si can significantly inhibit the release of K during biomass combustion by forming stable K-silicates [157, 166]. [**Paper VI**] deals with the measurements of potassium concentration and biomass temperature during biomass combustion have been developed with an improved LIBS calibration method. In addition, the effect of biomass type, Si content and initial mass of willow wood on the temporal release of K and particle temperature during biomass combustion are investigated in this study.

Reference

1. Machado, R.C., et al., *Solid sampling: advantages and challenges for chemical element determination—a critical review.* Journal of Analytical Atomic Spectrometry, 2020. **35**(1): p. 54-77.
2. Kurfürst, U., *Solid sample analysis : direct and slurry sampling using GF-AAS and ETV-ICP*. 1998, Berlin: Springer.
3. Abanades, S., G. Flamant, and D. Gauthier, *The kinetics of vaporization of a heavy metal from a fluidized waste by an inverse method.* Combustion and Flame, 2003. **134**: p. 315-326.
4. Nishiguchi, K., et al., *Gas to Particle Conversion-Gas Exchange Technique for Direct Analysis of Metal Carbonyl Gas by Inductively Coupled Plasma Mass Spectrometry.* Analytical Chemistry, 2014. **86**(20): p. 10025-10029.
5. Fichet, P., et al., *Comparisons between LIBS and ICP/OES.* Analytical and Bioanalytical Chemistry, 2006. **385**(2): p. 338-344.
6. Nishiguchi, K., K. Utani, and E. Fujimori, *Real-time multielement monitoring of airborne particulate matter using ICP-MS instrument equipped with gas converter apparatus.* Journal of Analytical Atomic Spectrometry, 2008. **23**(8): p. 1125-1129.
7. Bonta, M., et al., *Elemental mapping of biological samples by the combined use of LIBS and LA-ICP-MS.* Journal of Analytical Atomic Spectrometry, 2016. **31**(1): p. 252-258.
8. Kaveh, F. and D. Beauchemin, *Improvement of the capabilities of solid sampling ETV-ICP-OES by coupling ETV to a nebulisation/pre-evaporation system.* Journal of Analytical Atomic Spectrometry, 2014. **29**(8): p. 1371-1377.

9. Ge, L.Q. and F. Li, *Review of in situ X-ray fluorescence analysis technology in China.* X-Ray Spectrometry: p. 13.
10. Beckhoff, B., et al., *Handbook of Practical X-Ray Fluorescence Analysis*. 1 ed. 2006: Springer-Verlag Berlin Heidelberg. XXIV, 863.
11. McComb, J.Q., et al., *Rapid screening of heavy metals and trace elements in environmental samples using portable X-ray fluorescence spectrometer, A comparative study.* Water, air, and soil pollution, 2014. **225**(12): p. 2169.
12. AGENCY, I.A.E., *Sampling, Storage and Sample Preparation Procedures for X ray Fluorescence Analysis of Environmental Materials*. 1997, Vienna: INTERNATIONAL ATOMIC ENERGY AGENCY.
13. Towett, E.K., K.D. Shepherd, and B. Lee Drake, *Plant elemental composition and portable X-ray fluorescence (pXRF) spectroscopy: quantification under different analytical parameters.* X-Ray Spectrometry, 2016. **45**(2): p. 117-124.
14. Tighe, M. and N. Forster, *Rapid, Nondestructive Elemental Analysis of Tree and Shrub Litter.* Communications in Soil Science and Plant Analysis, 2014. **45**(1): p. 53-60.
15. Sapkota, Y., et al., *Portable X-Ray Fluorescence Spectroscopy for Rapid and Cost-Effective Determination of Elemental Composition of Ground Forage.* Frontiers in Plant Science, 2019. **10**(317).
16. Ravansari, R., S.C. Wilson, and M. Tighe, *Portable X-ray fluorescence for environmental assessment of soils: Not just a point and shoot method.* Environment International, 2020. **134**: p. 105250.
17. Börjesson, J., M. Isaksson, and S. Mattsson, *X-ray fluorescence analysis inmedical sciences: a review.* Acta Diabetologica, 2003. **40**(1): p. s39-s44.
18. Oyedotun, T.D.T., *X-ray fluorescence (XRF) in the investigation of the composition of earth materials: a review and an overview.* Geology, Ecology, and Landscapes, 2018. **2**(2): p. 148-154.
19. Stosnach, H., *Environmental Trace-Element Analysis Using a Benchtop Total Reflection X-Ray Fluorescence Spectrometer.* Analytical Sciences, 2005. **21**(7): p. 873-876.
20. Terrell, J., *PMI Technologies: What's the Difference Between XRF, LIBS, and OES?* 2019: ThermoFisher Scientific.
21. Kramar, U., *X-ray Fluorescence Spectrometers,* in *Encyclopedia of Spectroscopy and Spectrometry,* J.C. Lindon, Editor. 1999, Elsevier: Oxford. p. 2467-2477.

22. Arantes de Carvalho, G.G., et al., *Recent advances in LIBS and XRF for the analysis of plants.* Journal of Analytical Atomic Spectrometry, 2018. **33**(6): p. 919-944.
23. Luo, L., et al., *The effect of filters and collimators on Compton scatter and Pb K-series peaks in XRF bone lead analysis.* Nuclear Instruments and Methods in Physics Research Section B: Beam Interactions with Materials and Atoms, 2007. **263**(1): p. 258-261.
24. Marguí, E., et al., *High-energy polarized-beam EDXRF for trace metal analysis of vegetation samples in environmental studies.* X-Ray Spectrometry, 2006. **35**(3): p. 169-177.
25. Holmes, G.S., *The limitations of accurate "thin-film" X-ray fluorescence analysis of natural particulate matter: Problems and solutions.* Chemical Geology, 1981. **33**(1): p. 333-353.
26. Klockenkämper, R. and A. von Bohlen, *Elemental Analysis of Environmental Samples by Total Reflection X-Ray Fluorescence: a Review.* X-Ray Spectrometry, 1996. **25**(4): p. 156-162.
27. Arthur, R. and P. Scherer, *Application of total reflection X-Ray fluorescence spectrometry to quantify cobalt concentration in the presence of high iron concentration in biogas plants.* Spectroscopy Letters, 2020. **53**(2): p. 100-113.
28. E, M., et al., *X-ray fluorescence trace metal analysis of environmental liquid samples after membrane preconcentration.* Spectroscopy Europe, 2008. **20**: p. 11-14.
29. Malkov, A.V., et al., *Determination of Ni, Co, and Cu in seawater by total external reflection X-ray fluorescence spectrometry.* Journal of Analytical Chemistry, 2017. **72**(6): p. 608-616.
30. Cremers, D.A. and L.J. Radziemski, *History and fundamentals of LIBS*, in *Laser Induced Breakdown Spectroscopy*, A.W. Miziolek, I. Schechter, and V. Palleschi, Editors. 2006, Cambridge University Press: Cambridge. p. 1-39.
31. Rai, A., et al., *Laser-induced breakdown spectroscopy: A versatile technique for elemental analysis*. 2002.
32. Thakur, S.N. and J.P. Singh, *Chapter 1 - Fundamentals of Laser Induced Breakdown Spectroscopy,* in *Laser-Induced Breakdown Spectroscopy*. 2007, Elsevier: Amsterdam. p. 3-21.
33. Rai, V.N. and S.N. Thakur, *Chapter 4 - Physics of Plasma in Laser-Induced Breakdown Spectroscopy,* in *Laser-Induced Breakdown Spectroscopy*, J.P. Singh and S.N. Thakur, Editors. 2007, Elsevier: Amsterdam. p. 83-111.

34. Zorba, V., et al., *Laser-Induced Breakdown Spectroscopy (LIBS), Applications of A2 - Lindon, John C*, in *Encyclopedia of Spectroscopy and Spectrometry (Third Edition)*, G.E. Tranter and D.W. Koppenaal, Editors. 2017, Academic Press: Oxford. p. 571-578.
35. Peng, J., et al., *Challenging applications for multi-element analysis by laser-induced breakdown spectroscopy in agriculture: A review.* TrAC Trends in Analytical Chemistry, 2016. **85, Part C**: p. 260-272.
36. Minnikova, T.V., et al., *Assessing the effect of heavy metals from the Novocherkassk power station emissions on the biological activity of soils in the adjacent areas.* Journal of Geochemical Exploration, 2017. **174**: p. 70-78.
37. Michel, A.P.M. and F. Sonnichsen, *Laser induced breakdown spectroscopy for heavy metal detection in a sand matrix.* Spectrochimica Acta Part B: Atomic Spectroscopy, 2016. **125**: p. 177-183.
38. Cvejić, M., et al., *Neutral lithium spectral line 460.28 nm with forbidden component for low temperature plasma diagnostics of laser-induced plasma.* Spectrochimica Acta Part B: Atomic Spectroscopy, 2014. **100**: p. 86-97.
39. Suchoňová, M., et al., *Analysis of LiSn alloy at several depths using LIBS.* Fusion Engineering and Design, 2016.
40. Hernández-García, R., et al., *Quantitative analysis of Lead Zirconate Titanate (PZT) ceramics by laser-induced breakdown spectroscopy (LIBS) in combination with multivariate calibration.* Microchemical Journal, 2017. **130**: p. 21-26.
41. Zivkovic, S., et al., *Elemental analysis of aluminum alloys by Laser Induced Breakdown Spectroscopy based on TEA CO2 laser.* Journal of Alloys and Compounds, 2017. **700**: p. 175-184.
42. Suchoňová, M., et al., *Analysis of LiSn alloy at several depths using LIBS.* Fusion Engineering and Design.
43. Davari, S.A., S. Hu, and D. Mukherjee, *Calibration-free quantitative analysis of elemental ratios in intermetallic nanoalloys and nanocomposites using Laser Induced Breakdown Spectroscopy (LIBS).* Talanta, 2017. **164**: p. 330-340.
44. Tolaymat, T., et al., *Analysis of metallic and metal oxide nanomaterial environmental emissions.* Journal of Cleaner Production, 2017. **143**: p. 401-412.
45. Wang, Y., et al., *Atmospheric emissions of typical toxic heavy metals from open burning of municipal solid waste in China.* Atmospheric Environment, 2017. **152**: p. 6-15.

46. Wang, Z.Z., et al., *Rapid Detection of Trace Heavy Metals using Laser Breakdown Time-of-Flight Mass Spectrometry.* Procedia Environmental Sciences, 2013. **18**: p. 329-337.
47. Moosakhani, A., et al., *Radon decay monitoring in air using characteristic emission of species in metal-assisted LIBS.* Radiation Measurements, 2016. **92**: p. 39-48.
48. Dutouquet, C., et al., *Monitoring of heavy metal particle emission in the exhaust duct of a foundry using LIBS.* Talanta, 2014. **127**: p. 75-81.
49. Minkina, T.M., et al., *Content and distribution of heavy metals in herbaceous plants under the effect of industrial aerosol emissions.* Journal of Geochemical Exploration, 2017. **174**: p. 113-120.
50. Huber, N., et al., *In-line measurements of chlorine containing polymers in an industrial waste sorting plant by laser-induced breakdown spectroscopy.* Applied Surface Science, 2014. **302**: p. 280-285.
51. Monkhouse, P., *On-line diagnostic methods for metal species in industrial process gas.* Progress in Energy and Combustion Science, 2002. **28**(4): p. 331-381.
52. G. Arca, et al., *Trace Element Analysis in Water by the Laser-Induced Breakdown Spectroscopy Technique.* Applied Spectroscopy, 1997. **51**(8): p. 1102-1105.
53. L. Dudragne, Ph. Adam, and J. Amouroux, *Time-Resolved Laser-Induced Breakdown Spectroscopy: Application for Qualitative and Quantitative Detection of Fluorine, Chlorine, Sulfur, and Carbon in Air.* Applied Spectroscopy, 1998. **52**(10): p. 1321-1327.
54. Cardoso, P.G., et al., *Temporal characterization of mercury accumulation at different trophic levels and implications for metal biomagnification along a coastal food web.* Marine Pollution Bulletin, 2014. **87**(1–2): p. 39-47.
55. dos Santos Augusto, A., et al., *Calibration strategies for the direct determination of Ca, K, and Mg in commercial samples of powdered milk and solid dietary supplements using laser-induced breakdown spectroscopy (LIBS).* Food Research International, 2017. **94**: p. 72-78.
56. van Eyk, P.J., et al., *Simultaneous measurements of the release of atomic sodium, particle diameter and particle temperature for a single burning coal particle.* Proceedings of the Combustion Institute, 2009. **32**(2): p. 2099-2106.
57. Zhang, Z.H., et al., *Quantitative detection of Na released from burning microalgae particle using laser-induced breakdown spectroscopy*. 2013.

58. Yuan, Y., S. Li, and Q. Yao, *Dynamic behavior of sodium release from pulverized coal combustion by phase-selective laser-induced breakdown spectroscopy.* Proceedings of the Combustion Institute, 2015. **35**(2): p. 2339-2346.

59. Jagustyn, B., et al., *The content and emission factors of heavy metals in biomass used for energy purposes in the context of the requirements of international standards.* Journal of the Energy Institute.

60. Yang, X., et al., *Simultaneous determination of La, Ce, Pr, and Nd elements in aqueous solution using surface-enhanced laser-induced breakdown spectroscopy.* Talanta, 2017. **163**: p. 127-131.

61. López-López, M., et al., *An exploratory study of the potential of LIBS for visualizing gunshot residue patterns.* Forensic Science International, 2017.

62. Munson, C., et al., *Laser-Based Detection Methods for Explosives.* Counterterrorist Detection Techniques of Explosives, 2007.

63. Singh, J.P., et al., *Civilian and military environmental contamination studies using LIBS*, in *Laser Induced Breakdown Spectroscopy*, A.W. Miziolek, I. Schechter, and V. Palleschi, Editors. 2006, Cambridge University Press: Cambridge. p. 368-399.

64. Koral, C., et al., *Nanoparticle Enhanced Laser Induced Breakdown Spectroscopy for Improving the Detection of Molecular Bands.* Spectrochimica Acta Part B: Atomic Spectroscopy, 2016. **125**: p. 11-17.

65. Trautner, S., et al., *Laser-induced optical breakdown spectroscopy of polymer materials based on evaluation of molecular emission bands.* Spectrochimica Acta Part A: Molecular and Biomolecular Spectroscopy, 2017. **174**: p. 331-338.

66. Vadillo, J.M. and J.J. Laserna, *Chemical imaging of surfaces using LIBS*, in *Laser Induced Breakdown Spectroscopy*, A.W. Miziolek, I. Schechter, and V. Palleschi, Editors. 2006, Cambridge University Press: Cambridge. p. 254-281.

67. Anglos, D. and J.C. Miller, *Cultural heritage applications of LIBS*, in *Laser Induced Breakdown Spectroscopy*, A.W. Miziolek, I. Schechter, and V. Palleschi, Editors. 2006, Cambridge University Press: Cambridge. p. 332-367.

68. Béchard, S. and Y. Mouget, *LIBS for the analysis of pharmaceutical materials*, in *Laser Induced Breakdown Spectroscopy*, A.W. Miziolek, I. Schechter, and V. Palleschi, Editors. 2006, Cambridge University Press: Cambridge. p. 314-331.

69. Zheng, L., et al., *Comparative study of the matrix effect in Cl analysis with laser-induced breakdown spectroscopy in a pellet or in a dried solution layer on a metallic target.* Spectrochimica Acta Part B: Atomic Spectroscopy, 2016. **118**: p. 66-71.

70. Khumaeni, A., et al., *Enhancement of LIBS emission using antenna-coupled microwave.* Optics Express, 2013. **21**(24): p. 29755-29768.

71. Alvarez-Llamas, C., J. Pisonero, and N. Bordel, *A novel approach for quantitative LIBS fluorine analysis using CaF emission in calcium-free samples.* Journal of Analytical Atomic Spectrometry, 2017. **32**(1): p. 162-166.

72. Anderson, D.E., et al., *Characterization of LIBS emission lines for the identification of chlorides, carbonates, and sulfates in salt/basalt mixtures for the application to MSL ChemCam data.* Journal of Geophysical Research-Planets, 2017. **122**(4): p. 744-770.

73. Li, X., et al., *Spatial confinement in laser-induced breakdown spectroscopy.* Journal of Physics D: Applied Physics, 2016. **50**(1): p. 015203.

74. Zou, X.H., et al., *Accuracy improvement of quantitative analysis in laser-induced breakdown spectroscopy using modified wavelet transform.* Optics Express, 2014. **22**(9): p. 10233-10238.

75. Xiao, Q., et al., *In-situ analysis of the first wall by laser-induced breakdown spectroscopy in the TEXTOR tokamak: Dependence on the magnetic field strength.* Journal of Nuclear Materials, 2015. **463**: p. 911-914.

76. Li, Y., et al., *Optical emission enhancement of laser-produced copper plasma under a steady magnetic field.* Applied Optics, 2009. **48**(4): p. B105-B110.

77. Hao, Z., et al., *Sensitivity improvement in the detection of V and Mn elements in steel using laser-induced breakdown spectroscopy with ring-magnet confinement.* Journal of Analytical Atomic Spectrometry, 2014. **29**(12): p. 2309-2314.

78. Li, Y., et al., *A review of laser-induced breakdown spectroscopy signal enhancement.* Applied Spectroscopy Reviews, 2018. **53**(1): p. 1-35.

79. Qi, L.F., et al., *Application of Stand-off Double-Pulse Laser-Induced Breakdown Spectroscopy in Elemental Analysis of Magnesium Alloy.* Plasma Science & Technology, 2015. **17**(8): p. 676-681.

80. Hai, R., et al., *Enhanced laser-induced breakdown spectroscopy using the combination of circular and annular laser pulses.* Journal of Analytical Atomic Spectrometry, 2019. **34**(10): p. 1982-1987.

81. Zhao, S., et al., *Quantitative analysis of Pb in soil by femtosecond-nanosecond double-pulse laser-induced breakdown spectroscopy.* Results in Physics, 2019. **15**: p. 102736.

82. Yang, F., et al., *Emission enhancement of femtosecond laser-induced breakdown spectroscopy by combining nanoparticle and dual-pulse on crystal SiO2.* Optics & Laser Technology, 2017. **93**: p. 194-200.

83. Zhang, Y., et al., *Dual pulse laser induced breakdown spectroscopy on Cu concentration in CuSO4 solution with liquid jet*. Applied Optics and Photonics China (AOPC2017). Vol. 10461. 2017: SPIE.

84. Hunter, A.J.R. and L.G. Piper, *Spark-induced breakdown spectroscopy: a description of an electrically generated LIBS-like process for elemental analysis of airborne particulates and solid samples*, in *Laser Induced Breakdown Spectroscopy*, A.W. Miziolek, I. Schechter, and V. Palleschi, Editors. 2006, Cambridge University Press: Cambridge. p. 585-614.

85. Jabbar, A., et al., *Quantification of copper remediation in the Allium cepa L. leaves using electric field assisted laser induced breakdown spectroscopy.* Spectrochimica Acta Part B: Atomic Spectroscopy, 2019. **162**: p. 105719.

86. Nassef, O.A. and H.E. Elsayed-Ali, *Spark discharge assisted laser induced breakdown spectroscopy.* Spectrochimica Acta Part B: Atomic Spectroscopy, 2005. **60**(12): p. 1564-1572.

87. Li, K., et al., *Laser ablation assisted spark induced breakdown spectroscopy on soil samples.* Journal of Analytical Atomic Spectrometry, 2010. **25**(9): p. 1475-1481.

88. Jiang, Y., R. Li, and Y. Chen, *Elemental analysis of copper alloys with laser-ablation spark-induced breakdown spectroscopy based on a fiber laser operated at 30 kHz pulse repetition rate.* Journal of Analytical Atomic Spectrometry, 2019. **34**(9): p. 1838-1845.

89. Hassanimatin, M.M., et al., *A combination of electrical spark and laser-induced breakdown spectroscopy on a heated sample.* Physics of Plasmas, 2019. **26**(3): p. 10.

90. Kondo, H., N. Hamada, and K. Wagatsuma, *Determination of phosphorus in steel by the combined technique of laser induced breakdown spectrometry with laser induced fluorescence spectrometry.* Spectrochimica Acta Part B-Atomic Spectroscopy, 2009. **64**(9): p. 884-890.

91. Li, J., et al., *Investigation of excitation interference in laser-induced breakdown spectroscopy assisted with laser-induced fluorescence for chromium determination in low-alloy steels.* Optics and Lasers in Engineering, 2020. **124**: p. 105834.

92. Gao, P.Y., et al., *Determination of antimony in soil using laser-induced breakdown spectroscopy assisted with laser-induced fluorescence.* Applied Optics, 2018. **57**(30): p. 8942-8946.

93. Guo, L.B., et al., *Determination of boron with molecular emission using laser-induced breakdown spectroscopy combined with laser-induced radical fluorescence.* Optics Express, 2018. **26**(3): p. 2634-2642.

94. Zhao, N., et al., *Experimental investigation of laser-induced breakdown spectroscopy assisted with laser-induced fluorescence for trace aluminum detection in steatite ceramics.* Applied Optics, 2019. **58**(8): p. 1895-1899.

95. Wang, Y.R., et al., *Sensitive Analysis of Copper in Water by LIBS-LIF Assisted by Simple Sample Pretreatment.* Journal of Applied Spectroscopy, 2019. **86**(2): p. 353-359.

96. Li, Q., et al., *Determination of uranium in ores using laser-induced breakdown spectroscopy combined with laser-induced fluorescence.* Journal of Analytical Atomic Spectrometry, 2020.

97. Goueguel, C., et al., *Resonant laser-induced breakdown spectroscopy for analysis of lead traces in copper alloys.* Journal of Analytical Atomic Spectrometry, 2011. **26**(12): p. 2452-2460.

98. Rifai, K., et al., *Resonant laser-induced breakdown spectroscopy (RLIBS) analysis of traces through selective excitation of aluminum in aluminum alloys.* Journal of Analytical Atomic Spectrometry, 2013. **28**(3): p. 388-395.

99. Xiong, G., et al., *Phase-selective laser-induced breakdown spectroscopy of metal-oxide nanoparticle aerosols with secondary resonant excitation during flame synthesis.* Journal of Analytical Atomic Spectrometry, 2016. **31**(2): p. 482-491.

100. Khachatrian, A. and P.J. Dagdigian, *Laser-induced breakdown spectroscopy with laser irradiation resonant with vibrational transitions.* Applied Optics, 2010. **49**(13): p. C1-C7.

101. Tang, Z., et al., *Micro-destructive analysis with high sensitivity using double-pulse resonant laser-induced breakdown spectroscopy.* Journal of Analytical Atomic Spectrometry, 2019. **34**(6): p. 1198-1204.

102. Ikeda, Y. and R. Tsuruoka, *Characteristics of microwave plasma induced by lasers and sparks.* Applied Optics, 2012. **51**(7): p. B183-B191.

103. Khumaeni, A., et al., *The role of microwaves in the enhancement of laser-induced plasma emission.* Frontiers of Physics, 2016. **11**(4): p. 114209.

104. Tang, Y., et al., *Multielemental self-absorption reduction in laser-induced breakdown spectroscopy by using microwave-assisted excitation.* Optics Express, 2018. **26**(9): p. 12121-12130.

105. Viljanen, J., Z. Sun, and Z.T. Alwahabi, *Microwave assisted laser-induced breakdown spectroscopy at ambient conditions.* Spectrochimica Acta Part B: Atomic Spectroscopy, 2016. **118**: p. 29-36.

106. Efthimion, P.C. *Advances in Laser Assisted Microwave Plasma Spectroscopy (LAMPS)*. in *Imaging and Applied Optics Technical Papers*. 2012. Monterey, California: Optical Society of America.

107. Tampo, M., et al., *Enhancement of intensity in microwave-assisted laser-induced breakdown spectroscopy for remote analysis of nuclear fuel recycling.* Journal of Analytical Atomic Spectrometry, 2014. **29**(5): p. 886-892.

108. Wall, M., Z.W. Sun, and Z.T. Alwahabi, *Quantitative detection of metallic traces in water-based liquids by microwave-assisted laser-induced breakdown spectroscopy.* Optics Express, 2016. **24**(2): p. 1507-1517.

109. Viljanen, J., et al., *Real-time release of Na, K and Ca during thermal conversion of biomass using quantitative microwave-assisted laser-induced breakdown spectroscopy.* Spectrochimica Acta Part B: Atomic Spectroscopy, 2018. **149**: p. 76-83.

110. Iqbal, A., et al., *Sensitive elemental detection using microwave-assisted laser-induced breakdown imaging.* Spectrochimica Acta Part B: Atomic Spectroscopy, 2017. **136**(Supplement C): p. 16-22.

111. Liu, Y.A., M. Baudelet, and M. Richardson, *Elemental analysis by microwave-assisted laser-induced breakdown spectroscopy: Evaluation on ceramics.* Journal of Analytical Atomic Spectrometry, 2010. **25**(8): p. 1316-1323.

112. Chen, S.J., et al., *Design and application of near-field applicators for efficient microwave-assisted laser-induced breakdown spectroscopy.* Journal of Analytical Atomic Spectrometry, 2017. **32**(8): p. 1508-1518.

113. Kearton, B. and Y. Mattley, *Laser-induced breakdown spectroscopy: Sparking new applications.* Nature Photonics, 2008. **2**(9): p. 537-540.

114. Ali, K., et al., *Laser-induced plasma emission enhanced by microwaves in argon gas for potential application of nuclear fuel material analysis.* Journal of Physics: Conference Series, 2017. **820**(1): p. 012003.

115. Liu, Y., et al., *Improvement of the sensitivity for the measurement of copper concentrations in soil by microwave-assisted laser-induced breakdown spectroscopy.* Spectrochimica Acta Part B: Atomic Spectroscopy, 2012. **73**: p. 89-92.

116. Hu, H.Q., et al., *Study on the Enhancement Intensity of Cd in Rice with Microwave-Assisted Laser-Induced Breakdown Spectroscopy.* Spectroscopy and Spectral Analysis, 2016. **36**(4): p. 1180-1185.

117. Wall, M., Z. Sun, and Z.T. Alwahabi, *Quantitative detection of metallic traces in water-based liquids by microwave-assisted laser-induced breakdown spectroscopy.* Optics Express, 2016. **24**(2): p. 1507-1517.
118. Khumaeni, A., et al., *The effect of ambient gas on measurements with microwave-assisted laser-induced plasmas in MA-LIBS with relevance for the analysis of nuclear fuel.* Journal of Radioanalytical and Nuclear Chemistry, 2017. **311**(1): p. 77-84.
119. Rosenwasser, S., et al., *Development of a method for automated quantitative analysis of ores using LIBS.* Spectrochimica Acta Part B: Atomic Spectroscopy, 2001. **56**(6): p. 707-714.
120. Hahn, D.W. and N. Omenetto, *Laser-Induced Breakdown Spectroscopy (LIBS), Part II: Review of Instrumental and Methodological Approaches to Material Analysis and Applications to Different Fields.* Applied Spectroscopy, 2012. **66**(4): p. 347-419.
121. Tognoni, E. and G. Cristoforetti, *[INVITED] Signal and noise in Laser Induced Breakdown Spectroscopy: An introductory review.* Optics & Laser Technology, 2016. **79**: p. 164-172.
122. Harilal, S., et al., *Electron density and temperature measurements in a laser produced carbon plasma.* Journal of Applied Physics, 1997. **82**: p. 2140-2146.
123. Dimitrijevic, M.S. and S. Sahal-Brechot, *Stark Broadening Parameter Tables for Neutral Calcium Spectral Lines. I.* Serbian Astronomical Journal, 2000. **161**: p. 39.
124. Milan S. Dimitrijevic and S.S. Brechot;, *On The Stark broadening of Neutral Silver Spectral lines.* Journal of Research in Physics, 1999. **28**(3): p. 291-294.
125. Griem, H.R., *Plasma spectroscopy*. New York: McGraw-Hill. 1964.
126. McWhirter, R.W.P., *Plasma Diagnostic Techniques. Edited by Richard H. Huddlestone and Stanley L. Leonard. Library of Congress Catalog Card Number 65-22763. Published by Academic Press, New York.* 1965: p. 201.
127. Zalach, J. and S. Franke, *Iterative Boltzmann plot method for temperature and pressure determination in a xenon high pressure discharge lamp.* Journal of Applied Physics, 2013. **113**(4): p. 043303.
128. Reader, J., et al., *Wavelengths and transition probabilities for atoms and atomic ions : part I. wavelengths - part II. transition probabilities*. Vol. nsrds-nbs68. 1980, NSRDS; NISTresearchlibrary; fedlink; americana: National Bureau of Standards.
129. Wu, S., et al., *Quantitative analysis of nonmetal elements in steel using laser-induced breakdown spectroscopy combined with random forest.* Analytical Methods, 2015. **7**(6): p. 2425-2432.

130. Sun, L., et al., *Mechanism study of sulfur fertilization mediating copper translocation and biotransformation in rice (Oryza sativa L.) plants.* Environmental Pollution, 2017. **226**: p. 426-434.

131. Lee, Y., et al., *Laser-Ablation Sampling for Accurate Analysis of Sulfur in Edible Salts.* Applied Spectroscopy, 2017. **71**(4): p. 651-658.

132. Trichard, F., et al., *Detection and quantification of sulfur in oil products by laser-induced breakdown spectroscopy for on-line analysis.* Spectrochimica Acta Part B: Atomic Spectroscopy, 2016. **118**: p. 72-80.

133. Liu, H., et al., *Simultaneous volatilization characteristics of arsenic and sulfur during isothermal coal combustion.* Fuel, 2017. **203**: p. 152-161.

134. Khater, M.A., *Trace detection of light elements by laser-induced breakdown spectroscopy (LIBS): Applications to non-conducting materials.* Optics and Spectroscopy, 2013. **115**(4): p. 574-590.

135. Labutin, T.A., et al., *Determination of chlorine in concrete by laser-induced breakdown spectroscopy in air.* Journal of Applied Spectroscopy, 2013. **80**(3): p. 315-318.

136. Balcerzak, M., *Sample Digestion Methods for the Determination of Traces of Precious Metals by Spectrometric Techniques*. Vol. 18. 2002. 737-50.

137. Díaz, D., D.W. Hahn, and A. Molina, *Quantification of gold and silver in minerals by laser-induced breakdown spectroscopy.* Spectrochimica Acta Part B: Atomic Spectroscopy, 2017. **136**: p. 106-115.

138. Septianti, R.W., et al., *Rapid detection of the authenticity of silver jewelry by laser induced shockwave plasma spectroscopy using Nd:YAG laser 1064 nm*, in *7th International Seminar on New Paradigm and Innovation on Natural Science and Its Application*, B. Warsito, S.P. Putro, and A. Khumaeni, Editors. 2018, Iop Publishing Ltd: Bristol.

139. Rehan, I., M.A. Gondal, and K. Rehan, *Optimized laser-induced breakdown spectroscopy for determination of xenobiotic silver in monosodium glutamate and its verification using ICP-AES.* Applied Optics, 2018. **57**(12): p. 3191-3197.

140. Asimellis, G., et al., *Platinum group metals bulk analysis in automobile catalyst recycling material by laser-induced breakdown spectroscopy.* Spectrochimica Acta Part B: Atomic Spectroscopy, 2008. **63**(11): p. 1338-1343.

141. Antolini, E., *Palladium in fuel cell catalysis.* Energy & Environmental Science, 2009. **2**(9): p. 915-931.

142. Snyder, S.C., et al., *The detection of palladium particles in proton exchange membrane fuel-cell water by laser-induced breakdown spectroscopy (LIBS).* Applied spectroscopy, 2011. **65**(6): p. 642-647.

143. Liu, B., et al., *A new ratiometric ESIPT sensor for detection of palladium species in aqueous solution.* Chemical Communications, 2012. **48**(23): p. 2867-2869.

144. Garrett, C.E. and K. Prasad, *The art of meeting palladium specifications in active pharmaceutical ingredients produced by Pd-catalyzed reactions.* Advanced Synthesis & Catalysis, 2004. **346**(8): p. 889-900.

145. Rammelkamp, K., et al., *Towards LIBS Chlorine Quantification Using the CaCl Molecular Emission in Martian Atmospheric Conditions*, in *49th Lunar and Planetary Science Conference*. 2018: The Woodlands, Texas LPI Contribution No. 2083, id.1947.

146. González de Vega, C., et al., *Analytical potential of a laser ablation–glow discharge–optical emission spectrometry system for the analysis of conducting and insulating materials.* Analytica Chimica Acta, 2015. **877**: p. 33-40.

147. Pořízka, P., et al., *Detection of fluorine using laser-induced breakdown spectroscopy and Raman spectroscopy.* Journal of Analytical Atomic Spectrometry, 2017. **32**(10): p. 1966-1974.

148. Radziemski, L., et al., *Use of the vacuum ultraviolet spectral region for laser-induced breakdown spectroscopy-based Martian geology and exploration.* Spectrochimica Acta Part B: Atomic Spectroscopy, 2005. **60**(2): p. 237-248.

149. Xiao, X., et al., *Surrogate measurement of chlorine concentration on steel surfaces by alkali element detection via laser-induced breakdown spectroscopy.* Spectrochimica Acta Part B: Atomic Spectroscopy, 2017. **130**: p. 67-74.

150. Serrano, J., J. Moros, and J.J. Laserna, *Sensing Signatures Mediated by Chemical Structure of Molecular Solids in Laser-Induced Plasmas.* Analytical Chemistry, 2015. **87**(5): p. 2794-2801.

151. Mishra(Ed.), A.K. and L.M. (Ed), *Ruthenium Chemistry*. 1st Edition ed. 2018, New York: Jenny Stanford Publishing.

152. Seddon, E.A. and K.R. Seddon, *The Chemistry of Ruthenium*. 1984: Elsevier.

153. Yang, Q., et al., *Ru/UiO-66 Catalyst for the Reduction of Nitroarenes and Tandem Reaction of Alcohol Oxidation/Knoevenagel Condensation.* ACS Omega, 2018. **3**(4): p. 4199-4212.

154. Zhang, B., et al., *A Robust Ru/ZSM-5 Hydrogenation Catalyst: Insights into the Resistances to Ruthenium Aggregation and Carbon Deposition.* ChemCatChem, 2017. **9**(19): p. 3646-3654.

155. Al Shuaili, A.A., et al., *Improvement of palladium limit of detection by microwave-assisted laser induced breakdown spectroscopy.* Spectrochimica Acta Part B: Atomic Spectroscopy, 2019. **159**: p. 105666.

156. Sander, B., *Properties of Danish biofuels and the requirements for power production.* Biomass and Bioenergy, 1997. **12**(3): p. 177-183.

157. Knudsen, J.N., P.A. Jensen, and K. Dam-Johansen, *Transformation and release to the gas phase of Cl, K, and S during combustion of annual biomass.* Energy & Fuels, 2004. **18**(5): p. 1385-1399.

158. Bartolomé, C. and A. Gil, *Ash deposition and fouling tendency of two energy crops (cynara and poplar) and a forest residue (pine chips) co-fired with coal in a pulverized fuel pilot plant.* Energy & Fuels, 2013. **27**(10): p. 5878-5889.

159. Baxter, L.L., et al., *The behavior of inorganic material in biomass-fired power boilers: field and laboratory experiences.* Fuel processing technology, 1998. **54**(1-3): p. 47-78.

160. Vamvuka, D., D. Zografos, and G. Alevizos, *Control methods for mitigating biomass ash-related problems in fluidized beds.* Bioresource Technology, 2008. **99**(9): p. 3534-3544.

161. Johansen, J.M., et al., *Release of K, Cl, and S during pyrolysis and combustion of high-chlorine biomass.* Energy & Fuels, 2011. **25**(11): p. 4961-4971.

162. Jensen, P.A., et al., *Experimental investigation of the transformation and release to gas phase of potassium and chlorine during straw pyrolysis.* Energy & Fuels, 2000. **14**(6): p. 1280-1285.

163. Knudsen, J.N., et al., *Secondary capture of chlorine and sulfur during thermal conversion of biomass.* Energy & fuels, 2005. **19**(2): p. 606-617.

164. Zhao, H., Q. Song, and Q. Yao, *Release and transformation of K and Cl during the pyrolysis of KCl-loaded cellulose.* Fuel, 2018. **226**: p. 583-590.

165. Zhao, H.-b., et al., *Study on the transformation of inherent potassium during the fast-pyrolysis process of rice straw.* Energy & Fuels, 2015. **29**(10): p. 6404-6411.

166. Zhang, Z.-H., et al., *Influence of the atmosphere on the transformation of alkali and alkaline earth metallic species during rice straw thermal conversion.* Energy & Fuels, 2012. **26**(3): p. 1892-1899.

Chapter 3

Microwave-assisted laser induced breakdown molecular spectroscopy: quantitative chlorine Detection

M. A. Wakil and Zeyad T. Alwahabi*

School of Chemical Engineering and Advanced Materials, The University of Adelaide, SA 5005, Australia.

**E-mail: zeyad.alwahabi@adelaide.edu.au*

Journal of Analytical Atomic Spectrometry, 2019, 34, 1892

Statement of Authorship

Title of Paper	**Microwave-assisted laser induced breakdown molecular spectroscopy: quantitative chlorine detection**
Publication Status	☑ Published ☐ Accepted for Publication ☐ Submitted for Publication ☐ Unpublished and Unsubmitted work written in manuscript style
Publication Details	Journal of Analytical Atomic Spectrometry, 2019,34, 1892

Principal Author 1

Name of Principal Author (Candidate)	Md. Abdul Wakil		
Contribution to the Paper	I was responsible for the development of the measurement technique under the principal supervisor of Associate Professor Zeyad Alwahabi. I performed the measurement and data processing, wrote the first draft of the manuscript, and addressed all the comments and suggestion from other author in subsequent revisions of the manuscript. Interpretation of the data was my responsibility.		
Overall percentage (%)	80%		
Certification:	This paper reports on original research I conducted during the period of my Higher Degree by Research candidature and is not subject to any obligations or contractual agreements with a third party that would constrain its inclusion in this thesis. I am the primary author of this paper.		
Signature		Date	22.04.2020

Co-Author Contributions

By signing the Statement of Authorship, each author certifies that:

i. the candidate's stated contribution to the publication is accurate (as detailed above);

ii. permission is granted for the candidate in include the publication in the thesis; and

iii. the sum of all co-author contributions is equal to 100% less the candidate's stated contribution.

Name of Co-Author	Zeyad T. Alwahabi		
Contribution to the Paper	I was principal supervisor for the development of the work, contributed to both data interpretation and refining the manuscript. I hereby certify that statement of contribution is accurate and I have given written permission for this paper to be included in this thesis.		
Overall percentage (%)	20%		
Signature		Date	29.04.2020

JAAS

PAPER

View Article Online
View Journal | View Issue

Cite this: *J. Anal. At. Spectrom.*, 2019, **34**, 1892

Received 26th April 2019
Accepted 9th July 2019

DOI: 10.1039/c9ja00151d

rsc.li/jaas

Microwave-assisted laser induced breakdown molecular spectroscopy: quantitative chlorine detection

M. A. Wakil and Zeyad T. Alwahabi*

Quantitative detection of chlorine, through molecular emission from CaCl, using microwave assisted laser induced breakdown spectroscopy (MW-LIBS) has been demonstrated. CaCl emission is utilised in the spectral range of 617.9–621.5 nm. Using time-resolved emission spectra of CaCl at 617.9 nm, following a 1.5 ms microwave pulse, an optimum gate-width and gate-delay have been established. A linear relationship between the intensity of CaCl molecular emission and chlorine concentration on a cement surface has been validated. This yields a limit of detection (LoD) of 47 ± 7 μg g^{-1} and ~170 ± 59 μg g^{-1} for chlorine, based on 100 shots averaged and a single shot, respectively. The results represent a 10-fold improvement in the chlorine LoD on cement.

1. Introduction

The detection of chlorine is important in process industries because chlorine acts as an active corrosive agent in concrete structures. Harmful species such as chlorides may penetrate together with water through the capillary pore space, which may trigger different damaging processes.[1] The major destructive processes are the corrosion of reinforcement especially pitting corrosion and concrete corrosion.[2] More specifically, chlorine can play a role in the process of stress corrosion cracking of dry cask storage located in marine environments[3] as well as in partial melting of the Martian mantle.[4] Moreover, chlorine acts as a catalyst for pitting corrosion in steel in the presence of water and O_2.[5] On the other hand, chlorine acts as an essential element in chemical building blocks, food, water purification, medicines, advanced technological devices, air conditioning refrigerants, paints, energy efficient windows, *etc.* Despite that, insufficient disinfection of chlorine can cause many hazards, and adversely high concentrations lead to toxicity in human beings and animals.[6] For damage assessment of reinforced concrete and steel, this harmful species, which is chlorine, needs to be determined properly. The detection of chlorine is important for monitoring free chlorine in real life usage as mentioned above. It is also important for complete understanding of early Mars and the presence of water in Mars.[7]

Laser Induced Breakdown Spectroscopy (LIBS) is considered as a well-established laser-ablation based analysis technique due to its distinguishing characteristics, one being the ability to perform chemical analysis on any solid sample directly. Although LIBS is advantageous due to its unique features such as the lack of need for sample preparation, speed, ease of handling and that it is almost as non-destructive as methods reported in the literature,[8–10] it is found to be less sensitive to elements (such as those present in nuclear fuel) which have a complex structure,[11] low excitation efficiency[12] and high ionization energy[13] such as halogens. It is reported that halogens such as chlorine produce weak emission making them more difficult to characterise compared to elements with prominent peaks such as alkalis, alkaline earth elements and transition metals.[13,14] Detection limits for halogens are less than satisfactory for demanding applications. Direct detection of chlorine based on atomic emission is difficult because the resonance lines of Cl I belong to the deep VUV at 134–140 nm, corresponding to ^{4}P and 4^2P, which have very high excitation energy and are difficult to populate. It is worth noting that chlorine may also be detected near 754 nm and 837 nm; however these transitions originate from states at very high excitation energies, which are 85 735 cm^{-1} and 83 894 cm^{-1}.

One possible alternative to direct measurement of chlorine is to use the detection of alkali metals as a surrogate to deduce the presence of salts that have chlorine (Cl), assuming that the concentration of these metals is proportional to that of Cl,[3,15] but in this case, homogeneous salt deposition is also essential. Another prospective alternative for chlorine detection is to use molecular emission because the molecular structure has a strong influence on the final emission pattern.[16] It has been shown that by using molecular emission, the sensitivity of LIBS for chlorine can be significantly improved due to the simple molecules that form in the plasma.[7,13] Haisch *et al.* have shown that the detection limit for chlorine can be significantly enhanced using molecular emission bands.[17]

De Giacomo *et al.* concluded that there are three conditions need to be satisfied for a molecular emission bands to be

School of Chemical Engineering, The University of Adelaide, SA 5005, Australia. E-mail: zeyad.alwahabi@adelaide.edu.au

observed. These are: an appropriate plasma temperature, a sufficient reactants density and an observable molecular transition.[18] In accordance with that, since the past few years molecular LIBS is becoming an exciting area of study for proper characterisation of chlorine. Haisch *et al.* reported CuCl molecular emission at 440 nm.[17] Álvarez *et al.* observed CaF emission at around 535 nm (ref. 19) and reported the limit of detection for fluorine at about 50 μg g^{-1}. Yao *et al.* used CN molecular emission at 388.34 nm for analysing fly ash.[20] Rezaei *et al.* analysed the aluminium percentage in plastic bonded explosives using AlO and CN molecular bands.[21] Guo *et al.* determined boron using a BO molecular band at 255.14 nm.[22] However, few studies have been undertaken for molecular chlorine in spite of its importance mentioned above. Earlier studies used different alkali elements for successful chlorine (Cl) molecular emission. Haisch *et al.* considered CuCl and reported a ten-fold improvement in the detection limit for Cl but they did not mention the detection limit.[17] Bhatt *et al.* used SrCl and SrO emissions for determining Sr concentration.[23] They reported that the detection limit using molecular emission is worse than that using atomic emission. Vogt *et al.* examined two different alkali elements for Cl detection, namely MgCl and CaCl.[7] They reported that the MgCl molecular band is unclear with LIBS while CaCl is more sensitive for Cl detection. Gaft *et al.* detected Cl in a mixture of 0.4% $CaCl_2$ using a CaCl molecular emission band.[24] Vogt *et al.* suggested in their study that calcium-free salt is not suitable for detecting Cl *via* CaCl.[25] Alvarez-Llamas *et al.* used 100 mJ laser energy for fluorine detection using Ca free samples following CaF emission.[12] Bhatt *et al.* succeeded with a laser energy of 82 mJ to calculate the LoD for Sr in a mixture of $SrCl_2$ and Al_2O_3, following SrCl and SrO molecular emissions.[23] Guo *et al.* applied 60 mJ laser energy on a solid matrix mixture of H_3BO_3 and $C_6H_{12}O_6 \cdot H_2O$ and observed BO molecular emission.[22] In addition, Rezaei *et al.* observed AlO emission using 100 mJ laser energy on aluminized PBX samples.[21]

CaCl possesses relatively strong emission bands ($A^2\Pi \rightarrow X^2\Sigma$, $B^2\Sigma \rightarrow X^2\Sigma$) at 593.5, 606.8, 617.9, 620.5 and 631.4 nm,[26] making it suitable for low level Cl detection.[2,9]

MW-LIBS is a popular method in which low laser energy is sufficient for elemental detection instead of high laser energy for LIBS to improve the LoD. MW-LIBS offers several benefits such as long plasma lifetime, larger volume, strong emission intensity, stability with time and the ability to reduce self-absorption[27–30] A laser-assisted microwave plasma spectroscopy (LAMPS) system was reported based on the electric field to the laser induced plasma by the enclosed MW cavity.[31] This extends the plasma lifetime resulting in a promising improvement in sensitivity. The LAMPS technique was also reported by Efthimion,[32] with the achievement of ~200 times enhancement. Liu *et al.* applied a MW cavity system to examine ceramics and soil samples. They demonstrated an enhancement factor of ~33 for sodium detection.[33,34] In gaseous samples, Ikeda *et al.* used an antenna to study the characteristics of laser and spark induced plasmas where a 15 times enhancement for Pb was reported.[27] Antenna-coupled MW enhanced LIBS on solid samples was also introduced by Khumaeni *et al.* at low-pressure in enclosed cavity environments.[11,35] A loop antenna was used to deliver MW radiation and a 32 times enhancement of Gd lines was observed. Tampo *et al.* achieved a 50-fold enhancement of Gd lines at a low pressure of 0.6 kPa.[36] Viljanen *et al.* observed an approximately 93-fold higher LoD with MW-LIBS for copper using solid samples.[30] Wall *et al.* reported an 11.5-fold improved LoD for indium in a water solution.[37] MW-LIBS has been demonstrated for gas samples for the detection of Na, K and Ca in flames.[38] Furthermore, Iqbal demonstrated MW-LIBS with spectrometer free detection of indium, based on imaging.[39]

MW-LIBS offers extension of the lifetime of the laser induced plasma. This is usually followed by a relatively longer detection gate (~500 μs). A longer plasma lifetime along with a prolonged detection gate provides some difficulties because emission from molecules and radicals become stronger, blocking a large atomic spectral range. However, when the process of molecular formation and emission is carefully used, the process can benefit the detection of a few elements such as chlorine. This paper reports the application of MW-LIBS directed towards quantitative detection of Cl *via* CaCl ($A^2\Pi \rightarrow X^2\Sigma$) emission at 617.9 nm and 620.5 nm.

2. Materials and methods

2.1 MW-LIBS setup

The experimental setup of MW-LIBS used for this work is presented schematically in Fig. 1. A second harmonic from a Q-switch Nd:YAG laser, Quantel (Brilliant B), ~6 ns with a repetition of 10 Hz was used. The pulse energy was controlled using a half-wave plate (HWP) and Glan-laser polariser (P). The laser energy was measured with a Pyroelectric sensor (Thorlabs, ES 220C). The beam was focussed onto the sample surface using a fused silica lens with $f = 100$ mm. The spot size obtained at the focal point was estimated to be 140 μm^2 while the propagation of the laser beam was at an angle of 15° to the vertical. A 7.5 mJ laser energy was considered where 3.5–10 mJ laser energy was analysed for enhancement calculation. To achieve the ablation from the fresh sample surface for each shot, the sample was placed on a rotating disk with an angular velocity of 7 rotations per minute. A second CW laser, with a camera, was used to monitor the exact distance between the sample surface and the fused silica lens.

A water cooled pulsed-microwave system operated at 2.45 GHz (Seirem), shown in Fig. 1, was used. The microwave radiation was directed *via* a WR340 waveguide to a 3-stub impedance tuner and then to a waveguide-to-coaxial adaptor (WR340RN) through a quartz window. The waveguide-to-coaxial adaptor was connected to a 1 m flexible coaxial cable (50 Ω NN cable) with 0.14 dB @ 2.45 GHz. A semi-rigid cable (RG402/U) was then connected at the end of the coaxial cable. The other end of the semi-rigid cable was attached to a Near Field Applicator (NFA) as shown in ref. 30 and 40. The NFA was located about 1 mm above the sample surface and 0.5 mm horizontally away from the ablation spot. The microwave pulse duration and power were controlled with an analogue signal pulse generator (Aim-TTi).

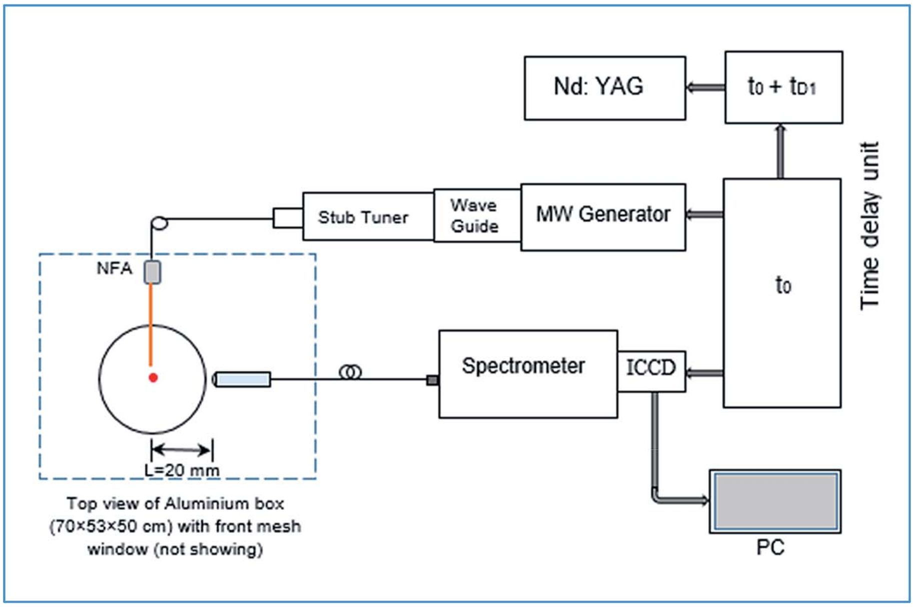

Fig. 1 Schematic diagram of the MW-LIBS setup.

For the spectroscopic detection, the plasma emission was collected directly using a bifurcated fibre bundle (Thorlabs, BFY400HS02). The fibre bundle has a core size of 400 μm and a transmission range of 250–1200 nm. The optical line, the sample holder, the NFA and one end of the fibre were placed inside an aluminium box to minimise the residual microwave radiation, as shown in Fig. 1. One side of the aluminium box was covered with metal mesh acting as an observation window.

The spectrometer (Andor Shamrock 500i) with a grating of 2400 lines per mm has a spectral resolving power of 10 000, and the spectral resolution is 0.031 nm in the spectral range of 320–332 nm. The attainable wavelength range for the spectrometer, with a holographic grating, is 200–705 nm. An intensified CCD camera (Andor, iStar) was utilized to record the spectral signal, and it was synchronised with the laser and the microwave generator. For each concentration, 100 single shots were recorded and averaged. The experiment was conducted in the atmospheric environment.

2.2 Samples

To assess the linearity in the calibration curve and the detection of chlorine (Cl), several calibration samples with different Cl concentrations were prepared by wet impregnation from cement and KCl. The KCl anhydrous (Sigma Aldrich) powder with different weights of 6.75–82.8 mg, considering the weight of Cl in KCl, was mixed with distilled water to make a solution.

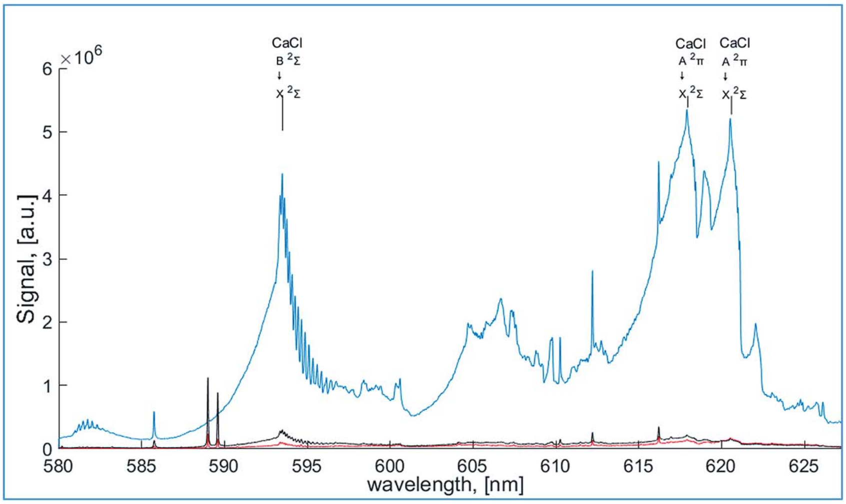

Fig. 2 MW-LIBS spectra of pure $CaCl_2$ (blue), $CaSO_4$ + KCl (2.07% Cl) (black), and cement + KCl (2.07% Cl) (red). The spectra were recorded using 7.5 mJ laser energy, 600 W microwave power, 500 ns gate-delay, 300 μs gate-width and an accumulation of 100 shots.

Each solution was mixed with an exact amount of cement (4 g) with an uncertainty of ±0.00033 g to make a paste, for all samples. Eleven samples were prepared with varying Cl concentrations from 0.08 to 2.07% (by weight). The paste was placed in a circular disk to make a pellet and dried with a dryer.

3. Results and discussion

3.1 Spectral information and enhancement

Typical spectra of molecular CaCl recorded in LIBS with microwave radiation are presented in Fig. 2. A MW-LIBS scan in the range of 580–630 nm was analysed to identify the best spectral range of CaCl required for the calibration. Four possible emission spectra of CaCl in this range, *i.e.*, 593.5 nm, 606.4 nm, 617.9 nm and 620.5 nm, as shown in Fig. 2 were identified. The MW-LIBS scan was done with three different sample sources. Samples made of pure $CaCl_2$ (Sigma Aldrich, 98% purity) were also tested for the confirmation of the absolute CaCl spectral range. The formation of CaCl molecular spectra depends largely on the calcium-based matrix.[25] Cement was used as a base material of calcium because of the large percentage of calcium in cement (~40% in Portland cement). The second reason for using cement as a base material for chlorine detection is corrosion related issues, such as pitting corrosion and concrete corrosion, in the concrete by chlorine. Fig. 3 also confirmed the presence of calcium with sufficiently high signals of calcium at 610.27 nm, 612.22 nm and 616.217 nm. Among all the possible emission spectra of CaCl, those at 617.9 nm and 620.5 nm were considered for the calibration curve because the spectral wavelength range had higher enhancement than in the range of 593.5 nm as shown in Fig. 4(a and b). Furthermore, it was observed that using MW-LIBS, there is another spectral feature near 593.5 nm that interferes with CaCl emission.

The spectral range of 616–625 nm was used to develop the calibration curve for Cl detection. This spectral range presents

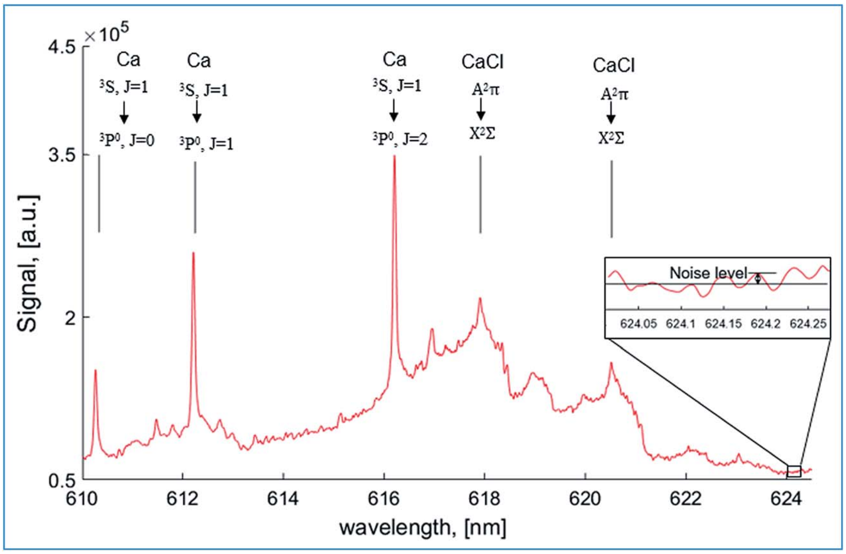

Fig. 3 MW-LIBS spectra of cement + KCl (2.07% Cl) at 7.5 mJ laser energy, 600 W microwave power, 500 ns gate-delay, 300 μs gate-width and an accumulation of 100 shots.

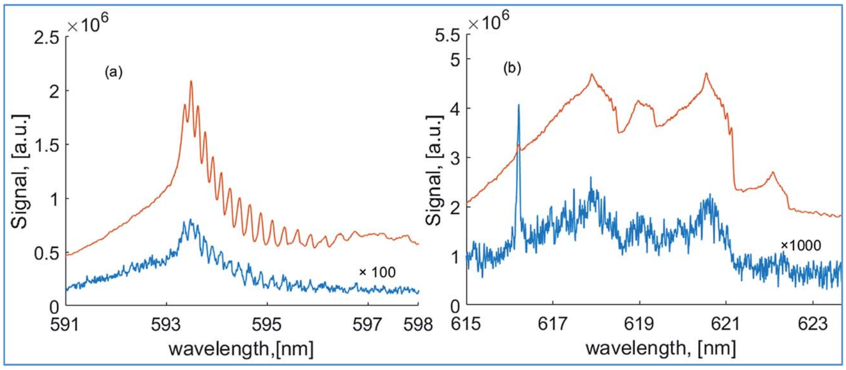

Fig. 4 Typical pure $CaCl_2$ spectra recoded at two spectral ranges (591–598 nm (a) and 615–623.5 nm (b)), with 600 W microwave power (red), and without microwave (blue), at 7.5 mJ laser energy, 500 ns gate-delay, and 300 μs gate-width. For clarity, the LIBS signal (blue) was multiplied by a factor of 100 and 1000 for spectral ranges (a) and (b), respectively.

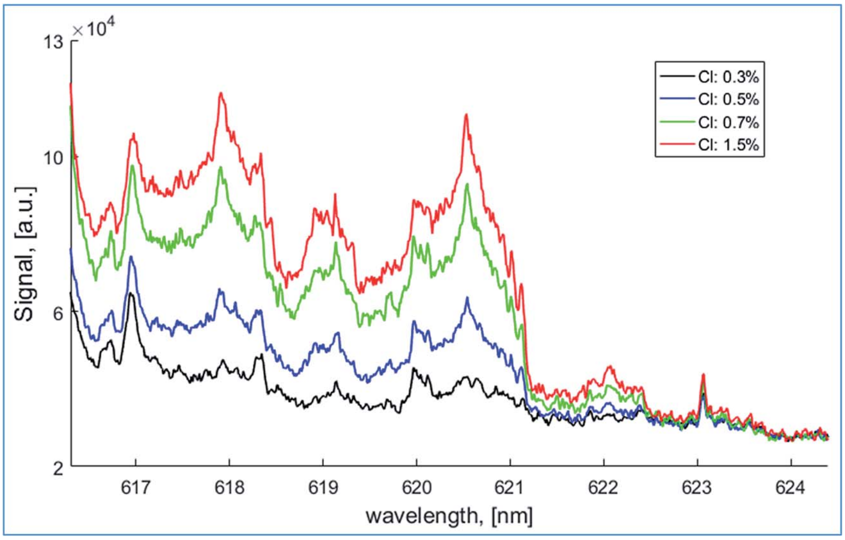

Fig. 5 MW-LIBS spectra for different chlorine concentrations at 7.5 mJ laser energy, 600 W microwave power, 500 ns gate-delay, 300 μs gate-width and an accumulation of 100 shots.

a suitable emission spectrum with minimum background noise. Fig. 5 shows the sample emission spectrum of CaCl for different concentrations of Cl using MW-LIBS.

3.2 Temporal evolution of MW-LIBS signal measurements

The temporal evolution of molecular emission intensity was investigated for MW-LIBS by maintaining a constant gate width of 300 μs and varying the gate delay from 0 ns to 2 μs. The temporal evolution of MW-LIBS is shown in Fig. 6. It was observed that the CaCl signal had an interference with the CaO signal at around 615 nm (ref. 24) shown in Fig. 6(a). A 300 μs gate width was found optimum to maximise the CaCl signal. Fig. 6(a) shows that the formation of the two radicals CaCl and CaO differs with respect to time. It was seen that the CaO signal was high initially and decreased with time until 1000 ns and increased again. Because of the constant amount of Ca present, the CaO signal was dominant initially and then the CaCl signal became stronger. To be able to investigate the optimum gate-delay, the intensities I_{CaCl} and I_{CaO} were first normalised to obtain $I_{\mathrm{CaCl}}^{\mathrm{norml}}$ and $I_{\mathrm{CaO}}^{\mathrm{norml}}$, respectively. The difference between the two normalised quantities ($I_{\mathrm{CaCl}}^{\mathrm{norml}} - I_{\mathrm{CaO}}^{\mathrm{norml}}$) was then plotted *versus* time, as shown in Fig. 6(b). Fig. 6(b) shows clearly that the quantity ($I_{\mathrm{CaCl}}^{\mathrm{norml}} - I_{\mathrm{CaO}}^{\mathrm{norml}}$) starts increasing at a gate-delay of 500 ns. Therefore, a gate-delay and gate-width of 500 ns and 300 μs, respectively, were used for CaCl detection.

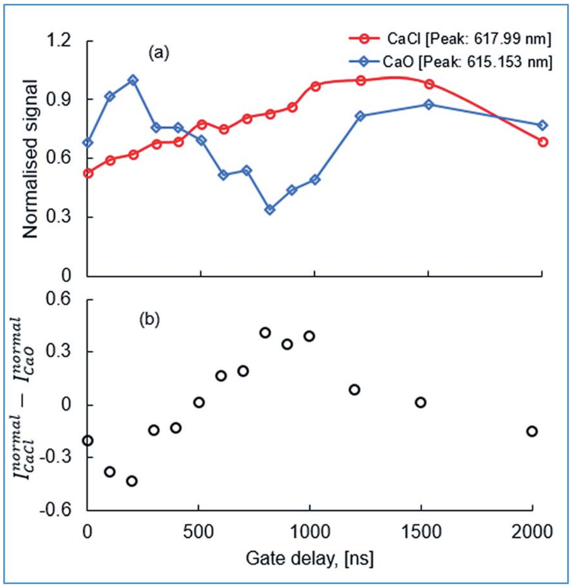

Fig. 6 Temporal evolution of the normalised MW-LIBS signal of CaO and CaCl (a) and the normalised signal difference ($I_{\mathrm{CaCl}}^{\mathrm{norml}} - I_{\mathrm{CaO}}^{\mathrm{norml}}$) (b) recoded on the sample with 1% Cl using 7.5 mJ laser energy and 600 W microwave power.

3.3 Dependence of microwave power on experimental parameters

The dependence of the MW-LIBS signal intensity on MW power at different laser energies was investigated, with the aim of optimising the MW-LIBS signal. Fig. 7(a) shows the effect of signal to noise ratio (SNR) on microwave power. The noise level was obtained in the range of 624.01 nm to 624.23 nm, as shown in the typical inset presented in Fig. 3. As shown in Fig. 7(a), the signal to noise ratio with MW-LIBS is higher than in LIBS. This is due to the signal enhancing ability of the microwave system. The external energy supplied, using microwave radiation, will sustain the free electrons present within the laser-induced plasma. These reenergized free electrons act as an excitation source, *via* collisional processes, leading to lifetime extension which finally leads to signal enhancement.[33,37] It is seen from Fig. 7(a) that the increase in microwave power did not increase the signal to noise ratio significantly because the increase in microwave power caused a higher noise level. Chen *et al.*[40] demonstrated the same behaviour of microwave power on the

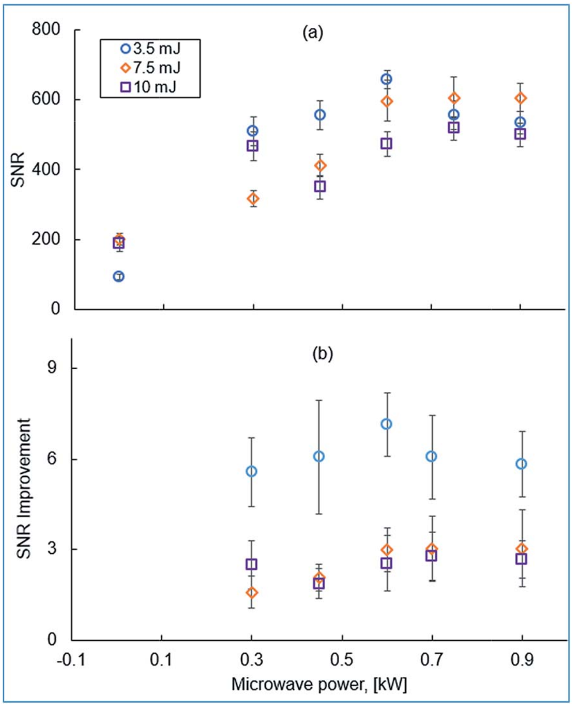

Fig. 7 (a) Signal to noise ratio (SNR) (a) and SNR improvement (b) of MW-LIBS of 2.07% Cl content samples recorded at 500 ns gate-delay, 300 µs gate-width and an accumulation of 100 shots.

SNR. It was observed from Fig. 7(a) that the increase of microwave power after 0.6 kW did not help to increase the SNR. For proper selection of microwave power for the detection of Cl, SNR improvement calculation was done as shown in Fig. 7(b). As Fig. 7(b) shows, 0.6 kW microwave power maximises the SNR improvement. Fig. 7(b) shows that the low laser energy (3.5 mJ) provides relatively higher enhancement than high laser energy (7.5 mJ or 10 mJ). This is due to the ease of microwave coupling at a lower laser energy. Increasing the laser energy will result in an increase in the electron density of the plasma's core which will result in a reduction of microwaves that penetrate into the plasma resulting in a measurement similar to that of a conventional LIBS.[30,37] It was found experimentally that by using 7.5 mJ laser energy, a reasonable MW-LIBS signal was possible even with low values of Cl concentration. Using 600 W microwave power, the chlorine SNR improved 2.5-fold, with respect to LIBS only. It is worth noting that the LIBS signal may be increased by using high laser energy. However, it is advantageous to use low laser energy to prevent sample damage and provide a practical pathway for mobile devices.

3.4 Quantitative detection of chlorine

The LoD of Cl using atomic lines reported by Wilsch *et al.* is 0.15% in concrete cores.[41] Burakov *et al.* found an LoD of 0.05% in cement based materials.[42] Weritz *et al.* analysed different building materials and reported the LoD of Cl at about 0.5%.[43] Gehlen *et al.* used UV lines of Cl (134.72 nm) and calculated 0.1% LoD from concrete.[44] For quantitative detection of Cl, molecular emission was considered rather than atomic lines. Calibration curves were determined with LIBS and MW-LIBS molecular signals of CaCl. For correct calibration, a Cl free sample was first investigated as shown in Fig. 8.

For developing the calibration curve, the experimental parameters were 7.5 mJ laser energy, 0.6 kW microwave power, 500 ns gate delay, 300 µs gate width and a microwave pulse duration of 1.5 ms. Fig. 9 and 10 show the calibration curve with LIBS and MW-LIBS for 100 shot accumulation and single shot simultaneously.

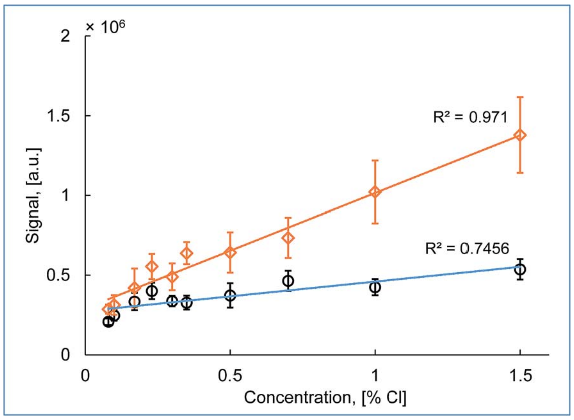

Fig. 9 Calibration curve of [Cl] with LIBS (blue) and MW-LIBS (red) at 7.5 mJ laser energy, 600 W microwave power, 500 ns gate-delay and 300 µs gate-width with an accumulation of 100 shots. The slope of the fitting is 724 466 and 185 593 for LIBS and MW-LIBS, respectively.

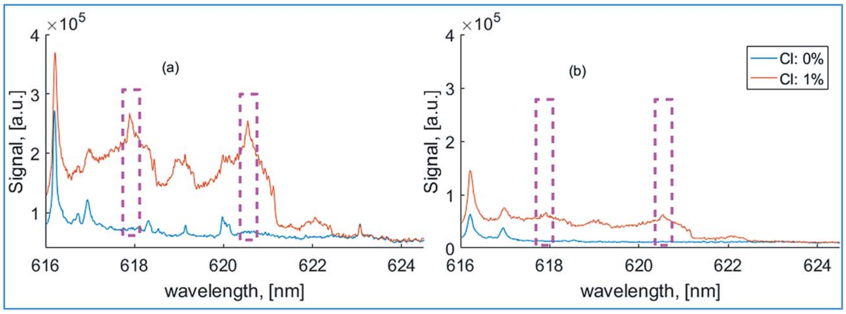

Fig. 8 MW-LIBS (a) and LIBS (b) spectra for Cl free and Cl containing samples at 7.5 mJ laser energy, 600 W microwave power, 500 ns gate-delay, and 300 µs gate-width with an accumulation of 100 shots.

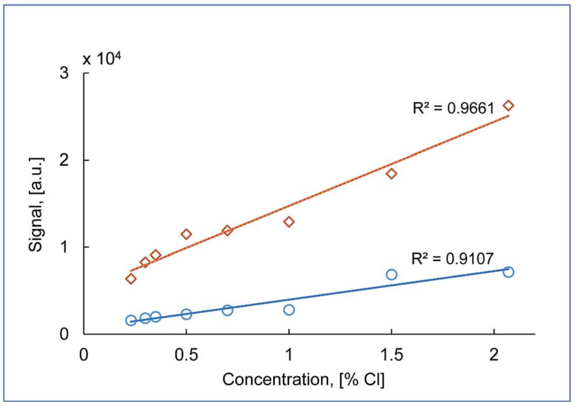

Fig. 10 Calibration curve of [Cl] with LIBS (blue) and MW-LIBS (red) at 7.5 mJ laser energy, 600 W microwave power, 500 ns gate-delay and 300 μs gate-width for one single shot. The slope of the fitting is 9651.7 and 3289.6 for LIBS and MW-LIBS, respectively.

Table 1 LoD reported in the literature

Method	Matrix	LoD	Reference
LIBS	Concrete core	0.15%	41
LIBS	Cement	0.05%	42
LIBS	Building material	0.1%	43
MW-LIBS	Cement	0.0047%	This work

The limit of detection (LoD) was calculated using the 3-sigma method.[38] The enhancing ability of MW-LIBS has been outlined in Fig. 7. The slope found using MW-LIBS data was ~4 times higher than the one from LIBS. The LoD was calculated for 100 shot accumulation and single shot measurements. The LoD for 100 shot accumulation was 47 ± 7 μg g^{-1} while for the single shot it was 170 ± 59 μg g^{-1}. The LoD found by MW-LIBS was compared with LIBS data from the same experiment. The corresponding value for 100 shot accumulation and a single shot with LIBS was 139 ± 23 μg g^{-1} and 168 ± 38 μg g^{-1}, respectively. The results show that the MW-LIBS yields a 3-fold improved limit of detection compared with LIBS. In addition to the superior chlorine LoD achieved, MW-LIBS offers ease of use and real-time detection. The LoD evaluated in this work represents a 10-fold improvement of the Cl detection limit reported in the literature as shown in Table 1.

4. Conclusion

Quantitative chlorine detection, *via* molecular emission, using a microwave assisted LIBS technique is reported. Chlorine detection with LIBS is also evaluated to show the benefit of using MW-LIBS over LIBS. Possible emission spectra of CaCl have been tested and the optimum emission spectrum of CaCl for developing the calibration curve has been identified. It was observed that the optimum signal of CaCl at around 617.9–621.5 nm was found at 500–1000 ns gate-delay and a gate-width of 300 μs. In addition, it was determined that a laser energy less than 7 mJ was not suitable for a proper calibration process. Using MW-LIBS, the LoD of chlorine is 47 ± 7 μg g^{-1}, and it presents a 3-fold improvement to that with LIBS. The LoD was obtained using a calibration curve of 10 cement samples, with different chlorine concentrations. The lowest chlorine concentration used was 800 μg g^{-1}. Although 800 μg g^{-1} is not very low, the recorded noise level was very low. The combination of the slope and the standard deviation, based on the 3-sigma method, yields the recorded 47 ± 7 μg g^{-1} LoD. The LoD evaluated in this work represents a 10-fold improvement to the Cl detection limit reported in the literature.

MW-LIBS offers a few advantages including usability at low laser energy and lifetime extension of the laser-induced-plasma. The former prevents significant sample damage and results in reliable averaging. The latter provides significant signal enhancement at a low noise level. This translates to an excellent LoD. MW-LIBS systems, however, require the use of microwave generators, waveguides and near field applicators. These additional elements add to the complexity of the detection setup, when compared to LIBS. Furthermore, a MW-LIBS setup, with a near field applicator, is not suitable for standoff applications.

Conflicts of interest

There are no conflicts to declare.

References

1 C. Gottlieb, T. Günther and G. Wilsch, *Spectrochim. Acta, Part B*, 2018, **142**, 74–84.
2 C. Gottlieb, S. Millar, T. Günther and G. Wilsch, *Spectrochim. Acta, Part B*, 2017, **132**, 43–49.
3 X. Xiao, S. Le Berre, K. C. Hartig, A. T. Motta and I. Jovanovic, *Spectrochim. Acta, Part B*, 2017, **130**, 67–74.
4 O. Forni, M. Gaft, M. J. Toplis, S. M. Clegg, S. Maurice, R. C. Wiens, N. Mangold, O. Gasnault, V. Sautter, S. Le Mouélic, P.-Y. Meslin, M. Nachon, R. E. McInroy, A. M. Ollila, A. Cousin, J. C. Bridges, N. L. Lanza and M. D. Dyar, *Geophys. Res. Lett.*, 2015, **42**, 1020–1028.
5 F. Weritz, D. Schaurich, A. Taffe and G. Wilsch, *Anal. Bioanal. Chem.*, 2006, **385**, 248–255.
6 C. Xiong, T. F. Zhang, D. Wang, Y. Lin, H. Qu, W. Chen, L. B. Luo, Y. B. Wang, L. Zheng and L. L. Fu, *Anal. Chim. Acta*, 2018, **1033**, 65–72.
7 D. S. Vogt, K. Rammelkamp, S. Schroder and H. W. Hubers, *Icarus*, 2018, **302**, 470–482.
8 S. Wu, T. Zhang, H. Tang, K. Wang, X. Yang and H. Li, *Anal. Methods*, 2015, **7**, 2425–2432.
9 N. Huber, S. Eschlböck-Fuchs, H. Scherndl, A. Freimund, J. Heitz and J. D. Pedarnig, *Appl. Surf. Sci.*, 2014, **302**, 280–285.
10 L. Dudragne, Ph. Adam and J. Amouroux, *Appl. Spectrosc.*, 1998, **52**, 1321–1327.
11 A. Khumaeni, T. Motonobu, A. Katsuaki, M. Masabumi and W. Ikuo, *Opt. Express*, 2013, **21**, 29755–29768.
12 C. Alvarez-Llamas, J. Pisonero and N. Bordel, *J. Anal. At. Spectrom.*, 2017, **32**, 162–166.

13 D. E. Anderson, B. L. Ehlmann, O. Forni, S. M. Clegg, A. Cousin, N. H. Thomas, J. Lasue, D. M. Delapp, R. E. McInroy, O. Gasnault, M. D. Dyar, S. Schroder, S. Maurice and R. C. Wiens, *J. Geophys. Res.*, 2017, **122**, 744–770.

14 K. Rammelkamp, D. S. Vogt, S. Schröder and H.-W. Hübers, presented in part at the *49th Lunar and Planetary Science Conference*, The Woodlands, Texas, LPI Contribution No. 2083, id. 1947, 2018.

15 T. A. Labutin, A. M. Popov, S. N. Raikov, S. M. Zaytsev, N. A. Labutina and N. B. Zorov, *J. Appl. Spectrosc.*, 2013, **80**, 315–318.

16 J. Serrano, J. Moros and J. J. Laserna, *Anal. Chem.*, 2015, **87**, 2794–2801.

17 C. Haisch, R. Niessner, O. I. Matveev, U. Panne and N. Omenetto, *Fresenius. J. Anal. Chem.*, 1996, **356**, 21–26.

18 A. De Giacomo and J. Hermann, *J. Phys. D: Appl. Phys.*, 2017, **50**, 17.

19 C. Álvarez, J. Pisonero and N. Bordel, *Spectrochim. Acta, Part B*, 2014, **100**, 123–128.

20 S. Yao, Y. Shen, K. Yin, G. Pan and J. Lu, *Energy Fuels*, 2015, **29**, 1257–1263.

21 A. H. Rezaei, M. H. Keshavarz, M. K. Tehrani and S. M. R. Darbani, *Laser Phys.*, 2018, **28**, 10.

22 L. B. Guo, Z. H. Zhu, J. M. Li, Y. Tang, S. S. Tang, Z. Q. Hao, X. Y. Li, Y. F. Lu and X. Y. Zeng, *Opt. Express*, 2018, **26**, 2634–2642.

23 C. R. Bhatt, B. Alfarraj, K. K. Ayyalasomayajula, C. Ghany, F. Y. Yueh and J. P. Singh, *Appl. Opt.*, 2015, **54**, 10264–10271.

24 M. Gaft, L. Nagli, N. Eliezer, Y. Groisman and O. Forni, *Spectrochim. Acta, Part B*, 2014, **98**, 39–47.

25 D. Vogt, K. Rammelkamp, S. Schröder and H.-W. Hübers, *presented in part at the LPSC 2017*, The Woodlands, USA, 2017.

26 A. A. Bol'shakov, X. Mao, J. J. González and R. E. Russo, *J. Anal. At. Spectrom.*, 2016, **31**, 119–134.

27 Y. Ikeda and R. Tsuruoka, *Appl. Opt.*, 2012, **51**, B183–B191.

28 A. Khumaeni, K. Akaoka, M. Miyabe and I. Wakaida, *Front. Phys.*, 2016, **11**, 114209.

29 Y. Tang, J. Li, Z. Hao, S. Tang, Z. Zhu, L. Guo, X. Li, X. Zeng, J. Duan and Y. Lu, *Opt. Express*, 2018, **26**, 12121–12130.

30 J. Viljanen, Z. Sun and Z. T. Alwahabi, *Spectrochim. Acta, Part B*, 2016, **118**, 29–36.

31 B. Kearton and Y. Mattley, *Nat. Photonics*, 2008, **2**, 537.

32 P. C. Efthimion, *Advances in Laser Assisted Microwave Plasma Spectroscopy (LAMPS)*, 2012.

33 Y. Liu, B. Bousquet, M. Baudelet and M. Richardson, *Spectrochim. Acta, Part B*, 2012, **73**, 89–92.

34 Y. Liu, M. Baudelet and M. Richardson, *J. Anal. At. Spectrom.*, 2010, **25**, 1316–1323.

35 A. Khumaeni, M. Miyabe, K. Akaoka and I. Wakaida, *J. Radioanal. Nucl. Chem.*, 2017, **311**, 77–84.

36 M. Tampo, M. Miyabe, K. Akaoka, M. Oba, H. Ohba, Y. Maruyama and I. Wakaida, *J. Anal. At. Spectrom.*, 2014, **29**, 886–892.

37 M. Wall, Z. W. Sun and Z. T. Alwahabi, *Opt. Express*, 2016, **24**, 1507–1517.

38 J. Viljanen, H. Zhao, Z. Zhang, J. Toivonen and Z. T. Alwahabi, *Spectrochim. Acta, Part B*, 2018, **149**, 76–83.

39 A. Iqbal, Z. Sun, M. Wall and Z. T. Alwahabi, *Spectrochim. Acta, Part B*, 2017, **136**, 16–22.

40 S. J. Chen, A. Iqbal, M. Wall, C. Fumeaux and Z. T. Alwahabi, *J. Anal. At. Spectrom.*, 2017, **32**, 1508–1518.

41 G. Wilsch, F. Weritz, D. Schaurich and H. Wiggenhauser, *Constr. Build. Mater.*, 2005, **19**, 724–730.

42 V. S. Burakov, V. V. Kiris and S. N. Raikov, *J. Appl. Spectrosc.*, 2007, **74**, 321–327.

43 F. Weritz, D. Schaurich and G. Wilsch, *Spectrochim. Acta, Part B*, 2007, **62**, 1504–1511.

44 C. D. Gehlen, E. Wiens, R. Noll, G. Wilsch and K. Reichling, *Spectrochim. Acta, Part B*, 2009, **64**, 1135–1140.

Chapter 4

Quantitative Fluorine and Bromine detection at ambient condition Via Molecular Emission

M.A. Wakil and Zeyad T. Alwahabi*

School of Chemical Engineering and Advanced materials, The University of Adelaide, SA 5005. Australia

**E-mail: zeyad.alwahabi@adelaide.edu.au*

Submitted to Journal of Analytical Atomic Spectrometry

Statement of Authorship

Title of Paper	**Quantitative Fluorine and Bromine detection at ambient condition Via Molecular Emission**	
Publication Status	☐ Published ☑ Submitted for Publication	☐ Accepted for Publication ☐ Unpublished and Unsubmitted work written in manuscript style
Publication Details	Submitted to Journal of Analytical Atomic Spectrometry	

Principal Author 1

Name of Principal Author (Candidate)	Md. Abdul Wakil		
Contribution to the Paper	I was responsible for the development of the measurement technique under the principal supervisor of Associate Professor Zeyad Alwahabi. I performed the measurement and data processing, wrote the first draft of the manuscript, and addressed all the comments and suggestion from other author in subsequent revisions of the manuscript. Interpretation of the data was my responsibility.		
Overall percentage (%)	80%		
Certification:	This paper reports on original research I conducted during the period of my Higher Degree by Research candidature and is not subject to any obligations or contractual agreements with a third party that would constrain its inclusion in this thesis. I am the primary author of this paper.		
Signature		Date	22.04.2020

Co-Author Contributions

By signing the Statement of Authorship, each author certifies that:

i. the candidate's stated contribution to the publication is accurate (as detailed above);

ii. permission is granted for the candidate in include the publication in the thesis; and

iii. the sum of all co-author contributions is equal to 100% less the candidate's stated contribution.

Name of Co-Author	Zeyad T. Alwahabi		
Contribution to the Paper	I was principal supervisor for the development of the work, contributed to both data interpretation and refining the manuscript. I hereby certify that statement of contribution is accurate and I have given written permission for this paper to be included in this thesis.		
Overall percentage (%)	20%		
Signature		Date	29.042020

Quantitative Fluorine and Bromine detection at ambient condition Via Molecular Emission

M.A. Wakil and Zeyad T. Alwahabi*

School of Chemical Engineering and Advanced materials, The University of Adelaide, SA 5005. Australia
**Corresponding author:* zeyad.alwahabi@adelaide.edu.au

Abstract

The fluorine and bromine limit of detection (LoD), based on emission from CaF and CaBr, using Microwave-assisted Laser Induced Breakdown Spectroscopy (MW-LIBS) have been determined. Molecular emission bands of CaF and CaBr in the spectral range of 605 nm and 627.1 nm are utilised for quantitative fluorine and bromine detection. The optimum gating has been established for the CaF, at 603.3 nm and 605 nm, following 1.5 ms long microwave pulses. The MW-LIBS plasma temperature and electron density against laser energy have been demonstrated at constant microwave power coupling to optimise laser energy using Ca I lines. A linear relationship between CaF signal strength and fluorine concentration, and CaBr signal strength and bromine in cement has been validated. The recorded limit of fluorine and bromine detection was 106±6 µg/g and 0.2±0.04%, respectively. The results represent an improved detection limit at low laser energy and 4-fold improved detection limit for bromine.

Keywords: Microwave assisted LIBS, molecular emission, fluorine, bromine, detection limit.

1. Introduction

The detection of halogenated elements is important for the process of analysis, environmental or geological exploration due to their diverse usage, and adverse impacts on the environment, for example depletion of the ozone layer. Given the recent trend in increasing the use of recycled products, halogenated compounds appear to be present in these new products. It is therefore important to analyse these elements under field conditions, which are very difficult to replicate in real time applications.

The uses of halogenated elements and more specifically, fluorine and bromine are evident in different industries. For example, fluorine exists in ionic or combined forms with other chemicals in minerals like fluorspar, fluorapatite, criolite and other compounds [1]. Fluorides released into the environment through volcanoes, power plants and other high temperature processes usually take the form of hydrogen fluoride gas. Fluorine contained in windblown soils normally consists of large particles, which may settle on the ground or is washed out by the rain [1]. Fluorine and its compounds can be found in fire extinguishers, pharmaceutical, agrochemical products, dental care, polymers, etc. [2, 3]. In addition, fluorine is used as a compound in industries for manufacturing metallic aluminium, ceramics, and ionic superconducting materials [4, 5] Meanwhile bromine, the 62nd most abundant element in the earth's crust, is used as a compound to prevent fouling of internal combustion engines, fire suppression and flame retardant [6]. Additionally, brominated compounds are present in many ordinary products such as in plastic in television sets, smartphones, insecticides, etc. [7]. Conversely, the extreme reactivity of fluorine is highly responsible for various forms of corrosion such as pitting corrosion in steel [8], corrosion of reinforcement materials [9], and structural material corrosion [10]. F_2 solution can cause stress-related corrosion cracking on commercially pure titanium, which can worsen the oral cavity [11]. However, the economic importance and usage of fluorine and bromine requires fast, effective detection for proper quantification.

LIBS is considered to be one of the most popular detection techniques due to its fast, direct, real time chemical analysis of any solid sample. Apart from these advantages, it is found to be less sensitive to certain elements (for example, nuclear fuel) having complex structures [12] low excitation efficiency [13] and high ionization energy[14] such as halogens. Detection limits for halogens using their atomic lines are less than satisfactory for demanding applications because of their high energy-level distributions. The use of buffer gas as an inert environment was an effective solution. Asimellis et al. detected fluorine at F I 685.6 nm for a concentration of 0.03% under a vacuum helium environment [15]. Gonzalez et al. reported the detection limit of fluorine (F) was 109 μg/g under reduced argon (Ar) and helium (He) atmosphere using the atomic line at F I 685.6 nm [5]. Pavel et al. found a 150 ppm detection limit under a low pressure He environment [3]. Meanwhile Quarles et al. discovered a 135 ppm detection limit for F I (685.6 nm) under He purged gas [16]. Kratochvil et al. applied double pulse LIBS under a helium environment and reported a 0.47% detection limit at F I 685.6 nm [17]. In their study, Menghan et al. observed a bromine (Br) signal at Br I 827.24 nm in an atmospheric environment [18]. Radziemski et al. used the vacuum ultra violet region and reported the detection limit of Br was 5.6% at 163.3 nm atomic line [19]. Barbier et al. reported the limits of detection for Br were 3.6% and 0.9% under air and helium atmospheres, respectively. Their measurements were performed at Br I 827.24 nm [20].

Other possible alternatives to increase the sensitivity of LIBS are to use surrogate measurement or molecular emission rather than atomic emission [21, 22]. Gaft et al. stated in their study that the use of molecular emission is a potential method to improve plasma emission sensitivity for halogens [4]. Alvarez et al. have shown in their study that the detection limit of F can be improved by a factor of 25 using CaF molecular emission instead of atomic emission [2]. Forni et al. detected a fluorine content amounting to approximately 0.4% using CaF molecular band for the first time on mars [23]. Alvarez et al. calculated a detection limit of 49 µg/g using CaF molecular emission in calcium-free samples [14]. Pavel et al. reported a 65 ppm detection limit of fluorine using a CaF band [3]. In another study, Gaft et al. used a bromine-containing compound and observed CaBr molecular emissions at 624.4 nm and 627 nm, respectively [7]. Microwave-assisted laser induced breakdown spectroscopy (MW-LIBS) is found to be one of the best signal enhancing techniques at a relatively low laser energy, and this improves the limit of detection (LoD) compared with LIBS. The MW-LIBS technique has been applied over the last decade due to its distinguishable benefits including: long plasma lifetime, larger volume, strong emission intensity, stability over time, and its ability to reduce self-absorption [13, 21, 24, 25]. MW-LIBS offers an extended lifetime to the laser induced plasma. This is usually followed by a relatively longer detection gate of ~500 µs. A longer plasma lifetime along with a prolonged detection gate provides some difficulties because the emission from molecules and radicals becomes stronger, blocking wide spectral range. However, when the process of molecular formation and emission is carefully used, the process can help the detection of halogen elements. Our recent paper on chlorine detection using molecular emission is an example [26]. Here, our focus is on the quantitative detection of fluorine and bromine using the MW-LIBS technique through molecular emissions, namely CaF and CaBr at 605 nm and 627.1 nm, respectively.

2. Experimental details

2.1 MW-LIBS methodology

The experimental setup is a conventional single pulse laser induced breakdown spectroscopy that incorporates microwave-assisted laser induced breakdown spectroscopy. The setup system contains a 532 nm Nd:YAG second harmonic laser, Quantel (Brilliant B), ~6 ns with a repetition rate of 10 Hz. A fused silica lens with F=100 mm was used to focus the beam onto the sample surface. The laser beam was propagated onto the sample surface at an angle of 15^{O}

to the vertical. 10 mJ and 15 mJ laser energies were used to analyse the CaF and CaBr molecular emission band, respectively. To achieve the ablation from the fresh sample surface for each shot, the sample was placed on a rotating disk with an angular velocity of 7 revolutions per minute. A second continuous-wave laser [27] armed with a camera served to monitor the exact distance between the sample surface and fused silica lens.

The microwave radiation from a water-cooled pulse-microwave system (Seirem) at 2.45 GHz was directed to a 3-stub impedance tuner through a WR340 waveguide and then to a waveguide-to-coaxial adaptor (WR340RN). A quartz window was used to finalise this process. The waveguide-to-coaxial adaptor was connected to a 1 m flexible coaxial cable (50 Ω NN cable) with 0.14 dB @ 2.45 GHz. A semi-rigid cable (RG402/U) was then connected to the end of the coaxial cable. The other end of the semi-rigid cable was attached to a Near Field Applicator (NFA) as shown in [13, 28]. The NFA was located about 1 mm above the sample surface and 0.5 mm horizontally away from the ablation spot. The microwave pulse duration and power were controlled with an analogue signal pulse generator (Aim-TTi). The microwave pulse duration was kept constant at 1.5 ms.

To analyse the plasma emission, a conventional spectrometer with gated CCD (Andor, Shamrock 500i) equipped with 300, 1200 and 2400 lines/mm diffraction grating was used. For the experiment, 1200 grating was used. The plasma emission from LIBS was collected directly through a perforated parabolic mirror (FL=152 mm) and then focussed by a plano-convex lens (FL=100 nm), onto the sample by a plano-convex UV fused silica lens. A second lens (FL=20 mm) was used to couple the emission onto an Achromatic Reflective Coupler (ARC), which is connected to a 7-fibre bundle (Thorlabs, BFL200HS02). The fibre bundle was Round-to-Linear Bundle, 7 x Ø200 µm.

2.2 Materials

Portland cement (~40% Ca) was used as a source of calcium and the NaF and KBr salts were supplied by Sigma-Aldrich. Several calibration samples, with different F and Br concentrations were prepared, by wet impregnation from cement and NaF (and KBr) in order to assess linearity in the calibration curves and detection of F and Br. Different weights of NaF anhydrous powder, ranging from 4 mg to 150 mg, was mixed with distilled water to make a solution. Each solution was mixed with the correct amount of cement (4 g) where the weight of F was considered for making the paste to be applied to all samples. Twelve samples were prepared with an increasing order of F concentration from 452 µg/g to 16958 µg/g. The pastes of all samples were placed in circular disks to form the pellets. The pellets were dried in a dryer and the same procedure was repeated for Br containing samples with different weights of KBr, ranging from 20 mg to 450 mg.

2.3 Plasma temperature and Electron density

The strong calcium lines were considered for plasma temperature measurement as presented in Table 1. Plasma temperature was calculated using Boltzmann plot to evaluate the plasma temperature during experiment [29].

Electron density was calculated using the calcium line (422.67 nm) according to the relation between full-width-at-half-maximum (FWHM) of the line $\Delta\lambda_{1/2}$, and electron density, N_e [30]. The stark width broadening parameter for Ca I at 422.67 nm was considered as (0.115671-0.118173) $\times 10^{-6}$ Å [31]. To understand if the plasma is at local thermodynamic equilibrium (LTE), the McWhirter criterion was calculated using equation 1[32]. Figure 1 represents a typical example of a Boltzmann plot (a) and full width half maximum (b) using the Ca I lines.

$$N_e \geq 1.6 \times 10^{12} \Delta E^3 T_e^{\frac{1}{2}} \ldots\ldots\ldots\ldots\ldots\ldots\ldots\ldots\ldots.. (1)$$

The instrumental broadening was determined to be 0.0321 nm by recoding the Hg line at 253.6 nm. The value of $\Delta\lambda_{1/2}$ was evaluated using a simple equation [33].

$$\Delta\lambda_{\text{measured}} = \Delta\lambda_{\text{actual}} + \Delta\lambda_{\text{instrument}}$$

Table 1: Spectroscopic data of calcium (Ca l) [34]

Wavelength (nm)	**A_{ki} (s^{-1})**	**E_k (eV)**	**g**
364.441	3.55×10^7	5.3	7
422.673	2.18×10^8	2.93251	3
430.253	1.36×10^8	4.77979	7
445.478	8.7×10^7	4.68133	7
458.587	2.29×10^7	5.22854	9

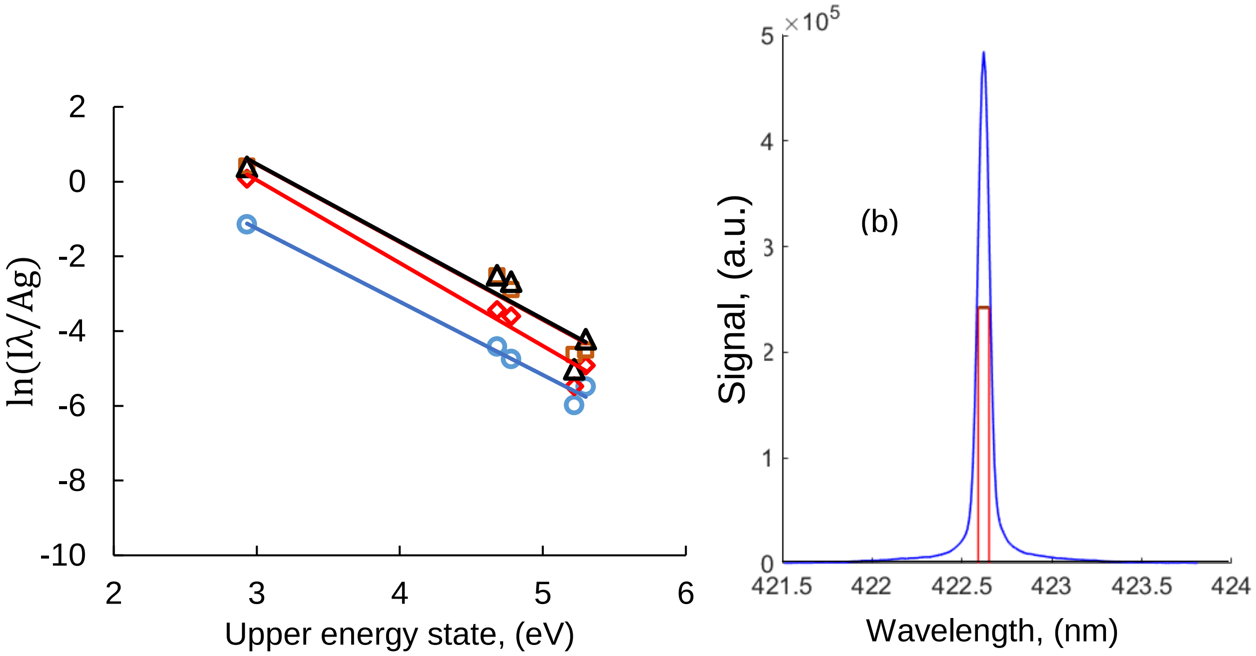

Figure 1. Boltzmann plot using Ca I lines (a) and typical example of full width half-maximum of Ca I at 422.67 nm. The experimental conditions were 10 mJ laser energy, 600 W microwave power, 400 ns gate-delay and 300 µs gate-width.

3. Results and Discussion

3.1 Spectral information

Typical MW-LIBS spectra concerning the molecular emission of CaF and CaBr are presented in Figure 2 and Figure 3, respectively. Figure 2(a) presents CaF in the 603.3 nm and 605 nm range, while Figure 3(a) illustrates the molecular band of CaBr in the 627.1 nm range. There is a strong emission of CaBr in the 624.8 nm range but this band is found to overlap with other molecular emissions, which makes it difficult to distinguish CaBr at 624.8 nm. The formation of the MW-LIBS molecular spectral range of CaF and CaBr is supported by other studies [4, 7]. It is seen in Figure 3(a) that at low wavelength (below 625 nm); the pure cement signal is larger than the signal for cement plus 10% bromine. The strong molecular CaO emission around 615 nm was responsible for this which subsequently subsided by adding bromine in cement. In addition, the strong emission near 631 nm was due to CaCl molecular emission at 631.4 nm [4]. The most intense molecular emission band of CaF lies in the interval between 602.43 and 608.69 and 529.1 nm according to Alvarez et al.[2]. Gaft et al. reported the strongest molecular

CaF bands are in the region of 532.1 nm and 602.9 nm [4]. Furthermore, Gaft et al. noted in their other study that the stronger CaBr molecular bands lie in the region of 624.4 nm and 627.0 nm [7]. Bahrini et al. asserted in their study there are molecular CaBr bands in the 377.7 nm, 381.6 nm, 389.4 nm and 393.4 nm regions [35].

CaF and CaBr molecular formation in the range of 530 nm were not investigated because the wavelength of the ablation laser was 532 nm. An investigation was done in the region of 370 nm-398 nm using MW-LIBS but surprisingly, no CaBr molecular emission band was found in this range. The formation of CaF and CaBr molecular spectra depends largely on a calcium-based matrix [36]. Cement was used as a base material for calcium due to the large amount of calcium found in cement (~ 40% in Portland cement). The spectral ranges 605 nm and 627.1 nm were used to develop the F and Br calibration curves. Figures 2(b) and 3(b) depict the sample emission spectra of CaF and CaBr for different concentrations of F and Br, respectively, using MW-LIBS.

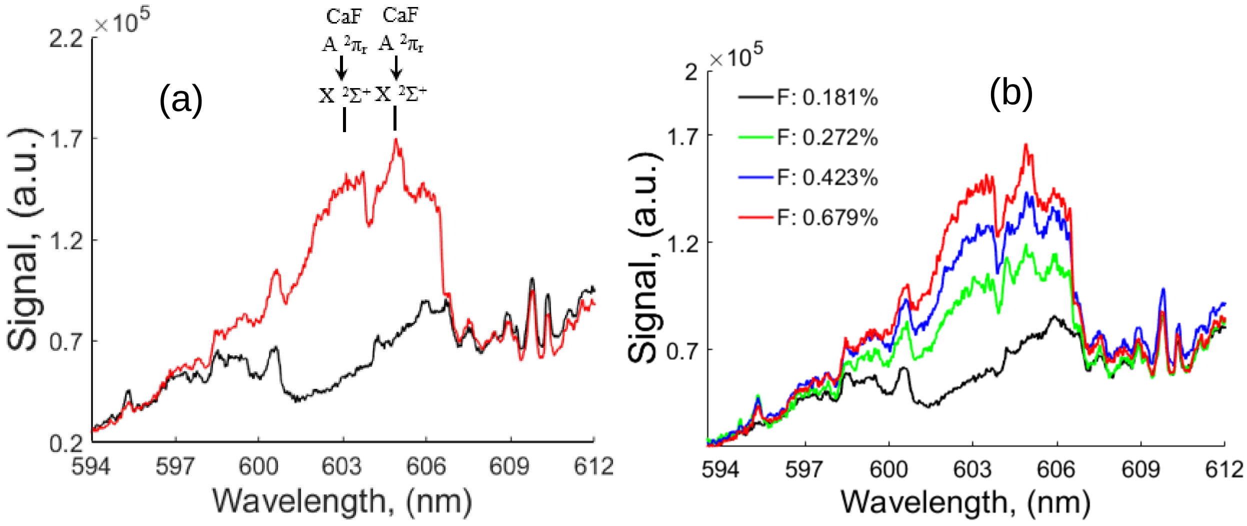

Figure 2. (a) Typical MW-LIBS spectra of pure Portland cement, black, and Cement+ 0.679% F, red, (b) MW-LIBS spectra for different fluorine concentration. The spectra recoded at 10-mJ laser energy, 600 W microwave power, 400 ns gate-delay, 300 µs gate-width and accumulation of 100 shots.

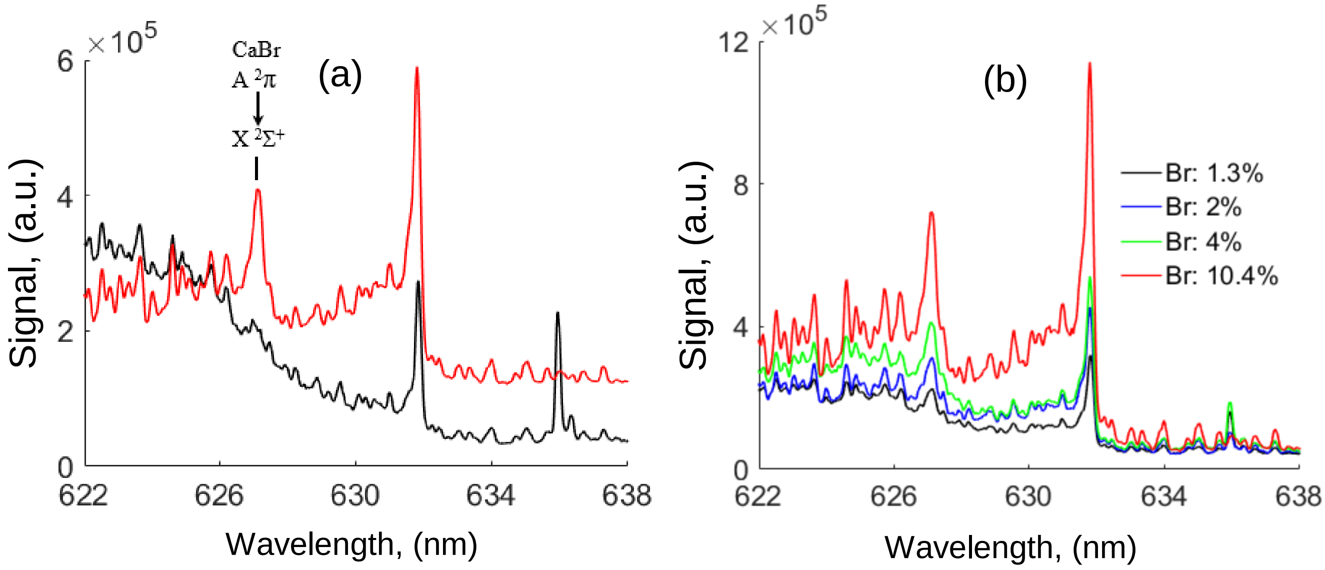

Figure 3. (a) Typical MW-LIBS spectra of pure Portland cement, black, and Cement+ 10% Br, red, (b) MW-LIBS spectra for different bromine concentration. The spectra recorded at 15-mJ laser energy, 750 W microwave power, 400 ns gate-delay, 300 µs gate-width and accumulation of 100 shots.

3.2 Effect of laser energy on Signal to Noise ratio and plasma parameters

The effect of laser energy with a constant MW power on MW-LIBS signal was investigated at ambient conditions to optimise the MW-LIBS signal. Figure 4(a) shows the effect of Signal-to-Noise ratio (SNR) on laser energy at 600 W microwave power. As shown in Figure 4(a), the SNR after 10 mJ starts to decrease. It was predicted that the microwave's coupling efficiency was the main reason for this result. The increase in laser energy causes electron density in the plasma to increase, which allows the microwave to drive fewer electrons into the plasma and thereby leading to less signal. The other reason is the increase in background noise. It has been demonstrated that the SNR can be increased by increasing microwave power [26]. Initially, the microwave cannot be coupled with LIBS plasma due to high electron density in the plasma, but during the relaxation of plasma the electron density at the periphery of the plasma falls to below the critical electron density [37]. This allows microwave radiation through the electromagnetic field to drive free electrons and provides them kinetic energy to excite the de-exited atoms and ions by multiple electron-atom or electron-ion collision.

As long as the microwave remains coupled with the plasma, the emission lifetime improves with longer microwave duration. It has also demonstrated that the microwave power after 600 W does help to increase the signal significantly but also increases the noise [26, 28, 38]. For that reason, 600 W microwave power was used in this study. The explanation of the experimental data in Figure 4(a) is supported by our next experiment as shown in Figure 4(b). Figure 4(b) shows the plasma temperature and electron density in the plasma. The plasma temperature and electron density were calculated using the strong Ca I lines as stated previously. It is seen from Figure 4(b) that the electron density of MW-LIBS is almost constant at fixed microwave power with the increase in laser energy although the plasma temperature increased. This caused less signal for MW-LIBS with the increase in laser energy for a constant microwave power. The maximum MW-LIBS plasma temperature was 7036K, recorded at laser energy, microwave power and gate-width of 20mJ, 600Watt and 1 ms respectively. It is worth noting that Khumaeni et al. reported MW-LIBS temperature of 7700 K at delay-time of 10 µs, measured under reduced-pressure Ar surrounding gas (0.6 kPa). [24]

To confirm the experiment did achieve local thermal equilibrium (LTE), the electron density was calculated using the McWhirter criterion and these values are found to be much lower than the electron density from plasma as shown in Figure 4 (b) using term LTE. For fluorine detection, 10 mJ laser energy was used with 600 W microwave power but for bromine detection, 15 mJ laser energy and 750 W microwave power were employed. The reason for this is due to the CaBr band being relatively weaker than the CaO band that is situated beside the CaBr signal. A slight increase in laser energy caused an increase in CaBr signal at 750 W microwave power but much high laser energy was not suitable for optimal CaBr signal. This finding agrees with Gaft et al. [7].

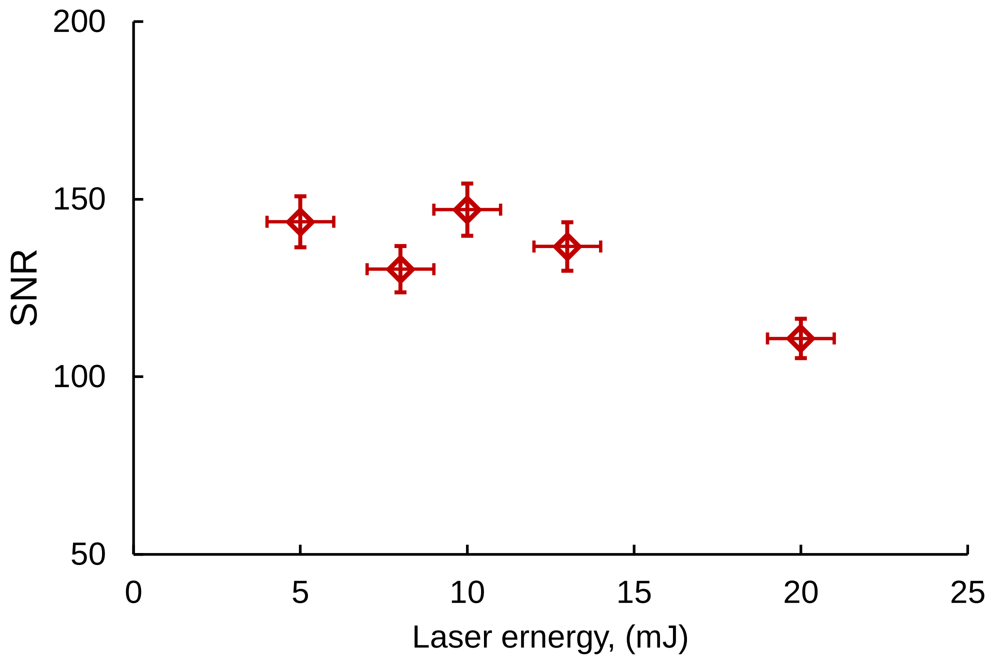

Figure 4(a). Signal to noise ratio of molecular CaF at 600 W microwave power, 400ns gate-delay, 300μs gate-width and an accumulation of 100 shots

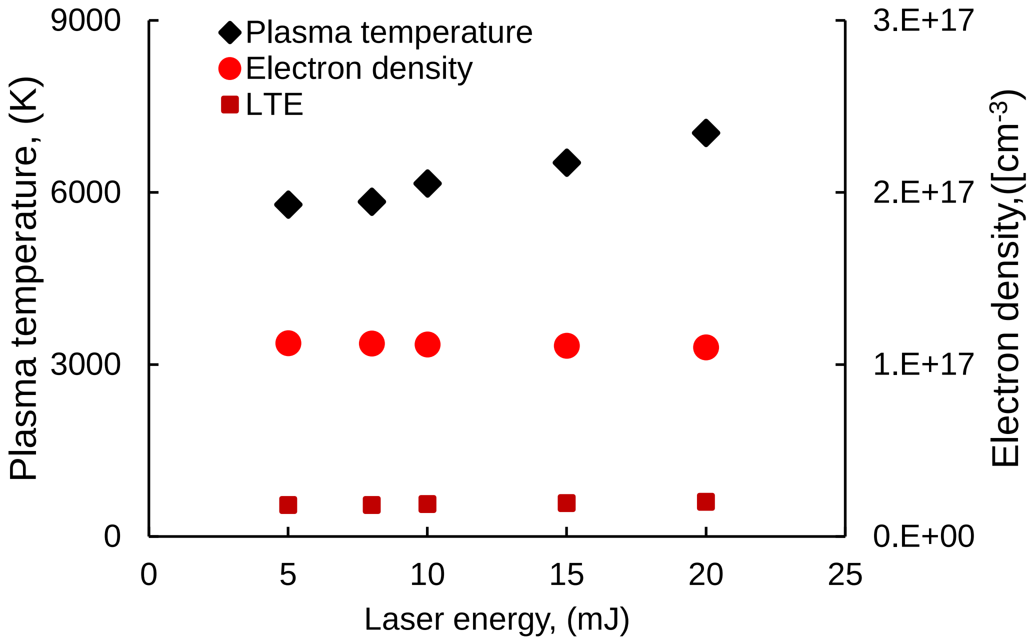

Figure 4(b). Plasma parameters at 600 W microwave power, 1ns gate-delay, 1ms gate-width with an accumulation of 100 shots

3.3 Temporal evolution of molecular Fluorine

The temporal evolution of molecular CaF emission intensity was investigated and it was found that the gate-delay varied from 0 µs to 800 µs for MW-LIBS. The temporal evolution of MW-LIBS for CaF signal-to-noise ratio is presented in Figure 5(a). It is observed from this figure that the SNR of CaF after 500 µs gate-delay started to decrease. Within 500 µs, an experiment was done maintaining a constant gate-width of 300 µs at 50 µs gate-delay interval as shown in Figure 5(b). A 300 µs gate-width was found to be the best for Ca-based molecular emission which is confirmed in another study [26]. As shown in Figure 5(b), the SNR of CaF was higher at the earlier gate-delay. In order to examine the optimum gate-delay, the SNR was calculated for 200 ns gate-delay intervals with constant gate-width of 300 µs as shown in Figure 5(c). It was observed, that at 400 ns gate-delay the SNR of the CaF molecular emission band emerged as the best. The same outcome was found for CaCl molecular emission as shown in our recent published paper [26]. Gaft et al. mentioned in their study that the emission lifetime of CaBr is shorter than CaO and the detection of CaBr was better with a short gate-delay [7]. From the experimental data and supporting information derived from the literature, 400 ns was considered the ideal gate-delay for F and Br detection using their strongest molecular emissions at 605 nm and 627.1 nm, respectively.

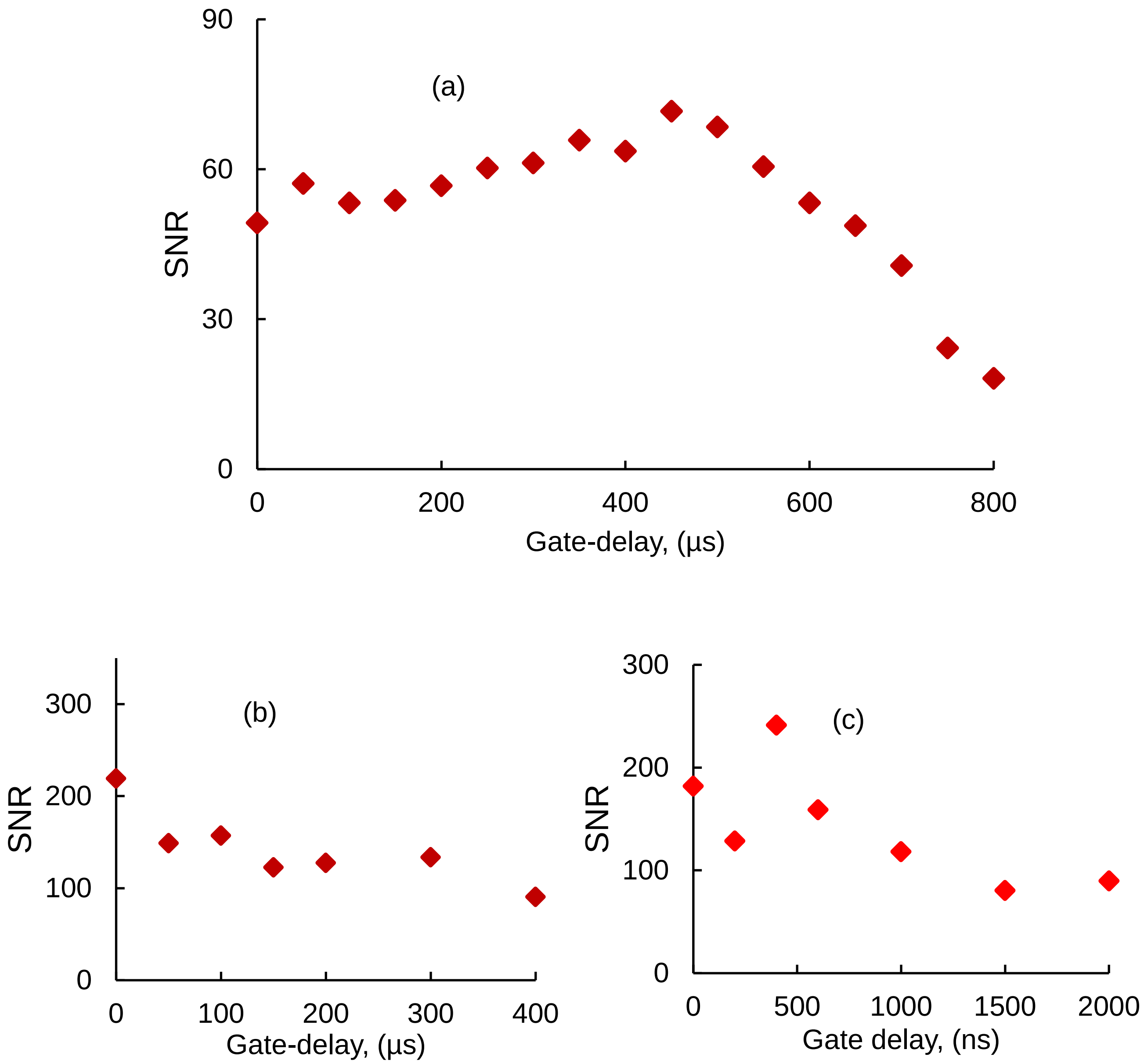

Figure 5. Temporal evolution (Signal to noise ratio) of CaF molecular emission at 10 mJ laser energy, 600 W microwave power with (a) 50 µs step and 50 µs gate-width, (b) 0-400 µs gate-delay and 300 µs gate-width and (c) 0-2000 ns gate-delay and 300 µs gate-width.

3.4 Quantitative detection of Fluorine and Bromine

Under optimum experimental conditions of 400 ns gate-delay and 300 µs gate-width, several samples with increasing amounts of fluorine and bromine were analysed to prepare the calibration curves. The temporal conditions were fixed at 400 ns gate-delay and 300 µs gate-width. Figure 6 and Figure 7 illustrate the variations in the CaF and CaBr net emission signal versus the fluorine and bromine mass content, respectively. It is observed that the calibration curves reveal a linear response. The calibration was prepared for both MW-LIBS and LIBS. The slope of the calibration curve using MW-LIBS was higher than that of LIBS. The reason for this has already been described in our previous paper [26]. The LoD was calculated using the 3-sigma method [39]. From the calibration curve, 106±6 µg/g LoD was obtained for fluorine using MW-LIBS where with LIBS it was 406.54 µg/g only. The relatively improved LoD with MW-LIBS was due to the enhanced signal of MW-LIBS. It was estimated that the enhanced CaF signal was 8 times better using MW-LIBS. This detection limit was not the best in terms of value because Alvarez et al.[14] reported a 0.49 µg/g detection limit. However, in terms of laser energy used, we have achieved 106±6 µg/g at 10 mJ laser energy whereas Alvarez et al.[14] reported 0.49 µg/g at 100 mJ laser energy. A better enhancement was found for the CaBr signal, evaluated to be15-fold. The LoD of 0.2±0.04% was estimated for bromine using the MW-LIBS which was 4 times higher than when utilising LIBS. With LIBS the LoD was 0.8±0.2%. Using molecular emission, this study is the first to report the Br detection limit.

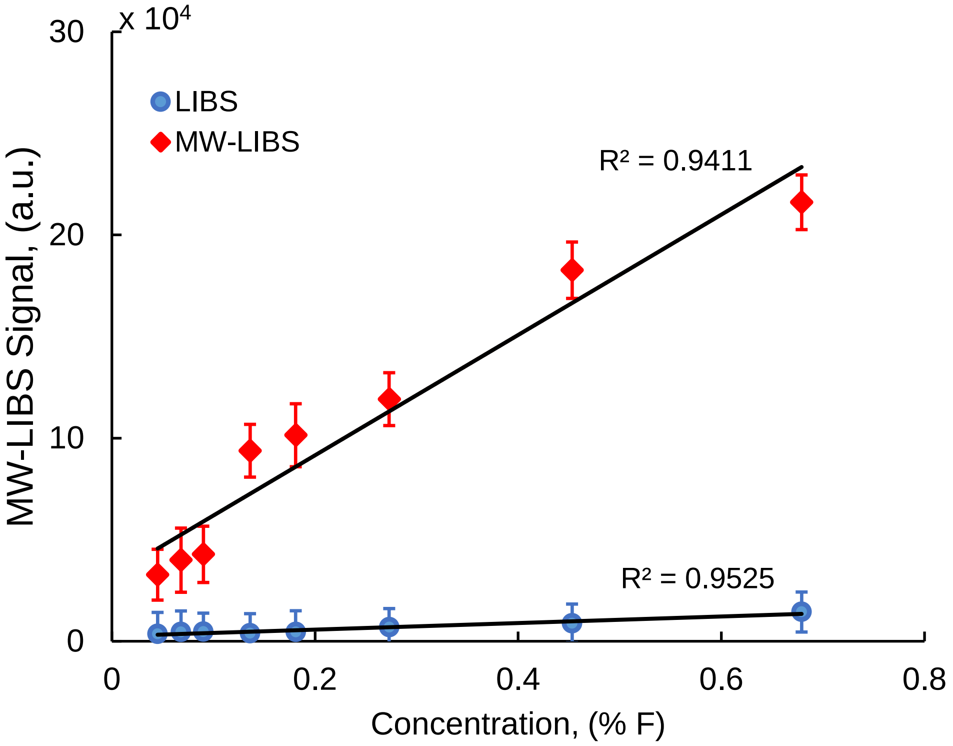

Figure 6. Calibration curve of F using CaF molecular emission at 10 mJ laser energy, 600 W microwave power, 400 ns gate-delay, 300 μs gate-width and an accumulation of 100 shots.

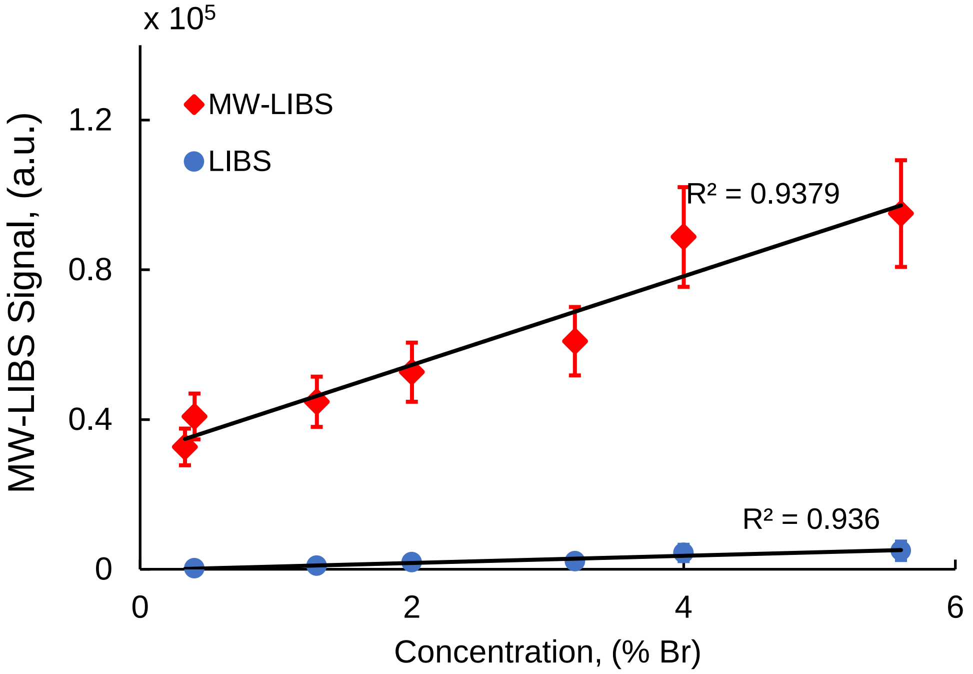

Figure 7. Calibration curve of Br using CaBr molecular emission at 15 mJ laser energy, 750 W microwave power, 400 ns gate-delay, 300 μs gate-width and an accumulation of 100 shots.

4. Conclusion

The main goal of this work was to quantify and accurately detect fluorine and bromine. MW-LIBS technique was employed via molecular emission band on samples of with different F and Br contents. Several Possible emission spectra of CaF and CaBr were been tested in the visible region. An optimum experimental conditions has been demonstrated using CaF emission bands at 603.3 nm and 605 nm. In addition, plasma parameters have been analysed at different laser energy for constant microwave power coupling to optimise the laser energy. Using MW-LIBS, at 400 ns gate-delay, the LoD of 106±6 µg/g and 0.2±0.04% were calculated for F and Br, respectively. The LoD was calculated using LIBS for F and Br and found to be 406.54 µg/g and 0.8±0.2%, showing that there was a quadruple improvement in LoD with MW-LIBS. The LoD was obtained using a linear calibration curve of samples containing an increasing order of F and Br in the samples. This study also reports a quadruple improvement in the detection limit of Br reported in the literature.

References

1. S. United and C. Clement International, *Toxicological profile for fluorides, hydrogen fluoride, and fluorine*, U.S. Dept. of Health and Human Services, Public Health Service, Agency for Toxic Substances and Disease Registry, [Atlanta, Ga.], 1993.
2. C. Alvarez-Llamas, J. Pisonero and N. Bordel, *Spectrochimica Acta Part B: Atomic Spectroscopy*, 2016, **123**, 157-162.
3. P. Pořízka, S. Kaski, A. Hrdlička, P. Modlitbová, L. Sládková, H. Häkkänen, D. Prochazka, J. Novotný, P. Gadas, L. Čelko, K. Novotný and J. Kaiser, *J. Anal. At. Spectrom.*, 2017, **32**, 1966-1974.
4. M. Gaft, L. Nagli, N. Eliezer, Y. Groisman and O. Forni, *Spectrochimica Acta Part B: Atomic Spectroscopy*, 2014, **98**, 39-47.
5. C. González de Vega, C. Álvarez Llamas, N. Bordel, R. Pereiro and A. Sanz-Medel, *Analytica Chimica Acta*, 2015, **877**, 33-40.
6. I. Rae, *Global Environment*, 2014, **7**.
7. M. Gaft, L. Nagli, Y. Raichlin, F. Pelascini, G. Panzer and V. M. Ros, *Spectrochimica Acta Part B: Atomic Spectroscopy*, 2019, **157**, 47-52.
8. R. LANDAU, *CORROSION*, 1952, **8**, 283-288.

9. A. Macías and M. L. Escudero, *Corrosion Science*, 1994, **36**, 2169-2180.
10. Y. Wang;, S. Zhang;, X. Ji;, P. Wang; and W. Li., *Int. J. Electrochem. Sci.*, 2018, DOI: 10.20964/2018.05.33, 4891 – 4900,.
11. A. Stájer, K. Ungvári, I. K. Pelsőczi, H. Polyánka, A. Oszkó, E. Mihalik, Z. Rakonczay, M. Radnai, L. Kemény, A. Fazekas and K. Turzó, *Journal of Biomedical Materials Research Part A*, 2008, **87A**, 450-458.
12. J. Serrano, J. Moros and J. J. Laserna, *Anal. Chem.*, 2015, **87**, 2794-2801.
13. J. Viljanen, Z. Sun and Z. T. Alwahabi, *Spectrochimica Acta Part B: Atomic Spectroscopy*, 2016, **118**, 29-36.
14. C. Alvarez-Llamas, J. Pisonero and N. Bordel, *J. Anal. At. Spectrom.*, 2017, **32**, 162-166.
15. G. Asimellis, S. Hamilton, A. Giannoudakos and M. Kompitsas, *Spectrochimica Acta Part B: Atomic Spectroscopy*, 2005, **60**, 1132-1139.
16. C. D. Quarles, J. J. Gonzalez, L. J. East, J. H. Yoo, M. Morey and R. E. Russo, *J. Anal. At. Spectrom.*, 2014, **29**, 1238-1242.
17. T. Kratochvíl, M. Pouzar, K. Novotný, V. Havránek, T. Černohorský and M. Zvolská, *Spectrochimica Acta Part B: Atomic Spectroscopy*, 2013, **88**, 26-31.
18. M. Wang, M. Zhao, S. Ye, M. Zhu, R. Yi, L. Liu and J. Qu, *J. Anal. At. Spectrom.*, 2018, **33**, 713-719.
19. L. Radziemski, D. A. Cremers, K. Benelli, C. Khoo and R. D. Harris, *Spectrochimica Acta Part B: Atomic Spectroscopy*, 2005, **60**, 237-248.
20. S. Barbier, S. Perrier, P. Freyermuth, D. Perrin, B. Gallard and N. Gilon, *Spectrochimica Acta Part B: Atomic Spectroscopy*, 2013, **88**, 167-173.
21. Y. Ikeda and R. Tsuruoka, *Applied Optics*, 2012, **51**, B183-B191.
22. D. E. Anderson, B. L. Ehlmann, O. Forni, S. M. Clegg, A. Cousin, N. H. Thomas, J. Lasue, D. M. Delapp, R. E. McInroy, O. Gasnault, M. D. Dyar, S. Schroder, S. Maurice and R. C. Wiens, *J. Geophys. Res.-Planets*, 2017, **122**, 744-770.
23. O. Forni, M. Gaft, M. J. Toplis, S. M. Clegg, S. Maurice, R. C. Wiens, N. Mangold, O. Gasnault, V. Sautter, S. Le Mouélic, P.-Y. Meslin, M. Nachon, R. E. McInroy, A. M. Ollila, A. Cousin, J. C. Bridges, N. L. Lanza and M. D. Dyar, *Geophysical Research Letters*, 2015, **42**, 1020-1028.
24. A. Khumaeni, K. Akaoka, M. Miyabe and I. Wakaida, *Frontiers of Physics*, 2016, **11**, 114209.

25. Y. Tang, J. Li, Z. Hao, S. Tang, Z. Zhu, L. Guo, X. Li, X. Zeng, J. Duan and Y. Lu, *Opt. Express*, 2018, **26**, 12121-12130.
26. M. A. Wakil and Z. T. Alwahabi, *J. Anal. At. Spectrom.*, 2019, **34**, 1892-1899.
27. M. Bahreini, B. Ashrafkhani and S. H. Tavassoli, *Applied Physics B*, 2014, **114**, 439-447.
28. S. J. Chen, A. Iqbal, M. Wall, C. Fumeaux and Z. T. Alwahabi, *J. Anal. At. Spectrom.*, 2017, **32**, 1508-1518.
29. J. Zalach and S. Franke, *Journal of Applied Physics*, 2013, **113**, 043303.
30. S. Harilal, C. Bindhu, R. Issac, V. P. N. Nampoori and C. Vallabhan, *Journal of Applied Physics*, 1997, **82**, 2140-2146.
31. M. Dimitrijevic and S. Sahal-Brechot, *Serbian Astronomical Journal*, 2000, **161**, 39-88.
32. R. W. P. McWhirter, 1965, 201.
33. V. N. Rai and S. N. Thakur, in *Laser-Induced Breakdown Spectroscopy*, eds. J. P. Singh and S. N. Thakur, Elsevier, Amsterdam, 2007, pp. 83-111.
34. J. Reader, C. H. Corliss, W. L. Wiese and G. A. Martin, *Wavelengths and transition probabilities for atoms and atomic ions : part I. wavelengths - part II. transition probabilities*, National Bureau of Standards, NSRDS; NISTresearchlibrary; fedlink; americana, 1980.
35. C. Bahrini, S. Douin, J. Rostas and G. Taieb, *Chemical Physics Letters*, 2006, **432**, 1-5.
36. D. Vogt, K. Rammelkamp, S. Schröder and H.-W. Hübers, presented in part at the LPSC 2017, The Woodlands, USA, 2017.
37. Y. A. Liu, M. Baudelet and M. Richardson, *J. Anal. At. Spectrom.*, 2010, **25**, 1316-1323.
38. A. A. Al Shuaili, A. M. Al Hadhrami, M. A. Wakil and Z. T. Alwahabi, *Spectrochimica Acta Part B: Atomic Spectroscopy,* 2019, **159**, 105666.
39. S. Rosenwasser, G. Asimellis, B. Bromley, R. Hazlett, J. Martin, T. Pearce and A. Zigler, *Spectrochimica Acta Part B: Atomic Spectroscopy,* 2001, **56**, 707-714.

Chapter 5

Contactless ruthenium detection at low level in real time

Abu Farhan Abu Kasim[†], M. A. Wakil[†], Kevin Grant, Milton Hearn, and Zeyad T. Alwahabi[*]

School of Chemical Engineering and Advanced Materials, The University of Adelaide, SA 5005, Australia.

[†] The first two authors contributed equally to this work

**E-mail: zeyad.alwahabi@adelaide.edu.au*

Submitted to Optics & Laser Technology

Statement of Authorship

Title of Paper	**Contactless ruthenium detection at low level in real time**	
Publication Status	☐ Published ☑ Submitted for Publication	☐ Accepted for Publication ☐ Unpublished and Unsubmitted work written in manuscript style
Publication Details	Optics & Laser Technology	

Principal Author 1

Name of Principal Author	Abu Farhan Abu Kasim		
Contribution to the Paper	I was responsible for the development of the measurement technique under the principal supervisor of Associate Professor Zeyad Alwahabi. I performed part of the experiment, wrote the draft of the manuscript, and addressed the comments and suggestion from other authors in subsequent revisions of the manuscript.		
Overall percentage (%)	30%		
Certification:	This paper reports on original research I conducted during the period of my Bachelor Degree and is not subject to any obligations or contractual agreements with a third party that would constrain its inclusion in this thesis. I am the primary author of this paper.		
Signature		Date	28.04.2020

Principal Author 2

Name of Principal Author (Candidate)	Md. Abdul Wakil		
Contribution to the Paper	I was responsible for the development of the measurement technique under the Associate Professor Zeyad Alwahabi I performed part of the experiment, refine the manuscript, and addressed the comments and suggestion from other authors in subsequent revisions of the manuscript.		
Overall percentage (%)	30%		
Certification:	This paper reports on original research I conducted during the period of my Higher Degree by Research candidature and is not subject to any obligations or contractual agreements with a third party that would constrain its inclusion in this thesis. I am the primary author of this paper.		
Signature		Date	22.04.2020

Co-Author Contributions

By signing the Statement of Authorship, each author certifies that:

i. the candidate's stated contribution to the publication is accurate (as detailed above);
ii. permission is granted for the candidate in include the publication in the thesis; and
iii. the sum of all co-author contributions is equal to 100% less the candidate's stated contribution.

Name of Co-Author	Kevin Grant

Contribution to the Paper	I was responsible for the development of the measurement technique under the Associate Professor Zeyad Alwahabi I performed part of the experiment.		
Overall percentage (%)	20%		
Signature		Date	28/4/20

Name of Co-Author	Milton Hearn		
Contribution to the Paper	I jointly contributed to both data interpretation and refining of the manuscript.		
Overall percentage (%)	10%		
Signature		Date	05.05.2020

Name of Co-Author	Zeyad T. Alwahabi		
Contribution to the Paper	I was principal supervisor for the development of the work, contributed to both data interpretation and refining the manuscript. I hereby certify that statement of contribution is accurate and I have given written permission for this paper to be included in this thesis.		
Overall percentage (%)	10%		
Signature		Date	29.04.2020

Contactless ruthenium detection at low level in real time

Abu Farhan Abu Kasim[†], M. A. Wakil[†], Kevin Grant, Milton Hearn, and Zeyad T. Alwahabi[*]

School of Chemical Engineering and Advanced Materials, The University of Adelaide, SA 5005. Australia

[†] The first two authors contributed equally to this work

[*]*Corresponding author:* zeyad.alwahabi@adelaide.edu.au

Abstract

Aqueous ruthenium, in flow jet, was detected in real-time at ambient condition by using Microwave-assisted Laser Induced Breakdown Spectroscopy (MW-LIBS). A 10mJ laser energy and 750W microwave power were directed at an open liquid jet sample of ruthenium, as a 5% (v/v) aqueous hydrochloric acid solution, with concentrations ranging from 50ppm to 2000ppm. At low concentration of ruthenium, using 10mJ of laser energy per pulse and without microwave application, no ruthenium signal could be reliably detected at high sensitivity. It was observed, for liquid flow, the coupling efficiency between the microwave and the laser-induced plasma was limited to 43%. The ruthenium's signal-to-noise ratio improvement for MW-LIBS, with respect to LIBS, was 76-fold. Based on MW-LIBS, the limit of detection (LoD) for ruthenium was determined to be 957±84ppb. This first example on real-time aqueous ruthenium detection paves the way for online monitoring of low concentration of Ru in industrial processes.

Keywords: MW-LIBS, Detection Limit, LoD, Ruthenium, Liquid detection

1. Introduction

Ruthenium (Ru) is a hard-metallic element that is part of the platinum-transition group 8 metals and is considered a rare element due to its very low mining rate [1]. Following its discovery and isolation by Karl Karlovich Klaus in 1844, scientists have been studying the numerous ways in which ruthenium can be utilized [2]. In its early applications, ruthenium was commercially used as an alloying agent for the hardening of platinum and palladium [3]. Because they exhibit rapid reversible redox processes involving a variety of coordination geometries and valence states, ranging from octavalent in RuO_4 to -2 valent in $Ru(CO)_4^{2-}$, Ru-based materials have subsequently attracted considerable interest in multiple fields, including the development of supercapacitors, in ruthenium-platinum alloys for methanol fuel cells and in photovoltaics [4, 5]. In addition, organometallic ruthenium complexes have found very wide application as catalyst in the homogeneous and heterogeneous syntheses of numerous organic compounds [6-8] and polymers [9-11], including reactions involving Z-selective olefin metathesis catalysts [12, 13] and many pharmaceutical compounds [14]. As a consequence, the versatility of ruthenium-based compounds now permits its routine use in today's chemical processing and pharmaceutical industries [15], including its role in the hydrogen evolution reaction [16] and aqueous-phase hydrogenation of biomass [17].

Despite the enormous scope of application of ruthenium-based catalysts, the detection and removal of residual ruthenium impurities from synthetic mixtures represents a significant challenge, particular for synthetic products destined to become active pharmaceutical ingredients (APIs). Depending on the reaction conditions, ruthenium can be dislodged from its catalytic complex and leach into the solution [18-20]. This phenomenon is common in heterogeneous catalytic reactions and occurs either by thermal effects that reduce the integrity of the catalyst carrier's structure and/or through pH effects [18]. Although considerable effort has been expended to develop more stable ruthenium-based catalysts [20, 21], losses are inevitable and can pose a significant health and business threat. From a more general perspective, the detection and recovery of ruthenium-related leachables could be carried out by simply removing the ruthenium catalyst by filtration during the process and observing whether further reaction occurs in the filtrate; with persistent product formation suggesting that leakage had occurred [22]. Despite being a definitive analysis, this method is often impractical as the majority of production industries now operate in a continuous mode.

Chemical species detection is important in many fields such as the food industry, chemical and pharmaceutical processing and manufacture, and the mining industry. To accommodate this task, numerous analytical methods, such as Atomic Absorption Spectroscopy (AAS), have been developed to both detect the presence, and quantify the amount of an element in a given sample [23]. One detection technique that has attracted considerable attention in recent years is Laser Induced Breakdown Spectroscopy (LIBS). The reason for this interest is that the analysis can be carried out with little to no sample preparation and hence allows extremely fast and *in-situ* detection [24, 25]. LIBS methods exploit the concept of atomic emission spectroscopy by using a laser pulsing in a range of nano- to femto-seconds as an ablation source. This approach allows analysis without the need for sample preparation as the laser energy is focused directly onto the sample allowing an ablation of the target regardless of its physical or chemical state [24, 26]. However, LIBS suffers from the disadvantages of low sensitivity, and low reproducibility [27, 28]. This is where assisted techniques such as Microwave-assisted LIBS (MW-LIBS) come into place [29].

MW-LIBS enhances the detective capability of LIBS by extending the lifetime of plasma produced by the laser up to hundreds of microseconds [30] rather than just a few [31]. The main reason for this is that with the addition of microwave, the laser-induced plasma can be reignited by mobilising the free electrons and ions and thus further prolonging their lifetime [28]. This can be achieved by employing a Near Field Applicator (NFA) to the system [32]. The effectiveness of microwave coupling to the system has recently been demonstrated. Enhancement factors for the Limit of Detection (LoD) parameter, lowest theoretical concentration detectable, ranging from 11 folds to 93 folds have been achieved for the analysis of indium(aq) and copper(s) respectively [33, 34].

MW-LIBS can offer an attractive solution for ruthenium detection at very low concentrations. This is because it enables *in-situ* real-time detection, whilst still maintaining a substantial sensitivity. In regard to process technologies and with respect to the current investigation, as soon as Ru leakage becomes evident and detected in the process stream or reactor during operation, the catalyst could be isolated, retrieved, and then immediately replaced with a fresh batch. In addition to not impeding the process and preserving a constant production rate, this approach will certainly avoid further losses in Ru based catalysts and extends its useful life as the extracted species can simply be re-used by re-adsorbing it to a new catalyst carrier [35]. Owing to the extreme demand for its use as a catalysis and because only 12 tonnes per year of this rare element are mined throughout the world [1] as opposed to 10 million tonnes for copper [36], having available a highly sensitive real time procedure to identify Ru in its aqueous state could consequently be very useful during its extraction from mineral sources and for its application.

In the case of liquid detection using MW-LIBS/LIBS, the simplest approach is to have a static liquid solution held in a suitable vessel and focusing the laser on the surface of the liquid. Although it can be easily operated, using this method usually yields unsatisfactory results as most of the laser energy is used to evaporate the bulk liquid causing lower quantity of excited atoms [31]. A solution to this problem is to have the liquid flowing as a jet instead of remaining stationary. This permits a much lower laser energy consumption during the vaporisation phase since a smaller volume is present per given time [33]. Several studies have been published for liquid MW-LIBS/LIBS and the reported detection limits are tabulated into Table 1.

Table 1: Limit of detection of various metals using LIBS and MW-LIBS for aqueous phase

Metal	Technique	LOD (ppm)	Laser Energy (mJ)	Liquid Handling	Ref.
Lithium	LIBS	10.5	47	Static Liquid System	[37]
Zirconium	LIBS	4	75	Liquid Circulation System	[38]
Chromium	LIBS	28.9	35	Liquid Circulation System	[39]
Sodium	LIBS	1	35	Liquid Circulation System	[39]
Indium	LIBS	123	6.69	Liquid Circulation System	[33]
Indium	MW-LIBS	10.8	6.69	Liquid Circulation System	[33]

An extensive study has been carried out by Balcerzak (2002) for the analytical detection of ruthenium in different samples. A variety of methods have been outlined with different detection limits including AAS, Inductively Coupled Plasma Atomic Emission Spectroscopy (ICP-AES) with Periodic Acid Solution, and UV-Vis Spectroscopy, with LoD of 0.1 ppm, 0.005 ppm. and 0.001 ppm respectively [40]. It is worth noting, however, that these analytical methods cannot be used in real-time as they require sample preparation. They are also more suitable to be employed in analytical laboratories. Currently, as previously stated, there is no reports on LoD for aqueous ruthenium (Ru(aq) detection with MW-LIBS. Thus, to the authors' best knowledge, this paper reports the first real-time detection of ruthenium in liquid samples.

2. Experimental

Figure 1 shows the schematic of the experimental MW-LIBS setup used for the detection of Ru. A Q-switched Nd: YAG (neodymium doped yttrium-aluminium-garnet) was used as the laser source producing a beam of 532nm in wavelength, 10Hz repetition, ~6ns in pulse duration and a beam width of 3mm. A half wave plate (HWP) combined with a Glan-laser polarizer (P) was used to alter the laser pulse energy. Pulse energy was measured with an ES220C Pyroelectric Sensor (EM) and set to an optimized energy to be determined. The laser beam passes through a perforated parabolic mirror with a focal length of 152mm and diameter 50.8mm and was then focused onto the liquid sample by a plano-convex UV fused silica lens with focal length of 100mm and diameter 50.8mm. The emission was collected by the emission detection unit which consists of Lens 1 (focal length of 100mm and diameter 50.8mm), an off-axis parabolic mirror (OPAM), Lens 2 (focal length of 20mm) and an Achromatic Reflective Coupler (ARC) as shown in Figure 1. The emission was channelled into a 7-fibre bundle (Thorlabs, BFL200HS02) connected to a spectrometer (Andor, Shamrock 500i with 2,400 lines/mm diffraction grating) equipped with an intensifier camera, ICCD, (Andor, iStar). As shown in Figure 1, an aluminium box, dotted line, was used to minimise the residual microwave radiation. One side of the aluminium box was covered with metal mesh acting as an observation window.

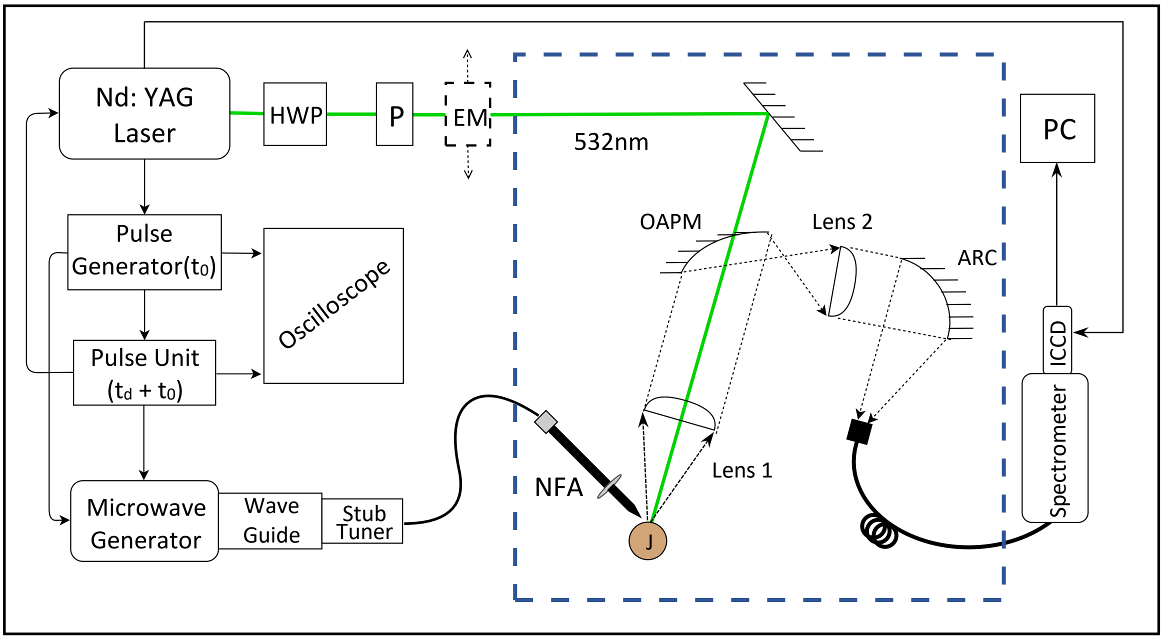

Figure 1: Schematic of apparatus setup. HWP: half-wave plate, P: polariser, EM: Energy meter, NFA: near-field applicator, OAPM: off-axis parabolic mirror, ARC: achromatic reflective coupler, ICCD: intensifier camera, J: jet)

Pulsed 2.45GHz microwave radiation was generated by a 3kW water cooled Sairem microwave system. The microwaves reflected power was monitored by a crystal detector consisting of a generator coupled to an isolator. A WR340 waveguide was utilised to guide microwave radiation to a 3-stub impedance tuner. Radiation passes a quartz window where a tuner was connected to a waveguide-to-coaxial adaptor (WR340RN). This adaptor was attached to a 1m flexible coaxial cable (50 ohms NN cable with 0.14 dB insertion loss at 2.45GHz). The end of this coaxial cable was connected with a Near-Field applicator (NFA) [32]. The tip of the NFA was located ~0.5mm horizontally and vertically, at an angle of 45° from the liquid jet containing the Ruthenium sample (Figure 2). The microwave pulse, duration and power were controlled by a pulse generator (Aim-TTi). This allows the microwave pulse to initiate 200μs prior to the laser pulse and was held for 1ms. When this happen, the premature triggering of the microwave radiation allows it to reach its full power before the laser pulse occurs, and thus, ensuring proper coupling.

A steady liquid circulation system was required to be arranged into the apparatus. To achieve this, a peristaltic pump (Ismatec, MW-MSC 1), a 25ml syringe as a sample reservoir, a circular nozzle with 0.8 mm diameter and a collection funnel were connected with plastic tubing (Masterflex, 6485-16) to create the flow pumping system as shown in Figure 3. At 300rpm pump operation, 50mL of sample was periodically added to the syringe reservoir to allow a steady jet of solution and avoid air bubbles in the system. It is worth noting that, distilled water was used to wash out the Ru sample in the flow to avoid contamination between each analysis.

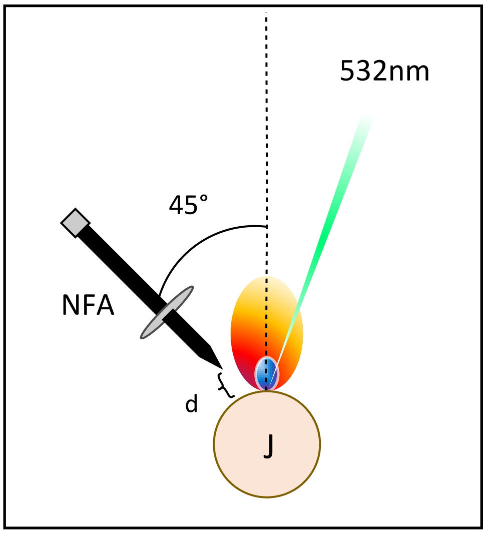

Figure 2: NFA's Orientation schematics, laser-induced plasma with microwave off, blue, and with microwave on, red, d=0.5mm

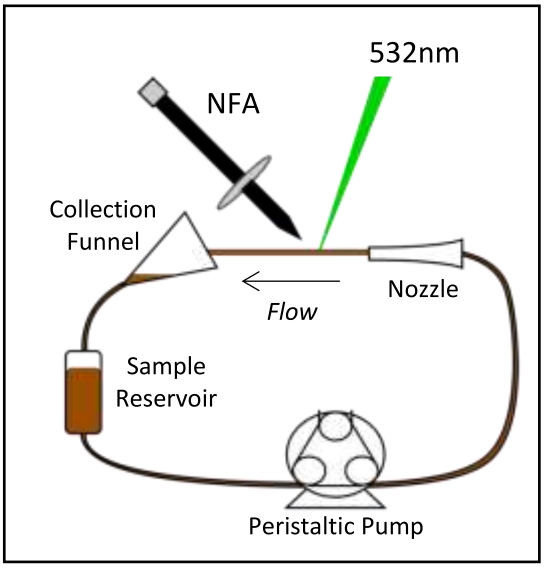

Figure 3: Liquid circulation system

A liquid stock solution of ruthenium, dissolved in 5% (v/v) aqueous hydrochloric acid, was supplied by Choice Analytical, Australia. The stock contained 10,000±50ppm of ruthenium solution and was used to prepare samples ranging from 50 to 2000ppm. These samples were diluted with distilled water using a 1ml volumetric pipette and 50ml beaker. Additional uncertainties will occur from the equipment used yielding ±0.005ml and ±5ml respectively. These errors were assumed to be independent, and the root sum square method was used to determine the absolute uncertainties corresponding to each concentration analysed and was shown in the related graphical figure (Figure 9) as horizontal error bars.

3. Results and Discussion

Table 2 shows the wavelengths, transition probability, and energy levels of few Ru I lines [41]. It was found that the three Ru lines, with a ground state as a common level, produce the best signal to noise ratio. Further analysis was performed based on these three regions of bound-to-bound transition depending on the concentration used, the significance of self-absorption during the experiment and overall noise present during the period of experiment, and the purpose of the analysis.

Table 2: Spectral parameters of Ruthenium [40]

Transition	Wavelength (***nm***)	Transition Probability (s^{-1})	Lower Energy Level ($\boldsymbol{cm^{-1}}$)	Upper Energy Level ($\boldsymbol{cm^{-1}}$)	Lower Level J_i	Upper Level J_k
$5\ a^5F_4 \leftarrow 5\ z^5G_5$	343.674	7.28x10^{+7}	1190.64	30279.68	4	5
$5\ a^5F_5 \leftarrow 5\ z^5G_6$	349.894	8.61x10^{+7}	0.00	28571.89	5	6
$5\ a^5F_1 \leftarrow 5\ z^5G_2$	358.922	9.11x10^{+7}	3105.49	30958.8	5	5
$5\ a^5F_2 \leftarrow 5\ z^5G_3$	359.302	8.17x10^{+7}	2713.24	30527.06	2	3
$5\ a^5F_3 \leftarrow 5\ z^3G_4$	359.618	4.20x10^{+7}	2091.54	29890.91	3	4
$5\ a\ ^5F_5 \leftarrow 5\ z\ ^5F_5$	372.803	8.20x10^{+7}	0.00	26816.23	5	5
$5\ a\ ^5F_4 \leftarrow 5\ z\ ^5D_3$	379.890	5.98x10^{+7}	1190.64	29427.32	4	3
$5\ a\ ^5F_5 \leftarrow 5\ z\ ^5D_4$	379.935	5.33x10^{+7}	0.00	26312.83	5	4

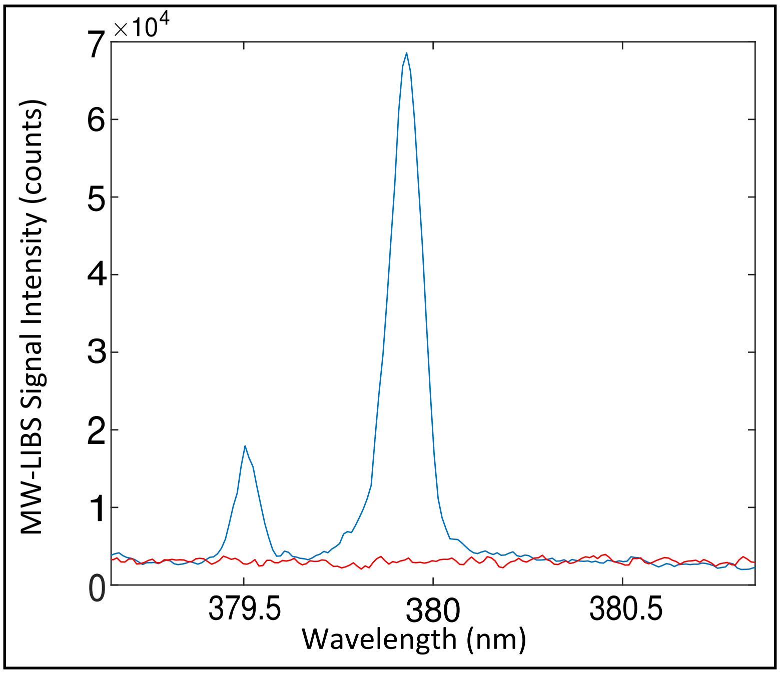

Figure 4: Signal intensity of a flow with a 600ppm Ru(aq) without microwave, red, and with microwave at 750 Watt, blue.

Figure 4 presents the difference in the signal intensity with and without microwave. The two spectra were recorded using 100 accumulation, at 1ms gate-width and without any gate-delay, prompt. The laser energy and microwave power were held constant at 10mJ and 750Watt, respectively. As can be seen from the Figure 4, using MW-LIBS allows the observation of clear and distinctive peak compared to using just LIBS. This was observed even for a lines with low transition probability, for example the 379.935nm transition. With LIBS only (microwave off), the Ru(aq) was essentially undetectable at 600ppm.

To study the microwave power and the laser energy dependence, Ru(aq) concentration of 2000ppm was chosen. The signal was taken based on the emission spectrum around 372.80nm, in an attempt to circumvent the effects of self-absorption, while the noise was computed from the standard deviation of regions that does not correspond to any elements that could be present. Seventy five (75) accumulations with a gate-delay of 0s and 1ms gate-width was set in order to obtain the results in Figure 5 and 6. Accordingly, in order to determine the effects of laser energy on the signal-to-noise ratio (SNR), the microwave power was held constant and the laser energy was increased from 8mj to a maximum of 15mJ. It is worth noting that the microwave power was kept below 750W as it was apparent that the degree of liquid splash increased with microwave power. This is a direct result of a more violent ablations as the microwave power was increased. All the tests were conducted at 750W as it was predicted from the literature, [33], higher microwave power yields consistently higher SNR.

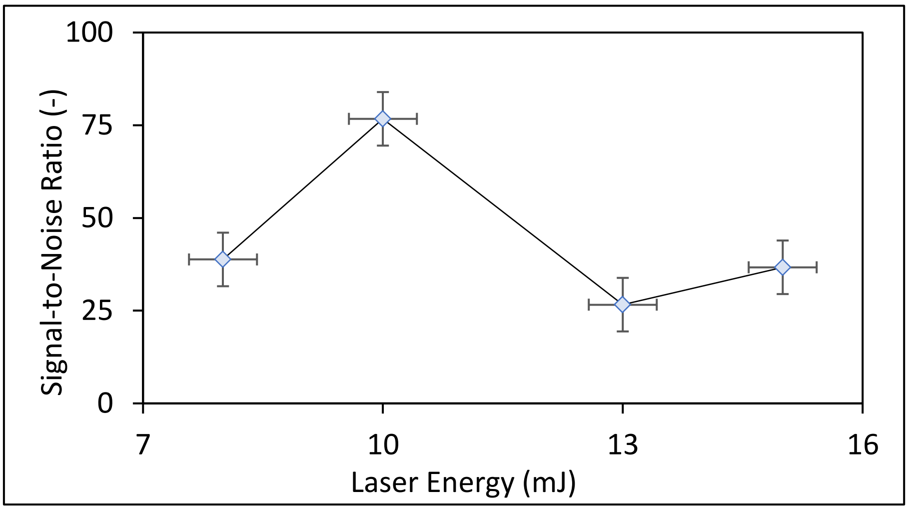

Figure 5: *Signal-to-noise-ratio vs laser energy at a constant microwave power of 750Watt*

Figure 5 shows that the SNR peaks at 10mJ laser energy, in which the signal was found to be present at 76 times the noise. This is to be expected as both the signal and the noise increases with laser energy. The only difference is the rate of which it increases [42]. Consequently, a point where the signal escalates faster than the noise was sought in a laser ablative study. Since it was found that a relatively low laser energy is needed to attain a high SNR, there is no practical reason to increase the laser energy further than the maximum point, 10mJ. This outcome was accompanied by several benefits, one of which is the reduction of sample destruction. This is always a useful trait because some samples are precious either due to their rarity or antiquity causing the need to preserve the sample to the utmost level. After the optimum laser energy has been determined, the relationship between microwave power and SNR was then confirmed and the data compared with the literature. This analysis was carried out at two different laser energies (10mJ and 15mJ) to improve the clarity of the results.

Figure 6 shows an increasing trend of SNR Improvement to microwave power, even at two different laser energies, indicating that the coupling of microwave radiation improves the SNR for the detection of Ru in aqueous solution. It should be noted that, at zero microwave power the SNR was taken to be 1 for graphical presentation of result. This relationship was also consistent with the literature because the magnitude of the impact of microwave employment on a plasma formed mainly by an element with a reasonably low upper energy level has been shown to greatly intensify the signal through the describe re-excitation [30, 32, 43, 44]. As mentioned earlier, the maximum microwave power is not to exceed 750W to maintain the safety and integrity of the equipment. This will inevitably limit the extent of manipulating the variable. From a comparably similar study that was undertaken for Indium detection in aqueous solution [33], it was found that that the highest microwave power used was 1.2kW to which it resulted in the highest SNR. Even though the same relationship was exhibited for this indium analysis, higher microwave power causes a larger SNR, the effects of using microwave power higher than 750W for the detection of Ruthenium with MW-LIBS remains to be seen.

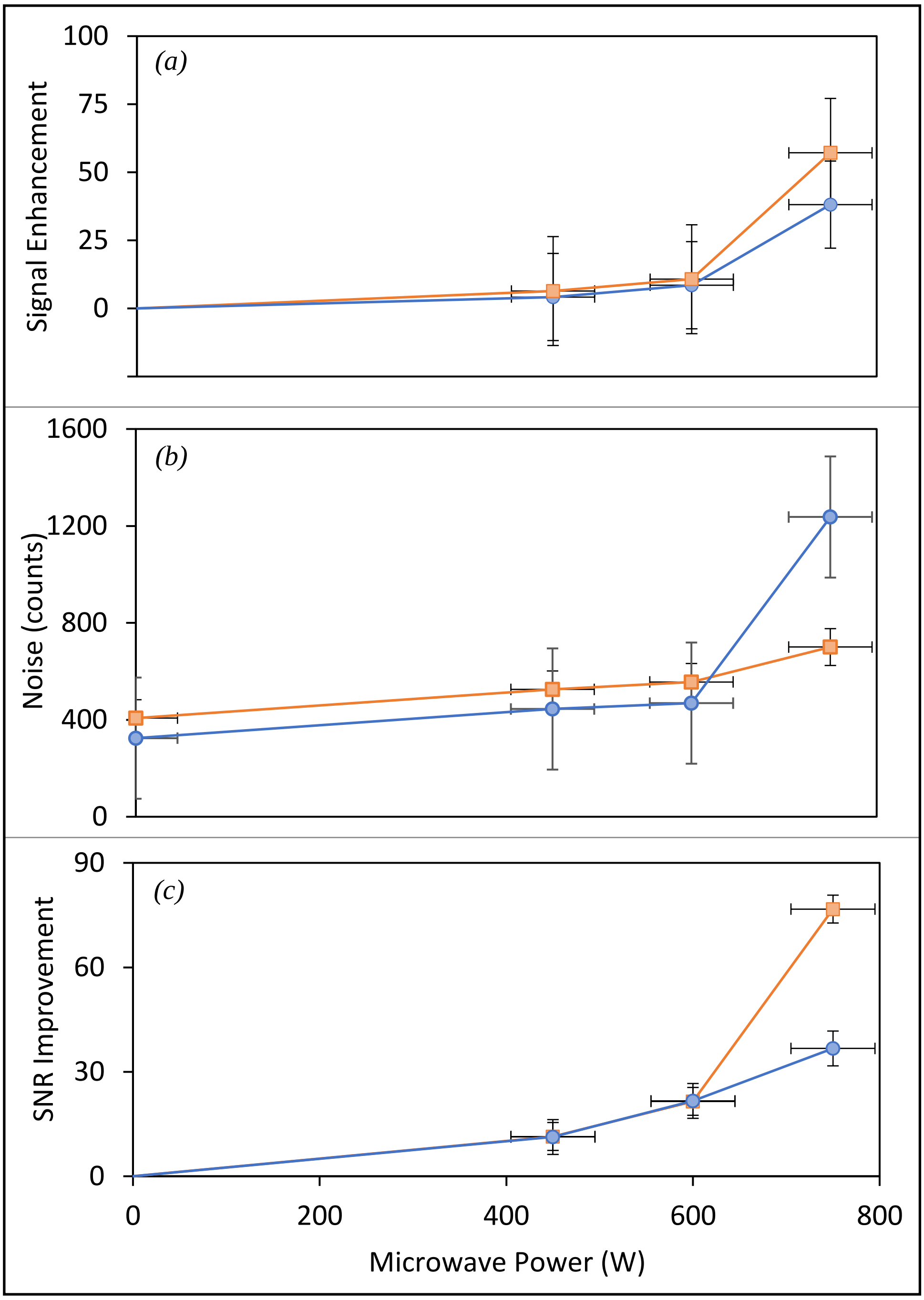

Figure 6: Microwave dependence with described parameters at laser energy of 15mJ, blue, and 10mJ, orange

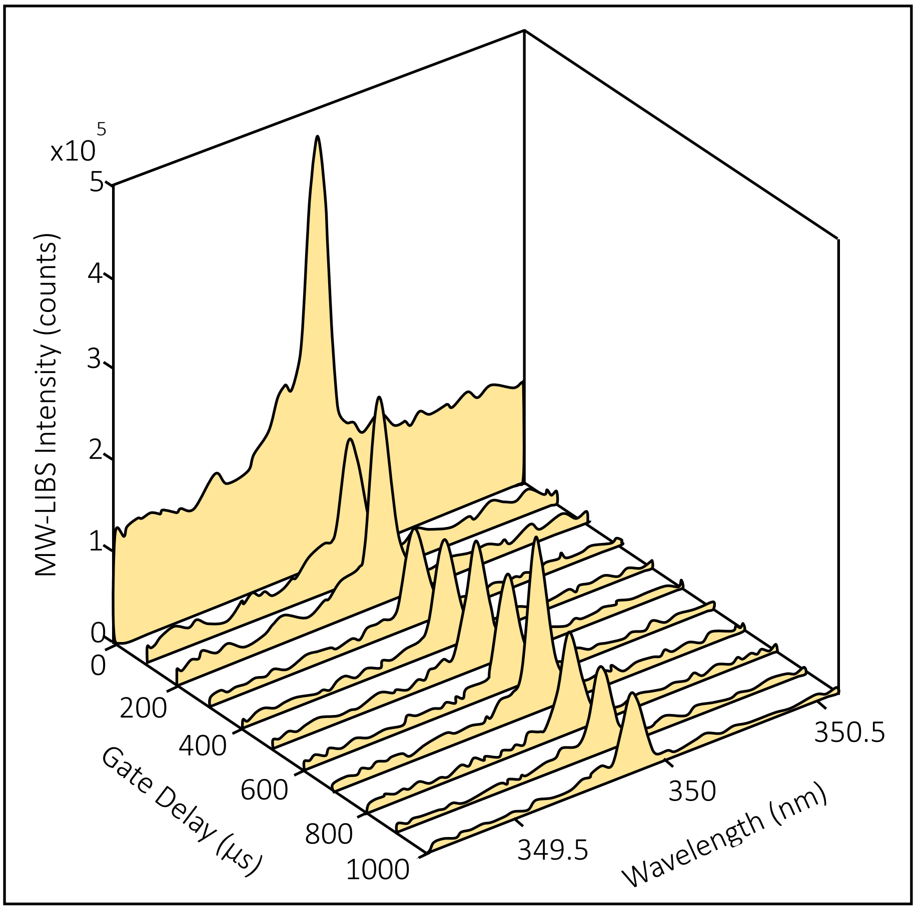

Figure 7: Temporal evolution of MW-LIBS Ru spectra recorded with a fixed gate-width of 100µS, laser energy and microwave power of 10mJ and 750W respectively

To present the capability of microwave as an enhancer, the temporal evolution of the sample was investigated. To achieve this using MW-LIBS, a 1000ppm ruthenium sample was examined based on 349.894nm detected line was detected at gate-delay step change of 100µs from 0s to 1000µs, constant gate-width of 100µs to ensure no overlapping between the timescale, and 100 accumulation shots. In addition, as determined from prior optimisations, 10mJ laser energy along with 750W of microwave power were used to achieve the results.

As can be seen from Figure 7, after the background emission at 0s, the signal persists all the way up to 1ms. This result was supported by other studies whereby the signal continues up to 700µs and 800µs, for indium (aqueous) and copper (in solid matrix) respectively, due to the extension of plasma lifetime by the microwave [33, 34]. The two sudden rises in peaks, 200ns and 700ns, could indicate misfires by the NFA due to being wetted by water droplets. Regardless, these results emphasise the effectiveness of microwave injection to the analysis.

Before the quantitative analysis of Ru(aq) detection with MW-LIBS was undertaken, two pilot experiments were performed on the liquid matrix sample, distilled water, and the microwave coupling rate based on shot to shot spectra. The reason for this was that an emission was found due to molecular transitions occurred near the 349.894nm line. This was then carried out at 100 accumulation shots, 100ns gate-delay and 1ms gate-width, and 10mJ/750W laser energy and microwave power combination in which the specific region was focused, and a transition wavelength that occurs near the similar range was presented into Figure 8.

As shown in Figure 8, in addition to clarifying the absence of signals at the 349.84nm transition line of Ru in zero concentration sample, band signals were received by the spectrometer at a wavelength range denoted as region M, ~351.43 – 353.6nm. Since the blank sample mainly contains the elements of hydrogen (H) and oxygen (O), it is most likely that this emission is a result of the OH* radicals [45] and [46]. The prior suggested that an OH* radical emission could indeed occur from H_2O discharge while the latter presented the UV bands of OH* that could occur from the same wavelength range as shown in Figure 8 which are mainly the $A^2\Sigma(v=1)\rightarrow X^2\Pi(v=2)$ transition. Given this circumstance, as the time-related emission of the decaying plasma studied previously was also at the same span of wavelength, the intensity of the Ru(aq) signal relative to the OH* band, both taken as the average peak values, was also investigated.

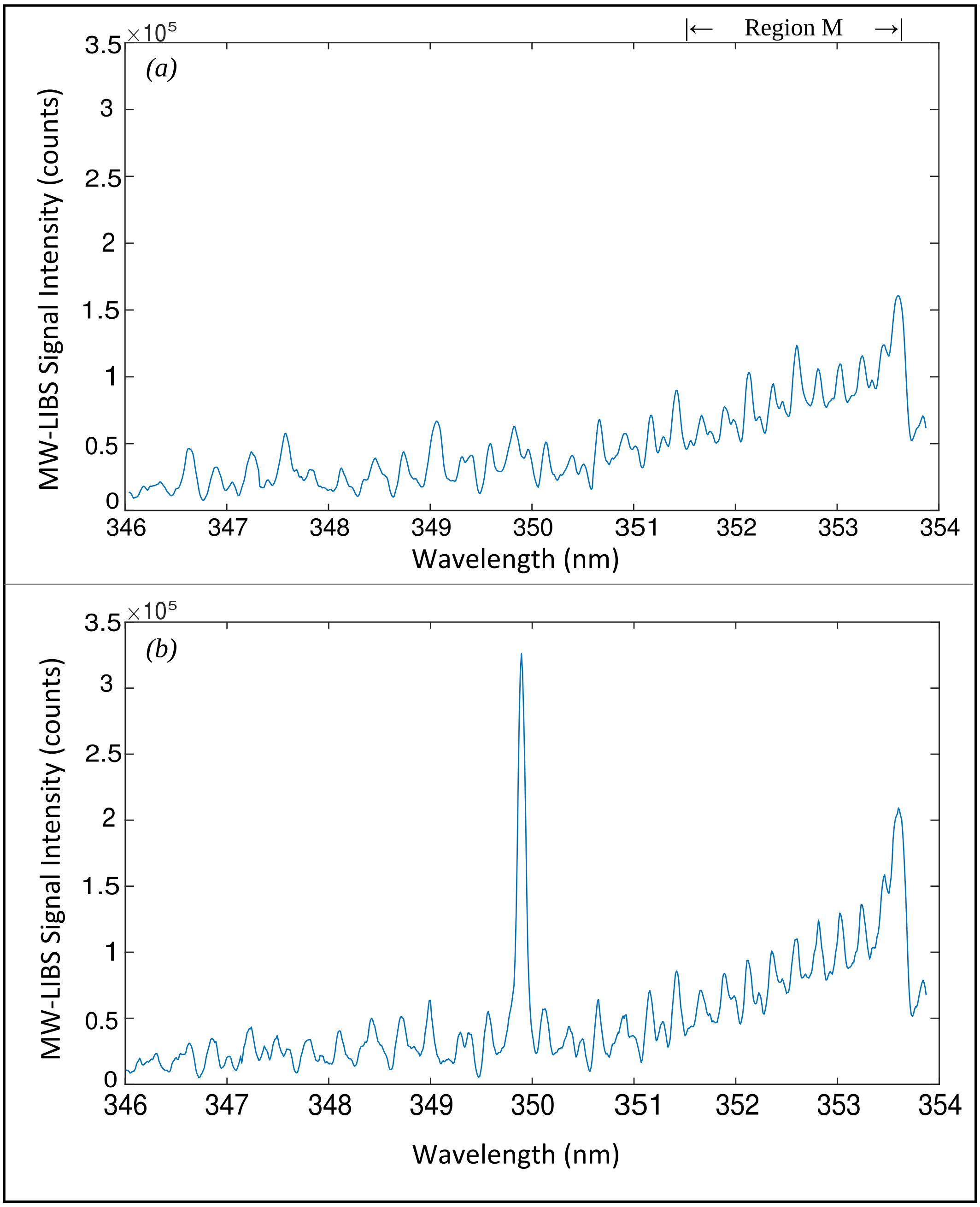

Figure 8: MW-LIBS spectra of a flow without Ru, (a), and with 100 ppm Ru(aq), (b), recorded at similar laser energy and microwave power

It should be noted that, spectrum at 0μs delay was brought to the baseline for this. All points were shown to have negligible increase as time progresses. With respect to this finding, the molecular emission of the OH* band was found to have no substantial effect on the detection of Ru(aq) implying that higher energy from the laser and microwave was absorbed for the excitation of the chemical species of interest instead of by liquid matrix.

Previously, it has been observed that not every microwave pulse produces optimum microwave-plasma coupling. This outcome is because some small water droplets may reach the tip of the NFA reducing its efficiency. The success rate of the microwave coupling on the laser induced plasma was investigated based on 100 single laser shots at 10mJ and 750W laser energy and microwave power pair, and 0ns gate-delay with 1ms gate-width. The deciding factor of what is a coupled plasma and what is not was determined from the presence or absence of the emissive signal at 379.935nm line. It was found that only 43 out of the 100 pulses generate strong Ru signal. It was concluded, for liquid detection, the coupling efficiency between the microwave and the laser induced plasma is 43%.

To understand the plasma parameters, plasma temperature has been measured using Boltzmann plot [47]. 5% $CaCl_2$ was added to water at 100 ml level to make aqua solution. To evaluate the plasma temperature in the aqua phase, three strong Ca I lines have chosen, namely, Ca I at 422.67 nm. Ca I at 430.25 nm and Ca I at 458.59 with variety of upper state energy level ranging from 2.93 eV – 5.3 eV. Figure 9 shows the typical example of Boltzmann plot which yields a plasm temperature of 3965±165 K, measured at laser energy and microwave power of 10mJ and 1200 Watt respectively.

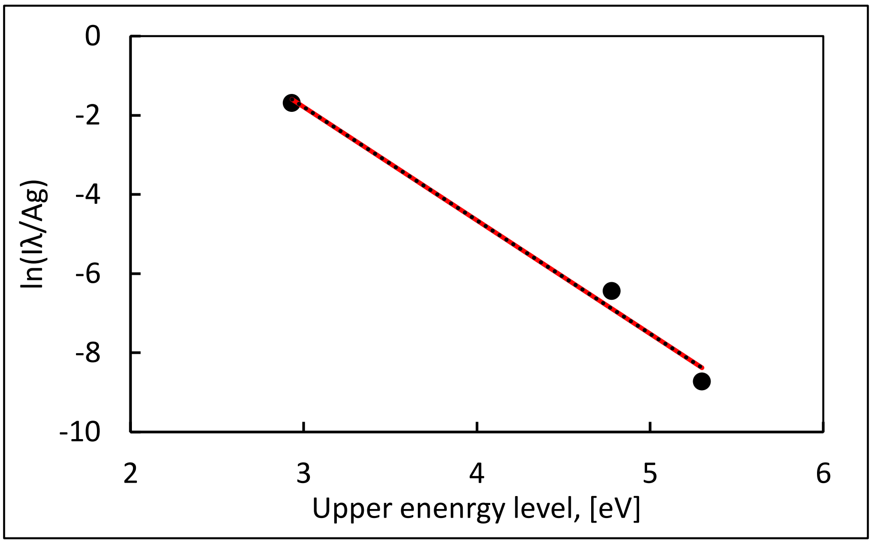

Figure 9: Boltzmann plot using Ca I lines at 10 mJ and 1200 W, 2 μs gate-delay and 500 μs gate-width.

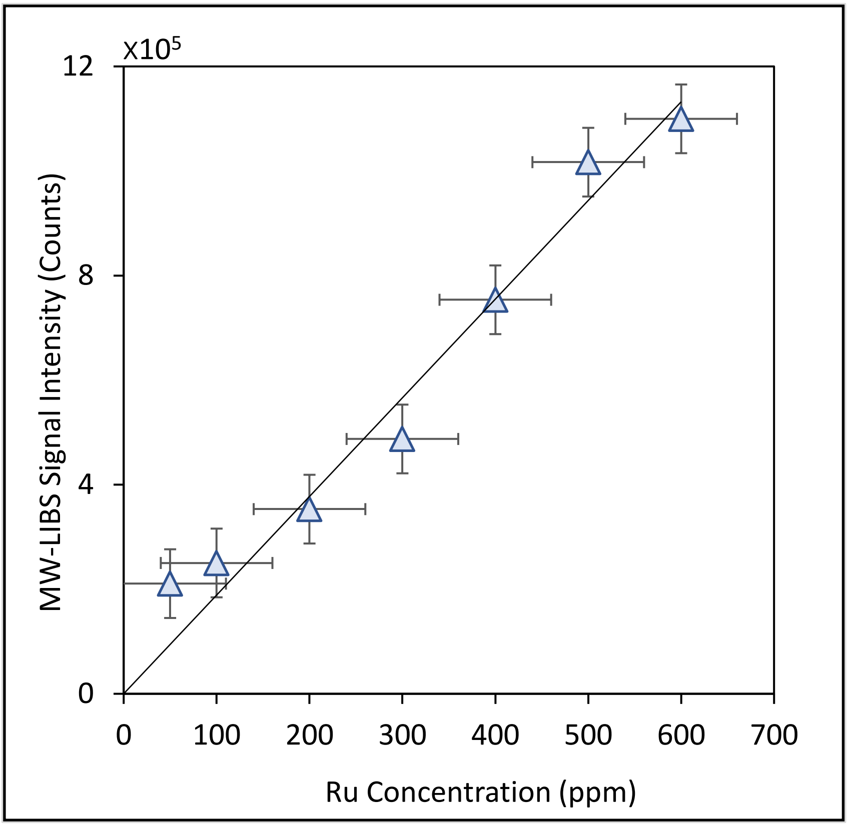

Figure 10: MW-LIBS signal intensity VS [Ru]

In order to quantitatively detect the presence of Ru(aq) using MW-LIBS, a calibration curve was constructed using varying concentrations of Ru(aq) ranging from 50ppm to 600ppm. To ensure no background emission, 100 accumulated shots, at 100ns and 1ms of gate-delay and gate-width respectively were made. The transition at 349.894nm was used due to its greater emission response and highest transition probability of the three lines chosen for this study, while being unaffected by the molecular emission of OH*. In addition, the laser energy and microwave power used were 10mJ and 750W respectively. It also worth noting that, the signals corresponding to each concentration were corrected for any possible convoluted noise based on average of three peak points in close vicinity to the line all of which to accommodate for worst-case scenario. Thus, Figure 10 represents the calibration curve for Ruthenium detection using MW-LIBS.

Figure 10 shows an increasing trend of signal with the concentration of Ru(aq). The regression has a high R^2 value, 0.9616, for the regression analysis with an intercept set to the origin and this suggests that the plot is statistically valid. Since three independent [Ru(aq)] measurements were performed, the vertical error bars were based on the deviation in signal intensity of these three measurements whilst the horizontal error bars were calculated based on equipment error during standards preparation. Thus, the LoD was calculated using; $LoD = k\overline{s_\iota}/b$. where; k is the implemented confidence level (95%) which yields a magnitude of 3; $\overline{s_\iota}$ is the average background standard deviation; b is the slope of the calibration curve [22, 25]. The error in the LoD was then taken from the deviation in the slope, which specifically is, a slope constructed from the extremum points of the error bars. Consequently, the LoD of Ru(aq) for this study is 957±84ppb.

4. Conclusion

The detection of Ru(aq) using MW-LIBS was successfully demonstrated in real-time, and at ambient pressure and temperature conditions, for the first time. This was achieved by directing the laser and microwave towards an open jet aqueous liquid sample of ruthenium at varying concentrations ranging from 50ppm to 2000ppm. It was found that the high sensitivity detection of ruthenium using LIBS at ambient conditions was insufficient and requires the enhancement of microwave injection. Furthermore, an optimum laser energy and microwave power combination of 10mJ and 750W were determined but in the absence of maximum turning point for the microwave power analysis. It was observed, for liquid detection, the coupling efficiency between the microwave and the laser induced plasma is 43%. Based on the MW-LIBS signal intensity versus [Ru] plot, the Ru(aq) LoD was determined to be 957±84ppb. Thus, the MW-LIBS technique is suitable for online monitoring of Ruthenium traces with concentration down to ~ 957ppb at ambient conditions.

5. Reference

[1] J. Emsley, Nature's building blocks : everything you need to know about the elements, New ed., [completely rev. and updated]. ed., Oxford University Press, Oxford, New York, 2011.
[2] D. McDonald, A history of platinum and its allied metals, Johnson Matthey : Distributed by Europa Publications, London, 1982.
[3] E.A. Seddon, The Chemistry of ruthenium, Elsevier, Amsterdam, New York, 1984.
[4] Q. Li, S. Zheng, Y. Xu, H. Xue, H. Pang, Ruthenium based materials as electrode materials for supercapacitors, Chemical Engineering Journal 333 (2018) 505-518.
[5] A.S. Moura, J.L.C. Fajín, M. Mandado, M.N.D.S. Cordeiro, Ruthenium–Platinum Catalysts and Direct Methanol Fuel Cells (DMFC): A Review of Theoretical and Experimental Breakthroughs, Catalysts 7(2) (2017) 47.
[6] T. Naota, H. Takaya, S.-I. Murahashi, Ruthenium-Catalyzed Reactions for Organic Synthesis, Chemical Reviews 98(7) (1998) 2599-2660.
[7] G.K. Zieliński, J. Majtczak, M. Gutowski, K. Grela, A Selective and Functional Group-Tolerant Ruthenium-Catalyzed Olefin Metathesis/Transfer Hydrogenation Tandem Sequence Using Formic Acid as Hydrogen Source, The Journal of Organic Chemistry 83(5) (2018) 2542-2553.
[8] J.C. Mol, Industrial applications of olefin metathesis, Journal of Molecular Catalysis A: Chemical 213(1) (2004) 39-45.
[9] Y. Dong, J.B. Matson, K.J. Edgar, Olefin Cross-Metathesis in Polymer and Polysaccharide Chemistry: A Review, Biomacromolecules 18(6) (2017) 1661-1676.
[10] K. Nomura, M. Abdellatif, Precise synthesis of polymers containing functional end groups by living ring-opening metathesis polymerization (ROMP): Efficient tools for synthesis of block/graft copolymers, Polymer 51 (2010) 1861-1881.
[11] N.D. Spiccia, E. Border, J. Illesinghe, W.R. Jackson, A.J. Robinson, Preparation of a Nylon-11 Precursor from Renewable Canola Oil, Synthesis 45(12) (2013) 1683-1688.
[12] V.M. Marx, L.E. Rosebrugh, M.B. Herbert, R.H. Grubbs, ChemInform Abstract: Cyclometalated Ruthenium Alkylidene Complexes: A Powerful Family of Z -Selective Olefin Metathesis Catalysts, ChemInform 47(28) (2016).
[13] X. Shen, T.T. Nguyen, M.J. Koh, D. Xu, A.W.H. Speed, R.R. Schrock, A.H. Hoveyda, Kinetically E-selective macrocyclic ring-closing metathesis, Nature 541(7637) (2017) 380-385.
[14] P. Wheeler, J.H. Phillips, R.L. Pederson, Scalable Methods for the Removal of Ruthenium Impurities from Metathesis Reaction Mixtures, Organic Process Research & Development 20(7) (2016) 1182-1190.
[15] C.P. Casey, 2005 Nobel Prize in Chemistry. Development of the Olefin Metathesis Method in Organic Synthesis, Journal of Chemical Education 83(2) (2006) 192.

[16] J. Mahmood, F. Li, S.-M. Jung, M.S. Okyay, I. Ahmad, S.-J. Kim, N. Park, H.Y. Jeong, J.-B. Baek, An efficient and pH-universal ruthenium-based catalyst for the hydrogen evolution reaction, Nature Nanotechnology 12(5) (2017) 441-446.
[17] C. Michel, P. Gallezot, Why Is Ruthenium an Efficient Catalyst for the Aqueous-Phase Hydrogenation of Biosourced Carbonyl Compounds?, ACS Catalysis 5(7) (2015) 4130-4132.
[18] I. Sádaba, M. López Granados, A. Riisager, E. Taarning, Deactivation of solid catalysts in liquid media: the case of leaching of active sites in biomass conversion reactions, Green Chemistry 17(8) (2015) 4133-4145.
[19] Q. Yang, H.-Y. Zhang, L. Wang, Y. Zhang, J. Zhao, Ru/UiO-66 Catalyst for the Reduction of Nitroarenes and Tandem Reaction of Alcohol Oxidation/Knoevenagel Condensation, ACS Omega 3(4) (2018) 4199-4212.
[20] B. Zhang, Q. Wu, C. Zhang, X. Su, R. Shi, W. Lin, Y. Li, F. Zhao, A Robust Ru/ZSM-5 Hydrogenation Catalyst: Insights into the Resistances to Ruthenium Aggregation and Carbon Deposition, ChemCatChem 9(19) (2017) 3646-3654.
[21] Y. Qiming, Z. Hong-Yu, W. Liping, Z. Yuecheng, Z. Jiquan, Ru/UiO-66 Catalyst for the Reduction of Nitroarenes and Tandem Reaction of Alcohol Oxidation/Knoevenagel Condensation, ACS Omega 3(4) (2018) 4199-4212.
[22] I.W.C.E. Arends, R.A. Sheldon, Activities and stabilities of heterogeneous catalysts in selective liquid phase oxidations: recent developments, Applied Catalysis A, General 212(1) (2001) 175-187.
[23] D.C.a. Harris, Quantitative chemical analysis, Ninth edition. ed., W.H. Freeman & Company2016.
[24] D.A. Cremers, Handbook of laser-induced breakdown spectroscopy, 2nd ed. ed., John Wiley & Sons, Ltd., Chichester, West Sussex, U.K., 2013.
[25] S.e. Musazzi, U.e. Perini, Laser-Induced Breakdown Spectroscopy Theory and Applications, Springer Berlin Heidelberg : Imprint: Springer2014.
[26] J.P. Singh, S.N. Thakur, Laser-induced breakdown spectroscopy, 1st ed. ed., Elsevier, Amsterdam, London, 2007.
[27] S. Konidala, G. Kamala, S. Koralla, Laser Induced Breakdown Spectroscopy, Research Journal of Pharmacy and Technology 9(1) (2016) 91-100.
[28] A. Khumaeni, K. Akaoka, M. Miyabe, I. Wakaida, The role of microwaves in the enhancement of laser-induced plasma emission, Frontiers of Physics 11(4) (2016) 114209.
[29] Y.C. Li, D. Tian, Y. Ding, G. Yang, K. Liu, C.H. Wang, X. Han, A review of laser-induced breakdown spectroscopy signal enhancement, Appl. Spectrosc. Rev. 53(1) (2018) 1-35.
[30] A. Iqbal, Z. Sun, M. Wall, Z.T. Alwahabi, Sensitive elemental detection using microwave-assisted laser-induced breakdown imaging, Spectrochimica Acta Part B: Atomic Spectroscopy 136 (2017) 16-22.
[31] R.a. Noll, Laser-Induced Breakdown Spectroscopy Fundamentals and Applications, Springer Berlin Heidelberg2012.
[32] S.J. Chen, A. Iqbal, M. Wall, C. Fumeaux, Z.T. Alwahabi, Design and application of near-field applicators for efficient microwave-assisted laser-induced breakdown spectroscopy, J. Anal. At. Spectrom. 32(8) (2017) 1508-1518.
[33] M. Wall, Z. Sun, Z.T. Alwahabi, Quantitative detection of metallic traces in water-based liquids by microwave-assisted laser-induced breakdown spectroscopy, Opt. Express 24(2) (2016) 1507.
[34] J. Viljanen, Z. Sun, Z.T. Alwahabi, Microwave assisted laser-induced breakdown spectroscopy at ambient conditions, Spectrochimica Acta Part B: Atomic Spectroscopy 118 (2016) 29-36.
[35] D.J.e. Cole-Hamilton, R.P.e. Tooze, Catalyst Separation, Recovery and Recycling Chemistry and Process Design, Springer Netherlands2006.
[36] D. Humphreys, Mining productivity and the fourth industrial revolution, Mineral Economics (2019).
[37] Y.G. He, X.S. Wang, S. Guo, A. Li, X.J. Xu, N. Wazir, C.J. Ding, T.Q. Lu, L.L. Xie, M. Zhang, Y. Hao, W. Guo, R.B. Liu, Lithium ion detection in liquid with low detection limit by laser-induced breakdown spectroscopy, Applied Optics 58(2) (2019) 422-427.

[38] A. Ruas, A. Matsumoto, H. Ohba, K. Akaoka, I. Wakaida, Application of laser-induced breakdown spectroscopy to zirconium in aqueous solution, Spectrochimica Acta Part B: Atomic Spectroscopy 131 (2017) 99-106.
[39] D.C. Zhang, Z.Q. Hu, Y.B. Su, B. Hai, X.L. Zhu, J.F. Zhu, X. Ma, Simple method for liquid analysis by laser-induced breakdown spectroscopy (LIBS), Opt. Express 26(14) (2018) 18794.
[40] M. Balcerzak, Analytical Methods for the Determination of Ruthenium: The State of the Art, Critical Reviews in Analytical Chemistry 32(3) (2002) 181-226.
[41] J.E. Sansonetti, W.C. Martin, Handbook of Basic Atomic Spectroscopic Data, Journal of Physical and Chemical Reference Data 34(4) (2005) 1559-2259.
[42] E. Tognoni, G. Cristoforetti, [INVITED] Signal and noise in Laser Induced Breakdown Spectroscopy: An introductory review, Optics and Laser Technology 79 (2016) 164-172.
[43] J. Viljanen, H. Zhao, Z. Zhang, J. Toivonen, Z.T. Alwahabi, Real-time release of Na, K and Ca during thermal conversion of biomass using quantitative microwave-assisted laser-induced breakdown spectroscopy, Spectrochimica Acta Part B: Atomic Spectroscopy 149 (2018) 76-83.
[44] A.A. Al Shuaili, A.M. Al Hadhrami, M.A. Wakil, Z.T. Alwahabi, Improvement of palladium limit of detection by microwave-assisted laser induced breakdown spectroscopy, Spectrochimica Acta Part B: Atomic Spectroscopy 159 (2019) 105666.
[45] T.A. Miller, The Spectroscopy of Simple Free Radicals, Annu. Rev. Phys. Chem. 27(1) (1976) 127-152.
[46] G.H. Dieke, H.M. Crosswhite, The ultraviolet bands of OH Fundamental data, Journal of Quantitative Spectroscopy and Radiative Transfer 2(2) (1962) 97-199.
[47] J. Zalach, S. Franke, Iterative Boltzmann plot method for temperature and pressure determination in a xenon high pressure discharge lamp, Journal of Applied Physics 113(4) (2013) 043303.

Chapter 6

Gated and non-gated Silver Detection using Microwave-assisted Laser Induced Breakdown Spectroscopy

M.A. Wakil and Zeyad T. Alwahabi*

School of Chemical Engineering and Advanced materials, The University of Adelaide, SA 5005. Australia

**E-mail: zeyad.alwahabi@adelaide.edu.au*

Submitted to Journal of Analytical Atomic Spectrometry

Statement of Authorship

Title of Paper	**Gated and non-gated Silver Detection using Microwave-assisted Laser Induced Breakdown Spectroscopy**
Publication Status	☐ Published ☐ Accepted for Publication ☑ Submitted for Publication ☐ Unpublished and Unsubmitted work written in manuscript style
Publication Details	Submitted to Journal of Analytical Atomic Spectrometry

Principal Author 1

Name of Principal Author (Candidate)	Md. Abdul Wakil		
Contribution to the Paper	I was responsible for the development of the measurement technique under the principal supervisor of Associate Professor Zeyad Alwahabi. I performed the measurement and data processing, wrote the first draft of the manuscript, and addressed all the comments and suggestion from other author in subsequent revisions of the manuscript. Interpretation of the data was my responsibility.		
Overall percentage (%)	80%		
Certification:	This paper reports on original research I conducted during the period of my Higher Degree by Research candidature and is not subject to any obligations or contractual agreements with a third party that would constrain its inclusion in this thesis. I am the primary author of this paper.		
Signature		Date	22.04.2020

Co-Author Contributions

By signing the Statement of Authorship, each author certifies that:

i. the candidate's stated contribution to the publication is accurate (as detailed above);
ii. permission is granted for the candidate in include the publication in the thesis; and
iii. the sum of all co-author contributions is equal to 100% less the candidate's stated contribution.

Name of Co-Author	Zeyad T. Alwahabi		
Contribution to the Paper	I was principal supervisor for the development of the work, contributed to both data interpretation and refining the manuscript. I hereby certify that statement of contribution is accurate and I have given written permission for this paper to be included in this thesis.		
Overall percentage (%)	20%		
Signature		Date	29.04.2020

Gated and non-gated Silver Detection using Microwave-assisted Laser Induced Breakdown Spectroscopy

M.A. Wakil and Zeyad T. Alwahabi*

School of Chemical Engineering and Advanced materials, The University of Adelaide, SA 5005. Australia
*Corresponding author: zeyad.alwahabi@adelaide.edu.au

Abstract:

The detection of silver using microwave-assisted laser induced breakdown spectroscopy (MW-LIBS) is demonstrated in solid and liquid samples at a 338.28 nm emission line. For solid sample analysis, the limit of detection (LoD) with a gated detector has been compared with a portable spectrometer with non-gated detector. The LoD achieved by the gated and non-gated detectors are 4.5±1.0 ppm and 7±2.3 ppm, respectively. For aqueous silver, The LoD was found to be 385±51 ppb. The LoD using MW-LIBS is more effective in liquid samples analysis than solid sample analysis for atomic detection. For MW-LIBS, it was observed that relatively low laser energy is sufficient to develop calibration curve and achieve outstanding LoD.

Keywords: Silver, quantitative detection, aqueous solution, gated and non-gated spectrometry.

1. Introduction

The precise, accurate and fast detection of precious metals is becoming an important aspect of the mining industry, in terms of exploration, development and production. Silver is one of the world’s most precious metals of the platinum family with uses across a wide variety of application such as antimicrobial, disinfectants, biosensor materials, composite fibres, cryogenic superconducting materials, cosmetic products, electrical components, food packaging, functionalized plastics, wound dressings, photographic materials and processing, electroless plating, coating, brazing and soldering uses, etc. [1-6]. Due to its intensive usage, it is suggested that silver is likely end up in the environment through landfill, wastewater, soil surface, and contamination of surface waters by natural leaching caused by bedrock and mining activities. Silver may exist in different oxidation stages such as Ag^0, Ag^{+1}, Ag^{+2} and Ag^{+3} [7]. Only a few silver compounds are deemed to be toxic, for example Ex. silver thiosulfate complex (less toxic), and silver nitrate (most toxic) [8]. However, the wastage of silver, given its economic value requires fast effective detection for proper quantification.

Several analytical techniques involving digestion methods for analysing quantification of precious metals are reported in the literature. These include, for instance fire assay, wet acid treatment, direct chlorination, alkaline oxidation fusion, etc.[9]. Maria Balcerzak [9] reviewed all the digestion methods including the advantages and hindrances of these methods. However, only a few detection techniques for silver are reported in the literature are the silver-specific DNA [10], and visual detection based on gold nanoparticles (AuNPs) [11] for silver ions. These techniques are limited to liquid samples and a long detection time. Laser induced breakdown spectroscopy (LIBS) technique is a promising fast detection technique that may satisfy the requirements of mining industries due to its substantial unique characteristics such as *in situ*, online and multi-element analysis with minimal or no sample preparation [12].

However, using LIBS. Daniel et al. detected silver in ore samples [13] and reported a limit of detection (LoD) of 1 ppm. R W Septianti et al. [14] checked the authenticity of silver jewellery and calculated the LoD of 2.74%. I. Rehan et al. [15] used monosodium glutamate and reported a detection limit of 0.57 ppm. However, there is a limitation to the LIBS technique in that it cannot estimate the extent of metals with complex structures, elements with high content (due to matrix and self-absorption effects) [16]. Poor repeatability is also a significant limitation of LIBS [16]. Another important limitation of LIBS observed by this present study's authors is the need to apply significantly high laser energy for proper signal analysis. For example, Daniel Diaz et al. applied 100-180 mJ laser energy in their experiment [13], I. Rehan and his group applied about 60 mJ for silver detection in their analysis [15]. The application of high laser energy makes the system more destructive when it is implemented outside the laboratory context.

Microwave-assisted LIBS technique (MW-LIBS) is a promising technique in that it enables the system to be less destructive because it employs significantly less laser energy. It is reported that the MW-LIBS system is more advantageous than LIBS because of certain benefits, for instance long plasma lifetime, larger volume, strong emission intensity, better stability and ability to reduce self-absorption [17, 18]. For example, Viljanen et al. observed an approximate 93-fold higher LoD with MW-LIBS compared to LIBS for copper [19] at 2.5 mJ laser energy. Adeel Iqbal et al.[20] reported a 14-fold improved LoD of indium than LIBS at only 2.5 mJ laser energy. M Wall et al. reported 11.5-fold enhanced LoD for indium at a laser pulse fluence of 85.2 J.cm^{-2} [21]. Ahlam et al. [22] established 8-fold improved LoD with MW-LIBS for palladium at 650 J.cm^{-2}. Similarly, Khumaeni et al. [23] reported about 32-fold enhancement for gadolinium (Gd) at 5 mJ laser energy.

This work focusses on the evaluation of MW-LIBS for silver detection in a laboratory at ambient condition in solid and liquid phase. The study will be carried out with two spectrometers, namely a spectrometer with an ICCD camera and a portable small spectrometer without an ICCD at low laser energy. The focus is comparing the detection limit using both the spectrometer with MW-LIBS in order to make the system compatible with practical conditions outside the laboratory. The experiment includes microwave dependence on signal-to-noise ratio (SNR), plasma temperature and electron density measurement and quantitative detection of silver. Calibration curve and the LoD was calculated using standard ore samples with different contents of silver.

2. MW-LIBS experimental setup

A schematic diagram of the MW-LIBS experimental setup is presented in Figure 1(a) and Figure 1(b) for solid and liquid detection, respectively. A Q-switch second order harmonic Nd:YAG laser with a wavelength of 532 nm was utilized as a light source. The pulse width was ~6 ns with a repetition of 10 Hz. A combined half-wave plate (HWP) and Glan-laser polarizer (P) was used for controlling the ablating pulse energy. The laser energy was measured with a Pyroelectric sensor (ES 220C). The laser beam was allowed to pass along the sample surface by a dichroic mirror (DM) with a high reflectivity in the spectral range of 500-550 nm. Then the beam was focussed on the sample surface using a fused silica lens (with f=100 mm). Propagation of the laser beam was at a 15° angle to the vertical surface and the spot size was estimated to be 7.32 µm. In this experiment, 2 mJ laser energy was considered while 1-3 mJ laser energy was used for the smallest amount of laser energy in our experiment. To achieve ablation from the fresh sample surface for each shot, the sample was placed on a rotating disk at an angular velocity of 7 revolutions per minute. A second continuous-wave (CW) [24] laser armed with a cameras served to monitor the uniform height between sample and laser beam with a camera connected to a display unit.

For liquid samples, a steady liquid circulation system was used. To achieve this, a peristaltic pump (Ismatec, MW-MSC 1), a 25 ml syringe as a sample reservoir, a circular nozzle with a 0.8 nm diameter and a collection funnel were connected to rubber-plastic tubing (Masterflex 6485-16). This process created the liquid circulation system as shown in Figure 1(b). At 360 rpm of pump operation, ~50 ml solution from liquid samples was periodically added to the syringe in order to avoid any bubble in the liquid circulation system.

A water-cooled 3000-Watt Seirem microwave system was utilized with a frequency of 2.45 GHz. The microwave was directed via a WR340 waveguide to a 3-stub impedance tuner and then to a waveguide-to-coaxial adaptor (WR340RN) through a quartz window. The waveguide-to-coaxial adaptor was connected to a 1 m flexible coaxial cable (50 Ω NN cable) with 0.14 dB @ 2.45 GHz. One end of this coaxial cable was connected to a semi-regid cable (RG402/U).

To avoid contaminaiton from the silver coating for core wire, the tip of the other end of the was soldered to pure plutinum wire (99.9%) to act as a near field applicator (NFA). The NFA was positioned 1 mm above the sample surface and 0.5 mm horizontally away from the ablation spot. Microwave pulse duration and microwave power were controlled with an analogue signal from an Aim-TTi type pulse generator. For solid matrix and for liquid matrix, 450W and 1200 W microwave power was used respect at pulse duration of 1.5 ms.

To analyse the plasma emission resulting from ablation, two spectrometers were employed, namely the gated (spectrometer with ICCD) and non-gated (spectrometer without ICCD) types. For the gated deetcion, the plasma emission was collected directly through a perforated parabolic mirror (FL=152 mm) and then focussed by a plano-convex lens (FL=100 nm), onto the sample by a plano-convex UV fused silica lens with a focal length of 100 mm and diameter of 50.8 mm. The emission was collimated by plano-convex lens (FL=100 nm) and then focused by an off-axis parabolic mirror. A second lens (FL=20 mm) coupled the emission onto an Achromatic Reflective Coupler (ARC), which is connected to a 7-fibre bundle (Thorlabs, BFL200HS02). The fibre bundle was Round-to-Linear Bundle, 7 x Ø200 µm Core. The spectrometer (Andor Shamrock 500i) with a grating of 2400 lines/mm has a spectral resolving power of 10,000, i.e., the spectral resolution is 0.031 nm in the 320-332 nm spectral range. An intensified CCD camera (Andor, iStar) recorded the spectral signal, which was then synchronized with the laser and the microwave generator with an external signal delay box (Princeton Technology Corporation). In this study, the microwave pulse duration was kept constant at 1.5 ms.

Referring to non-gated spectrometry, the plasma emission was collected by a 600 um, 0.25 m long, solarisation-resistant fibre. The fibre, placed 20 mm away from the plasma, was connected to a Mayo2000-Pro (Ocean Optics) equipped with a 25 μm entrance slit and nitrogen gas purge port. The spectrometer had a vacuum deep UV mirror and a UV Holographic grating with a groove density of 1200. Spectra were recorded by a windowless and back-illuminated uncooled detector (Hamamatsu S10420). The detector contains 2048 x 64 active pixels and a quantum efficiency of 60% at 250 nm; this configuration improves light collection and signal-to-noise ratio significantly. The integration time was fixed at 8 ms for this spectrometer with wavelength ranging from 179 nm to 400 nm.

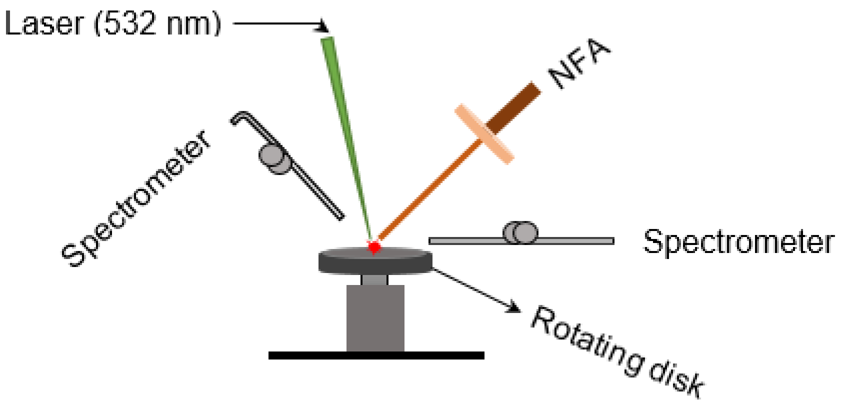

Figure 1(a). Schematic diagram of the experiment for solid silver

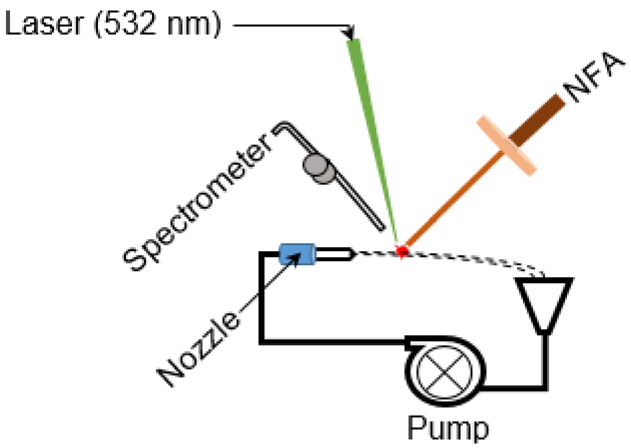

Figure 1(b). Schematic diagram of the experiment for liquid silver

2.2 Samples

The study was carried out with solid ore samples and high purity standard of 1% liquid silver for calculating the silver detection limit. Certified reference materials from GEOSTATS Mining Industry Consultants Reference material Manufacture and Sales was purchased, namely, GBC915-3, GBC616-2, GLC915-1, GBC916-3, GLC316-2, and GLC615-6. These samples containing silver of different certified concentrations (58±5 ppm -1373±84 ppm). All the samples were made by paste mixing with distilled water and organic binder. The paste was placed in a circular disk to make pellets and then dried with a dryer. All the samples were prepared as the same type of pellets for the best suited on the rotating disk. The liquid silver of 1% was purchased from choice analytical for analysis purposes. The liquid samples of different concentrations (10 ppm - 500 ppm) were prepared by diluting the pure sample with distilled water.

3. Results and discussion

3.1 Spectral information

Typical silver atomic lines recorded using MW-LIBS are presented in Figure 2. Silver (Ag I) has two strong transition lines at 328.06 nm and 338.28 nm with the same transition 5P $^2P^0 \rightarrow 5S$ ^2S which is between 0.0 cm^{-1} - 30472.66 cm^{-1} and 0.00 cm^{-1} - 29552.05 cm^{-1}. Copper has a very strong line at 327.4 nm which is closer to 328.0 nm (Ag I) as shown in Figure 2. For that reason, the line at 328.06 nm was not considered for this study. The experimental analysis was continued for both LIBS and MW-LIBS with two different spectrometers (variable configurations) but at relatively low laser energy (2 mJ), LIBS did not give any visible spectra for Ag at 338.28 nm as shown in Figure 3(a) and Figure 3(b). It is seen from Figure 3 that the signal with the portable non-gated spectrometer is smaller (Figure 3(b)) than when employing the gated spectrometer (Figure 3(a)). This may be due to the gated spectrometer's detector gain. The aim of this study was to determine the spectra at very low laser energy. At 2 mJ, MW-LIBS shows sufficient signal strength for calculating the limit of detection (LoD). Figure 3(c) represents the silver spectra in liquid phase. To check the contamination of silver from distilled water, the experiment was conducted for distilled water utilizing the same operating conditions that are illustrated in Figure 3(c) (black). It was observed that no contamination of silver from distilled water occurred. The experiment for liquid silver was conducted at 10 mJ laser energy, which was higher than the laser energy in solid phase because of inconsistent laser plasma below 10 mJ in liquid samples. Figure 4(a) and Figure 4(b) show the samples emission spectra of Ag I at 338.28 nm for different concentrations of Ag with MW-LIBS in solid and liquid of silver containing samples, respectively.

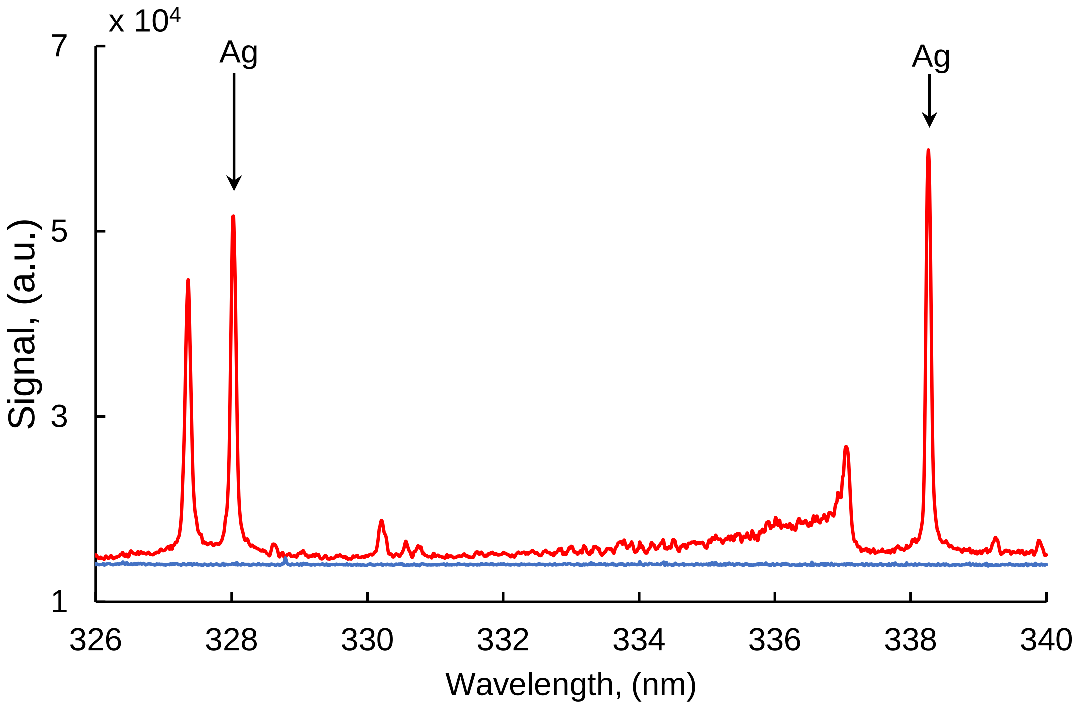

Figure 2. Typical MW-LIBS silver signal from certified ore sample at 2mJ laser energy, 450 W microwave power, 1ns gate-delay, 1000 us gate-width with an average of 30 shots, LIBS (blue), MW-LIBS (red).

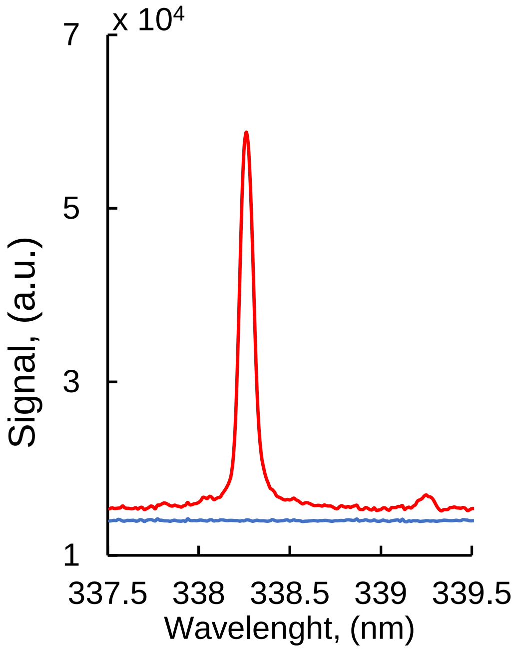

Figure 3(a). Signal from 1373 ppm Ag containing samples at 2mJ laser energy, 450 W microwave power, recorded with gated detector of 1ns gate-delay, 1000 µs gate-width with an average of 30 shots, LIBS (blue), MW-LIBS (red).

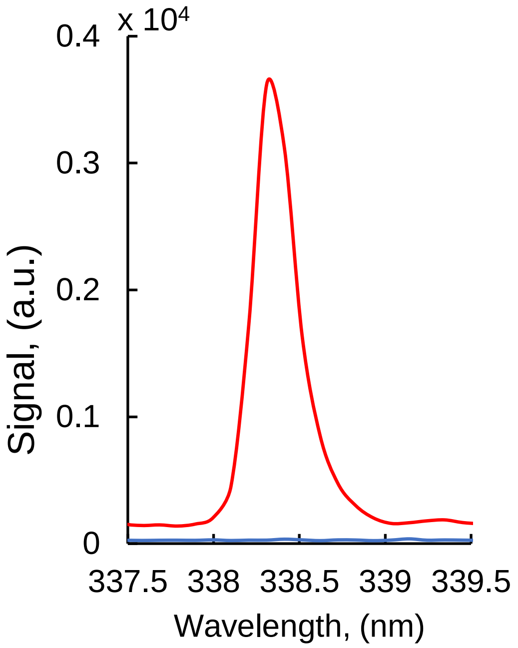

Figure 3(b). Signal from 1373 ppm Ag containing samples at 2mJ laser energy, 450 W microwave power, 8 ms recorded with non-gated detector with integration time with an average of 30 shots, LIBS (blue), MW-

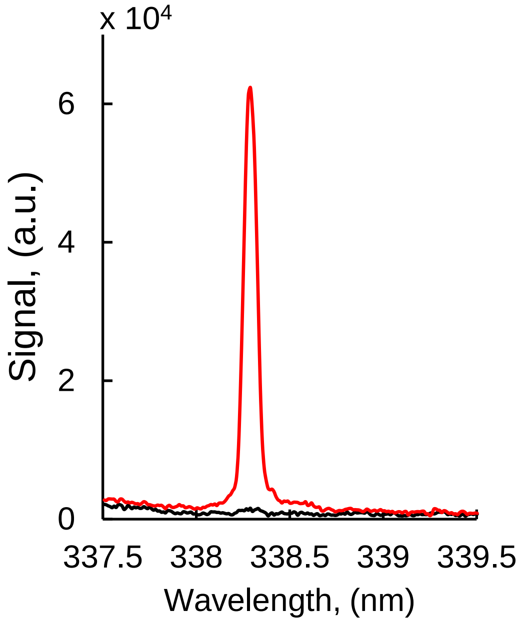

Figure 3(c). Typical MW-LIBS signal of 500-ppm Ag containing liquid sample at 10mJ laser energy, 1200 W microwave power, recorded with gated detector at 2 µs gate-delay, 500 µs gate-width with an average of 100 shots, distilled water (black), 500 ppm [Ag] (red).

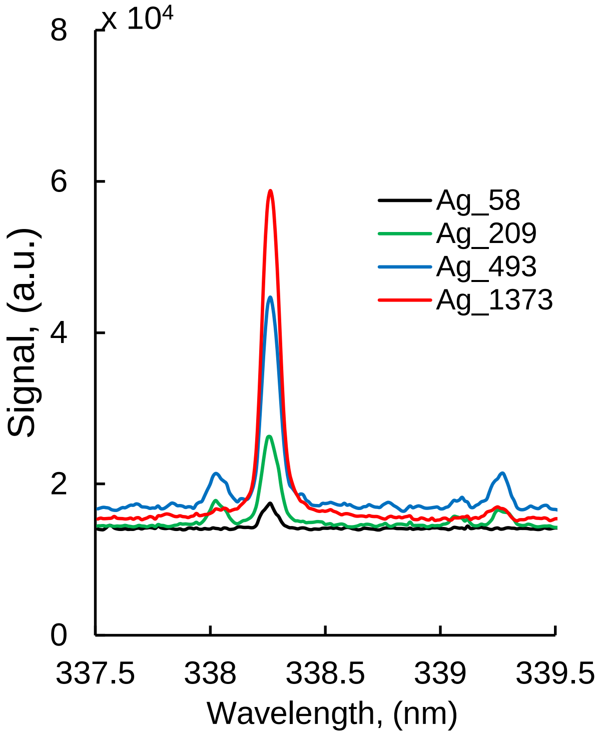

Figure 4(a). Typical spectra of MW-LIBS signal of different silver concentration from certified ore samples at 2mJ, 450 W, 1ns gate-delay and 1ms gate-width

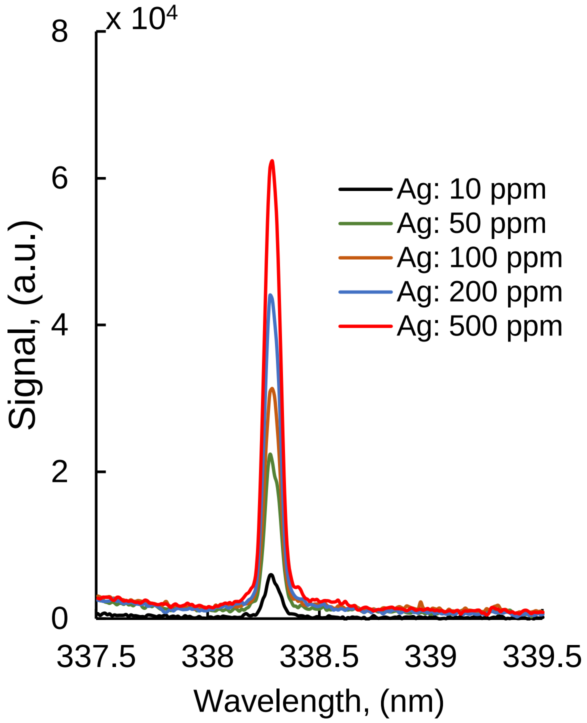

Figure 4(b). Typical spectra of MW-LIBS signal of different concentration with liquid samples at 10 mJ, 1200 W, 2 µs gate-delay and 500 µs gate-width

3.2 Signal to noise ratio measurement

To justify the operating conditions used for calculating the limit of detection, the dependence of microwave power at different laser energies was investigated for optimized signal-to-noise ratio (SNR). Figure 5(a) and Figure 5(b) present the silver SNR with solid and liquid samples, respectively. It is seen from Figure 5 that, at very low laser energy, there is sufficient SNR with MW-LIBS where there is no signal with LIBS only both in solid (1-3 mJ) and liquid (5-10 mJ), respectively. This is due to the signal microwave system's enhancing ability. The external energy supplied, using the microwave radiation, will sustain free electrons present within the laser induced plasma. These reenergized free electrons act as an excitation source, via collisional processes, leading to an extended life, which in turn finally results in signal enhancement [21, 25]. Figure 5(a) shows that the increase in SNR with increasing MW power in solid samples differs slightly from the liquid samples. For the solid sample, SNR increases until 600 W is reached and beyond this figure there is no significant impact of microwave power on SNR. The same result was documented in our paper on chlorine [26] and an unpublished report on sulphur. On the other hand, microwave power wields a significant impact on SNR in the case of liquid samples as shown in Figure 5(b). There is always an increasing order of SNR when the microwave power also increases. A microwave power below 600 W has not been considered in this study due to the instability of microwave plasma. The other reason for the weaker plasma from LIBS is explained by the reflective nature of the thin water jet, which requires more microwave power for proper coupling with LIBS plasma. The results published by Matthew Wall et al. [21] support our experimental outcomes. Laser energy below 5 mJ is not suitable for plasma formation in a liquid jet.

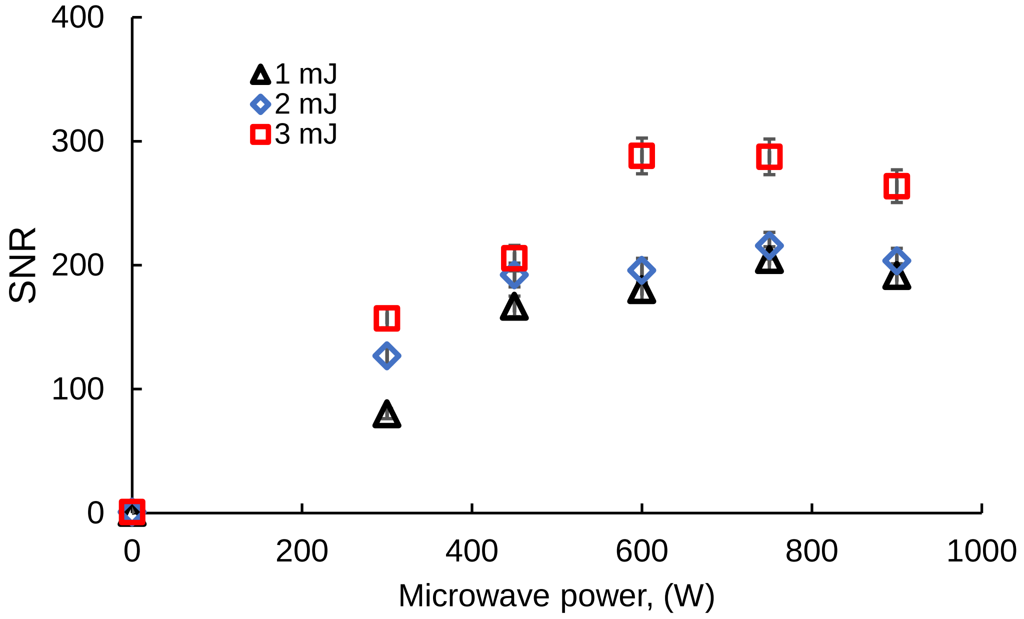

Figure 5(a). Signal to noise ratio (SNR) for solid sample with 1373 ppm [Ag] at 150 µs gate-delay, 500 µs gate-width and 30 shots.

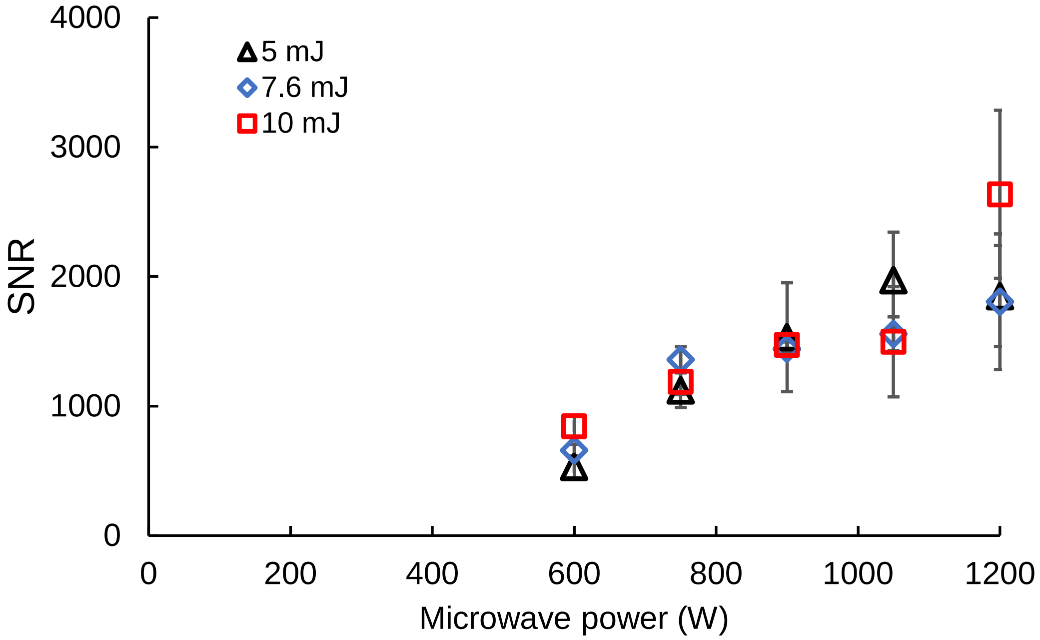

Figure 5(b). Signal to noise ratio (SNR) for liquid sample with 1000 ppm [Ag] at 1ns gate-delay, 1000 µs gate-width and 50 shots.

3.3 Plasma temperature and electron density measurement

To study the MW-LIBS plasma, detailed information about plasma parameters is required. Considering the local thermodynamic equilibrium (LTE), the plasma temperature was measured using Boltzmann plot [27]. To measure the plasma temperature for liquid matrix four strong lines of Ca I were used. The spectral information from NIST for plasma temperature measurement is given in Table 1. The Boltzmann plots Ca I is shown in Figures 6. The plasma temperature calculated for liquid matrix using MW-LIBS was 4122±192 K at 10 mJ and 1200 W. This analysis employed minimum laser energy and microwave power for silver detection. For solid sample, 2 mJ laser energy with 450 W microwave power gave sufficient SNR for developing calibration curve but for liquid, we employed 10 mJ laser energy with 1200 W microwave power. The reason for using relatively high laser energy and high microwave power is to ensure consistent MW-LIBS plasma.

Table 1: Spectroscopic data of calcium (Ca l) [28]

Wavelength (nm)	A_{ki} (s^{-1})	E_k (eV)	**g**
364.44	3.55×10^{7}	5.3	7
422.67	2.18×10^{8}	2.93	3
430.25	1.36×10^{8}	4.779	5
445.48	4.70×10^{7}	4.681	7

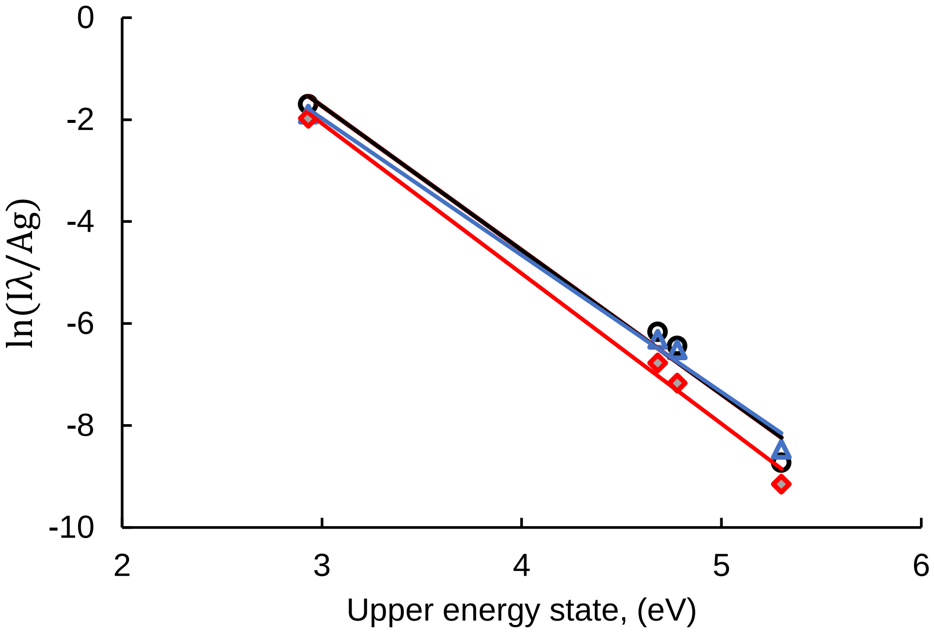

Figure 6. Boltzmann plot made from Ca I lines at 10 mJ laser energy, 1200 W microwave power, 2 µs gate-delay, 500 µs gate-width.

The electron density of the MW-LIBS plasma was calculated using a well-isolated spectral line of Ag I at 338.288 nm with a transition of 5P $^2P^0 \rightarrow 5S\ ^2S$. The plasma electron density was calculated using the relation of full-width-half-maximum (FWHM) and electron density as expressed by Harilal et al [29]. The stark width broadening parameter for Ag I at 338.28 nm was considered as 0.00392 Å and 0.004 Å [30]. The full-width at half-maximum (FWHM) was measured using the stark broadened silver line as depicted in Figure 7. The FWHM was corrected by subtracting the instrumental broadening. The instrumental broadening was measured to be 0.0321 by recoding the Hg line at 253.6 nm. The electron density measured for solid plasma was $4.95 \times 10^{17} cm^{-3}$ at laser energy and microwave power of 2 mJ and 450 W, respectively. while for the liquid plasma; it was $5.12 \times 10^{17}\ cm^{-3}$ at laser energy and microwave power of 10 mJ and 1200 W, respectively. It was observed that electron density in liquid plasma was comparatively lower than solid plasma considering laser energy. To understand if the plasma is at local thermodynamically equilibrium (LTE), the McWhirter criterion was calculated using equation 1 [31]. Considering $\Delta E = 5.03$ eV and $T = 2747$ k for solid samples, the lower limit of electron density was calculated using equation 1 and found to be 1.06×10^{16}

cm^{-3}. For the liquid plasma the lower limit of electron density was 1.51x10^{16} cm^{-3} considering ΔE = 5.3 eV and T = 4019 k. These values are much lower than the electron densities calculated for solid and liquid samples, which substantiates the LTE condition:

$$N_e \geq 1.6 \times 10^{12} \Delta E^3 T_e^{\frac{1}{2}} \ldots\ldots\ldots\ldots\ldots\ldots\ldots\ldots..(1)$$

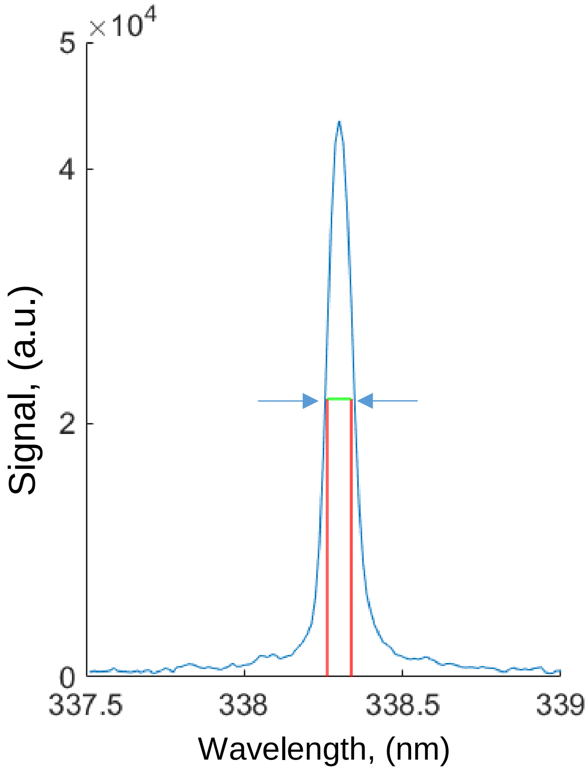

Figure 7. Typical example of full width half-maximum of 493 ppm silver containing solid sample at 2 mJ laser energy, 450 W microwave power.

3.4 Quantitative detection of Silver

Calibration curves were generated using the MW-LIBS signal for both solid and liquid matrices. Calibration curves were developed using the strong silver line at 338.28 nm. For calculating the LoD in solid and liquid phases, the experimental conditions were different.

3.4.1 LoD of silver in solid phase

For the certified ore sample, the experimental conditions were 2 mJ laser energy, 450 W microwave power, 1 ns gate-delay, 1 ms gate-width with accumulation of 30 shots. Figure 8(a) shows the calibration curve for solid silver with gated spectrometer. LoD was calculated using the 3-sigma method [32, 33] and found to be 4.5±1.0 ppm LoD. The same experiment was done with a non-gated portable spectrometer as shown in Figure 8(b), and here the LoD was 7±2.3 ppm. It was evident that a portable spectrometer can detect silver with MW-LIBS, which helps to make the experimental system portable for outside uses. LoD was calculated for liquid silver samples by developing the calibration curve.

3.4.2 LoD of silver in liquid phase

Figure 8(c) shows the calibration curve for liquid silver at 10 mJ laser energy and 1200 W microwave power. What emerged was an improved LoD of silver in liquid matrix that was better than the solid matrix. The relatively lower noise in liquid phase with MW-LIBS is the main reason for improved LoD. The LoD found in liquid samples was 385±51 ppb.

However, the studies [13-15] have been undertaken for the detection of silver as discussed in the introduction section. To the best of our knowledge, the best LoD for silver was reported by Rehan et al. [15] using silver containing salt samples. They reported LoD as 0.57 ppm which is lower than our present study of 4.5 ppm, but they employed high laser energy (60 mJ) while our experiment was conducted with only 2 mJ laser energy. To the best of our knowledge, our study is the first to report silver detection in liquid samples with MW-LIBS. Paing et al. reported 3.1 ppm silver detection in liquid via the liquid sampling-atmospheric glow discharge optical emission spectroscopy (LS-APGD-OES) method [34].

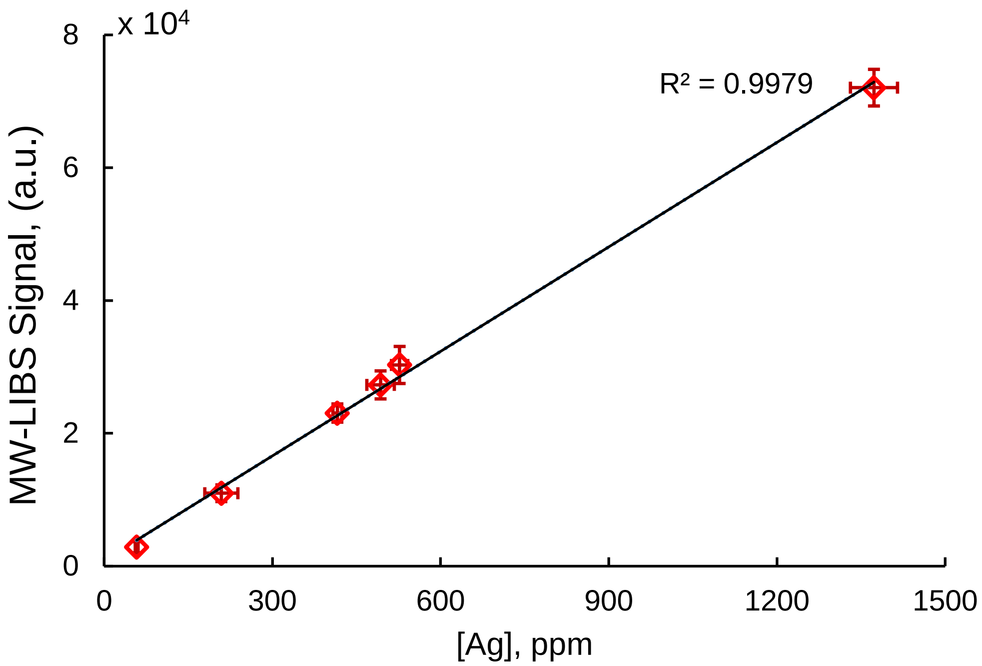

Figure 8(a). Calibration curve of solid silver with MW-LIBS at 2 mJ laser energy, 450 W microwave power, 1 ns gate-delay, 1 ms gate-width with accumulation of 30 single shots.

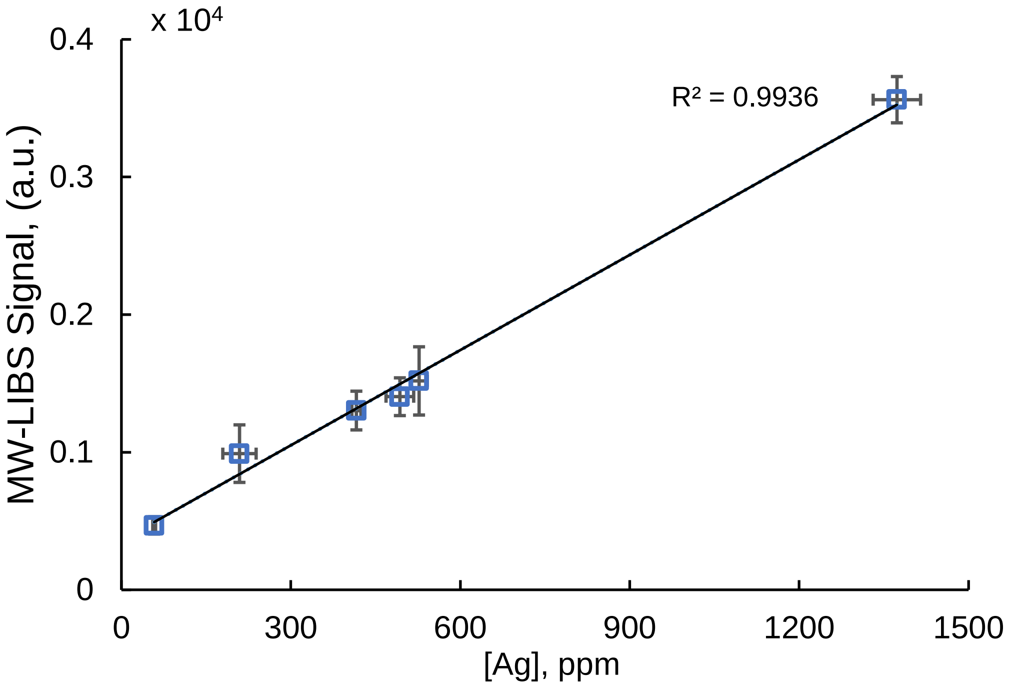

Figure 8(b). Calibration curve of solid silver with MW-LIBS at 2 mJ laser energy, 450 W microwave power, 2.5 ms microwave pulse duration and 8 ms integration time with accumulation of 30 single shots.

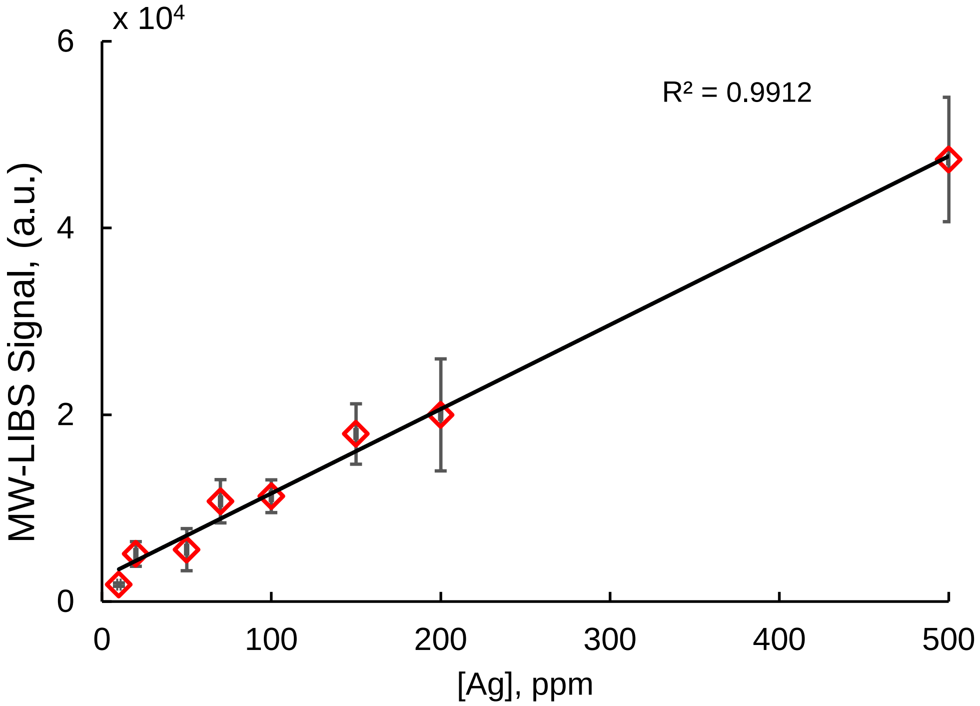

Figure 8(c). Calibration curve of silver in aqua phase with MW-LIBS at 10 mJ laser energy, 1200 W microwave power, 2 µs gate-delay, 500 µs gate-width with accumulation of 50 single shots.

4. Conclusion

Quantitative silver detection with gated and non-gated spectrometers using microwave-assisted LIBS technique is reported for the first time. Silver detection has been described here for solid and liquid samples. The limit of detection with laboratory-scale gated spectrometer was compared to the portable non-gated spectrometer. The MW-LIBS technique is more sensitive in liquid than in solid for achieving a superior detection limit. The experimental study was carried out at very low laser energy, the objective being to establish the effectiveness of MW-LIBS when compared to LIBS. It has been shown that MW-LIBS is able to achieve a strong signal with low laser energy, yet LIBS is unable to detect any signal by using silver at 338.28 nm. The limit of detection reported in this study is 4.5±1.0 ppm in solid and 0.385±0.051 ppm in liquid. The detection limit of silver is also calculated using a portable spectrometer at 7±2.3 ppm.

Reference

1. P. Verma and S. K. Maheshwari, *International Journal of Nano Dimension*, 2019, **10**, 18-36.
2. T. W. Purcell and J. J. Peters, *Environmental Toxicology and Chemistry*, 1998, **17**, 539-546.
3. S. Senapati, PhD, Savitribai Phule Pune University, 2005.
4. T. Klaus-Joerger, R. Joerger, E. Olsson and C.-G. Granqvist, *Trends in Biotechnology*, 2001, **19**, 15-20.
5. J. Fabrega, S. N. Luoma, C. R. Tyler, T. S. Galloway and J. R. Lead, *Environment International*, 2011, **37**, 517-531.
6. C. Zhang, Z. Hu and B. Deng, *Water Research*, 2016, **88**, 403-427.
7. E. McGillicuddy, I. Murray, S. Kavanagh, L. Morrison, A. Fogarty, M. Cormican, P. Dockery, M. Prendergast, N. Rowan and D. Morris, *Science of The Total Environment*, 2017, **575**, 231-246.
8. H. T. Ratte, *Environmental Toxicology and Chemistry*, 1999, **18**, 89-108.
9. M. Balcerzak, *Sample Digestion Methods for the Determination of Traces of Precious Metals by Spectrometric Techniques*, 2002.
10. K. Jang, J. You, C. Park and S. Na, *New Journal of Chemistry*, 2017, **41**, 1840-1845.
11. B. Liu, H. Tan and Y. Chen, *Microchimica Acta*, 2013, **180**, 331-339.
12. *Laser Induced Breakdown Spectroscopy*, Cambridge University Press, Cambridge, 2006.
13. D. Díaz, D. W. Hahn and A. Molina, *Spectrochimica Acta Part B: Atomic Spectroscopy*, 2017, **136**, 106-115.
14. R. W. Septianti, W. S. Budi, H. Sugito and A. Khumaeni, in *7th International Seminar on New Paradigm and Innovation on Natural Science and Its Application*, eds. B. Warsito, S. P. Putro and A. Khumaeni, Iop Publishing Ltd, Bristol, 2018, vol. 1025.
15. I. Rehan, M. A. Gondal and K. Rehan, *Applied Optics*, 2018, **57**, 3191-3197.
16. D. A. Cremers and L. J. Radziemski, in *Laser Induced Breakdown Spectroscopy*, eds. A. W. Miziolek, I. Schechter and V. Palleschi, Cambridge University Press, Cambridge, 2006, DOI: DOI: 10.1017/CBO9780511541261.002, pp. 1-39.
17. Y. Ikeda and R. Tsuruoka, *Applied Optics*, 2012, **51**, B183-B191.
18. Y. Tang, J. Li, Z. Hao, S. Tang, Z. Zhu, L. Guo, X. Li, X. Zeng, J. Duan and Y. Lu, *Opt. Express*, 2018, **26**, 12121-12130.

19. J. Viljanen, Z. Sun and Z. T. Alwahabi, *Spectrochimica Acta Part B: Atomic Spectroscopy*, 2016, **118**, 29-36.
20. A. Iqbal, Z. Sun, M. Wall and Z. T. Alwahabi, *Spectrochimica Acta Part B: Atomic Spectroscopy*, 2017, **136**, 16-22.
21. M. Wall, Z. W. Sun and Z. T. Alwahabi, *Opt. Express*, 2016, **24**, 1507-1517.
22. A. A. Al Shuaili, A. M. Al Hadhrami, M. A. Wakil and Z. T. Alwahabi, *Spectrochimica Acta Part B: Atomic Spectroscopy*, 2019, **159**, 105666.
23. A. Khumaeni, T. Motonobu, A. Katsuaki, M. Masabumi and W. Ikuo, *Opt. Express*, 2013, **21**, 29755-29768.
24. M. Bahreini, B. Ashrafkhani and S. H. Tavassoli, *Applied Physics B*, 2014, **114**, 439-447.
25. Y. Liu, B. Bousquet, M. Baudelet and M. Richardson, *Spectrochimica Acta Part B: Atomic Spectroscopy*, 2012, **73**, 89-92.
26. M. A. Wakil and Z. T. Alwahabi, *J. Anal. At. Spectrom.*, 2019, DOI: 10.1039/C9JA00151D.
27. J. Zalach and S. Franke, *Journal of Applied Physics*, 2013, **113**, 043303.
28. J. Reader, C. H. Corliss, W. L. Wiese and G. A. Martin, *Wavelengths and transition probabilities for atoms and atomic ions : part I. wavelengths - part II. transition probabilities*, National Bureau of Standards, NSRDS; NISTresearchlibrary; fedlink; americana, 1980.
29. S. Harilal, C. Bindhu, R. Issac, V. P. N. Nampoori and C. Vallabhan, *Journal of Applied Physics*, 1997, **82**, 2140-2146.
30. Milan S. Dimitrijevic and S. S. Brechot;, *Journal of Research in Physics*, 1999, **28**, 291-294.
31. R. W. P. McWhirter, 1965, 201.
32. S. Rosenwasser, G. Asimellis, B. Bromley, R. Hazlett, J. Martin, T. Pearce and A. Zigler, *Spectrochimica Acta Part B: Atomic Spectroscopy*, 2001, **56**, 707-714.
33. D. W. Hahn and N. Omenetto, *Applied spectroscopy*, 2012, **66**, 347-419.
34. H. W. Paing, K. A. Hall and R. K. Marcus, *Spectrochimica Acta Part B: Atomic Spectroscopy*, 2019, **155**, 99-106.

Chapter 7

Signal Enhancement Tendency of Microwave-assisted Laser Induced Breakdown Spectroscopy: Application to Sulphur Detection

M.A. Wakil and Zeyad T. Alwahabi*

School of Chemical Engineering and Advanced materials, The University of Adelaide, SA 5005. Australia

**E-mail: zeyad.alwahabi@adelaide.edu.au*

Submitted to Spectrochimica Acta Part B: Atomic Spectroscopy

Statement of Authorship

Title of Paper	**Signal Enhancement Tendency of Microwave-assisted Laser Induced Breakdown Spectroscopy: Application to Sulphur Detection**
Publication Status	☐ Published ☐ Accepted for Publication ☑ Submitted for Publication ☐ Unpublished and Unsubmitted work written in manuscript style
Publication Details	Submitted to Spectrochimica Acta Part B: Atomic Spectroscopy

Principal Author 1

Name of Principal Author (Candidate)	Md. Abdul Wakil		
Contribution to the Paper	I was responsible for the development of the measurement technique under the principal supervisor of Associate Professor Zeyad Alwahabi. I performed the measurement and data processing, wrote the first draft of the manuscript, and addressed all the comments and suggestion from other author in subsequent revisions of the manuscript. Interpretation of the data was my responsibility.		
Overall percentage (%)	80%		
Certification:	This paper reports on original research I conducted during the period of my Higher Degree by Research candidature and is not subject to any obligations or contractual agreements with a third party that would constrain its inclusion in this thesis. I am the primary author of this paper.		
Signature		Date	22.04.2020

Co-Author Contributions

By signing the Statement of Authorship, each author certifies that:

i. the candidate's stated contribution to the publication is accurate (as detailed above);

ii. permission is granted for the candidate in include the publication in the thesis; and

iii. the sum of all co-author contributions is equal to 100% less the candidate's stated contribution.

Name of Co-Author	Zeyad T. Alwahabi		
Contribution to the Paper	I was principal supervisor for the development of the work, contributed to both data interpretation and refining the manuscript. I hereby certify that statement of contribution is accurate and I have given written permission for this paper to be included in this thesis.		
Overall percentage (%)	20%		
Signature		Date	29.04.2020

Signal Enhancement Tendency of Microwave-assisted Laser Induced Breakdown Spectroscopy: Application to Sulphur Detection

M. A. Wakil and Zeyad T. Alwahabi*

School of Chemical Engineering and Advanced materials, The University of Adelaide, SA 5005. Australia
**Corresponding author:* zeyad.alwahabi@adelaide.edu.au

Abstract:

The signal enhancement tendency of Microwave-assisted Laser Induced Breakdown Spectroscopy (MW-LIBS) are reported in this study. Six elements with emission lines at upper energy level (UEL) ranging from 3.65 eV to 6.86 eV were selected, namely Ag, Cu, Fe, Mg, Pb and S. The signal-to-noise (SNR) improvement, for each element, has been examined experimentally and the effects of microwave power and detector gain on signal enhancement were assessed. The plasma temperature has been evaluated, based on Ca I and Pb I lines, as function of microwave power and time delay. It is found that the SNR improvement inversely depends on the value of UEL. Using microwave radiation, significant enhancement is possible for the elements with the UEL below 5eV and the cut-off limit of signal enhancement is found to be ~7eV. Based on data, a simple model is developed to predict the SNR improvement for elements. The model predicts that the highest SNR improvements may be achieved for potassium, namely 530±15 times and 150±4 times, with and without detector gain, respectively. Based on atomic detection, it is demonstrated that microwave radiation will not improve SNR for elements such as fluorine, chlorine, bromine and iodine. It confirms that plasma temperature in MW-LIBS plasma is virtually independent of delay-time and the microwave exerts no reheating impact in plasma. The detection of sulphur at 180.73 nm, using a portable spectrometer equipped with a non-gated detector validated the model. Employing 10 mJ at 532 nm, 2-fold signal enhancement and 312 µg/g limit of detection was recorded experimentally. The model is based on 5 mJ laser energy.

Keywords: MW- LIBS, Upper state energy level, SNR improvement model, Sulphur, Detection limit.

1. Introduction:

Laser induced breakdown spectroscopy (LIBS) has become popular due to its outstanding advantages, such as no need for sample preparation, fast, easy to operate. Conversely, LIBS suffers in terms of sensitivity, self-absorption, matrix of material. Many techniques have been developed and applied to improve the sensitivity of LIBS [1-5]. More precisely, double pulse LIBS (DP-LIBS), spark discharge LIBS (SD-LIBS), resonant LIBS (RELIBS), nanoparticle LIBS are found to be effective approach to improve the analytical performance of LIBS. Zhao et al. found 3 times improved LoD for Pb in soil using DP-LIBS [6]. Jiang et al. demonstrated 3-9 times improved LoD for Pb I, Fe I and Al I at 368.35 nm, 358.12 nm and 396.15 nm respectively using SD-LIBS than LIBS [7]. Khachatrian et al. claimed the significant enhancement for H, C and Si with RELIBS [8]. However, there are limitations of these techniques. For example, SD-LIBS technique is limited with conductive samples and currently predominately used for alloy analysis [9]. DellAglio et al. reported that nanoparticle enhanced LIBS requires careful sample preparation [10]. MW-LIBS has been demonstrated as well suited for the signal enhancements and improve the limit of detection (LoD) [11-13].

1.1 MW-LIBS signal enhancement

The MW-LIBS mechanism relies on the coupling of microwave radiation with laser induced plasma at a critical electron density. The critical electron density is about 7×10^{10} cm^{-3} for microwave radiation at 2.45 GHz [14]. Initially, the laser induced plasma consists of high electron density in the order of 10^{17} -10^{19} cm^{-3} where the plasma acts as a reflector to the microwave [14] but during the relaxation of plasma, the electron density at the periphery of the plasma falls below the critical electron density. This allows the microwave, through the electromagnetic field, to drive the motion of free electrons and provides the kinetic energy to excite the surrounding atoms and ions via multiple electron-atom and/or electron-ion collisions. As long as the microwave is coupled with plasma, the emission's lifetime increases to the microwave duration.

MW-LIBS offers several benefits, for example long plasma life, strong uniform plasma emission intensity, stability over time and the ability to reduce self-absorption [11, 12, 15, 16], which subsequently enhances the signal's intensity. It is interesting to consider that the signal enhancement with MW-LIBS is different as noted in the literature although the experimental conditions were not the same. Viljanen et al. observed ~100 times greater signal enhancement with MW-LIBS than LIBS at 0.8 mJ laser energy for Cu I at 324.75 nm [12]. Tampo et al. observed a ~50 times enhancement at 5 mJ for Gd II at 367.12 nm [17], while Khumaeni et al.

observed a 10-fold improvement for Ca I at 422.6 nm and a 40-fold enhancement for Gd I at 470.9 nm at 5 mJ [11, 18]. Meanwhile, Liu et al. found enhancement of 33, 22, 16 and 11 for Na I at 589.6 nm, Ca I at 422.7 nm, Mg I at 285.2 nm and Al I at 396.2 nm, respectively [14]. Wall et al. obtained a signal enhancement of 60 times for In I at 451.13 nm [13]. Ahlam et al. achieved 92 times enhancement for Pd I at 340.46 nm [19]. Abu et al. observed 76 times signal to noise ration improvement in ruthenium aqua solution at 10 mJ [paper submitted]. However, it is important to study the factors, which effect the MW-LIBS signal enhancement.

1.2 Sulphur detection

An accurate and reliable detection of sulphur is important in many industrial processes. Sulphur is important non-metal light element that affects the matrix of a material [20, 21] and the oil refining system [22]. Liu et al. reported that sulphur content plays an important role in arsenic volatilisation and especially in coal burning [23].

The high energy level of sulphur has made the optical emission difficult to analyse. For example, most of its energy levels are high (7-8 eV) and lies below 190 nm. Other atomic levels are near the infrared region with high energy levels and lower transition strength [1, 24]. Nevertheless, the disadvantage of using these lines is the strong influence of atmospheric O_2 [25]. For that reason, all the potential detection wavelengths of sulphur are reported in the literature such as in the ultraviolet [1, 24], visible [21, 26] and near infrared [22, 27]. LIBS is considered to be the best technique in most studies for detecting sulphur because of its successfully direct quantitative elemental analysing ability [28]. Many studies have been conducted in low pressure [22, 24, 29-31] and under inert environment [27, 32]. Hrdlicka et al.[33] calculated LoD of 0.025% for sulphur in concreate samples using low pressure helium environment at 100 mJ laser energy. Burakov et al. [1] applied double pulse laser on coal samples and detected sulphur in the 0.1-0.2% range. Trautner et al. [34] achieved 0.14% LoD of sulphur for butadiene rubber (BR) applying a double pulse laser. In addition, Timur et al. [35] applied the double pulse option and achieved 1500 ppm LoD for sulphur analysis of their concrete samples. However, this study is dealing with the application of MW-LIBS for sulphur detection. Khumaeni et al. [11] have demonstrated that the sensitivity of MW assisted LIBS is about 8 times higher than DP-LIBS.

A compact LIBS system is now becoming popular because of its portability and better commercial usage [36]. The wide range of spectral wavelength at a single scan and lower background noise makes the small spectrometer popular for analysing multiple elements in one scan [37, 38]. Despite its instrumental simplicity and compact size, the spectrometer is able to support analytical studies relevant to archaeological, historical and elemental detection in wider ranges, particularly when quick data acquisition is required in the context large numbers of objects and samples being surveyed [39].

This motivation of the study is two-fold. First, it addresses the MW-LIBS signal enhancement tendency of any elements, and second, to report on the LoD of sulphur using a MW-assisted LIBS technique with a non-gated portable small spectrometer.

2. Experimental

2.1 MW-LIBS setup

Two experimental setups have been used in this study. The first is based on a portable spectrometer and the second based on a laboratory spectrometer equipped with ICCD.

The first experimental setup is presented schematically in Figure 1(a). A second harmonic Q-switched Nd:YAG laser, Quantel (Brilliant B) at 532 nm wavelength with an initial beam width of (~3 mm) served as an ablation source with pulse repetition of 10 Hz and pulse width of ~6 ns. A half-wave plate coupled with a Glan-laser polariser was employed to adjust the laser energy, which was measured with a Pyroelectric sensor (ES 220C). The laser beam was focused on a solid sample by using a plano-convex UV fused silica lens (f_1 = 100 mm, D_1 = 50.8 mm) to generate a tiny plasma on a solid target. The spot size obtained at the focal point was estimated to be 7.32 µm while the propagation of the laser beam was at an angle of 15^O to the vertical [13]. To achieve the ablation from fresh sample surface for each shot, the sample was placed on a rotating disk with an angular velocity of 7 revolution per minute. A second continuous wave laser and a camera helped to monitor the exact height between the sample surface and near field applicator [40].

A water-cooled 3 kW Sairem Microwave system was used as microwave pulse at 2.5 GHz. A WR 340 waveguide directed the microwave power through a 3-stub impedance tuner to a wave-guide-to-coaxial adapter after passing through a quartz window. The NFA (near field applicator) was connected with a waveguide-to-coaxial adapter via a 1 m flexible coaxial cable (50 Ω NN cable) with 0.14 dB at 2.45 GHz. The NFA was designed to generate a strong electrical field near the tip without emitting any microwave radiation [12]. The NFA was located about 1 mm above the sample surface and 0.5 mm horizontally away from the ablation spot. Microwave pulse duration and microwave power were controlled with an analogue signal originating from an Aim-TTi type pulse generator.

For the spectroscopic detection stage, the plasma emission was collected by a 600 µm, 0.25 m long, solarisation-resistant fibre. The fibre, placed 20 mm away from the plasma, was connected to a Mayo2000-Pro (Ocean Optics) equated to a 25 µm entrance slit and nitrogen gas purge port. The spectrometer has a vacuum deep UV mirror and a UV Holographic grating with a groove density of 1200. The spectra were recorded with a windowless and back-illuminated uncooled-detector (Hamamatsu S10420), comprising 2048 x 64 active pixels and a quantum efficiency of 60% at 250 nm. This configuration improves light collection and the signal-to-noise ratio significantly. The integration time was fixed at 8 ms for the spectrometer as shown in Figure 1(b). Meanwhile the wavelength of the spectrometer ranged from 179 nm to 400 nm. A 99.99% pure N_2 was used as purging gas in the spectrometer with a flow rate of 4 l/min. For analysing the emission spectra, 100 single shots were recorded and then averaged. The optical line, sample holder, NFA and one end of the fibre were placed inside an aluminium box to minimize the residual microwave radiation. The experiment was conducted in an atmospheric environment.

In the second experimental setup, the ablation beam was directed to pass through a perforated parabolic mirror (FL= 152 mm), and then focused by a plano-convex lens (FL= 100 mm), onto the sample via a plano-convex UV fused silica lens with a focal length of 100 mm and diameter of 50.8 mm. The emission was collimated by plano-convex lens and then focused by an off-axis parabolic mirror (OPAM). A second lens (FL= 20 mm) coupled the emission onto an Achromatic Reflective Coupler (ARC), which was connected to a 7-fibre bundle (Thorlabs, BFL200HS02). The fibre was then connected to a spectrometer (Andor, Shamrock 500i with 2,400 lines/mm grating) equipped with an intensifier camera, ICCD (Andor, iStar). The configuration of the spectrometer is described in our previous paper [13, 19, 41, 42].

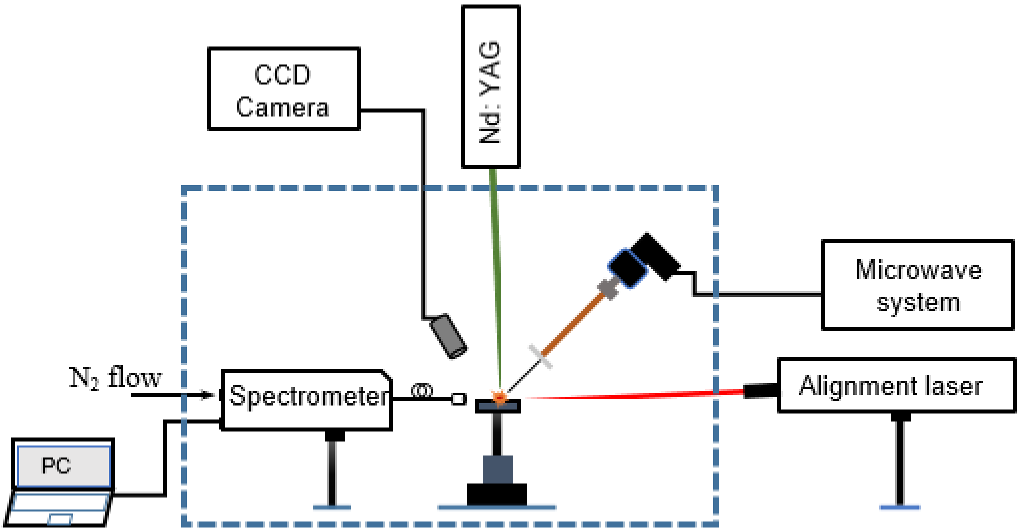

Figure 1(a). Schematic diagram of the experimental for the portable spectrometer (dotted box represents aluminium box)

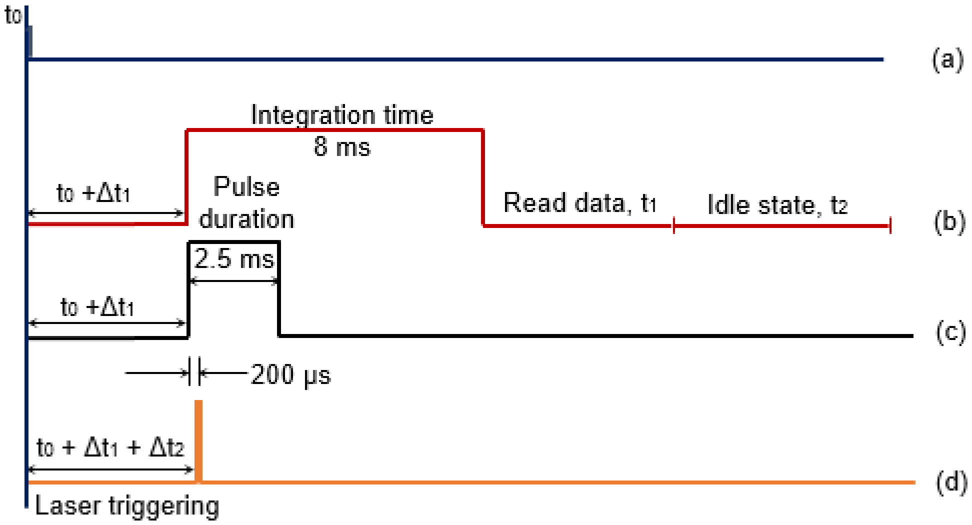

Figure 1(b). Timing diagram showing the primary pulse (t_0), a, the portable spectrometer, b, the microwave trigger pulse, c, the laser pulse, d.

2.2 Samples

In order to assess the linearity and detection limit of sulphur, solid samples (OREAS 350-351, 600, 603, 620-623) of Rhyodacite matrix containing sulphur of different concentrations (1.07% - 9.07%) were obtained from ORE Research & Exploration Pty Ltd. For signal enhancement and plasma parameters calculation as required in this study, different elements containing samples (OREAS 350-351) of Concentrate matrix were selected and these were purchased from the same company. All the samples were prepared as the same type of pellets (20.45±0.1 mm dia. and 1.8±0.02 mm thick) by simple green compacting using aluminium holder that were best suited for the rotating disk. Table 1 represents the spectral lines and spectroscopic data for plasma temperature measurement, signal enhancement and SNR improvement calculation. The elements presented in Table 1 were used to analyse the SNR improvement belonged to the same matrix of OREAS except calcium. Pure $CaCl_2$ solid powder was used as a source of calcium.

Table 1: Spectral lines in the present work [43]

Element	**Wavelength, nm**	**Transition strength, A_{ki} (s^{-1})**	**Upper state energy level, (eV)**	**g**
Pb	280.20	1.61×10^{08}	5.74	7
	287.30	3.80×10^{07}	5.63	5
	363.95	3.20×10^{07}	4.37	3
	368.35	1.37×10^{08}	4.33	1
Ca	364.44	3.55×10^{07}	5.30	7
	422.67	2.18×10^{08}	2.93	3
	430.25	1.36×10^{08}	4.78	5
	445.48	4.70×10^{07}	4.68	7
	458.59	2.29×10^{07}	5.23	9
Cu	324.74	1.39×10^{08}	3.82	4
Fe	344.10	1.24×10^{07}	3.65	7
Mg	285.21	4.91×10^{08}	4.34	3
Ag	338.28	1.30×10^{08}	3.66	2
S	180.73	3.27×10^{08}	6.86	3
Zn	330.26	1.20×10^{08}	7.78	5

3. Results and discussion

3.1 Signal enhancement

3.1.1 Effect of Microwave power and time delay on plasma temperature

To understand the role of microwave power in signal enhancement, plasma temperature with and without microwave were investigated in this research. This study was carried out with a non-gated portable spectrometer. Determining plasma temperature is important because plasma temperature is one of the major key factors for signal enhancement. The signal enhancement is the ratio of the signals from MW-LIBS and LIBS. Plasma temperature measurement was measured using two different elements, lead and calcium. Lead and calcium have many strong atomic lines with variety of UEL. These two elements were chosen to verify the plasma temperature. The atomic database is presented in Table 1. Plasma temperature may be calculated using Boltzmann plot. Figure 2 is the typical example of plasma temperature measurement at 5 mJ laser energy and 600 W microwave power as marked red circle in Figure 3 (b). The strong lines of Pb I 280.2 nm, Pb I 287.3 nm, Pb I 363.95 nm, and Pb I 368.35 nm were applied to determine plasma temperature. Figure 3 depicts the effects of microwave power on plasma temperature.

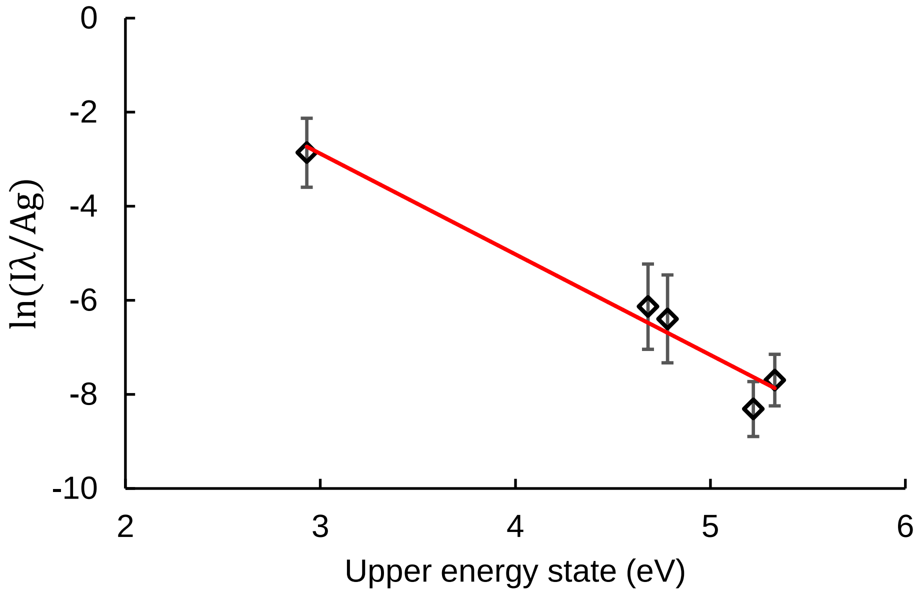

Figure 2: Boltzmann plot made from Ca I lines at 5 mJ laser energy, 600 W microwave power, 1ns gate-delay and 1000µs gate-width using a gated spectrometer.

It is observed from Figure 3(a) that plasma temperature is largely dependent on laser energy. Plasma temperatures calculated at 5 mJ, 7 mJ and 10 mJ were 13087 K and 13408 K and 14001 K, respectively. Plasma temperature at zero microwave power provides higher value than with microwave. Microwave radiation leads to an enhancement in plasma duration due to large integration time. The plasma lifetime from LIBS is in fact very short. As soon as the plasma

wanes, the MW provides motion energy to the free electrons and this enhances the plasma lifetime. Microwave radiation does not only increase its lifetime but also plasma size.
It has been observed that the plasma temperature for MW-LIBS is almost constant at ~6400 K. Also, note that as the plasma becomes larger, it affects the plasma temperature and electron density. So may be at high microwave power (900 Watt), plasma temperature declines slightly because of the larger plasma. The plasma size as a function of microwave power was published by Iqbal et al.[42, 44]. This result is supported by other research conducted by Khumaeni et al.[11]. The average plasma temperature calculated with LIBS is about 13500 K and with MW-LIBS is 6400 K.

Similar results were found when experimenting with a conventional gated spectrometer as shown in Figure 3(b). This time, strong Ca I lines were considered. In Figure 3(b), LTE square represents the electron density level, which meets the McWhirter criterion. The electron density was determined using the FWHM of strong Ca I line at 422.67 nm and ω of Ca I at 422.67 nm was derived from literature [45]. The value of ω considered in this study was 0.1169 ×10^{-6} nm. The instrumental broadening was determined to be 0.0321 nm by recoding the Hg line at 253.6 nm. The value of $\Delta\lambda_{1/2}$ was evaluated using a simple equation [46],

$$\Delta\lambda_{\text{Total}} = \Delta\lambda_{\text{line}} + \Delta\lambda_{\text{spectrometer}}$$

To understand if the plasma is at local thermodynamically equilibrium (LTE), the McWhirter criterion was calculated using equation (1) [47].

$$N_e \geq 1.6 \times 10^{12} \Delta E^3 T_e^{\frac{1}{2}} \ldots\ldots\ldots\ldots\ldots\ldots\ldots\ldots\ldots..(1)$$

Where ΔE (eV) is the largest observed transition energy for which the condition holds, and T_e, is the excitation temperature (K)

It is interesting to note that microwave power caused an increase in electron density until a certain level was reached, which confirmed that an increase in microwave power could improve emission intensity. The microwave power increase can cause more motion energy to the free electrons and make stronger plasma, which subsequently helps to increase the emission intensity.

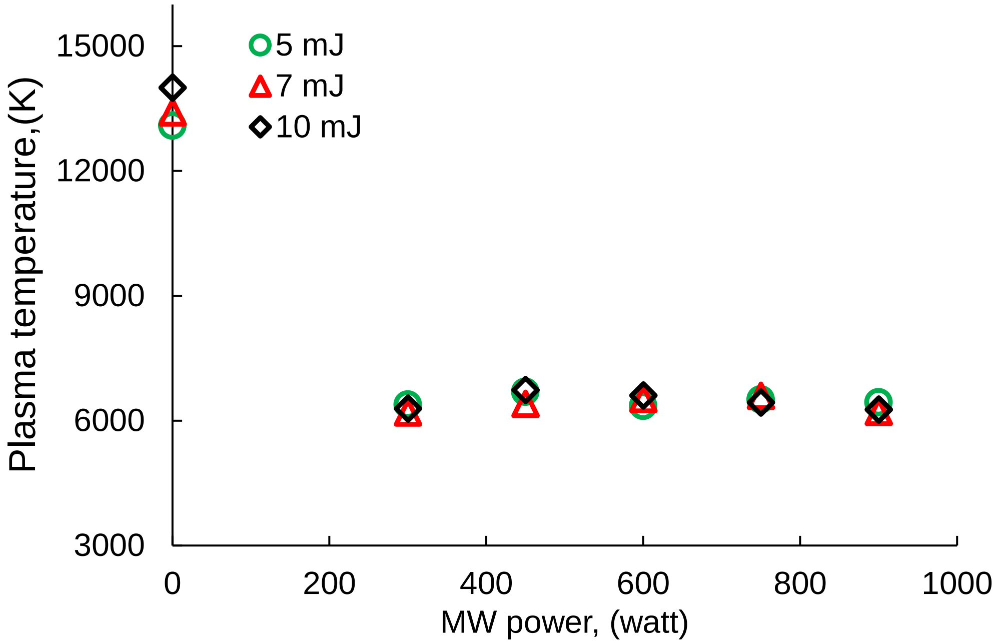

Figure 3(a). Plasma temperature dependence on microwave power of MW-LIBS at 2.5 ms microwave pulse duration and 8 ms integration time with accumulation of 50 single shots using Pb I lines. This experiment was conducted with a non-gated spectrometer.

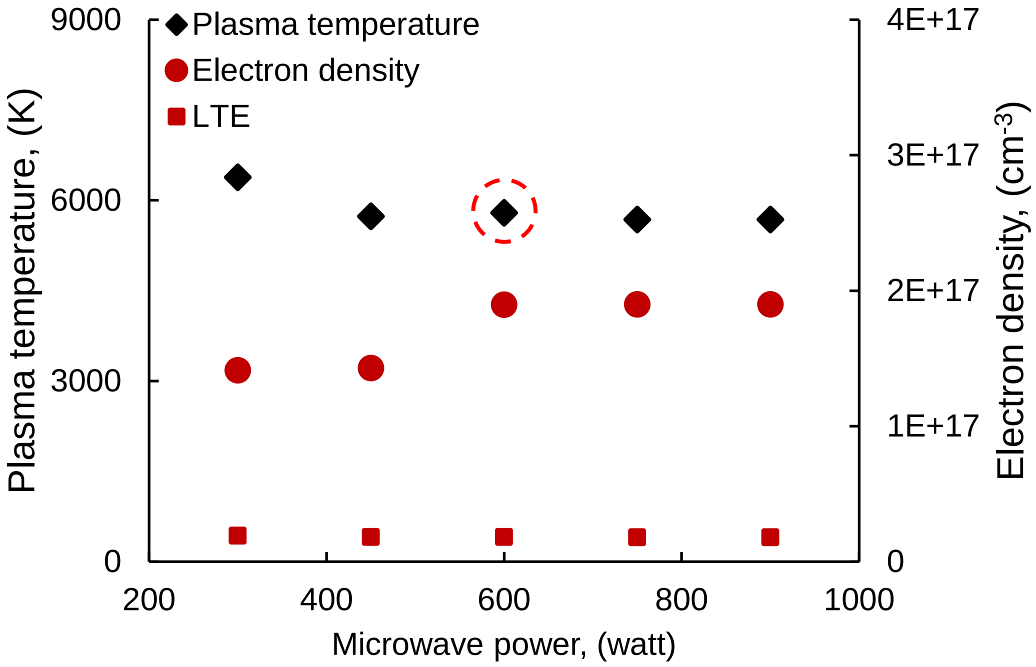

Figure 3(b). Plasma temperature and electron density dependence on microwave power of MW-LIBS at 5mJ laser energy, 1 ns gate-delay, 1000 µs gate-width with accumulation of 50 using Ca I lines. This experiment was conducted with gated spectrometer.

Since the small spectrometer consisted of a fixed gate-delay and long integration time, the experiments was conducted with a gated spectrometer to demonstrate the effects of time-delay on plasma temperature. In this case, the Ca-containing sample ($CaCl_2$ powder) was used because Ca I has many strong lines as shown in Table 1. Figure 4 shows the effect of gate-delay on plasma temperature. It can be seen from Figure 4 that the plasma temperature was initially high and then after 50 µs gate-delay, the plasma temperature dropped significantly. After 100 µs, plasma temperature was virtually stable until 800 µs except at 350 µs. It is predicted that the variation is due to the coupling effect of the microwave with LIBS plasma. It is predicted that the microwave starts coupling in the 0 to 50 µs range and becomes stable at around 100 µs. This is supported by the electron density calculation in Figure 4 because microwave power cannot couple with high electron density containing LIBS plasma until the electron density drops to a critical value. The critical electron density has been calculated as $1.9x10^{17}$ cm^{-3} for laser energy and microwave power of 5mJ and 600 Watt, respectively. However, the average temperature calculated during delay variation with 50 µs gate-width was 6000 K, where a long gate-width of 1 ms resulted in 6800 K. Figure 3(b) deals with the effect of microwave power on plasma temperature where Figure 4 deals with the effect of time delay on plasma temperature. Figure 3(b) was an independent study than Figure 4.

Figure 4 shows that the plasma temperature is independent of time and there is no reheating of the plasma due to of microwave coupling. The Microwave can only increase the lifetime of emission intensity as shown in this figure.

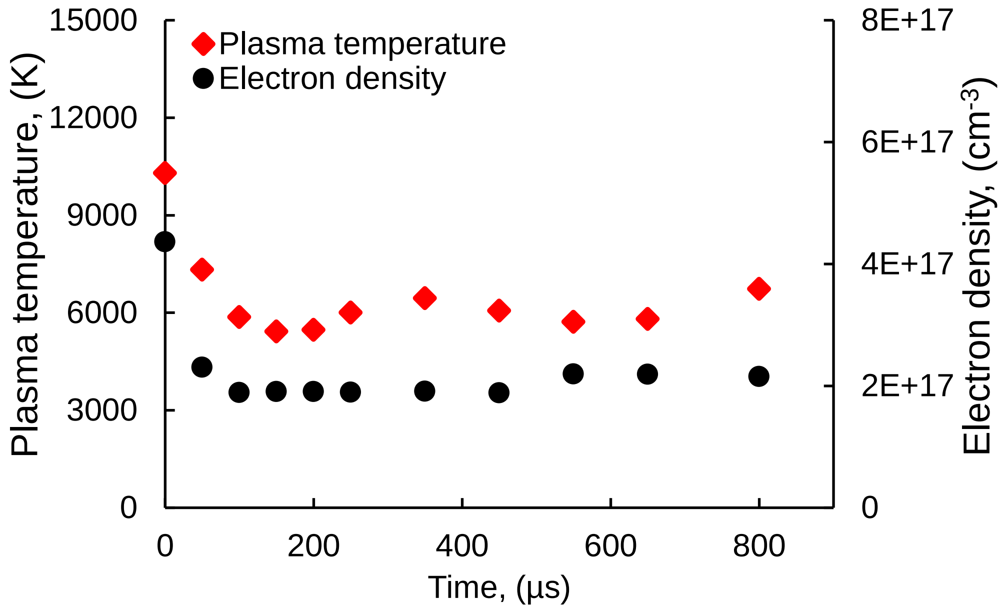

Figure 4. Plasma temperature and electron density dependence on time at 4mJ laser energy, 600 W microwave power, 50 µs gate width, 1.5 microwave pulse duration with accumulation of 25 single shots using Ca I lines. This experiment was conducted with a gated spectrometer.

3.1.2 Effect of upper energy level (UEL) and detector gain on SNR improvement

The second important variable that affected the signal enhancement is the value of UEL if the plasma temperature becomes constant. It was demonstrated in section 3.1.1 that the plasma temperature is independent on the microwave power. Figure 5 shows four distinguished emission lines, with different UEL of lead (Pb I). These lines were considered because, within these four-wavelength regions, there was no contamination with other lines as indicated in Table 1. Figure 5 shows Pb I signal enhancement for four different UEL. It is evident from Figure 5 there is a sharp increase in signal enhancement at a low energy level (4.33 eV) but enhancement at a high energy level (5.74 eV) is very small for the same operating conditions. The increased in the microwave power yields no signal enhancement based on lines with high-energy upper level. A similar analysis was done with other elements, namely Ag, Fe, Cu, Pb, Mg and, having different UEL as shown in Figure 6. Figure 6 depicts a linear relationship between ln (SNR improvement) and upper energy state.

Using Figure 6, a prediction model has been developed for SNR improvement as made possible by equation (2) written here:

$$SNR\ Improvement = 810 \pm 100e^{-(1.01\pm0.06)E_k} \ldots\ldots\ldots\ldots\ldots (2)$$

Where, SNR improvement is the ratio of SNR with MW-LIBS and the SNR with LIBS only, E_k is the upper state energy level of the element in eV. Equation 4 predicts that potassium (K), with eK= 1.62 eV, has the maximum SNR improvement of 150±4 times. On the other end of the energy level, Equation 4 predicts minimum SNR improvement is for carbon C, namely 0.79 times. It is clear that for elements with higher upper energy >7 eV such as chlorine (Cl), fluorine (F), bromine (B), and iodine (I), there will be no signal enhancement using MW-LIBS. The cut-off limit of enhancement in terms of upper state energy level is found to be ~7eV. The recoded MW-LIBS plasma temperature of ~6000K is reason for this cut-off.

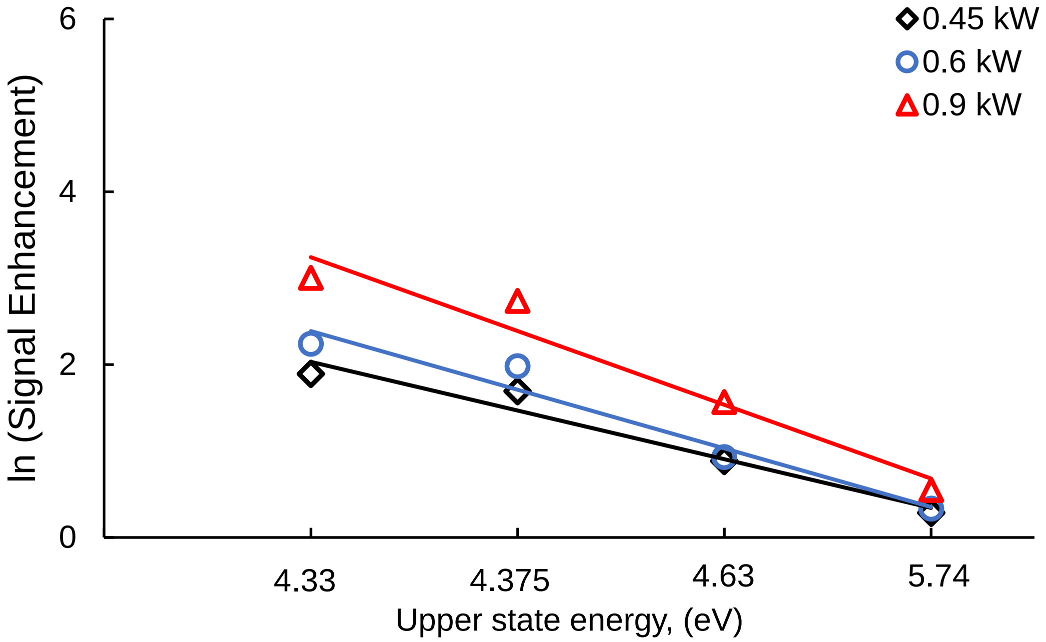

Figure 5. Signal enhancement of sample OREAS 351 for Pb at 7 mJ laser energy, 2.5 ms microwave pulse duration and 8 ms integration time with accumulation of 60 single shots. This experiment was conducted with non-gated spectrometer.

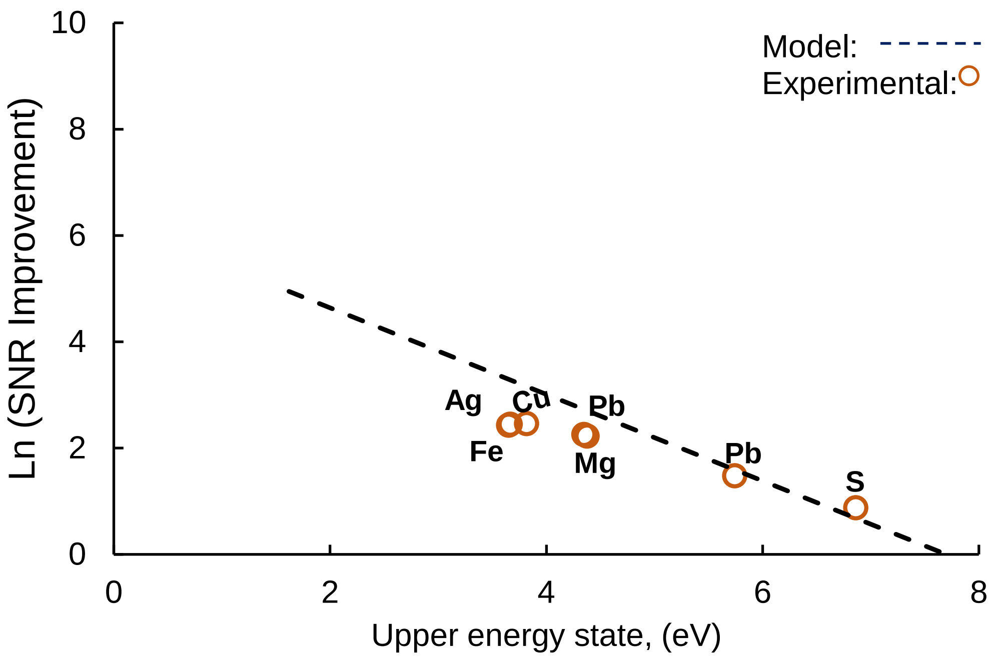

Figure 6. ln of SNR improvement against upper energy state of sample OREAS 351 for different element at 5 mJ laser energy, 2.5 ms microwave pulse duration and 8 ms integration time with accumulation of 60 single shots. This experiment was conducted with non-gated spectrometer.

To check the effect of the detector gain, the maximum SNR improvement, the same experiment was conducted with a gated spectrometer having ICCD as shown in Figure 7. Experimental conditions and samples were the same. Plasma temperature was measured using lead lines. Figure 7 shows that the detector gain of 50 wields a significant impact on SNR improvement. Figure 7 was determined using all the lines listed in Table 1 without a sulphur line due to the spectrometer’s wavelength limitation.

It was observed that SNR improvement could be increased ~3.5 times more with detector gain than without using detector gain. Using the prediction model, the SNR improvement for any element, based on their strongest transition, has been predicted. Figure 8 shows a typical example of projected SNR improvement for the elements in the periodical table with and without detector gain using equation (3) and (4). Using equation (4), it has been calculated that the SNR improvement of potassium can be improve to 530±15 times by increasing detector gain. In the periodic table, some elements such as Ca, Mg, Cu, Ru, Fe, Ag, In, Pb and S (bold red mark in the figure 8) have been demonstrated experimentally in our lab, which achieved similar SNR improvement as data from prediction model. Few data have been published elsewhere already [12, 13, 19].

$$SNR\ Improvement = (810 \pm 100)e^{-(1.01 \pm 0.06)E_k} \dots\dots\dots\dots\dots (3)$$

$$SNR\ Improvement_{With\ gain} = (2745.9 \pm 339)e^{-(1.01 \pm 0.06)E_k} \dots\dots\dots\dots\dots (4)$$

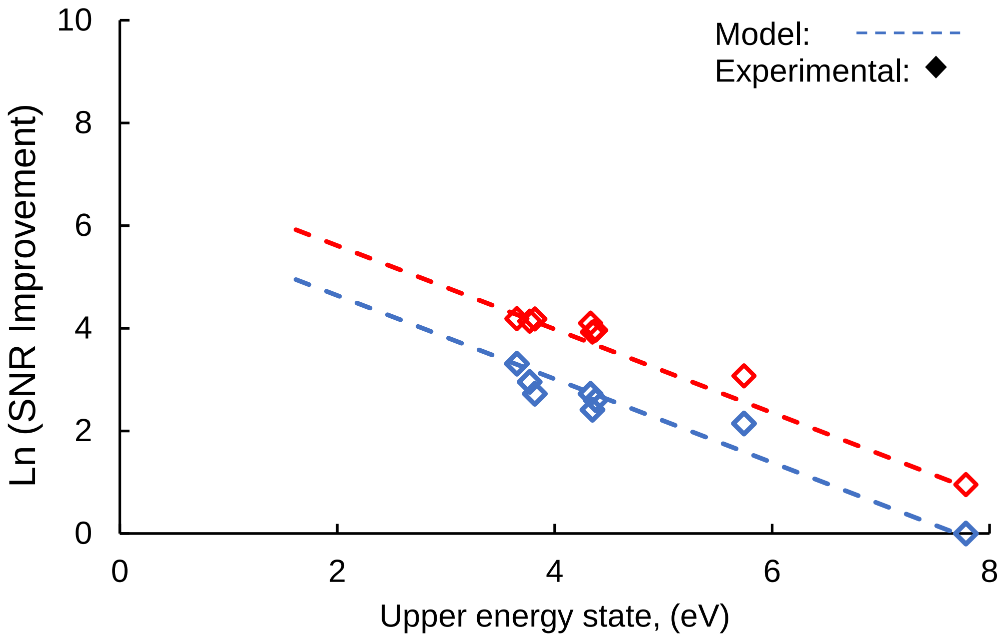

Figure 7. ln of SNR improvement against upper energy state of sample OREAS 351, with gain (red circle) and without gain (blue circle), of different element at 5 mJ laser energy, 750 W microwave power, 0.1 ns gate-delay, 1 ms gate-width with accumulation of 50 single shots.

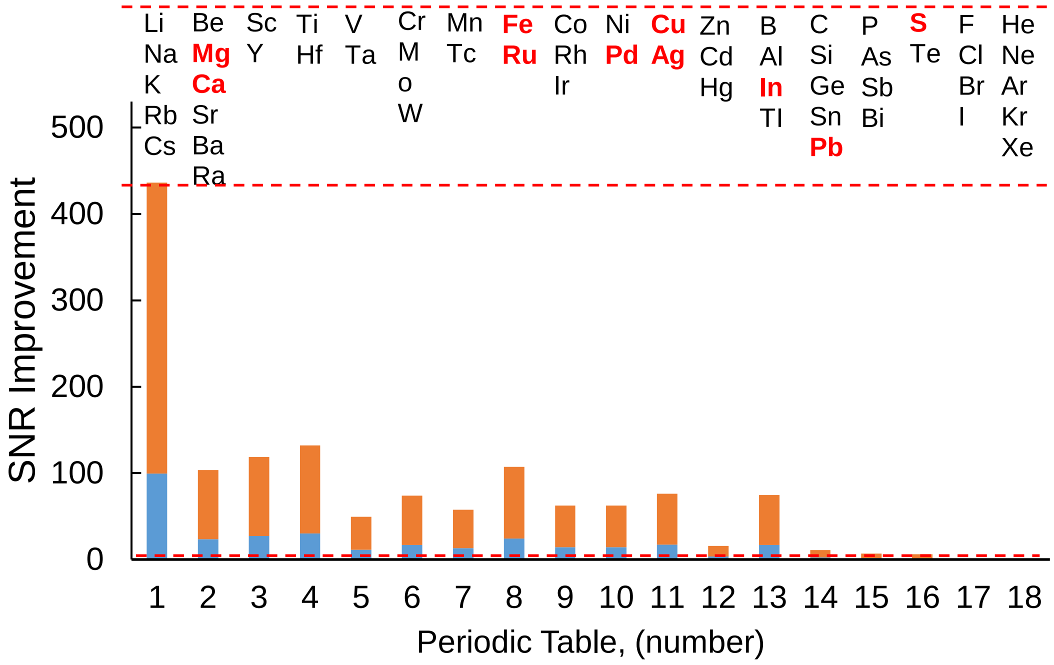

Figure 8. Typical example of projected SNR improvement for elements in periodic table, without detector gain (blue), with detector gain (orange).

3.2 Sulphur detection

3.2.1 Spectral information and enhancement

Spectral emissions in the 180-230 nm range were recorded in LIBS with and without microwave using a portable spectrometer without ICCD as shown in Figure 9 (a). In this study, the strong line of sulphur at 180.73 nm, namely $^3S_0$, J=1→ ^3P, J=2, was selected. The other sulphur line at 182.03 nm was not considered due to its comparatively poor transition strength. The spectra in Figure 9 (a) reveal no significant improvement in the sulphur signal. This validates the signal enhancement behaviour with reference to upper energy state. The upper energy state of sulphur at 180.73 nm is 6.86 eV. Figure 9 (b) shows the variation in sulphur signal when sulphur is in different concentrations.

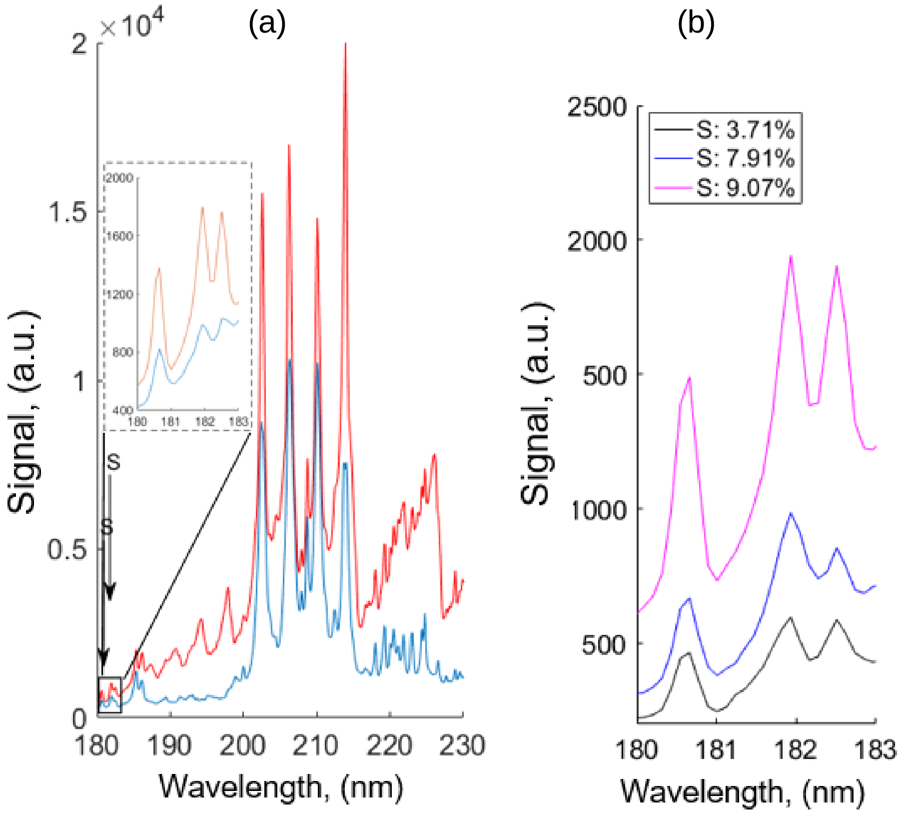

Figure 9: Spectra of ore samples (a) with LIBS, blue and MW-LIBS, red recorded at 10 mJ/pulse and 0.75 kW microwave power. The spectra of Sulphur of varying concentration with MW-LIBS also recorded in (b). The spectra were accumulated over 100 laser shots with microwave pulse duration 2.5 ms and integration time 8 ms.

3.2.2 Effect of Microwave power on Sulphur Signal and enhancement

The dependence of the MW-LIBS signal intensity on MW power at different laser energies was investigated. The effect of microwave power on signal-to-noise ratio (SNR) for sulphur is presented in Figure 10. As shown in Figure 10, the SNR with MW-LIBS was higher than in LIBS. This is due increasing the sampling time. The external energy supplied, using the microwave radiation, sustains the free electrons present in the laser induced plasma. These reenergised free electrons act as an excitation source via collisional processes, leading to a longer lifetime [13, 48]. It is evident from Figure 10 that an increase in microwave power does not raise the signal-to-noise ratio significantly, because the increase in microwave power causes a higher noise level with the signal [44]. It is worth noting that the noise level and the data processing was evaluated using the same procedure as our recent published paper [41]. The laser energy does exert an impact on SNR as shown in Figure 10. When the laser energy increases the signal-to-noise ratio also increases. From Figure 10, the best signal-to-noise ratio was 0.45 kW for 5 mJ laser energy. Similarly, this ratio existed at 0.6 kW for 7 mJ and 0.75 kW for 10 mJ, respectively. The SNR improvement is shown in Figure 11 (a). It is important to note that the microwave power does not increase the SNR significantly. Figure 11 (b) shows that the signal enhancement is about double that of sulphur. This confirmed outcome is due to higher UEL (6.86 eV) of sulphur at 180.73 nm, which has been discussed in the previous section.

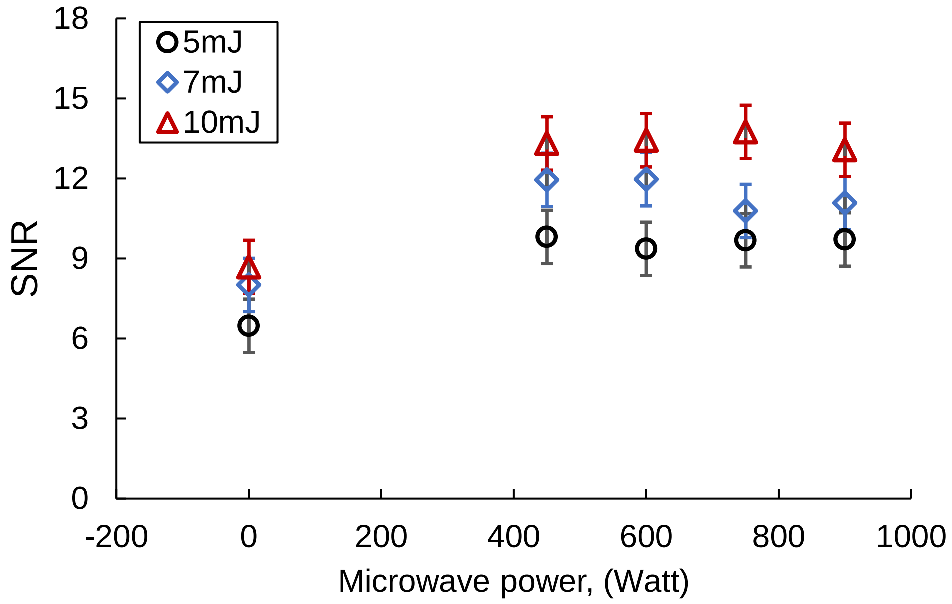

Figure 10. Signal to noise ratio of 9.07 % Sulfur content sample for three different laser powers, at 2.5 ms microwave pulse duration and 8 ms integration time with accumulation of 100 single shots. This experiment was conducted with non-gated spectrometer.

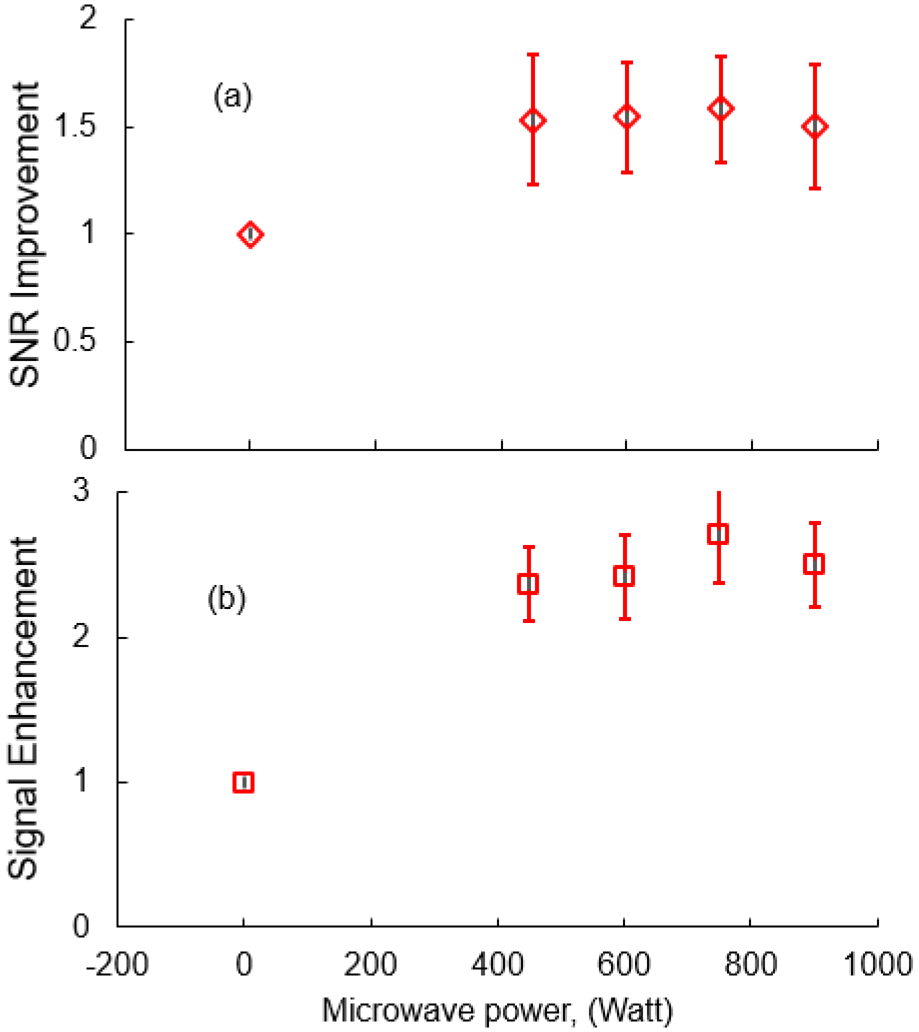

Figure 11. Sulfur SNR improvement, a and signal enhancement, b of 9.07 % Sulfur content sample at 10 mJ laser energy, 2.5 ms microwave pulse duration and 8 ms integration time with accumulation of 100 single shots. This experiment was done with non-gated spectrometer.

3.2.3 Quantitative detection of Sulphur

Calibration curves were produced for LIBS and MW-LIBS using the prepared ore samples. This study concentrated on sulphur detection in solid phase. For plotting the calibration curve, the experimental parameters were 0.6 kW for 7 mJ and 0.75 kW for 10 mJ at 2.5 ms microwave pulse duration and 100 shots serving as the spectral accumulation. Figure 12 shows the calibration curve at 10 mJ laser energy. LoD was calculated with the most usable 3-sigma method [49, 50]. It was observed that MW-LIBS did not help in increasing the signal enhancement for the 180.73 nm line, due to high upper energy as discussed previously. The LoD of sulphur obtained with MW-LIBS at 7 mJ and 10 mJ were 476 µg/g and 312 µg/g, respectively. The LoD with LIBS were only 525 µg/g and 400 µg/g for 7 mJ and 10 mJ, respectively. The experimental study was carried out in an atmospheric environment. Since this study has been conducted in an atmospheric environment, its results have been compared with other analyses undertaken in this kind of environment. Table 2 represents the LoD of sulphur in solid phase documented in a previous study and our current study. The difference between this study and prior ones is that the application of low laser energy can be done in an atmospheric environment and a portable small spectrometer without having ICCD. The application of low laser energy results in the sample remaining undamaged after the experiment.

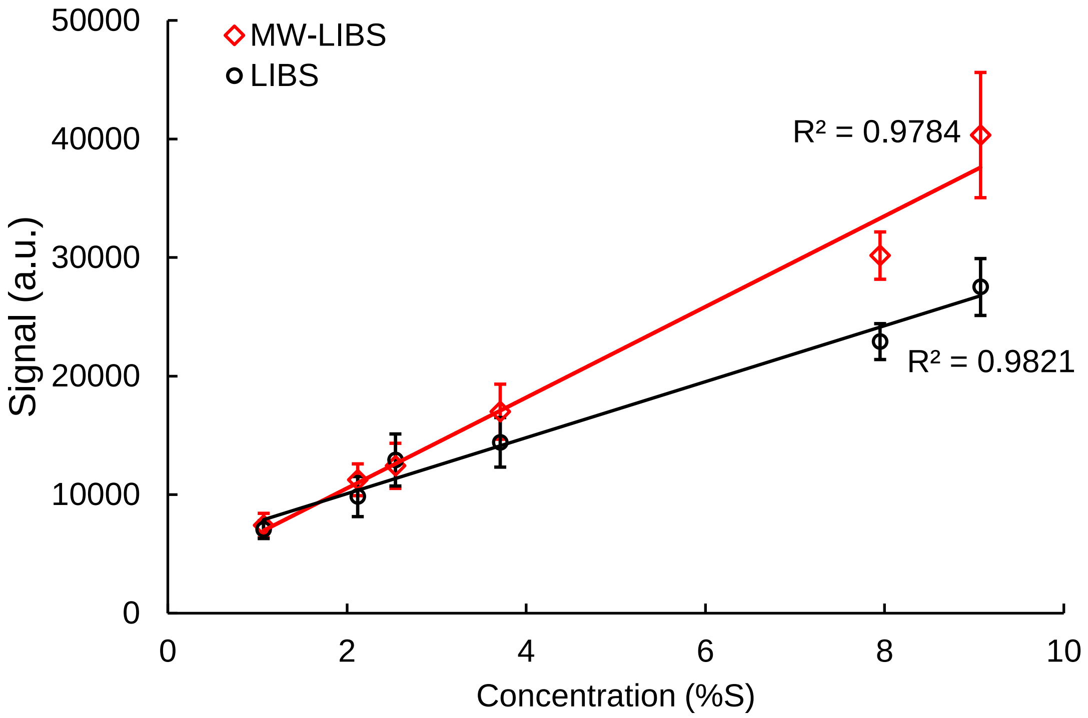

Figure 12. Calibration curve of Sulfur with LIBS, black and MW-LIBS, red at 10 mJ laser energy, 2.5 ms microwave pulse duration and 8 ms integration time with accumulation of 100 single shots. This experiment was done with non-gated spectrometer.

Table 2: Limit of detection from previous and current work

Method	**Laser Power (mJ)**	**Additional gas**	**Detection device**	**LoD**	**Reference**
LIBS	20	Helium	CCD	0.12%	[32]
	38	Helium	ICCD	0.20%	[22]
	25	Atmospheric	Photodiode	0.60%	[51]
Double pulse	55	Atmospheric	CCD	0.15%	[35]
MW-LIBS	7	Atmospheric	CCD	0.048%	This work
MW-LIBS	10	Atmospheric	//	0.031%	//

4. Conclusion

Signal enhancement behaviour for atomic detection is demonstrated using the MW-LIBS technique. It is observed that the upper state energy level of any element plays a significant role in signal enhancement. Significant enhancement is possible for the element containing a upper energy state below 5eV but is unable to enhance elements containing higher upper energy (>7 eV) such as chlorine, bromine, fluorine, iodine, etc. This study reports that signal enhancement can be improved by increasing a gated spectrometer's detector gain. A simple enhancement model is developed based on the experimental data. The projected SNR improvement of elements in the periodic table has been reported with and without detector gain. Potassium is predicted to be the best element with highest SNR improvement while carbon is the poorest. It is also observed that the plasma temperature remains quite stable over time and microwave has no reheating impact on the LIBS plasma. Sulphur detection in ore solid sample was conducted with MW-LIBS to validate the model. Spectral wavelength considered for this study was in the ultraviolet region at 180.73 nm using a portable spectrometer without having ICCD at low laser energy. The signal enhancement for sulphur achieved was ~ 2-fold with MW-LIBS and not LIBS. The LoD reported for sulphur with MW-LIBS was 312 µg/g, which improved LoD 1.4-fold than with LIBS. Consequently, MW-LIBS is a promising technique and emerges as a sound choice for improved detection limit for elements having a low upper energy state.

Reference

[1] V.S. Burakov, N.V. Tarasenko, M.I. Nedelko, V.A. Kononov, N.N. Vasilev, S.N. Isakov, Analysis of lead and sulfur in environmental samples by double pulse laser induced breakdown spectroscopy, Spectrochimica Acta Part B: Atomic Spectroscopy, 64 (2009) 141-146.

[2] R.W. Septianti, W.S. Budi, H. Sugito, A. Khumaeni, Rapid detection of the authenticity of silver jewelry by laser induced shockwave plasma spectroscopy using Nd:YAG laser 1064 nm, in: B. Warsito, S.P. Putro, A. Khumaeni (Eds.) 7th International Seminar on New Paradigm and Innovation on Natural Science and Its Application, Iop Publishing Ltd, Bristol, 2018.

[3] X.K. Shen, H. Wang, Z.Q. Xie, Y. Gao, H. Ling, Y.F. Lu, Detection of trace phosphorus in steel using laser-induced breakdown spectroscopy combined with laser-induced fluorescence, Applied Optics, 48 (2009) 2551-2558.

[4] L.B. Guo, Z.H. Zhu, J.M. Li, Y. Tang, S.S. Tang, Z.Q. Hao, X.Y. Li, Y.F. Lu, X.Y. Zeng, Determination of boron with molecular emission using laser-induced breakdown spectroscopy combined with laser-induced radical fluorescence, Opt. Express, 26 (2018) 2634-2642.

[5] A. Seifalinezhad, M. Bahreini, M.M.H. Matin, S.H. Tavassoli, Feasibility Study on Discrimination of Neo-plastic and Non-Neoplastic Gastric Tissues Using Spark Discharge Assisted Laser Induced Breakdown Spectroscopy, J. Lasers Med. Sci., 10 (2019) 64-69.

[6] S. Zhao, C. Song, X. Gao, J. Lin, Quantitative analysis of Pb in soil by femtosecond-nanosecond double-pulse laser-induced breakdown spectroscopy, Results in Physics, 15 (2019) 102736.

[7] Y. Jiang, R. Li, Y. Chen, Elemental analysis of copper alloys with laser-ablation spark-induced breakdown spectroscopy based on a fiber laser operated at 30 kHz pulse repetition rate, J. Anal. At. Spectrom., 34 (2019) 1838-1845.

[8] A. Khachatrian, P.J. Dagdigian, Laser-induced breakdown spectroscopy with laser irradiation resonant with vibrational transitions, Applied Optics, 49 (2010) C1-C7.

[9] A.J.R. Hunter, L.G. Piper, Spark-induced breakdown spectroscopy: a description of an electrically generated LIBS-like process for elemental analysis of airborne particulates and solid samples, in: A.W. Miziolek, I. Schechter, V. Palleschi (Eds.) Laser Induced Breakdown Spectroscopy, Cambridge University Press, Cambridge, 2006, pp. 585-614.

[10] M. Dell'Aglio, R. Alrifai, A. De Giacomo, Nanoparticle Enhanced Laser Induced Breakdown Spectroscopy (NELIBS), a first review, Spectrochimica Acta Part B: Atomic Spectroscopy, 148 (2018) 105-112.

[11] A. Khumaeni, K. Akaoka, M. Miyabe, I. Wakaida, The role of microwaves in the enhancement of laser-induced plasma emission, Frontiers of Physics, 11 (2016) 114209.

[12] J. Viljanen, Z. Sun, Z.T. Alwahabi, Microwave assisted laser-induced breakdown spectroscopy at ambient conditions, Spectrochimica Acta Part B: Atomic Spectroscopy, 118 (2016) 29-36.

[13] M. Wall, Z.W. Sun, Z.T. Alwahabi, Quantitative detection of metallic traces in water-based liquids by microwave-assisted laser-induced breakdown spectroscopy, Opt. Express, 24 (2016) 1507-1517.

[14] Y.A. Liu, M. Baudelet, M. Richardson, Elemental analysis by microwave-assisted laser-induced breakdown spectroscopy: Evaluation on ceramics, J. Anal. At. Spectrom., 25 (2010) 1316-1323.

[15] Y. Ikeda, R. Tsuruoka, Characteristics of microwave plasma induced by lasers and sparks, Applied Optics, 51 (2012) B183-B191.

[16] Y. Tang, J. Li, Z. Hao, S. Tang, Z. Zhu, L. Guo, X. Li, X. Zeng, J. Duan, Y. Lu, Multielemental self-absorption reduction in laser-induced breakdown spectroscopy by using microwave-assisted excitation, Opt. Express, 26 (2018) 12121-12130.

[17] M. Tampo, M. Miyabe, K. Akaoka, M. Oba, H. Ohba, Y. Maruyama, I. Wakaida, Enhancement of intensity in microwave-assisted laser-induced breakdown spectroscopy for remote analysis of nuclear fuel recycling, J. Anal. At. Spectrom., 29 (2014) 886-892.

[18] A. Khumaeni, M. Miyabe, K. Akaoka, I. Wakaida, The effect of ambient gas on measurements with microwave-assisted laser-induced plasmas in MA-LIBS with relevance for the analysis of nuclear fuel, Journal of Radioanalytical and Nuclear Chemistry, 311 (2017) 77-84.

[19] A.A. Al Shuaili, A.M. Al Hadhrami, M.A. Wakil, Z.T. Alwahabi, Improvement of palladium limit of detection by microwave-assisted laser induced breakdown spectroscopy, Spectrochimica Acta Part B: Atomic Spectroscopy, 159 (2019) 105666.

[20] S. Wu, T. Zhang, H. Tang, K. Wang, X. Yang, H. Li, Quantitative analysis of nonmetal elements in steel using laser-induced breakdown spectroscopy combined with random forest, Analytical Methods, 7 (2015) 2425-2432.

[21] M.A. Gondal, A. Dastageer, M. Maslehuddin, A.J. Alnehmi, O.S.B. Al-Amoudi, Detection of sulfur in the reinforced concrete structures using a dual pulsed LIBS system, Optics & Laser Technology, 44 (2012) 566-571.

[22] F. Trichard, V. Forquet, N. Gilon, C.P. Lienemann, F. Baco-Antoniali, Detection and quantification of sulfur in oil products by laser-induced breakdown spectroscopy for on-line analysis, Spectrochimica Acta Part B: Atomic Spectroscopy, 118 (2016) 72-80.

[23] H. Liu, C. Wang, C. Zou, Y. Zhang, J. Wang, Simultaneous volatilization characteristics of arsenic and sulfur during isothermal coal combustion, Fuel, 203 (2017) 152-161.

[24] L. Peter, V. Sturm, R. Noll, Liquid steel analysis with laser-induced breakdown spectrometry in the vacuum ultraviolet, Applied Optics, 42 (2003) 6199-6204.

[25] F. Weritz, S. Ryahi, D. Schaurich, A. Taffe, G. Wilsch, Quantitative determination of sulfur content in concrete with laser-induced breakdown spectroscopy, Spectrochimica Acta Part B: Atomic Spectroscopy, 60 (2005) 1121-1131.

[26] F. Ma, D. Dong, A Measurement Method on Pesticide Residues of Apple Surface Based on Laser-Induced Breakdown Spectroscopy, Food Analytical Methods, 7 (2014) 1858-1865.

[27] F. Weritz, D. Schaurich, A. Taffe, G. Wilsch, Effect of heterogeneity on the quantitative determination of trace elements in concrete, Anal. Bioanal. Chem., 385 (2006) 248-255.

[28] M.A. Khater, Trace detection of light elements by laser-induced breakdown spectroscopy (LIBS): Applications to non-conducting materials, Optics and Spectroscopy, 115 (2013) 574-590.

[29] M.H. Nunez, P. Cavalli, G. Petrucci, N. Omenetto, Analysis of sulfuric acid aerosols by laser-induced breakdown spectroscopy and laser-induced photofragmentation, Applied Spectroscopy, 54 (2000) 1805-1816.

[30] J. Jasik, J. Heitz, J.D. Pedarnig, P. Veis, Vacuum ultraviolet laser-induced breakdown spectroscopy analysis of polymers, Spectroc. Acta Pt. B-Atom. Spectr., 64 (2009) 1128-1134.

[31] I. Radivojevic, C. Haisch, R. Niessner, S. Florek, H. Becker-Ross, U. Panne, Microanalysis by laser-induced plasma spectroscopy in the vacuum ultraviolet, Anal. Chem., 76 (2004) 1648-1656.

[32] Y. Lee, J. Chirinos, J. Gonzalez, D. Oropeza, V. Zorba, X. Mao, J. Yoo, R.E. Russo, Laser-Ablation Sampling for Accurate Analysis of Sulfur in Edible Salts, Applied Spectroscopy, 71 (2017) 651-658.

[33] A. Hrdlička, J. Hegrová, K. Novotný, V. Kanický, D. Prochazka, J. Novotný, P. Modlitbová, L. Sládková, P. Pořízka, J. Kaiser, Sulfur determination in concrete samples using laser-induced breakdown spectroscopy and limestone standards, Spectrochimica Acta Part B: Atomic Spectroscopy, 142 (2018) 8-13.

[34] S. Trautner, J. Lackner, W. Spendelhofer, N. Huber, J.D. Pedarnig, Quantification of the Vulcanizing System of Rubber in Industrial Tire Rubber Production by Laser-Induced Breakdown Spectroscopy (LIBS), Anal. Chem., 91 (2019) 5200-5206.

[35] T.A. Labutin, A.M. Popov, S.N. Raikov, S.M. Zaytsev, N.A. Labutina, N.B. Zorov, Determination of chlorine in concrete by laser-induced breakdown spectroscopy in air, Journal of Applied Spectroscopy, 80 (2013) 315-318.

[36] Q.D. Zeng, L.B. Guo, X.Y. Li, M. Shen, Y.N. Zhu, J.M. Li, X.Y. Yang, K.H. Li, J. Duan, X.Y. Zeng, Y.F. Lu, Quantitative analyses of Mn, V, and Si elements in steels using a portable laser-induced breakdown spectroscopy system based on a fiber laser, J. Anal. At. Spectrom., 31 (2016) 767-772.

[37] F. Ammari, L. Bassel, C. Ferrier, D. Lacanette, R. Chapoulie, B. Bousquet, Multi-block analysis coupled to laser-induced breakdown spectroscopy for sorting geological materials from caves, Talanta, 159 (2016) 287-291.

[38] L. Gómez-Nubla, J. Aramendia, S. Fdez-Ortiz de Vallejuelo, J.M. Madariaga, Analytical methodology to elemental quantification of weathered terrestrial analogues to meteorites using a portable Laser-Induced Breakdown Spectroscopy (LIBS) instrument and Partial Least Squares (PLS) as multivariate calibration technique, Microchemical Journal, 137 (2018) 392-401.

[39] P. Siozos, A. Philippidis, D. Anglos, Portable laser-induced breakdown spectroscopy/diffuse reflectance hybrid spectrometer for analysis of inorganic pigments, Spectrochimica Acta Part B: Atomic Spectroscopy, 137 (2017) 93-100.

[40] M. Bahreini, B. Ashrafkhani, S.H. Tavassoli, Elemental analysis of fingernail of alcoholic and doping subjects by laser-induced breakdown spectroscopy, Applied Physics B, 114 (2014) 439-447.

[41] M.A. Wakil, Z.T. Alwahabi, Microwave-assisted laser induced breakdown molecular spectroscopy: quantitative chlorine detection, J. Anal. At. Spectrom., 34 (2019) 1892-1899.

[42] A. Iqbal, Z. Sun, M. Wall, Z.T. Alwahabi, Sensitive elemental detection using microwave-assisted laser-induced breakdown imaging, Spectrochimica Acta Part B: Atomic Spectroscopy, 136 (2017) 16-22.

[43] J. Reader, C.H. Corliss, W.L. Wiese, G.A. Martin, Wavelengths and transition probabilities for atoms and atomic ions : part I. wavelengths - part II. transition probabilities, National Bureau of Standards, NSRDS; NISTresearchlibrary; fedlink; americana, 1980.

[44] S.J. Chen, A. Iqbal, M. Wall, C. Fumeaux, Z.T. Alwahabi, Design and application of near-field applicators for efficient microwave-assisted laser-induced breakdown spectroscopy, J. Anal. At. Spectrom., 32 (2017) 1508-1518.

[45] M.S. Dimitrijevic, S. Sahal-Brechot, Stark Broadening Parameter Tables for Neutral Calcium Spectral Lines. I, Serbian Astronomical Journal, 161 (2000) 39.

[46] V.N. Rai, S.N. Thakur, Chapter 4 - Physics of Plasma in Laser-Induced Breakdown Spectroscopy, in: J.P. Singh, S.N. Thakur (Eds.) Laser-Induced Breakdown Spectroscopy, Elsevier, Amsterdam, 2007, pp. 83-111.

[47] R.W.P. McWhirter, Plasma Diagnostic Techniques. Edited by Richard H. Huddlestone and Stanley L. Leonard. Library of Congress Catalog Card Number 65-22763. Published by Academic Press, New York, (1965) 201.

[48] Y. Liu, B. Bousquet, M. Baudelet, M. Richardson, Improvement of the sensitivity for the measurement of copper concentrations in soil by microwave-assisted laser-induced breakdown spectroscopy, Spectrochimica Acta Part B: Atomic Spectroscopy, 73 (2012) 89-92.

[49] S. Rosenwasser, G. Asimellis, B. Bromley, R. Hazlett, J. Martin, T. Pearce, A. Zigler, Development of a method for automated quantitative analysis of ores using LIBS, Spectrochimica Acta Part B: Atomic Spectroscopy, 56 (2001) 707-714.

[50] D.W. Hahn, N. Omenetto, Laser-induced breakdown spectroscopy (LIBS), part II: review of instrumental and methodological approaches to material analysis and applications to different fields, Applied spectroscopy, 66 (2012) 347-419.

[51] D. Gagnon, S. Lessard, M. Verhaegen, P. Mutchmore, P. Bouchard, F.R. Doucet, M. Sabsabi, Multiband sensor using thick holographic gratings for sulfur detection by laser-induced breakdown spectroscopy, Applied Optics, 51 (2012) B7-B12.

Chapter 8

In Situ Measurement of Potassium Release during Biomass Combustion Using Laser-Induced Breakdown Spectroscopy: Effect of Silicate on Potassium Release

Haibo Zhao[a,†], M.A. Wakil[b,†], Jan Viljanen[c], Qiang Song[a,*], Qiang Yao[a], C. W. Kwong[b], and Zeyad T. Alwahabi[b,*],

[a] *Key Laboratory of Thermal Science and Power Engineering of Ministry of Education, Tsinghua University, Beijing 100084, China*
[b] *School of Chemical Engineering and Advanced Materials, The University of Adelaide, S.A. 5005, Australia*
[c] *Laboratory of Photonics, Tampere University of Technology, FIN-33101, Tampere, Finland*
[†] *The first two authors contributed equally.*

Energy and Fuel 2020, 34, 3262-3271

Statement of Authorship

Title of Paper	**In-situ measurement of potassium release during biomass combustion using laser-induced breakdown spectroscopy: effect of silicate on potassium release**
Publication Status	☑ Published ☐ Accepted for Publication ☐ Submitted for Publication ☐ Unpublished and Unsubmitted w ork w ritten in manuscript style
Publication Details	Energy and Fuels , 2020, 34, 3262−3271

Principal Author 1

Name of Principal Author	Haibo Zhao		
Contribution to the Paper	I was responsible for the development of the measurement technique under the Associate Professor Zeyad Alwahabi. I was also responsible for the development of the analytical model under joint supervision of Prof. Qiang Song and Associate Prof. Zeyad Alwahabi. I performed part of the experiment, wrote the draft of the manuscript, and addressed the comments and suggestion from other authors in subsequent revisions of the manuscript.		
Overall percentage (%)	25%		
Certification:	This paper reports on original research I conducted during the period of my Higher Degree by Research candidature and is not subject to any obligations or contractual agreements with a third party that would constrain its inclusion in this thesis. I am the primary author of this paper.		
Signature		Date	22.04.2020

Principal Author 2

Name of Principal Author (Candidate)	Md. Abdul Wakil		
Contribution to the Paper	I was responsible for the development of the measurement technique under the principal supervisor of Associate Professor Zeyad Alwahabi. I performed part of the experiment, wrote the draft of the manuscript, and addressed the comments and suggestion from other authors in subsequent revisions of the manuscript.		
Overall percentage (%)	25%		
Certification:	This paper reports on original research I conducted during the period of my Higher Degree by Research candidature and is not subject to any obligations or contractual agreements with a third party that would constrain its inclusion in this thesis. I am the primary author of this paper.		
Signature		Date	21.04.2020

Co-Author Contributions

By signing the Statement of Authorship, each author certifies that:

i. the candidate's stated contribution to the publication is accurate (as detailed above);
ii. permission is granted for the candidate in include the publication in the thesis; and
iii. the sum of all co-author contributions is equal to 100% less the candidate's stated contribution.

Name of Co-Author	Jan Viljanen		
Contribution to the Paper	I jointly contributed to both data interpretation and refining of the manuscript.		
Overall percentage (%)	10%		
Signature		Date	27.04.2020

Name of Co-Author	Qiang Song		
Contribution to the Paper	I jointly contributed to both data interpretation and refining of the manuscript.		
Overall percentage (%)	10%		
Signature		Date	28.04.2020

Name of Co-Author	Qiang Yao		
Contribution to the Paper	I jointly contributed to both data interpretation and refining of the manuscript.		
Overall percentage (%)	10%		
Signature		Date	28.04.2020

Name of Co-Author	C. W. Kwong		
Contribution to the Paper	I jointly contributed to both data interpretation and refining of the manuscript.		
Overall percentage (%)	10%		
Signature		Date	29 April 2020

Name of Co-Author	Zeyad T. Alwahabi		
Contribution to the Paper	I was principal supervisor for the development of the work, contributed to both data interpretation and refining the manuscript. I hereby certify that statement of contribution is accurate and I have given written permission for this paper to be included in this thesis.		
Overall percentage (%)	10%		
Signature		Date	29.04.2020

energy&fuels

pubs.acs.org/EF Article

In Situ Measurement of Potassium Release during Biomass Combustion Using Laser-Induced Breakdown Spectroscopy: Effect of Silicate on Potassium Release

Haibo Zhao,[‖] M.A. Wakil,[‖] Jan Viljanen, Qiang Song,* Qiang Yao, C. W. Kwong, and Zeyad T. Alwahabi*

Cite This: *Energy Fuels* 2020, 34, 3262−3271

Read Online

ACCESS | Metrics & More | Article Recommendations | Supporting Information

ABSTRACT: In this study, an improved calibration method for the in situ measurement of potassium (K) concentration in the flame field was developed using laser-induced breakdown spectroscopy. The temporal behaviors of K release and particle temperature were recorded simultaneously during biomass combustion. During combustion of raw willow wood, the majority of K was released during the ash-cooking stage, followed by char combustion stage, and only a small amount of K was released during the initial devolatilization stage. The results indicated that during the devolatilization stage, K was released because of the decomposition of organic K. Char-K was subsequently converted to K_2CO_3, and most K_2CO_3 was subsequently released during the final ash-cooking stage. In the case of rice straw combustion, K was mainly released during the initial devolatilization stage, most likely as KCl. The transformation of char-K and the K−Si reaction forming K−silicates mainly occurred during the char combustion stage; K was found to be released slowly from K−silicates during the ash-cooking stage. The combustion of willow wood with different Si contents demonstrated that Si significantly inhibited the K release during both char combustion and the ash-cooking stage.

1. INTRODUCTION

In recent years, because of the energy crisis and environmental issues caused by the consumption of fossil fuels, the renewable energy generated from CO_2 neutral biomass has been attracting more attention. However, biomass usually contains abundant mineral elements, such as potassium (K), calcium (Ca), magnesium (Mg), chlorine (Cl), silicon (Si), and phosphorus (P), which can induce serious technical problems, such as slagging, fouling, and corrosion in thermal conversion systems.[1−5] Among those elements, K plays an important role in ash-related problems because of its high concentration and volatility.[1,6] Therefore, it is necessary to carry out detailed investigation to understand the K release characteristics and mechanisms during the biomass thermal conversion process.

Direct combustion is an effective way to utilize biomass for energy generation. Previous researchers have conducted numerous experimental investigations focusing on the migration of K during various biomass combustion.[7−10] In most studies, biomass was investigated using a fixed-bed or drop tube reactor, and the ash residues were analyzed in order to obtain the distribution of K in gas and solid phases. It was found that a significant part of K (20−100%) is released to the gas phase in the form of KCl, KOH, or K.[2,11,12] The distribution of K was correlated to the forms of K and the co-presence of other mineral elements, especially Cl and Si.[13−16] On the other hand, the combustion temperature can also affect the release ratio. K exists in the biomass as a form of inorganic salts and/or associated with other organics.[2,17,18] When the combustion temperature is lower than 700 °C, the release of K mainly originates from the decomposition of organic K. When the temperature is higher than 700 °C, the inorganic K-containing salts, especially KCl, are directly released to the gas phase due to the increase of vapor pressure. The release rates of K from K_2CO_3 and K_2SO_4 are significantly lower than those of KCl. After devolatilization, part of the organic K and KCl might be transformed into the K embedded with the char (char-K).[17,19,20] During the char combustion stage, part of char-K can decompose and be released to the gas phase directly, while the remaining part is likely to be transformed into K_2CO_3 or other inorganic forms and subsequently released to the gas phase.[13] A previous study has indicated that Cl in biomass can facilitate the release of K because of the high volatility of KCl.[2,11,21] With the co-presence of high level of Si in the biomass, K can react with Si to form thermally stable K−silicates to inhibit the release of K.[2,14]

During combustion, biomass would undergo successively devolatilization, char combustion, and ash-cooking stages. The occurrence forms and corresponding migration characteristics of K may also vary at different stages. Therefore, it is imperative to investigate the temporal release patterns of K during the combustion process. In recent years, along with the development of measurement science and technology, some online measurement methods, such as surface ionization (SI),

Received: November 19, 2019
Revised: February 11, 2020
Published: February 14, 2020

https://dx.doi.org/10.1021/acs.energyfuels.9b03966
Energy Fuels 2020, 34, 3262−3271

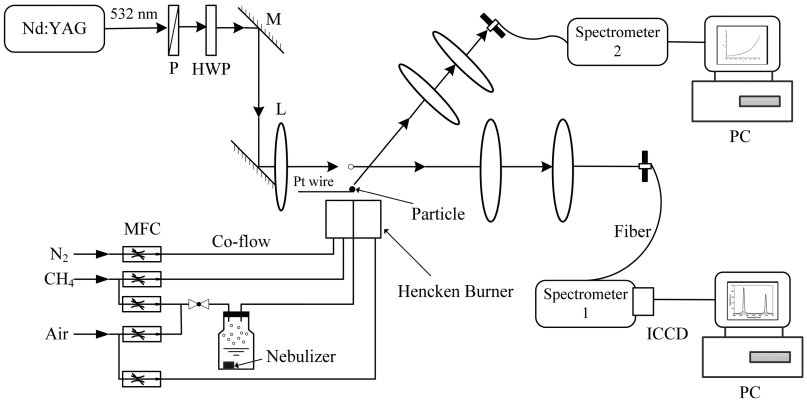

Figure 1. Experimental arrangement used for K and particle temperature measurements. P: polarizer, HWP: half-wave plate; M: mirror; and L: lens.

excimer laser-induced fragmentation fluorescence, atomic emission spectroscopy (AES), and molecular beam mass spectrometer (MBMS) have been used to detect the profile of K release in the gas phase.[18,22−25] For example, Davidsson et al.[22] detected the dynamic release of K during pyrolysis of birch particles using the SI technique. The release curve showed a bimodal distribution at devolatilization and the char pyrolysis stage at a high temperature. Mason et al.[25] measured the spontaneous emission of K during combustion of willow wood pellets using the AES method. They found that the release of K during the devolatilization stage is very small and K was mainly released at char combustion and ash-cooking stages, which is consistent with the results from Jone et al.[26] van Eyk et al.[27,28] used planar laser-induced fluorescence to detect the temporal release of K during combustion of brown coal and found that the Na release pattern was similar to that of K during biomass combustion. However, Bläsing et al.[24] conducted the steam gasification experiment of coal at 1400 °C and measured the signals of different K species in the gas phase using MBMS. The results showed that K was mainly released during the devolatilization stage, mainly as Na^+/K^+ and NaCl/KCl. Although the above measurement methods have made significant progress in the measurement of the alkali metal release, there are still some obvious shortages to be resolved. In particular, they are unable to achieve a quantitative measurement of K in the gas phase, which limits further application and mechanistic investigation on K migration during biomass combustion.

Laser-induced breakdown spectroscopy (LIBS) has achieved rapid development and become one of the leading online elemental analysis techniques because of its abilities in simultaneous elemental analysis, fast response, wide adaptability, and low interference. LIBS has been successfully applied to the quantitative measurement of K during combustion of biomass combustion. Hsu et al.[23] pioneered the development of a calibration method for K concentration in a flame field. The calibration result had shown a good linearity when the K concentration in the gas phase is lower than 4 ppm. They used this calibration method to quantify the amount of K released to the gas phase during combustion of pine wood particles. Zhang et al.[29] obtained a linear calibration result in the range of 0−20 ppm by adapting the seeding way of K-containing solutions with an oxidizing atmosphere. The LIBS measurement technique also has some limitations. Even though the LIBS technique can only quantify the total amount of K in all species at one point, it is still considered as an excellent method for in situ elemental analysis, especially in a flame field. In addition, the simultaneous measurement of the particle temperature using a two-color method was also conducted. The results showed that the temporal release characteristics of K during wood particle combustion are similar to those obtained using other online measurement methods as mentioned above. They concluded that the release of K mainly occurred during char combustion and ash-cooking stages, and the release ratio of K during the devolatilization stage is relatively low. However, the calibration ranges in previous research studies are limited. At higher K concentrations, because of the strong self-absorption effect of K in the flame field, the LIBS signal usually appears nonlinear or even saturated. As a result, the content of K in the biomasses used in the existing studies is usually low to allow a reliable measurement signal. The temporal K release behavior from biomass fuels with more abundant K content, especially the information with herbaceous biomass are scarce. Further, the Si content of the biomass used in previous studies with LIBS measurement techniques was relatively low, which implied that the effect of Si on K release is negligible. Nevertheless, studies indicated that Si can significantly inhibit the release of K during biomass combustion by forming stable K−silicates.[2,14] However, the interactions between Si and K at different stages are likely to be different. Therefore, it is important to understand the temporal release behavior of K from Si-containing biomass and investigate the effect of Si on K release at different combustion stages.

In this study, an improved calibration method was established to allow a broader range of K linear calibration in the flame field for the quantitative measurement of temporal K release during biomass combustion. Willow wood with different Si contents and rice straw were used to investigate the release characteristics and main migration pathways of K during different combustion stages, especially the effect of Si on K release.

2. EXPERIMENTAL SECTION

2.1. Experimental System. Figure 1 shows the experimental system for the simultaneous measurement of K concentration and particle temperature during single particle biomass combustion. The system consists of four parts: the burner and the gas handling system, the seeding system, the optical setup for LIBS, and temperature measurement system.

A Hencken style flat burner was used in the experiment, and the structure has been described elsewhere.[29,30] Briefly, the burner consists of two copper tubes, and the internal diameter of the inner tube is 23.4 mm while that of the internal diameter of the outer tube is 40.5 mm. The fuel, CH_4, was supplied with the inner tube through a packed bed and then evenly distributed into 58 stainless steel tubes with an internal diameter of 1 mm before entering the burner. Each fuel jet is directly adjacent to six hexagonal air flows where the combustion air is first fed through a packed bed and then a stainless steel honeycomb with an inner brass tube before entering the burner. CH_4 and air are mixed above the burner to form a uniform and stable flat flame. Co-flowing N_2 was also fed into the outlet of the brass tube to enhance the stability of the flame. The CH_4 flow rate was fixed at 450.0 mL/min, and the air flow was fixed at 5.0 L/min. The N_2 co-flow was fixed at 8.0 L/min. The resulting equivalence ratio was about 0.86. Table 1 shows the exhaust gas composition with the above combustion configuration. The temperature of the exhaust gas above the burner is 1570 ± 70 K measured using a R-type thermocouple and corrected using the radiation-correction method. In the biomass combustion experiment, the cylindrical biomass pellet was supported by a platinum wire horizontally located 5 mm above the center of the burners. The cylindrical biomass pellet was placed vertically on the platinum wire.

Table 1. Composition of CH_4 Combustion Exhaust

composition	CO_2	O_2	H_2O	N_2
mole fraction (%)	8.2	2.7	16.5	72.6

Before each experiment, the Pt wire was cleaned using HNO_3.

The K seeding system was built for the calibration of K concentration in the high-temperature field for further quantifying the K concentration released during the combustion of biomass pellets. It consists of a bottle containing 100 mL of KCl solution with a mass percent of 8% and an ultrasonic nebulizer located under the liquid surface. During the calibration process, a fog of droplets containing KCl salt was produced in the bottle by a nebulizer. A stream of CH_4 and air mixture was used as a carrier gas. It carried the K-containing droplets into the flame field through a brass tube with a diameter of 1 mm in the center of the burner. The seeding rate of KCl is controlled by adjusting the flow rate of the carrier gas.

The LIBS measurement system mainly consists of a pulsed laser, a polarizer, a half-wave plate, mirrors, plano-convex lens, optical fibers, and a spectrometer. Laser pulse, at wavelength of 532 nm, 6 ns pulse width, and 10 Hz repetition rate, from frequency doubled Nd:YAG (Quantel YG) was used. The laser energy was controlled by a Glan laser polarizer and a half-wave plate and then focused 22 mm above the center of the burner to provide stable plasma. The plasma emission was captured and then directed to the spectrometer (Andor SR-500) using an optical fiber. The spectrometer was equipped with 1200 groove/mm gratings and connected with an ICCD camera (Andor iStar). During the calibration and biomass combustion experiments, the frequency of the spectrum acquired by the spectrometer was 5 Hz.

The temperature measurement system mainly consists of convex lens, an optical fiber, and a second spectrometer (USB4000-XR1-ES, Ocean optics). The radiation from the hot biomass surface was captured by a convex lens and passed to an optical fiber connected to the spectrometer. The spectrometer was equipped with a 500 groove/mm gratings and a detector with a 3648 pixel CCD chip (TCD 1304 AP).

2.2. Parameter Determination. Figure S1 of the Supporting Information shows the typical LIBS spectrum of K recorded at 75 mJ laser energy with K sending rates at 6 and 20 mL/min. As can be seen, the spectrum has two characteristic peaks at 766.78 and 770.18 nm, respectively. In this study, the area around the peak at 766.78 nm was used to calibrate and quantify the K concentration because of its relative higher intensity. By careful choice of few parameters, a stable and clear K spectrum can be obtained. These parameters include the laser pulse power and the ICCD gate-delay time and gate-width.

Figure S2 of the Supporting Information shows the LIBS signal of K as a function of laser energy at one constant K seeding rate (20 mL/min). In the range of 0−32 mJ, the measured K signal intensity is low and remains constant with the increase of laser energy. In this range, the plasma is not generated, and the observed K signal is due to the spontaneous emission of K. From 32 mJ laser energy, the plasma spot can be seen in the flame field. In the range of 32−88 mJ, the spectral intensity of K exhibits an approximately linear increase with the increase of pulse energy. It was observed that increasing the laser energy above 88 mJ, the K signal intensity remains nearly constant with the increase of laser energy. In this range, small fluctuations of the laser pulse energy would have little effect on the K signal intensity. As a consequence, the laser energy was set to be 100 mJ to reduce the effect of the small fluctuations of laser power.

Figure S3 of the Supporting Information shows the K signal evolution with gate-delay time at a certain seeding rate (ICCD gate width 2 μs). When the gate delay time is zero, the spectral intensity in the entire spectrum range is quite high due to the continuous emission. At 2 μs, the intensity of the K spectrum and the continuous emission are both significantly reduced, and the emission for K becomes apparent. With the further increase of gate-delay, the background noise approaches a low value, and the emission for K becomes clearer. With a gate-delay time above 10 μs, the spectral lines of continuous emission and other elements almost disappeared, and the LIBS emission of K is very clear. In the range of 10−50 μs, the intensity of the K signal gradually decreased with time.

At the high-temperature environment of the flame, there might be an obvious spontaneous emission due to the excitation of nonground state K atoms by high temperature and the corresponding electronic energy level transition.[26] During the LIBS measurement process, the spontaneous emission signal of K will be added to the LIBS signal, which will adversely affect the linear calibration of LIBS. Based on the result above, considering the need to obtain K emission with a high value of the signal to noise ratio (SNR) and to avoid the effect of spontaneous emission. A gate-delay and a gate-width of 10 μs were found to produce an optimum SNR that was used in the following sections.

2.3. Quantitative Calibration of K in the Flame. To achieve the quantitative measurement of K concentration released during combustion of biomass pellets, the relationship between K concentration and LIBS signal intensity was required. In this work, the calibration process was performed as follows:

After the K containing droplets enter the combustion zone through the tube in the center of the burner, it would diffuse during the downstream flow due to the concentration gradient. Given the K feeding rate, the molar concentration of K at the measurement point can be calculated by CFD simulation. Then, the K signal intensity at the measurement point can be measured by the LIBS system. Finally, the relationship between the K concentration and signal intensity was obtained.

The seeding rates of K containing droplets at different carrier gas flows were determined by a gravimetric method. The K feeding system is operated stably for 12 h under a certain carrier gas flow rate, and the weight loss rate of the K-containing solution is calculated by measuring the mass of the solution bottle before and after the operation. It was found that the seeding rate of K-containing droplets is linear with the carrier gas flow rate, as shown in Figure S4 of the Supporting Information.

A CFD simulation of the flow in the flame field was conducted to obtain the radial concentration distribution of K at different seeding flow rates. Several assumptions were made first as follows: the flow is laminar steady-state and the radial temperature profile of the flame was measured to be spatially uniform (<80 K) within the radius of 4 mm. For the CFD simulation, the value for temperature was set at 1570 K; the temperature of the co-flow is room temperature, set to be 298 K. The diffusivity coefficients of each gas were taken as the binary diffusion system in N_2, which is obtained according to the Chapman−Enskog equation. The simulation results are shown in Figure S5 of the Supporting Information.

On the other hand, the K spectral signal can be partly absorbed by the K atoms in the ground state in the flame field.[23,31,32] As a consequence, the K signal recorded by the spectrometer is the result of the coupling of the emission excited by the LIBS and the absorption by the K atoms in the ground state. When the K concentration in the gas phase is high, the self-absorption would have a significant effect on the LIBS signal of K, which would cause the nonlinearity in the concentration and signal intensity relation. In previous reports, the computational method was applied to account for self-absorption.[23,29] However, the population of the ground state of K in the flame field needs to be estimated, which would cause poor accuracy at high K concentrations. In this work, a linear calibration result suitable for the high K concentration range is obtained by a reasonable selection of the spectrum area to avoid the absorption effect in the areas where the absorption is severe.

First, the relationship between the recorded spectrum of K with the emission spectrum excited by LIBS and absorption by the atoms in the ground state is shown in eq 1:[30,33]

$$S(\lambda) = I_{\text{emission}}(\lambda)\cdot G(\lambda) \tag{1}$$

where $S(\lambda)$ is the recorded spectrum by a spectrometer; $I_{\text{emission}}(\lambda)$ is the emission spectrum excited by LIBS; and $G(\lambda)$ is the absorption by the K atoms in the ground state.

Equation 1 can be further expressed as eq 2:[34]

$$S(\lambda) = I_{\text{emission}}(\lambda_c)\cdot\frac{1}{1+\left(\frac{2\cdot(\lambda-\lambda_c)}{a}\right)^2}\cdot\exp\left(\frac{-\alpha L}{1+\left(\frac{2\cdot(\lambda-\lambda_c)}{b}\right)^2}\right) \tag{2}$$

where λ_c is the wavelength in the center of the K peak spectrum, 766.78 nm and a, b, α, and L are constants.

According to $S(\lambda)$, $I_{\text{emission}}(\lambda)$ can be obtained by nonlinear fitting using Matlab.

Figure S6 of the Supporting Information shows the recorded spectrum $S(\lambda)$ and the emission spectrum excited by LIBS $I_{\text{emission}}(\lambda)$ calculated according to eq 2. The region between $S(\lambda)$ and $I_{\text{emission}}(\lambda)$ represents the absorption effect by the K atom in the ground state. As can be seen, at the center of K peak, the absorption effect is most significant and the further away from the center, the weaker the absorption effect. As a consequence, the shadow area shown in Figure S6 was used to calibrate the K concentration to avoid the effect of self-absorption.

Figure 2a shows the obtained calibration curve. Each point contains the average value obtained after at least three times of measurement and the calculated standard deviation. During each measurement, the calibration points were averaged over 200 shots. As can be seen, in the range of 0−200 ppm, there is a good linear relationship between the intensity and K concentration.

2.4. Particle Temperature Measurement. The temperature of the particle during the combustion process was measured using an emission method, which will be described below.

According to Plank equation, the radiation intensity of the solid surface at temperature T can be expressed as eq 3.

$$I_\lambda = \varepsilon_\lambda c_1 \lambda^{-5}(e^{c_2/\lambda T} - 1)^{-1} \tag{3}$$

where I_λ is the radiation intensity at the wavelength of λ (W/m^2 μm); ε_λ is the emissivity; c_1 is the first radiation constant, 3.742×10^8 W μm^4/m^2; c_2 is the second radiation constant, 1.439×10^4 μm/K; λ is the wavelength, nm; and T is the temperature of the solid surface, K.

During the combustion process, the char particle can be treated as a gray body, which means the emissivity remains nearly constant with wavelength.[35−38] The radiation intensity from the solid surface was recorded by the spectrometer and then the temperature T was obtained by nonlinear fitting using Matlab based on eq 2. Figure S7 of the Supporting Information shows an example of the recorded radiation spectrum and the fitting curve. It can be seen that the fitting curve and the measured spectrum have a good coincidence, indicating that the previous assumption of the gray body is reasonable.

During the measurement, the characteristic spectrum emitted from the radicals and excited elements in the flame will also be collected. The characteristic features of the excited free-radical have been removed before the fitting was attempted. The tip of the thermocouple was placed in the flame 5 mm above the center of the burner. The thermocouple is perpendicular to the convex lens to ensure that only the emission from the tip of the thermocouple can be captured by the convex lens shown in Figure 1.

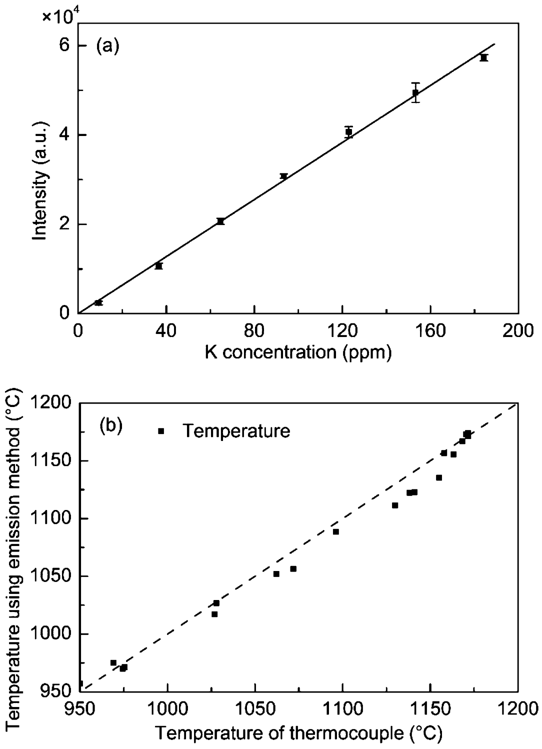

Figure 2. (a) LIBS signal intensity vs the K concentration and (b) comparison of the temperature measurement between the emission method and thermocouple.

The temperature of the flame was adjusted by changing the flow rate of CH_4 and air. Figure 2b shows the temperature calculated using the emission method and that obtained by the thermocouple. It can be seen that in the measurement range, the two temperatures are in good agreement with a difference lower than 20 °C. Therefore, it can be considered that the emission method is accurate enough to measure the temperature of the particle during the combustion process.

2.5. Samples. Willow wood and rice straw from China were used in this study. Their ash compositions are shown in Table 2. In order to investigate the effect of Si on K release, willow wood with different Si contents was also prepared by mixing Si-free willow wood and different amounts of SiO_2. The biomass sample was pulverized to an average particle size of less than 150 μm and dried at 105 °C for 10 h. The pulverized samples were compressed into cylindrical pellets with three different masses, 10 ± 1, 15 ± 1, and 20 ± 1 mg. The pellet diameter was 3.5 mm with the height between 1 and 2.5 mm, depending on the sample density and pellet mass.

3. RESULTS AND DISCUSSION

3.1. Temporal K Release during Willow Wood Combustion.

The temporal evolution of K concentration and particle temperature during combustion of raw willow wood pellets with different masses are presented in Figure 3. To our knowledge, this is the first study to measure the K release concentration profile and particle temperature simultaneously during the entire combustion process. The temperature profile can help distinguish different combustion stages together with the analysis of the K release curve. It will also be useful for developing the kinetic model of K release during the combustion process. It was found that the K release profile

Table 2. Chemical Composition of Willow Wood and Rice Straw

	main ash-forming elements (mg/g, dry basis; molar ratio)											
materials	K	Na	Cl	Si	Ca	Mg	S	P	Al	K/Si	Si/(Ca + Mg)	K/Cl
Willow wood	3.41	0.08	0.02	0.21	7.29	1.24	0.3	1.17	0.03	11.66	0.03	154.3
Willow wood + SiO_2	3.41	0.08	0.02	2.08	7.29	1.24	0.3	1.17	0.03	1.18	0.32	154.3
	3.41	0.08	0.02	4.50	7.29	1.24	0.3	1.17	0.03	0.54	0.69	154.3
	3.41	0.08	0.02	7.03	7.29	1.24	0.3	1.17	0.03	0.35	1.07	154.3
	3.41	0.08	0.02	9.98	7.29	1.24	0.3	1.17	0.03	0.25	1.52	154.3
rice straw	24.18	0.49	9.49	37.21	5.07	1.53	2.3	0.83	0.20	0.47	6.98	2.31

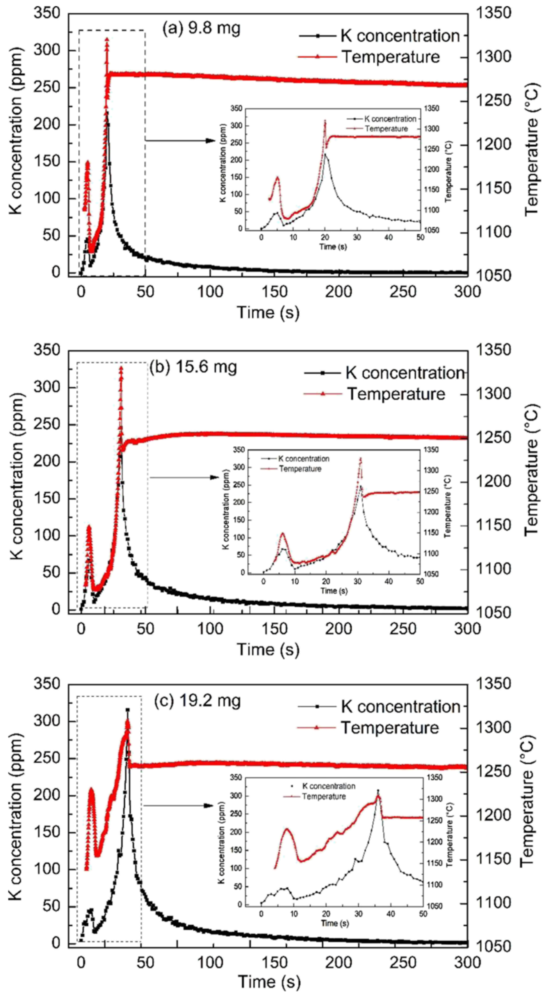

Figure 3. Temporal evolution of K concentration and particle temperature during combustion of willow wood with initial mass (a) 9.8, (b) 15.6, and (c) 19.2 mg.

shows a clear bimodal distribution, which is consistent with the previous studies.[23,29] The temperature profile of the particle surface also shows a bimodal distribution, and the peak time of the particle temperature corresponds to that of the K release rate.

It should be noted that during the particle combustion process, the emission from the volatiles and soots can also be collected by the spectrometer and influence the result. However, considering the oxy-rich condition and the large volume of the particle, the emission intensity from the volatiles and soot particles are significantly weaker than that form the particle surface. As such, it is believed that the temperature obtained by the emission method is representative for the particle temperature.

In Figure 3a, after the ignition of willow wood, K released rapidly and the concentration reached a peak of 50 ppm in about 5 s after the ignition and then gradually decreased to a minimum at around 10 ppm at 7 s. The temperature of the particle is observed to be synchronized with the K and volatile release profiles because the K concentration and temperature both reached maximum at the same time when the devolatilization and volatile combustion were believed to be the most intensive. It is believed that K is released with other volatile species during devolatilization, and the increase of temperature is due to the volatile combustion around the particle. The devolatilization process is considered to be completed when the K concentration and temperature reached minimum after the first peak.

The char combustion stage commenced after the completion of devolatilization at around 10 s. During the char combustion stage, it was found that both K release and particle temperature increased with time. The increase of the particle temperature is due to the exothermic heat of char combustion. During this initial char combustion stage, the particle gradually shrinks and collapses. By comparing the K release and temperature profiles with the video recording of the particle combustion process, it was found that the time of the final collapse of the char particles was consistent with the time when the temperature and the K concentration peaked. Therefore, the time when temperature and K concentration peaked was considered as the completion of char combustion.

The ash-cooking stage commenced after the char combustion stage. It is observed that from 20 s onward, the particle temperature decreased by around 50 °C from a peak temperature. During the ash-cooking stage, K concentration decreased rapidly from the peak values and then slowly to almost zero. On the other hand, the temperature of the pellets increased slightly and remained stable until the completion of K release. This indicated that the ash and the flame field were in thermal equilibrium. Because of the variations of the volume, shape, and surface areas of the particles during the combustion process, the observed peak temperature values are different in the experimental conditions with different initial masses of biomass. Nevertheless, the overall profile of the temperature and K concentration is similar to a clear bimodal distribution during the combustion of particles with different initial masses.

The chemical composition of the ash residues after the combustion experiments were analyzed using inductively coupled plasma–AES (ICP–AES; ThermoElemental, USA). It was found that Ca, Mg, and P were the major elements present in the ash while the content of K is negligible. No Ca signal was detected during the combustion process, indicating that nearly all Ca remained in the solid phase, which was consistent with previous studies.[39] If Ca was considered as a conserved element in the solid phase, it was estimated that the residual K in the ash accounted for only 0.6% of the total K content from the initial biomass. Therefore, it is believed that most of the K was released to the gas phase rather than forming the insoluble K−silicates in the solid phase.

Table 3 shows the K release ratios as well as the standard deviations at different stages during combustion of willow wood particles with different initial particle masses. The release ratio of K in each stage is consistent with the different initial particle mass. It was found that the majority (>67%) of K was released during the ash-cooking stage, followed by the char combustion stage at about 25%. Only <6% of K was released during the devolatilization stage.

Table 3. Ratios of K Released at Each Stage during Combustion of Willow Wood Particles

particle mass (mg)	devolatilization (%)	char combustion stage (%)	ash-cooking stage (%)
10	5.6 ± 1.1	25.1 ± 0.9	69.3 ± 2.0
15	4.9 ± 0.2	27.6 ± 0.5	67.5 ± 0.5
20	4.8 ± 1.3	26.5 ± 2.4	68.7 ± 2.1

The Cl content in the willow wood in this study was quite low, as shown in Table 2. This indicated that KCl did not exist in willow wood, and therefore, the K release should mainly be originated from the decomposition of organic K during devolatilization.

According to previous research,[6,13,17] K mainly present in char as char-K after devolatilization. During the char combustion process, char-K was converted into different types of inorganic K, such as K_2CO_3, K_2SO_4, and K_3PO_4. For the combustion of willow wood, K_2SO_4 in char should be negligible after devolatilization because the S content in willow wood was low and was much lower than the K content (Table 2). On the other hand, ash residue analysis indicated that the P content in the ash after combustion was high. This implied that almost all P remained in ash after combustion if Ca was considered as a tracer. Considering all K was released to the gas phase after the experiment, the amount of K in the form of K_3PO_4 in the ash after combustion can be neglected. As a result, the char-K was mainly transformed into K_2CO_3, and part of K_2CO_3 was released to the gas phase during the char combustion stage. On the other hand, with the oxidation reaction of organic matter combined with K, K in char-K may also be directly released into the gas phase in the form of K or KOH.[40] Nevertheless, nearly 68% of the total K remained in ash was in the form of K_2CO_3 after char combustion. This indicated that the majority of char-K was transformed into K_2CO_3 during the char combustion stage. It also indicated that the K_2CO_3 release rate was significantly lower than the char oxidation rate, resulting in K_2CO_3 accumulation in the solid phase. As shown in Figure 3, the K concentration increased with time during the char combustion stage due to (1) the consumption of the organic matrix during the combustion process, the char-K was continuously transformed into K_2CO_3, resulting in the accumulation of K_2CO_3, and thus the increase of K release rate and (2) the increase in char particle temperature.

3.2. Temporal K Release from Rice Straw during Combustion. Figure 4 shows the temporal evolution of K concentration and particle temperature during the combustion of the rice straw particle with an initial mass of 10.5 mg. To our knowledge, this is the first study to carry out the in situ measurement of K using LIBS during combustion of herbaceous biomass with high K and Si contents. It was found that the temporal release behavior of K during the combustion of rice straw was different from willow wood (Figure 3) and those reported in the literature.[33,41] During the combustion of rice straw, the K release profile showed a mono distribution with a single peak at around 7 s. After the ignition of the pellet, the K concentration increased rapidly before reaching the maximum level of around 620 ppm at 7 s and then decreased gradually with combustion time. From 30 s onward, the K concentration slowly decreased with time. During the ash-cooking stage (40−200 s), a low release of K was observed. During the combustion process, the temperature of the straw pellet increased rapidly to around 1170 °C and then decreased to around 1130 °C. During the ash-cooking stage, the temperature increased slightly to around 1150 °C. However, in general, the particle temperature remained stable at around 1130−1170 °C during the whole combustion process. The first peak of the particle temperature was attributed to the combustion of volatiles around the particles. After the devolatilization process, the slight decrease in temperature was attributed to the higher ash content of the rice straw. During combustion of char particles, the emissivity would change with the change of the ratio between char and the ash composition in the remaining solid particle.[42] In particular, rice straw contains a large amount of Si, which would form a pronounced molten silicate in the latter stage of combustion, thus affecting the radiative heat transfer behavior on the surface of the particles and inducing the observed profile of the surface temperature.

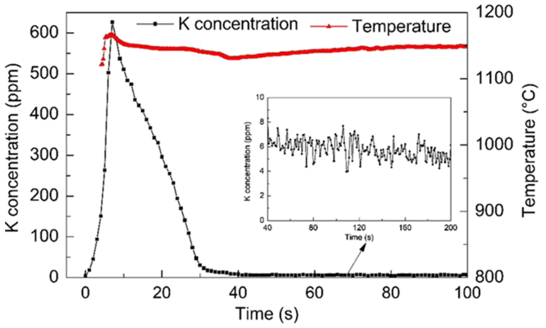

Figure 4. Temporal evolution of K concentration and particle temperature during combustion of rice straw at a fixed initial mass of 10.5 mg.

The temporal K release profiles during combustion of rice straw with different initial masses are shown in Figure 5. It was found that all the K release profiles from different initial masses showed a distribution with a single peak. With the increase of straw initial masses from 10.5 to 19.9 mg, the peak level of K was lowered by around 100 ppm and peak position was shifted from 6 to 10 s. The shift of the peak was attributed to the increase in the burnout time with the increased initial mass. During rice straw combustion, the K concentration increased rapidly and reached a peak during the devolatilization stage. Unlike the combustion of willow wood, no relationship was observed between K and volatile release. Considering the fact that during the willow wood devolatilization stage, the K concentration was low and the release profile was consistent with devolatilization. Therefore, K release during the devolatilization stage of the rice straw is believed to be independent to the decomposition of organic K. As shown in

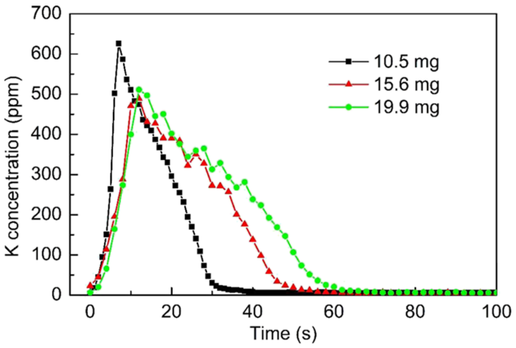

Figure 5. Temporal evolution of K concentration during combustion of rice straw with different initial particle masses as indicated.

Table 1, rice straw contains high content of Cl, and KCl was the most important inorganic K in straw according to previous reports.[18] KCl was released directly to the gas phase at high temperatures, and therefore, KCl release profile follows with the increase of the particle temperature during devolatilization and subsequently, in the combustion stage (Figure 4). KCl release is a thermodynamic process, and the release rate is sensitive to KCl concentration and temperature. The decrease of the K release rate from 7 s was attributed to the decrease of the KCl amount in the solid phase. As shown in Figure 5, the highest K release rate decreased with the increase of particles mass. It was due to the increased diffusion resistance of KCl with larger particles, resulting in a decrease in the K release rate. During the ash-cooking stage of rice straw, a slow release of K was observed and the release rate was low but stable even after 60 s. On the contrary, during the ash-cooking stage of willow wood, the K release rate decreased gradually with time and nearly all the K was released to the gas phase after 300 s. The difference in the K release profile was attributed to the compositional difference between willow wood and rice straw. The rice straw in this study contains a large amount of Si and the ash exhibited significant melting morphology after combustion. This indicated that the K silicates were formed in the ash and was released during the slow decomposition of K−silicates in the ash cooking stage.

Table 4 shows the K release ratio during the rice straw combustion process. It is calculated based on the contents of K in the rice straw (Table 1) and the integration of K release concentration during the whole combustion process. It is assumed that the concentration profile of K was uniform in the gas phase and followed the concentration profile from the LIBS measurement. It was found that only about 30% of the total K was released to the gas phase during rice straw combustion. This implied that about 70% of total K remained in the solid phase and was in the form of K−silicates. The results indicated that during combustion of biomass at high temperatures, K is more likely to react with Si to form stable silicates, thereby inhibiting the gas phase release of K. With the increase of the initial straw pellet mass, the K release ratio decreased slightly due to the increase of diffusion resistance with larger particle mass. The effect was especially pronounced during the latter stage of char combustion; the melting silicates would significantly inhibit the release of K and aggravate the K−Si reaction, thereby inhibiting the vapor phase release of K.

Table 4. Total Release Ratio of K during the Combustion Process of Rice Straw with Different Initial Masses

particle initial masses (mg)	10	15	20
release ratio (%)	33.6 ± 2.2	30.1 ± 1.7	29.4 ± 1.3

3.3. Effect of Si Content on K Release Behavior during Willow Wood Combustion.

In order to further investigate the effect of Si on K release, willow wood pellets containing different Si contents were prepared. The temporal release behavior of K during the combustion process are shown in Figure 6a. It was found that the Si content significantly affected the K release behavior. During the devolatilization stage, the addition of Si had shown a little effect on the temporal release of K, while Si had shown an obvious effect on K release after devolatilization. Nevertheless, it is difficult to distinguish the char combustion stage and the ash-cooking stage after the introduction of the additional Si in the initial biomass matrix. In the case of the willow wood with 0.20% Si content, the peak concentration of K at about 25 ppm after devolatilization was observed at around 50 s. This is much lower than that from the raw willow wood (without Si addition). When the content of Si was increased from 0.20 to 0.70%, the K release was further decreased. However, no further decrease was observed when the Si content was increased to 1.00%. During the ash-cooking stage of the raw willow wood combustion, the concentration of K decreased rapidly first and then slowly until reaching zero. In the case of the willow wood with 0.2% Si content, the K concentration decreased slowly with time and sustained a low level of K release during the entire ash-cooking stage. It was also observed that the K release during the ash-cooking stage was further reduced with the elevated biomass Si content. When the Si content was further increased to 0.70%, no K release was

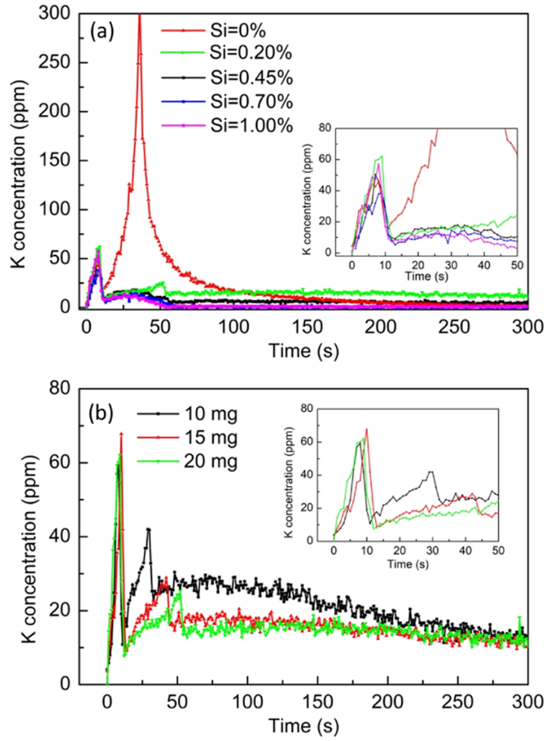

Figure 6. Temporal evolution of K concentration during combustion of willow wood with (a) different Si content, as indicated, at fixed initial mass of (10 mg) and (b) different initial mass, as indicated, at a fixed Si content of 0.20%.

observed during the ash-cooking stage. It can be seen that when Si was introduced to the willow wood, the K release profile during the ash-cooking stage is comparable to that from the rice straw, which also implied that the sustained K release from straw ash was attributed to the decomposition of K−silicates from the K−Si reaction. During the char combustion stage, the K release from Si-containing willow wood was much lower than that from raw willow wood, indicating that K_2CO_3 generated from the decomposition of char-K was mainly converted into K−silicates and lowered the release ratio of K (Table 4).

Figure 6b shows the K release profile during combustion of willow wood containing 0.20% Si content with different initial masses. It was found that with the increase of the initial mass, no major difference in K release was observed during the devolatilization stage, which implied that the addition of Si has little effect on K release at this stage. However, a significant difference was observed for the temporal K release profile after the devolatilization stage. With the increase of the initial particle mass, the K release peak was appeared to shift to the later stage of the char combustion and with a boarder shoulder. The overall K release amount was also appeared to be inversely proportional to the initial particle mass, and thus the release ratio of K was decreased significantly with the increase of the initial particle mass. This observation is consistent with the trend of the K release ratio with the increase of the initial mass of the rice straw pellets (Table 4). However, the K release ratio during the straw combustion process only decreased slightly with the increase of pellet mass, and the tendency is lower than that from Si-containing willow wood. This is believed to be the consequence of high KCl content in the rice straw. During the combustion process of the rice straw, KCl would release rapidly and dominated the overall K release. The increase in initial particle mass would have a minimum effect on KCl release. Therefore, the effect of the increase in initial pellet mass on the K release ratio was less pronounced than that on the Si containing willow wood.

4. CONCLUSIONS

Simultaneous measurements of potassium concentration and biomass temperature during biomass combustion have been developed with an improved LIBS calibration method. The effect of biomass type, Si content, and initial mass of willow wood on the temporal release of K and particle temperature during biomass combustion were investigated. The main migration pathways of K during different combustion stages, especially the effect of Si on K release, were also analyzed. With the combustion of Si-free willow wood, it was found that the majority of K was released during the ash-cooking stage, followed by the char combustion stage, only a small amount of K was released during the initial devolatilization stage. With rice straw combustion, it was found that about 30% of the total K was released rapidly during the initial devolatilization stage, most likely as KCl. Results indicated that the release of K during the combustion of rice straw was suppressed by the presence of Si with the formation of K−silicates. The inhibitive effect of biomass Si content on K release was further demonstrated by the introduction of Si in willow wood. Results also indicated that Si had little effect on the release of K during the devolatilization stage but significantly inhibited the release of K during the char combustion and ash-cooking stage.

■ ASSOCIATED CONTENT

Supporting Information

The Supporting Information is available free of charge at https://pubs.acs.org/doi/10.1021/acs.energyfuels.9b03966.

LIBS spectrum in the calibration flame; LIBS signal intensity of K as a function of laser pulse energy; temporal evolution of the LIBS signal intensity of K; seeding rate of KCl solution as a function of carrying gas flow rates; radial distribution of K concentration as a function of the distance from the centre line; a typical example of the absorption correction with the fitting method; and real-time wavelength-resolved particle's emission intensity (PDF)

■ AUTHOR INFORMATION

Corresponding Authors

Qiang Song − *Key Laboratory of Thermal Science and Power Engineering of Ministry of Education, Tsinghua University, Beijing 100084, China;* orcid.org/0000-0002-5484-3594; Email: qsong@tsinghua.edu.cn

Zeyad T. Alwahabi − *School of Chemical Engineering and Advanced Materials, The University of Adelaide, Adelaide, South Australia 5005, Australia;* orcid.org/0000-0003-4831-7798; Email: zeyad.alwahabi@adelaide.edu.au

Authors

Haibo Zhao − *Key Laboratory of Thermal Science and Power Engineering of Ministry of Education, Tsinghua University, Beijing 100084, China*

M.A. Wakil − *School of Chemical Engineering and Advanced Materials, The University of Adelaide, Adelaide, South Australia 5005, Australia;* orcid.org/0000-0002-4070-1499

Jan Viljanen − *Photonics Laboratory, Physics Unit, Tampere University, FI-33101 Tampere, Finland*

Qiang Yao − *Key Laboratory of Thermal Science and Power Engineering of Ministry of Education, Tsinghua University, Beijing 100084, China*

C. W. Kwong − *School of Chemical Engineering and Advanced Materials, The University of Adelaide, Adelaide, South Australia 5005, Australia*

Complete contact information is available at: https://pubs.acs.org/10.1021/acs.energyfuels.9b03966

Author Contributions

[‖]H.Z. and M.A.W. are contributed equally.

Notes

The authors declare no competing financial interest.

■ ACKNOWLEDGMENTS

This work was financially supported by the National Natural Science Foundation of China under grant 51076072 and National Basic Research Program of China (973 Program) 2013CB228500.

■ REFERENCES

(1) Sander, B. Properties of Danish biofuels and the requirements for power production. *Biomass Bioenergy* **1997**, *12*, 177−183.

(2) Knudsen, J. N.; Jensen, P. A.; Dam-Johansen, K. Transformation and release to the gas phase of Cl, K, and S during combustion of annual biomass. *Energy Fuels* **2004**, *18*, 1385−1399.

(3) Bartolomé, C.; Gil, A. Ash deposition and fouling tendency of two energy crops (cynara and poplar) and a forest residue (pine

chips) co-fired with coal in a pulverized fuel pilot plant. *Energy Fuels* **2013**, *27*, 5878−5889.

(4) Baxter, L. L.; Miles, T. R.; Miles, T. R., Jr.; Jenkins, B. M.; Milne, T.; Dayton, D.; Bryers, R. W.; Oden, L. L. The behavior of inorganic material in biomass-fired power boilers: field and laboratory experiences. *Fuel Process. Technol.* **1998**, *54*, 47−78.

(5) Vamvuka, D.; Zografos, D.; Alevizos, G. Control methods for mitigating biomass ash-related problems in fluidized beds. *Bioresour. Technol.* **2008**, *99*, 3534−3544.

(6) Johansen, J. M.; Jakobsen, J. G.; Frandsen, F. J.; Glarborg, P. Release of K, Cl, and S during pyrolysis and combustion of high-chlorine biomass. *Energy Fuels* **2011**, *25*, 4961−4971.

(7) Jenkins, B. M.; Baxter, L. L.; Miles, T. R., Jr; Miles, T. R. Combustion properties of biomass. *Fuel Process. Technol.* **1998**, *54*, 17−46.

(8) van Lith, S. C.; Alonso-Ramírez, V.; Jensen, P. A.; Frandsen, F. J.; Glarborg, P. Release to the gas phase of inorganic elements during wood combustion. Part 1: development and evaluation of quantification methods. *Energy Fuels* **2006**, *20*, 964−978.

(9) Niu, Y.; Tan, H.; Wang, X.; Liu, Z.; Liu, H.; Liu, Y.; Xu, T. Study on fusion characteristics of biomass ash. *Bioresour. Technol.* **2010**, *101*, 9373−9381.

(10) Eom, I.-Y.; Kim, J.-Y.; Kim, T.-S.; Lee, S.-M.; Choi, D.; Choi, I.-G.; Choi, J.-W. Effect of essential inorganic metals on primary thermal degradation of lignocellulosic biomass. *Bioresour. Technol.* **2012**, *104*, 687−694.

(11) Jensen, P. A.; Frandsen, F. J.; Dam-Johansen, K.; Sander, B. Experimental investigation of the transformation and release to gas phase of potassium and chlorine during straw pyrolysis. *Energy Fuels* **2000**, *14*, 1280−1285.

(12) Knudsen, J. N.; Jensen, P. A.; Lin, W.; Dam-Johansen, K. Secondary capture of chlorine and sulfur during thermal conversion of biomass. *Energy Fuel.* **2005**, *19*, 606−617.

(13) Van Lith, S. C.; Jensen, P. A.; Frandsen, F. J.; Glarborg, P. Release to the gas phase of inorganic elements during wood combustion. Part 2: influence of fuel composition. *Energy Fuels* **2008**, *22*, 1598−1609.

(14) Zhang, Z.-H.; Song, Q.; Yao, Q.; Yang, R.-M. Influence of the atmosphere on the transformation of alkali and alkaline earth metallic species during rice straw thermal conversion. *Energy Fuels* **2012**, *26*, 1892−1899.

(15) Quyn, D. M.; Wu, H.; Bhattacharya, S. P.; Li, C.-Z. Volatilisation and catalytic effects of alkali and alkaline earth metallic species during the pyrolysis and gasification of Victorian brown coal. Part II. Effects of chemical form and valence. *Fuel* **2002**, *81*, 151−158.

(16) Novaković, A.; van Lith, S. C.; Frandsen, F. J.; Jensen, P. A.; Holgersen, L. B. Release of potassium from the systems K− Ca− Si and K− Ca− P. *Energy Fuels* **2009**, *23*, 3423−3428.

(17) Zhao, H.; Song, Q.; Yao, Q. Release and transformation of K and Cl during the pyrolysis of KCl-loaded cellulose. *Fuel* **2018**, *226*, 583−590.

(18) Zhao, H.-b.; Song, Q.; Wu, X.-y.; Yao, Q. Study on the transformation of inherent potassium during the fast-pyrolysis process of rice straw. *Energy Fuels* **2015**, *29*, 6404−6411.

(19) Rahim, M. U.; Gao, X.; Garcia-Perez, M.; Li, Y.; Wu, H. Release of chlorine during mallee bark pyrolysis. *Energy Fuels* **2012**, *27*, 310−317.

(20) Wornat, M. J.; Hurt, R. H.; Yang, N. Y. C.; Headley, T. J. Structural and compositional transformations of biomass chars during combustion. *Combust. Flame* **1995**, *100*, 131−143.

(21) Olsson, J. G.; Jäglid, U.; Pettersson, J. B. C.; Hald, P. Alkali metal emission during pyrolysis of biomass. *Energy Fuels* **1997**, *11*, 779−784.

(22) Davidsson, K. O.; Stojkova, B. J.; Pettersson, J. B. C. Alkali emission from birchwood particles during rapid pyrolysis. *Energy Fuels* **2002**, *16*, 1033−1039.

(23) Hsu, L.-J.; Alwahabi, Z. T.; Nathan, G. J.; Li, Y.; Li, Z. S.; Aldén, M. Sodium and potassium released from burning particles of brown coal and pine wood in a laminar premixed methane flame using quantitative laser-induced breakdown spectroscopy. *Appl. Spectrosc.* **2011**, *65*, 684−691.

(24) Bläsing, M.; Müller, M. Investigations on the influence of steam on the release of sodium, potassium, chlorine, and sulphur species during high temperature gasification of coal. *Fuel* **2012**, *94*, 137−143.

(25) Mason, P. E.; Darvell, L. I.; Jones, J. M.; Williams, A. Observations on the release of gas-phase potassium during the combustion of single particles of biomass. *Fuel* **2016**, *182*, 110−117.

(26) Jones, J. M.; Darvell, L. I.; Bridgeman, T. G.; Pourkashanian, M.; Williams, A. An investigation of the thermal and catalytic behaviour of potassium in biomass combustion. *Proc. Combust. Inst.* **2007**, *31*, 1955−1963.

(27) van Eyk, P. J.; Ashman, P. J.; Alwahabi, Z. T.; Nathan, G. J. Simultaneous measurements of the release of atomic sodium, particle diameter and particle temperature for a single burning coal particle. *Proc. Combust. Inst.* **2009**, *32*, 2099−2106.

(28) van Eyk, P. J.; Ashman, P. J.; Alwahabi, Z. T.; Nathan, G. J. The release of water-bound and organic sodium from Loy Yang coal during the combustion of single particles in a flat flame. *Combust. Flame* **2011**, *158*, 1181−1192.

(29) Zhang, Z.-h.; Song, Q.; Alwahabi, Z. T.; Yao, Q.; Nathan, G. J. Temporal release of potassium from pinewood particles during combustion. *Combust. Flame* **2015**, *162*, 496−505.

(30) Viljanen, J.; Zhao, H.; Zhang, Z.; Toivonen, J.; Alwahabi, Z. T. Real-time release of Na, K and Ca during thermal conversion of biomass using quantitative microwave-assisted laser-induced breakdown spectroscopy. *Spectrochim. Acta, Part B* **2018**, *149*, 76−83.

(31) Hahn, D. W.; Omenetto, N. Laser-induced breakdown spectroscopy (LIBS), part II: review of instrumental and methodological approaches to material analysis and applications to different fields. *Appl. Spectrosc.* **2012**, *66*, 347−419.

(32) Le Drogoff, B.; Margot, J.; Chaker, M.; Sabsabi, M.; Barthélemy, O.; Johnston, T. W.; Laville, S.; Vidal, F.; Von Kaenel, Y. Temporal characterization of femtosecond laser pulses induced plasma for spectrochemical analysis of aluminum alloys. *Spectrochim. Acta, Part B* **2001**, *56*, 987−1002.

(33) Zhang, Z. H.; Alwahabi, Z.; Song, Q.; Yao, Q.; Lewis, D. Quantitative Detection of Na Released from Burning Microalgae Particle Using Laser-Induced Breakdown Spectroscopy. *Proceedings of the 9th Asia-Pacific Conference on Combustion, ASPACC 2013*, 2013.

(34) Demtröder, W. *Laser Spectroscopy*, 4th ed.; Berlin Springer, 2008.

(35) Graeser, P.; Schiemann, M. Char particle emissivity of two coal chars in oxy-fuel atmospheres. *Fuel* **2016**, *183*, 405−413.

(36) Hernberg, R.; Stenberg, J.; Zethraus, B. Simultaneous in situ measurement of temperature and size of burning char particles in a fluidized bed furnace by means of fiberoptic pyrometry. *Combust. Flame* **1993**, *95*, 191−205.

(37) Joutsenoja, T.; Heino, P.; Hernberg, R.; Bonn, B. Pyrometric temperature and size measurements of burning coal particles in a fluidized bed combustion reactor. *Combust. Flame* **1999**, *118*, 707−717.

(38) Salinero, J.; Gómez-Barea, A.; Tripiana, M.; Leckner, B. Measurement of char surface temperature in a fluidized bed combustor using pyrometry with digital camera. *Chem. Eng. J.* **2016**, *288*, 441−450.

(39) Arvelakis, S.; Jensen, P. A.; Dam-Johansen, K. Simultaneous thermal analysis (STA) on ash from high-alkali biomass. *Energy Fuel.* **2004**, *18*, 1066−1076.

(40) Tchoffor, P. A.; Davidsson, K. O.; Thunman, H. Effects of steam on the release of potassium, chlorine, and sulfur during char conversion, investigated under dual-fluidized-bed gasification conditions. *Energy Fuels* **2014**, *28*, 6953−6965.

(41) Fatehi, H.; He, Y.; Wang, Z.; Li, Z. S.; Bai, X. S.; Aldén, M.; Cen, K. F. LIBS measurements and numerical studies of potassium release during biomass gasification. *Proc. Combust. Inst.* **2015**, *35*, 2389−2396.

(42) Bhattacharya, S. P.; Wall, T. F. Development of emittance of coal particles during devolatilisation and burnoff. *Fuel* **1999**, *78*, 511–519.

Chapter 9

Conclusion

Concern for environmental impact and process analysis associated with elemental detection using traditional methods and the application of different elements in diversifying fields provide motivation for introducing potential technique for elemental detection. The requirement of precise, accurate and fast detection of precious and toxic elements is imperative of the mining industry, pharmaceutical and food industries, medical, space and defence in terms of exploration, analysis and imaging. In addition, combustion is a complex phenomenon, which release many elements, and compounds in time, which need to be, understand properly. Optical techniques are sensitive, selective and enable spatially localized, temporal measurements without physical sampling. In this thesis, two optical methods such as Laser Induced Breakdown Spectroscopy (LIBS) and Microwave-assisted Laser Induced Breakdown Spectroscopy (MW-LIBS) were demonstrated in ambient conditions to detect elements and to achieve the best limit of detection (LoD) as an analytical performance of MW-LIBS compared with LIBS. LIBS and MW-LIBS were applied in solid and liquid phases. In addition, LIBS were applied to monitor elemental release during thermal conversion of biomass fuels.

MW-LIBS has proven to be one of the most versatile signal enhancing techniques for achieving the improved LoD both in solid and liquid phase of a sample with reduced adverse self-absorption effects in high concentration condition. The MW-LIBS technique was more sensitive in liquid than in solid for achieving a superior LoD. It has been shown that MW-LIBS was able to achieve a strong signal with low laser energy, yet LIBS was unable to detect any signal by using silver at 338.28 nm. In this thesis, several elements such as chlorine, fluorine, bromine, palladium, ruthenium, silver and sulphur of different UEL were tested and calculated the LoD. In this study, molecular emissions were considered for measuring chlorine, fluorine and bromine with MW-LIBS to achieve the satisfactory LoD especially for chlorine, which was a challenge for LIBS measurement. The LoD evaluated in this work represents 10-fold improvement of Cl LoD reported in literature. This study also reports a quadruple improvement in the LoD of Br reported in the literature. In addition, this thesis reports an improved LoD of silver using very low laser energy (2 mJ) until today compared the data available in literature and first-time ruthenium measurement in liquid.

As MW-LIBS is a signal enhancement technique, it was important to understand the signal enhancement behaviour of MW-LIBS and the factors, which played the key role for signal enhancement. This thesis has reported the signal enhancement behaviour of MW-LIBS for the first time in ambient conditions. The effects of microwave power and detector gain on signal enhancement were assessed in this analysis. It was observed that the UEL plays an important role in signal enhancement. Using microwave radiation, significant enhancement is possible for the elements consisting of the UEL below 5eV; however, the cut-off limit of signal enhancement is found to be ~7eV. The MW-LIBS vs LIBS signal-to-noise (SNR) improvement was examined experimentally for Ag, Cu, Fe, Mg, Pb and S. Based on data, a simple model was developed to predict the SNR improvement concerning all elements. The model has predicted that the highest SNR improvements can be achieved for potassium, which are 370 times and 100 times, based on with and without detector gain, respectively. Based on atomic detection, it was demonstrated that microwave radiation would not improve SNR for elements such as fluorine, chlorine, bromine and iodine. In addition, the effect of microwave power and time delay on plasma temperature have been studied. It has confirmed that plasma temperature in MW-LIBS plasma is virtually independent of time and microwave exerts no reheating impact in LIBS plasma.

LIBS has been proven to be one of the most versatile techniques for monitoring high temperature chemistry. A simultaneous measurement of potassium (K) concentration and biomass temperature during biomass combustion have been developed with an improved LIBS calibration method. The effect of biomass type, Si content and initial mass of willow wood on the temporal release of K and particle temperature during biomass combustion were investigated. The main migration pathways of K during different combustion stages, especially the effect of Si on K release was also analysed. With the combustion of Si -free willow wood, it was found that the majority of K was released during ash-cooking stage, followed by char combustion stage, only a small amount of K was released during the initial devolatilization stage. With rice straw combustion, it was found that about 30% of the total K was released rapidly during the initial devolatilization stage, most likely as KCl. Results indicated that the release of K during the combustion of rice straw was suppressed by the presence of Si with the formation of K-silicates. The inhibitive effect of biomass Si content on K release was further demonstrated by the introduction of Si in willow wood. Results also indicated that Si had little effect on the release of K during devolatilization stage, but significantly inhibited the release of K during char combustion and ash-cooking stage.

MW-LIBS offers few advantages including the usability at low laser energy and the lifetime extension of the laser-induced-plasma. The former prevents significant samples damage and results in reliable averaging. The later, provides significant signal enhancement at low noise level. This translates to an excellent LoD. A longer plasma lifetime along with a prolonged detection gate provides some difficulties because emission from molecules and radicals become stronger, blocking large atomic spectral range. However, when the process of molecular formation and emission is carefully used, this process can benefit for detecting the elements, which are usually difficult in LIBS. Table 9.1 represents the signal enhancement and LoD calculated using MW-LIBS technique, which have already been placed in our papers for publication.

Table 9.1: Thesis Summary

Element	Matrix phase	Microwave power (Watt)	Detection type	Emitting species	Detection wavelength (nm)	Emitting state energy (eV)	SNR Improvement (fold)	LoD Solid: µg/g Liquid: ppm	Paper (#)
Cl	Solid	600	gated	Molecular (CaCl)	617.9	2	2.5	47±7	I
Cl	Solid	0	gated	Molecular (CaCl)	617.9	2	-	139±23	I
F	Solid	600	gated	Molecular (CaF)	605	2.04	8	106±6	II

F	Solid	0	gated	Molecular (CaF)	605	2.04	-	406.54	II
Br	Solid	750	gated	Molecular (CaBr)	627.1	1.97	15	0.2±0.04 %	II
Br	Solid	0	gated	Molecular (CaBr)	627.1	1.97	-	0.8%	II
Ru	Liquid	750	gated	Atomic	349.89	3.54	76	0.96±84	III
Ru	Liquid	0	gated	Atomic	349.89	3.54	-	-	III
Ag	Solid	450	gated	Atomic	338.28	3.77	-	4.5±1	IV
Ag	Solid	0	gated	Atomic	338.28	3.77	-	-	IV
Ag	Solid	450	Non-gated	Atomic	338.28	3.77	-	7±2.3	IV
Ag	Solid	0	Non-gated	Atomic	338.28	3.77	-	-	IV
Ag	Liquid	1200	gated	Atomic	338.28	3.77	-	0.38±51	IV
Ag	Liquid	0	gated	Atomic	338.28	3.37	-	-	IV
S	Solid	750	Non-gated	Atomic	180.73	6.86	1.4	312	V
S	Solid	0	Non-gated	Atomic	180.73	6.86	-	400	V
Pd	Solid	750	gated	Atomic	340.46	4.45	~15	5	Additional
Pd	Solid	0	gated	Atomic	340.46	4.45	-	40	Additional
Cu	Solid	750	gated	Atomic	324.745	3.817	65	-	V
Cu	Solid	750	Non-gated	Atomic	324.745	3.817	11.74	-	V
Mg	Solid	750	gated	Atomic	285.21	4.345	50	-	V
Mg	Solid	750	Non-gated	Atomic	285.21	4.345	9.56	-	V
Fe	Solid	750	gated	Atomic	344.1	3.65	65	-	V
Fe	Solid	750	Non-gated	Atomic	344.1	3.65	11.38	-	V
Pb	Solid	750	gated	Atomic	363.95	4.375	50	-	V
Pb	Solid	750	Non-gated	Atomic	363.95	4.375	9.24	-	V
K	Gas	0	gated	Atomic	766.49	1.62	-	-	VI

Moreover, these characteristics of MW-LIBS will lead an opportunity to analyse isotopes for rear elemental analysis, which needs further study. From this comprehensive study, it can be confirmed that MW-LIBS can be a leading detection technique compared to others that are currently used in industries specially XRF. The performance of MW-LIBS in liquid detection is even more than in solid detection when XRF is struggling in liquid detection. MW-LIBS can be applied easily on-line detection in gaseous phase. MW-LIBS systems, however, require the use microwave generators, waveguides and near field applicators. These additional elements add to the complexity of the detection setup, when it compares to LIBS. Furthermore, a MW-LIBS setup, with a near field applicator, is not suitable for standoff applications.

Additional paper

Improvement of palladium limit of detection by Microwave-assisted Laser-Induced Breakdown Spectroscopy

Ahlam A. Al Shuaili[†], Ahlam M. Al Hadhrami[†], MA Wakil and Zeyad T. Alwahabi[*]

School of Chemical Engineering and Advanced Materials, The University of Adelaide, SA 5005, Australia.

[†] The first two authors contributed equally to this work

**E-mail: zeyad.alwahabi@adelaide.edu.au*

Statement of Authorship

Title of Paper	**Improvement of palladium limit of detection by microwave-assisted laser induced breakdown spectroscopy**	
Publication Status	☑ Published ☐ Submitted for Publication	☐ Accepted for Publication ☐ Unpublished and Unsubmitted work written in manuscript style
Publication Details	Spectrochimica Acta Part B: Atomic Spectroscopy, 2019,159, 105666	

Principal Author 1

Name of Principal Author	Ahlam A. Al Shuaili		
Contribution to the Paper	I was responsible for the development of the measurement technique under the principal supervisor of Associate Professor Zeyad Alwahabi. I performed part of the experiment, wrote the draft of the manuscript,		
Overall percentage (%)	35%		
Certification:	This paper reports on original research I conducted during the period of my Bachelor Degree and is not subject to any obligations or contractual agreements with a third party that would constrain its inclusion in this thesis. I am the primary author of this paper.		
Signature		Date	22.04.2020

Principal Author 2

Name of Principal Author	Ahlam M. Al Hadhrami		
Contribution to the Paper	I was responsible for the development of the measurement technique under the principal supervisor of Associate Professor Zeyad Alwahabi. I performed part of the experiment.		
Overall percentage (%)	35%		
Certification:	This paper reports on original research I conducted during the period of my Bachelor Degree and is not subject to any obligations or contractual agreements with a third party that would constrain its inclusion in this thesis. I am the primary author of this paper.		
Signature		Date	22.04.2020

Co-Author Contributions

By signing the Statement of Authorship, each author certifies that:

i. the candidate's stated contribution to the publication is accurate (as detailed above);
ii. permission is granted for the candidate in include the publication in the thesis; and
iii. the sum of all co-author contributions is equal to 100% less the candidate's stated contribution.

Name of Co-Author	

Contribution to the Paper	I jointly contributed to both experiment, data processing and refining the manuscript and addressed the comments and suggestion from other authors in subsequent revisions of the manuscript.		
Overall percentage (%)	20%		
Certification:	This paper reports on original research I conducted during the period of my Higher Degree by Research candidature and is not subject to any obligations or contractual agreements with a third party that would constrain its inclusion in this thesis. I am the co-author of this paper.		
Signature		Date	22.04.2020

Name of Co-Author	Zeyad T. Alwahabi		
Contribution to the Paper	I was principal supervisor for the development of the work, contributed to both data interpretation and refining the manuscript. I hereby certify that statement of contribution is accurate and I have given written permission for this paper to be included in this thesis.		
Overall percentage (%)	10%		
Signature		Date	29.04.2020

Spectrochimica Acta Part B 159 (2019) 105666

Contents lists available at ScienceDirect

Spectrochimica Acta Part B

journal homepage: www.elsevier.com/locate/sab

Analytical note

Improvement of palladium limit of detection by microwave-assisted laser induced breakdown spectroscopy

Ahlam A. Al Shuaili[1], Ahlam M. Al Hadhrami[1], M.A. Wakil, Zeyad T. Alwahabi*

School of Chemical Engineering, University of Adelaide, Adelaide, SA 5005, Australia

ARTICLE INFO

Keywords:
Laser-induced breakdown spectroscopy
Microwave assisted
Signal enhancement
Palladium detection

ABSTRACT

Detecting elements such as heavy metals is important in many industrial processes. The techniques currently used are time consuming and require excessive sample preparation. In this paper, we demonstrate microwave-assisted laser-induced breakdown spectroscopy (MW-LIBS) to detect palladium (Pd) in solid samples at ambient conditions. Microwave radiation was introduced by a near field applicator to couple the microwave radiation with the plasma. The results were a 92–fold enhancement in palladium signal with 8-fold improvement in the limit of detection at laser energy levels below 5 mJ (1250 J/cm^2 laser pulse fluence). We also investigate the optimum experimental parameters of palladium detection for both laser-induced breakdown spectroscopy (LIBS) and MW-LIBS. The maximum signal to noise ratio improvement was achieved at microwave power of 750 W and laser pulse fluence of 157 J/cm^2 for Pd I 340.46 nm. Finally, we examine the location of the near field applicator (NFA) with respect to the sample to show that the MW-LIBS signal strength was significantly affected by the vertical position compared to the horizontal. The detection limits of palladium with LIBS and MW-LIBS were 40 ppm and 5 ppm respectively.

1. Introduction

Element detection is a requirement in several industrial applications, including in the pharmaceutical, water treatment, mining and food industries. In the food industry, the detection of heavy metals is necessary to ensure that products are top quality, as heavy metals are a common contaminant [1]. Element detection also plays an important role in leaching, recovery and the recycling of precious metals or nuclear waste [2,3].

There are several techniques currently available for metal detection in industry. Some of the common techniques are induced coupled plasma spectroscopy ICP [4], atomic absorption [5] and X-ray fluorescents [6], which show outstanding results and extreme sensitivity. Despite their advantages, these techniques suffer from some common drawbacks; they are time consuming and require excessive sample preparation [7–12].

Laser-induced breakdown spectroscopy (LIBS) is an analytical technique in which a laser beam is used to detect elements directly from samples [13]. In the past decade, the application of LIBS has grown rapidly due to its real time analysis and the minimal preparation required, which lead to relatively fast measurements compared to other techniques [13]. LIBS has attracted interest in the industrial processes, as it is the ideal candidate for metal detection.

The disadvantages of LIBS include relatively low pulse to pulse repeatability, and low sensitivity [13,14]. To overcome these, several methods have been introduced. One of the most common techniques to increase the sensitivity of LIBS is the use of double pulse laser to create the plasma [2,14–17], which has attracted great interest due to its ability to enhance the signal as well as improve the limit of detection (LoD) [14]. Another common enhancing technique is the use of an additional source of energy to enhance the plasma of the element and to increase the sensitivity of detection [14]. These sources of secondary energy can be provided in many forms, such as resonant laser [18], spark discharge [19], stable flame [20], long pulse laser [21] and microwave-assisted laser-induced breakdown spectroscopy (MW-LIBS) [7–12,22].

MW-LIBS has been proven to enhance sensitivity by increasing the lifetime of the plasma [7–12,22]. The external energy supplied, using microwave radiation, sustains the free electrons present within the laser-induced plasma. These reenergized free electrons act as an excitation source, via collisional processes, extending the life of the short-lived laser-induced plasma. The coupling of microwave radiation with the plasma allows sufficient time for detection [11,8,12]. It has been shown recently that, by using MW-LIBS, the self-absorption issue can be

---

* Corresponding author.
E-mail address: zeyad.alwahabi@adelaide.edu.au (Z.T. Alwahabi).

[1] The first two authors contributed equally.

https://doi.org/10.1016/j.sab.2019.105666
Received 22 February 2019; Received in revised form 30 July 2019; Accepted 30 July 2019

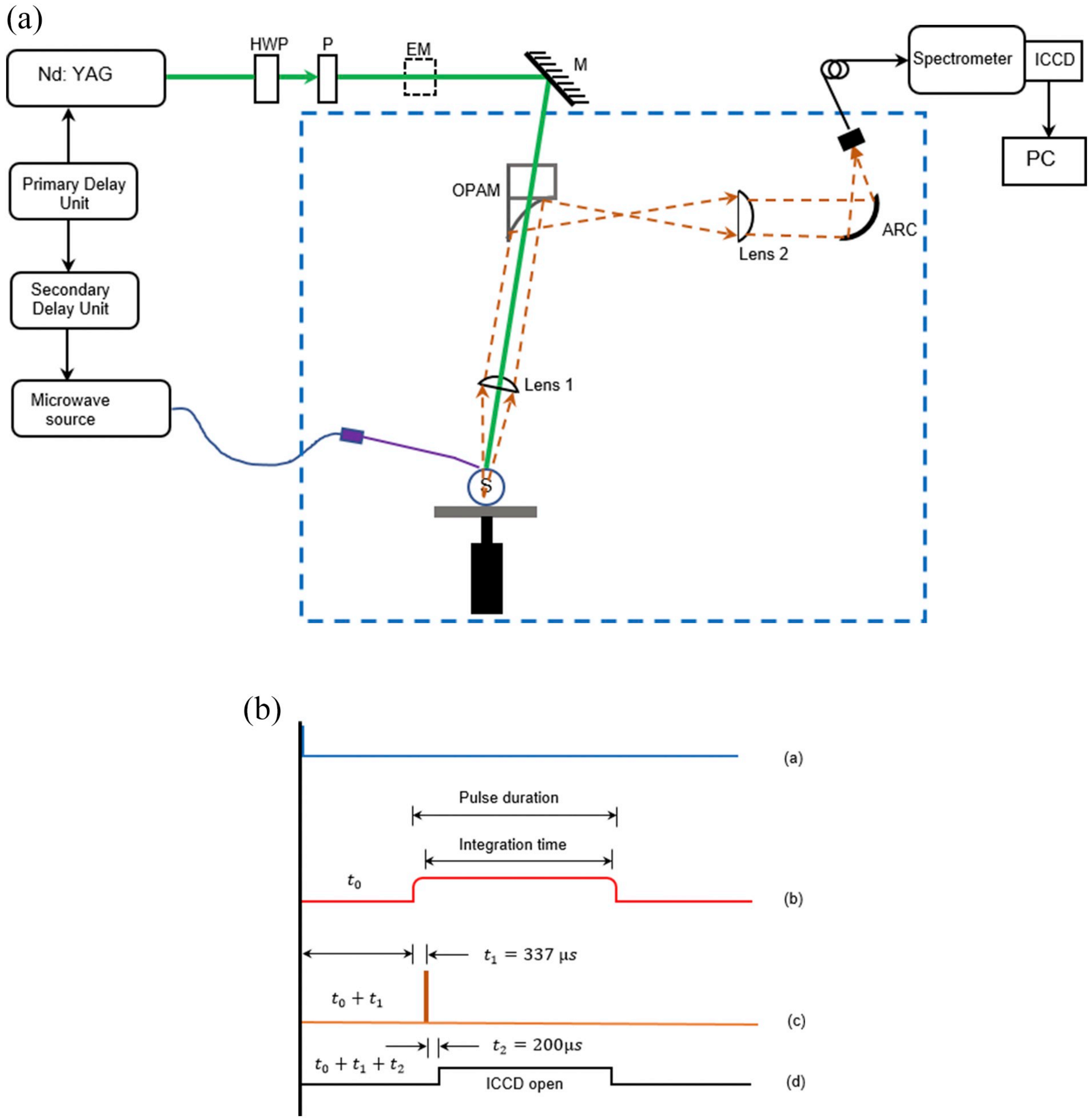

Fig. 1. (a): Schematic of the experimental setup, where HWP is halfwave plate, P is polarizer, EM is energy meter, M is mirror, OPAM is off-axis parabolic mirror, ARC is achromatic reflective coupler, and S is sample. (b): The timing diagram showing the primary pulse (t_0), a, the microwave trigger pulse, b, the laser trigger pulse, c, and the ICCD trigger pulse, d.

reduced significantly [11,23].

Several ways have been demonstrated to introduce MW power to the plasma, such as by using an enclosed cavity [8,10] or antenna [8,10,22], and most recently with a near field applicator (NFA) [11,12,24]. MW enhancement in the LoD using an enclosed cavity was 20-fold, 24-fold and 12.5-fold for copper [9], oxide calcium [25] and europium [10] respectively. The use of NFA at ambient condition achieved 93-fold and 11.5-fold improvements in the LoD for copper in solid samples [11] and indium in liquid traces [12] respectively.

To the best of our knowledge, MW-LIBS has not yet been demonstrated for palladium (Pd) detection. Palladium is a platinum group metal and it plays a key role in several industrial applications. Approximately 40% of automobile catalysts consist of palladium [26]; it is a cheaper alternative to the platinum fuel cell [27,28]. However, palladium is a limited natural resource and the cost of extracting and recycling it is high [29]. A sensitive detection method for palladium in the recyclable product would be valuable. Palladium detection is also useful in the pharmaceutical and food industries [30]. For example, palladium is used in some pharmaceutical tools. Here, detection of palladium is required due to the potential for severe health damage that may be caused by the complex biomolecules that are formed when palladium is combined with DNA and RNA [29]. A restriction limit of palladium contamination in the final product is strictly enforced.

Several studies have detected palladium by conventional LIBS. A study by Asimellis et al. [26] investigated palladium detection in a real automobile catalyst at a low concentration of 127 ppm, where several

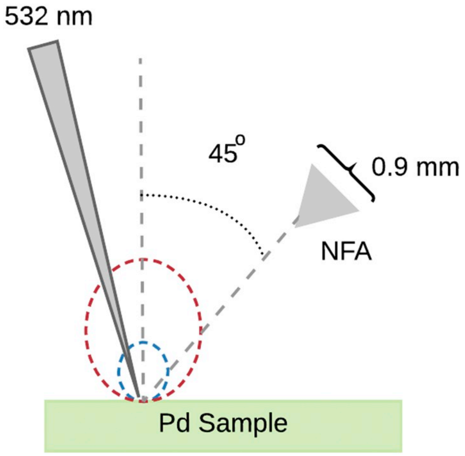

Fig. 2. Schematic presentation of the near field applicator (NFA) location related to the solid sample and the laser beam. The plasma without and with microwave is shown in blue and red respectively. (For interpretation of the references to colour in this figure legend, the reader is referred to the web version of this article.)

lines were observed for palladium detection, with high intensity lines at wavelengths of 340.46 nm and 342.12 nm [26]. Identical lines were also observed by Snyder et al. [28] where palladium was detected on a proton exchange membrane fuel cell in aqueous suspension [28]. Palladium was also detected in a bacterial cellulose membrane in both wet and dry matrices [31]. Here, the dry membrane was concluded to be the best matrix for palladium detection.

This paper demonstrates the effect of MW-LIBS in palladium spectral signals and the effect of various experimental parameters, such as MW power and laser pulse dependence, NFA position dependence, and line dependence of MW-LIBS on the signal enhancement.

2. Experimental set up

Several calibration samples containing a range of palladium concentrations (100 to 1000 ppm) were fabricated by mixing 0.1% palladium stock solution in 5 % HCl with 10 *wt.* % of sodium chloride solution and 5 *wt.* % of organic binder solution (polyethylene glycol). The additional water in the solutions was then evaporated at 250°C. The paste mixtures were transformed into a cylindrical uniform disc of 21 mm in diameter and 3.5 mm in thickness. The samples were dried at a temperature of 51 °C for 20 min.

The experimental setup of MW-LIBS used for this work is presented schematically in Fig. 1(a). The 10 Hz, second harmonic output from a Q-switch Nd:YAG laser, Quantel (Brilliant B), ~6 ns was used. The pulse energy was controlled by a half-wave plate (HWP) and Glan-laser polarizer (P). The laser energy was measured with a Pyroelectric sensor (Thorlabs, ES 220C). The beam was focussed onto the sample surface using a fused silica lens (L1, with f = 100 mm). The spot size obtained at the focal point was estimated to be 140 μm^2 while the propagation of laser beam was at an angle of 15° to the verticle. To achieve the ablation from a fresh sample surface for each shot, the sample was placed on a rotating disk at 7 rotations per minute. A second CW laser, with a camera, was used to monitor the exact distance between the sample surface and L1. The timing diagram for the experiment is shown in Fig. 1(b).

A water cooled pulsed-microwave system operated at 2.45 GHz (Seirem), shown in the Fig. 1(a), was used. The microwave radiation was directed via a WR340 waveguide to a 3-stub impedance tuner and then to a waveguide-to-coaxial adaptor (WR340RN) through a quartz window. The waveguide-to-coaxial adaptor was connected to a 1 m flexible coaxial cable (50 Ω NN cable) with 0.14 dB @ 2.45 GHz. A semi rigid cable (RG402/U) was then connected at the end of the coaxial cable. The other end of the semi rigid cable was connected to a NFA, as was shown [11,32]. The NFA pointed tip was located at 45 ° with a distance of 0.5 mm vertically and horizontally from the solid sample, as shown in Fig. 2. A pulse generator (Aim-TTi) was used to control the microwave duration and power, and the microwave pulse was trigged prior to the laser pulse with a pulse duration of 1 ms.

The ablation beam was directed to pass through a perforated parabolic mirror (FL = 152 mm), then to focused by a plano-convex lens (FL = 100 mm), L1, onto the sample by a plano-convex UV fused silica lens with focal length of 100 mm and diameter 50.8 mm. The emission was collimated by L1 and then focused by an off-axis parabolic mirror (OPAM). A second lens L2 (FL = 20 mm) was used to couple the emission onto an Achromatic Reflective Coupler (ARC), which is connected to a 7-fibre bundle (Thorlabs, BFL200HS02). The fibre was

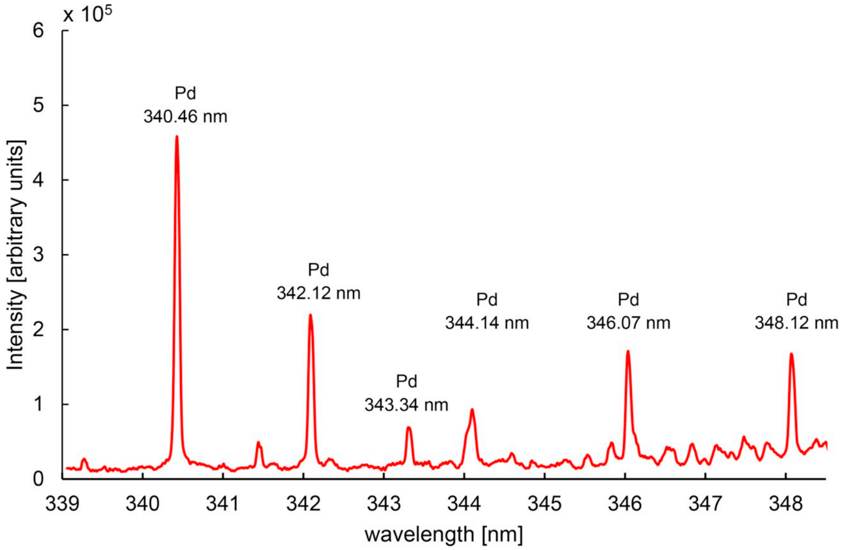

Fig. 3. Typical MW-LIBS spectra of 0.1 wt% Pd recorded at 1006 J/cm^2 laser fluence, 960 W microwave power, 450 ns gate-delay, 1 ms gate-width, and the spectral is for an accumulation of 100 shots.

Table 1
Summary of Pd I spectral lines in the present work [33].

Wavelength (nm)	Transition probability (s^{-1})	E_i (cm^{-1})	E_k (cm^{-1})	Lower level J_i	Upper level J_k
340.46	1.3×10^8	6564.148	35,927.948	3	4
342.12		7755.025	36,975.973	2	2
343.34		11,721.809	40,838.874	2	1
344.14		11,721.809	40,771.510	2	2
346.07	3.0×10^7	6564.148	35,451.443	3	3
348.977		11,721.8	40,368.796	2	1

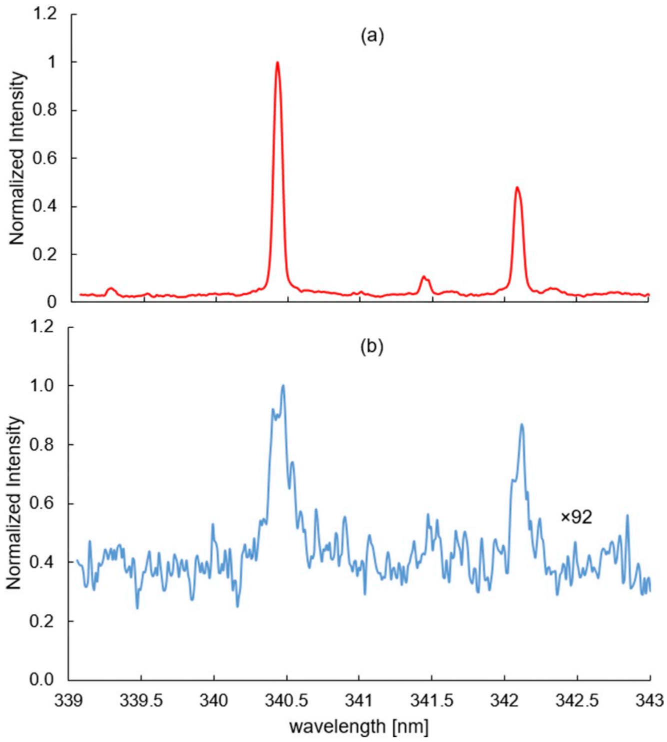

Fig. 4. Typical MW-LIBS, a, and LIBS, b, spectra of 0.08 wt% Pd, recorded at 650 J/cm^2 laser fluence, 960 W microwave power, 450 ns gate-delay and 1 ms gate-width for 100 shots. The intensity of the LIBS signal was multiplied by a factor of 92 for clarity.

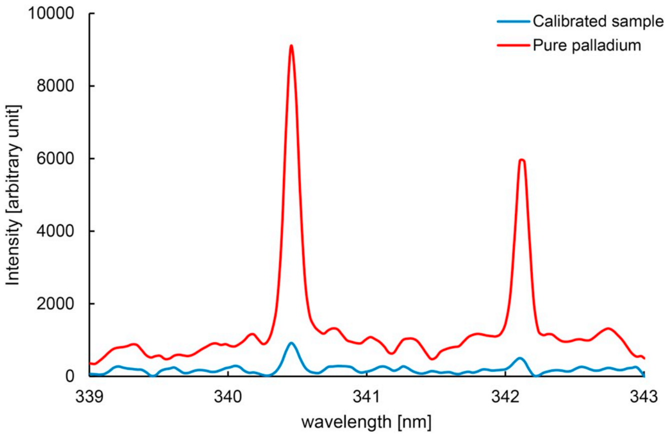

Fig. 5. Typical MW-LIBS spectra of pure sample (99 wt% Pd), red and calibrated sample (0.08 wt% Pd), blue, recorded at 650 J/cm^2 laser fluence, 960 W microwave power, 450 ns gate-delay, 1 ms gate-width for 100 shots. (For interpretation of the references to colour in this figure legend, the reader is referred to the web version of this article.)

connected to a spectrometer (Andor, Shamrock 500i with 2400 lines/mm grating) equipped with an intensifier camera, ICCD, (Andor, iStar). As shown in Fig. 1(a).

The optical line, sample holder, NFA and one end of the fibre were placed inside an aluminum box to minimize the residual microwave radiation, as shown in Fig. 1(a). One side of the aluminum box was covered with metal mesh acting as an observation window. The spectrometer (Andor Shamrock 500i) with a grating of 2400 lines/mm has a spectral resolving power of 10,000; that is, the spectral resolution is 0.031 nm in the spectral range of 320–332 nm. The maximum attainable wavelength range for the spectrometer, with the Holographic grating, is 200–705 nm. An intensified CCD camera (Andor, iStar) was used to record the spectral signal, which was synchronized with the laser and the microwave generator.

3. Results & discussion

Spectral emissions for both LIBS and MW-LIBS were recorded for palladium in the range of 339–350 nm where several lines were observed with various intensity, as shown in Fig. 3 and Table 1, which summarise the utilities' energy levels for each line. However, two transitions of palladium, namely 340.46 nm and 342.12 nm with the upper energy state of 35,927.948 cm^{-1} and 36,975.973 cm^{-1}, were selected for analyzing experimental parameters, though only 340.46 nm was used to calculate LoD (Fig. 4).

Fig. 5 demonstrates the spectral emissions for the 0.08 wt% palladium calibrated sample with the pure palladium sample (99 wt%) to validate the signal profile with the pure sample. Both samples show similar profiles with no variation in the signal at both 340.46 nm and 342.12 nm, which validates the accuracy of the measured calibrated sample.

The signal to noise ratio (SNR) improvement as a function of MW power at various laser fluences was measured for the palladium calibrated sample of 0.08 wt% and is shown in Fig. 6. The gate-delay and gate-width were kept at a fixed value of 450 ns and 1 ms respectively. Fig. 6 shows a linear increase of SNR improvement with increasing MW power, reaching a maximum near ~750 W and then a decrease with the increase of MW power after that point.

In relation to the laser fluence selected, Fig. 6 also shows that maximum SNR improvement can be achieved at MW power 750 W for each element. The maximum enhancement of the MW-LIBS can be achieved at the lowest laser fluence of 157 J/cm^2. This is due to the ease of MW power coupling at a lower fluence. Increasing the laser fluence will result in an increase in electron density of the plasma's core, which in turn will result in a reduction of MW power to penetrate to the plasma for the coupling and a measurement similar to that of a conventional LIBS [12,32]. The larger volume will reduce the influence of the MW to re-excite the core and instead it will excite the plasma fringes, as demonstrated by Chen et al. [32].

Fig. 7 shows the noise, signal enhancement and SNR improvement as a function of MW power. Note that increasing the MW power results in an increase in the signal enhancement until it reaches a maximum point and then starts to decrease. This may be related to the significant

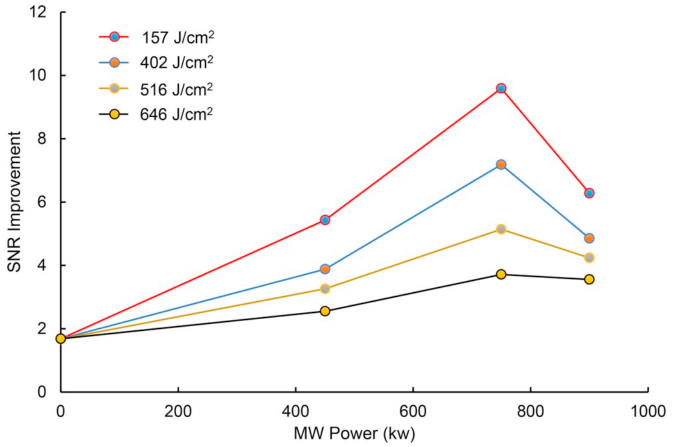

Fig. 6. Signal to noise ratio improvement of 0.08% Pd at a 450 ns gate-delay and 1 ms gate-width for 100 shots.

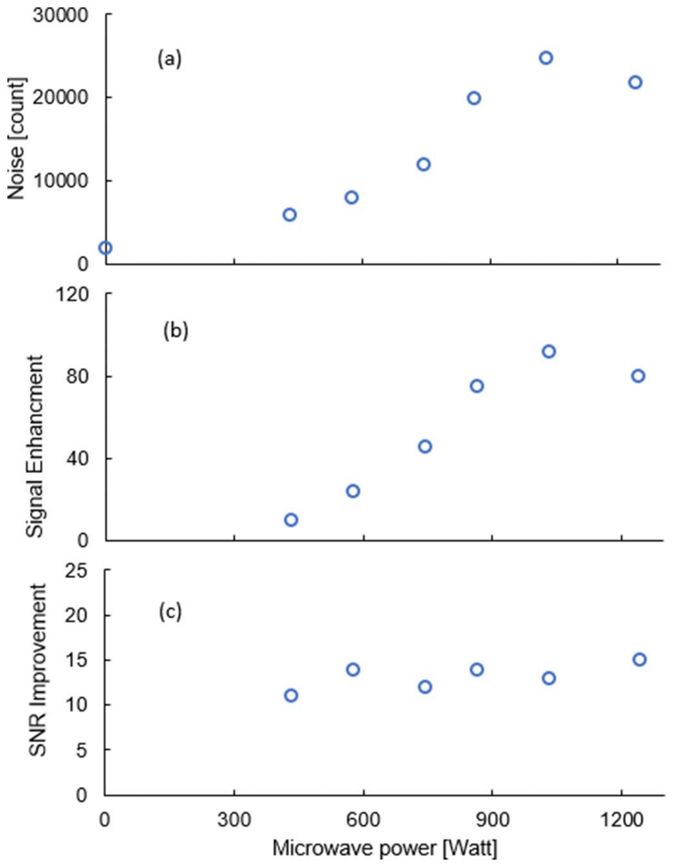

Fig. 7. The (a) noise level (counts), (b) signal enhancement, and (c) SNR improvement of 0.1 wt% Pd at laser pulse fluence of 650 J/cm^2, 450 ns gate-delay, 1 ms gate-width and an accumulation of 100 shots.

increase of the noise level at that stage, where increasing the MW power will significantly increase the noise level in addition to increasing the signal intensity. This is also shown in Fig. 7(c) as a nearly flat trend of the SNR improvement with the increase of MW power. This is due to the non-linear increase of the plasma's volume in relation to the MW power. It creates a non-stable plasma and a measurement that generates a significant noise level, as was noted by Iqbal et al. [24] for the study of the intensity and the plasma's volume as a function of MW power.

Another significant factor affecting MW power enhancement is the position of the NFA relative to the laser beam spot on the sample. The effect of signal enhancement as a function of NFA position both vertically and horizontally has been evaluated.

Fig. 8 represents the effect of the vertical and horizontal position on the signal intensity. A constant horizontal position of 0.4 mm was considered for the effect of vertical distance measurement, and a 0.7 mm vertical position was fixed for the horizontal distance measurement. Fig. 8 shows a significant sensitivity of signal intensity with both horizontal and vertical locations of NFA from the point of laser heating on the sample surface. Note that the signal intensity is significantly sensitive to the vertical location of the NFA compared to the horizontal position of the NFA. For each 0.1 mm change in vertical position of the NFA, the signal intensity drops significantly until it reaches the effect of convectional LIBS, where the decreasing trend of signal intensity with the horizontal distance is not so fast. This might be due to the actual shape of the palladium plasma. From the measurement, it appears that the shape is a horizontal oval where increasing the NFA distance vertically represents a measurement in the plasma fringes rather in the core. The increasing horizontal direction still allows the MW coupling since the NFA is still located in the plasma. The closer the NFA is to the sample, the higher the electric field, which produces higher enhancement of the signal due to higher coupling.

Fig. 9 shows the dependence of the signal intensity as a function of horizontal distance of the NFA at various vertical distances. The effect of the horizontal distance can be varied by increasing the vertical distance of the NFA from the laser beam. The signal intensity becomes more sensitive to the horizontal distance with the increase of the vertical position of the NFA, which might be due to the plasma dimensions and shape. In Fig. 9, it can also be seen that the optimum position for the MW power enhancement can be at the point of 0.7 mm vertical and 0.2 mm horizontally for the NFA position which is the point that represents the highest signal enhancement and the lowest noise level which was selected for the study carried.

Calibration of palladium in solid samples was done for both MW-LIBS and conventional LIBS under identical experimental conditions of 650 J/cm^2 laser pulse fluence, 750 W microwave power, 450 ns gate-delay and 1 ms gate-width. The quantitative detection was carried over the calibrated salt sample with various palladium concentrations. Fig. 10 represents the calibration curve for both LIBS and MW-LIBS, with linear fitting for the maximum intensity line of 340.46 nm. The slope of MW-LIBS is greater than the slope of LIBS only, which represents the increase in detection sensitivity with MW-LIBS. Detection increases almost the same as the increase in concentration of palladium in the sample, which corresponds to the accurate measurement and lower LoD obtained.

The LoD of palladium was calculated using Eq. (1):

$$LoD = \frac{k.\, s_i}{b} \tag{1}$$

where k is a constant (set to 3), s_i is the standard deviation of the background, and b is the slope of the calibration curve. It was found that the LoD is 40 ppm and 5 ppm for LIBS and MW-LIBS respectively. This leads to an 8-fold improvement in the LoD of palladium in solid samples. This improvement factor is within the range of previous quantitative MW-LIBS studies for solid phase [8–12,24,25]. As mentioned previously, palladium detection using LIBS has been investigated in several studies for both calibrating and mapping palladium samples unfortunately, even though some of the studies carried out were for quantitative measurement of palladium, there has not been a clear identification of LoD. Therefore, the LoD obtained for this study cannot be compared to others.

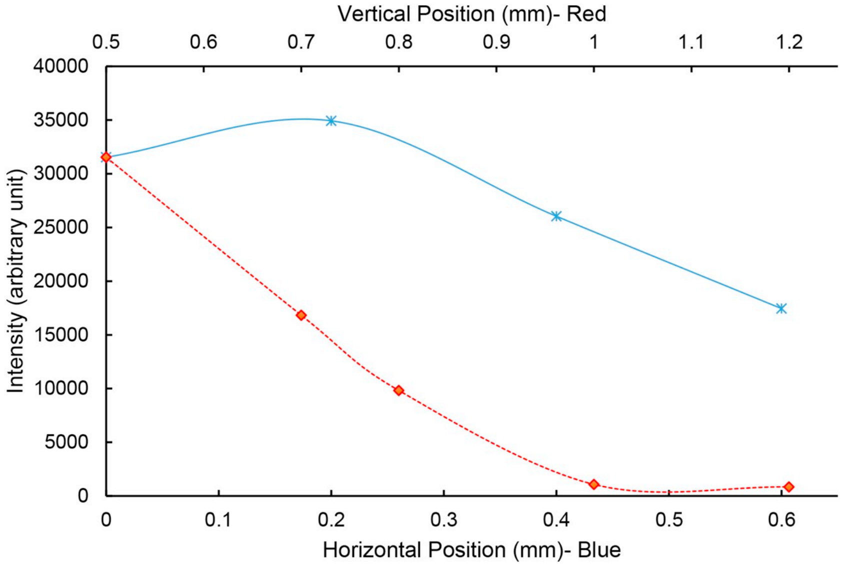

Fig. 8. The dependence of MW-LIBS signal intensity on the vertical distance of the NFA above the sample surface and the horizontal distance to the laser beam measured at 650 J/cm^2 laser fluence, 750 W microwave power, 450 ns gate-delay, 1 ms gate-width with an accumulation of 100 shots.

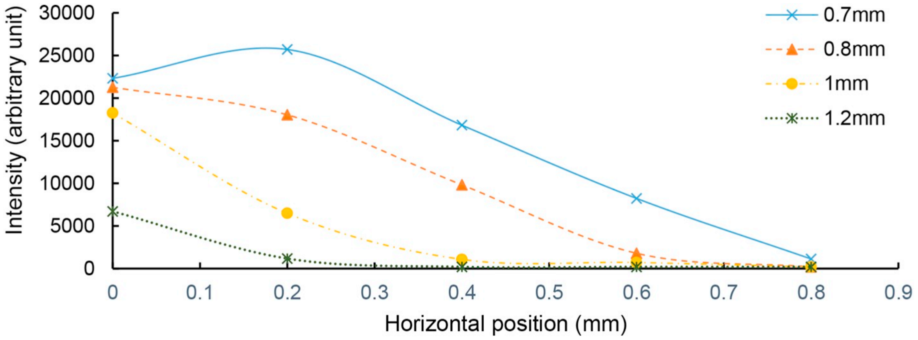

Fig. 9. Intensity as a function of horizontal position of the NFA, relative to the vertical position, indicated, of the NFA of 0.08 wt% Pd sample at 650 J/cm^2 laser fluence, 750 W microwave power, 450 ns gate-delay, 1 ms gate-width with the accumulation of 100 shots.

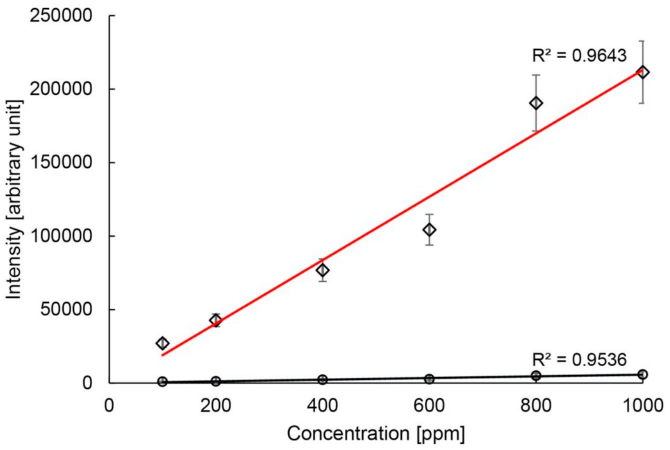

Fig. 10. Calibration curves of Pd (340.46 nm) with MW-LIBS, diamond, and LIBS, circle, at 650 J/cm^2 laser fluence, 750 W microwave power, 450 ns gate-delay, 1 ms gate-width. Error bars are standard deviation of 100 shots.

4. Conclusion

This study has demonstrated, for the first time, that MW-LIBS detects palladium in solid samples. We found that the signal was enhanced 92-fold with MW-LIBS, leading to an 8-fold improvement in LoD by MW-LIBS when compared with LIBS. The detection limit of palladium with LIBS and MW-LIBS were 40 ppm and 5 ppm respectively. The laser pulse fluence shows a maximum enhancement for the signal to noise at lower laser energy independent of the applied MW power. It was found that a point of maximum intensity is reached at a microwave power of 750 W. The position of NFA, was also demonstrated for the study to improve the LoD.

Novelty statement

We demonstrated for the first-time new LoD for Pd using an optimised-Microwave assisted Laser Induced Breakdown Spectroscopy. We achieved 11 folds improved in the detection sensitivity of Pd.

A new LoD of 5 ppm of Pd in sold sample was recorded using laser energy below 5 mJ.

References

[1] T. Balaji, S.A. El-Safty, H. Matsunaga, T. Hanaoka, F. Mizukami, Optical sensors based on nanostructured cage materials for the detection of toxic metal ions, Angew. Chem. 118 (2006) 7360–7366.

[2] K. Rifai, S. Laville, F. Vidal, M. Sabsabi, M. Chaker, Quantitative analysis of metallic traces in water-based liquids by UV-IR double-pulse laser-induced breakdown spectroscopy, J. Anal. At. Spectrom. 27 (2012) 276–283.

[3] O. Samek, D.C. Beddows, J. Kaiser, S.V. Kukhlevsky, M. Liska, H.H. Telle, A.J. Whitehouse, Application of laser-induced breakdown spectroscopy to in situ analysis of liquid samples, Opt. Eng. 39 (2000) 2248–2263.

[4] E. Herincs, M. Puschenreiter, W. Wenzel, A. Limbeck, A novel flow-injection method for simultaneous measurement of platinum (Pt), palladium (Pd) and rhodium (Rh) in aqueous soil extracts of contaminated soil by ICP-OES, J. Anal. At.

Spectrom. 28 (2013) 354–363.
[5] J.L. Molloy, J.A. Holcombe, Detection of palladium by cold atom solution atomic absorption, Anal. Chem. 78 (2006) 6634–6639.
[6] K. Van Meel, A. Smekens, M. Behets, P. Kazandjian, R. Van Grieken, Determination of platinum, palladium, and rhodium in automotive catalysts using high-energy secondary target X-ray fluorescence spectrometry, Anal. Chem. 79 (2007) 6383–6389.
[7] A. Khumaeni, K. Akaoka, M. Miyabe, I. Wakaida, The role of microwaves in the enhancement of laser-induced plasma emission, Front. Phys. 11 (2016) 114209.
[8] Y. Liu, M. Baudelet, M. Richardson, Elemental analysis by microwave-assisted laser-induced breakdown spectroscopy: evaluation on ceramics, J. Anal. At. Spectrom. 25 (2010) 1316–1323.
[9] Y. Liu, B. Bousquet, M. Baudelet, M. Richardson, Improvement of the sensitivity for the measurement of copper concentrations in soil by microwave-assisted laser-induced breakdown spectroscopy, Spectrochim. Acta B At. Spectrosc. 73 (2012) 89–92.
[10] M. Tampo, M. Miyabe, K. Akaoka, M. Oba, H. Ohba, Y. Maruyama, I. Wakaida, Enhancement of intensity in microwave-assisted laser-induced breakdown spectroscopy for remote analysis of nuclear fuel recycling, J. Anal. At. Spectrom. 29 (2014) 886–892.
[11] J. Viljanen, Z. Sun, Z.T. Alwahabi, Microwave assisted laser-induced breakdown spectroscopy at ambient conditions, Spectrochim. Acta B At. Spectrosc. 118 (2016) 29–36.
[12] M. Wall, Z. Sun, Z.T. Alwahabi, Quantitative detection of metallic traces in water-based liquids by microwave-assisted laser-induced breakdown spectroscopy, Opt. Express 24 (2016) 1507–1517.
[13] D.W. Hahn, N. Omenetto, Laser-induced breakdown spectroscopy (LIBS), part I: review of basic diagnostics and plasma–particle interactions: still-challenging issues within the analytical plasma community, Appl. Spectrosc. 64 (2010) 335A–366A.
[14] D.W. Hahn, N. Omenetto, Laser-induced breakdown spectroscopy (LIBS), part II: review of instrumental and methodological approaches to material analysis and applications to different fields, Appl. Spectrosc. 66 (2012) 347–419.
[15] V. Babushok, F. DeLucia Jr., J. Gottfried, C. Munson, A. Miziolek, Double pulse laser ablation and plasma: laser induced breakdown spectroscopy signal enhancement, Spectrochim. Acta B At. Spectrosc. 61 (2006) 999–1014.
[16] F. Colao, V. Lazic, R. Fantoni, S. Pershin, A comparison of single and double pulse laser-induced breakdown spectroscopy of aluminum samples, Spectrochim. Acta B At. Spectrosc. 57 (2002) 1167–1179.
[17] D.-H. Lee, S.-C. Han, T.-H. Kim, J.-I. Yun, Highly sensitive analysis of boron and lithium in aqueous solution using dual-pulse laser-induced breakdown spectroscopy, Anal. Chem. 83 (2011) 9456–9461.
[18] D. Cleveland, R.G. Michel, Quantitative analysis by resonant laser ablation with optical emission detection: resonant laser-induced breakdown spectroscopy, Microchem. J. 95 (2010) 120–123.
[19] O.A. Nassef, H.E. Elsayed-Ali, Spark discharge assisted laser induced breakdown spectroscopy, Spectrochim. Acta B At. Spectrosc. 60 (2005) 1564–1572.
[20] L. Liu, S. Li, X. He, X. Huang, C. Zhang, L. Fan, M. Wang, Y. Zhou, K. Chen, L. Jiang, Flame-enhanced laser-induced breakdown spectroscopy, Opt. Express 22 (2014) 7686–7693.
[21] D.K. Killinger, S.D. Allen, R.D. Waterbury, C. Stefano, E.L. Dottery, Enhancement of Nd: YAG LIBS emission of a remote target using a simultaneous CO 2 laser pulse, Opt. Express 15 (2007) 12905–12915.
[22] A. Khumaeni, M. Miyabe, K. Akaoka, I. Wakaida, The effect of ambient gas on measurements with microwave-assisted laser-induced plasmas in MA-LIBS with relevance for the analysis of nuclear fuel, J. Radioanal. Nucl. Chem. 311 (2017) 77–84.
[23] Y. Tang, J. Li, Z. Hao, S. Tang, Z. Zhu, L. Guo, X. Li, X. Zeng, J. Duan, Y. Lu, Multielemental self-absorption reduction in laser-induced breakdown spectroscopy by using microwave-assisted excitation, Opt. Express 26 (2018) 12121–12130.
[24] A. Iqbal, Z. Sun, M. Wall, Z.T. Alwahabi, Sensitive elemental detection using microwave-assisted laser-induced breakdown imaging, Spectrochim. Acta B At. Spectrosc. 136 (2017) 16–22.
[25] A. Khumaeni, T. Motonobu, A. Katsuaki, M. Masabumi, W. Ikuo, Enhancement of LIBS emission using antenna-coupled microwave, Opt. Express 21 (2013) 29755–29768.
[26] G. Asimellis, N. Michos, I. Fasaki, M. Kompitsas, Platinum group metals bulk analysis in automobile catalyst recycling material by laser-induced breakdown spectroscopy, Spectrochim. Acta B At. Spectrosc. 63 (2008) 1338–1343.
[27] E. Antolini, Palladium in fuel cell catalysis, Energy Environ. Sci. 2 (2009) 915–931.
[28] S.C. Snyder, W.G. Wickun, J.M. Mode, B.D. Gurney, F.G. Michels, The detection of palladium particles in proton exchange membrane fuel-cell water by laser-induced breakdown spectroscopy (LIBS), Appl. Spectrosc. 65 (2011) 642–647.
[29] B. Liu, H. Wang, T. Wang, Y. Bao, F. Du, J. Tian, Q. Li, R. Bai, A new ratiometric ESIPT sensor for detection of palladium species in aqueous solution, Chem. Commun. 48 (2012) 2867–2869.
[30] C.E. Garrett, K. Prasad, The art of meeting palladium specifications in active pharmaceutical ingredients produced by Pd-catalyzed reactions, Adv. Synth. Catal. 346 (2004) 889–900.
[31] M. Martin, B. Evans, H. O'Neill, J. Woodward, Laser-induced breakdown spectroscopy used to detect palladium and silver metal dispersed in bacterial cellulose membranes, Appl. Opt. 42 (2003) 6174–6178.
[32] S.J. Chen, A. Iqbal, M. Wall, C. Fumeaux, Z.T. Alwahabi, Design and application of near-field applicators for efficient microwave-assisted laser-induced breakdown spectroscopy, J. Anal. At. Spectrom. 32 (2017) 1508–1518.
[33] S.G. Johnson, NIST Standard Reference Database Journal of Physical and Chemical Reference Data Reprints, Energy 41 (2012).